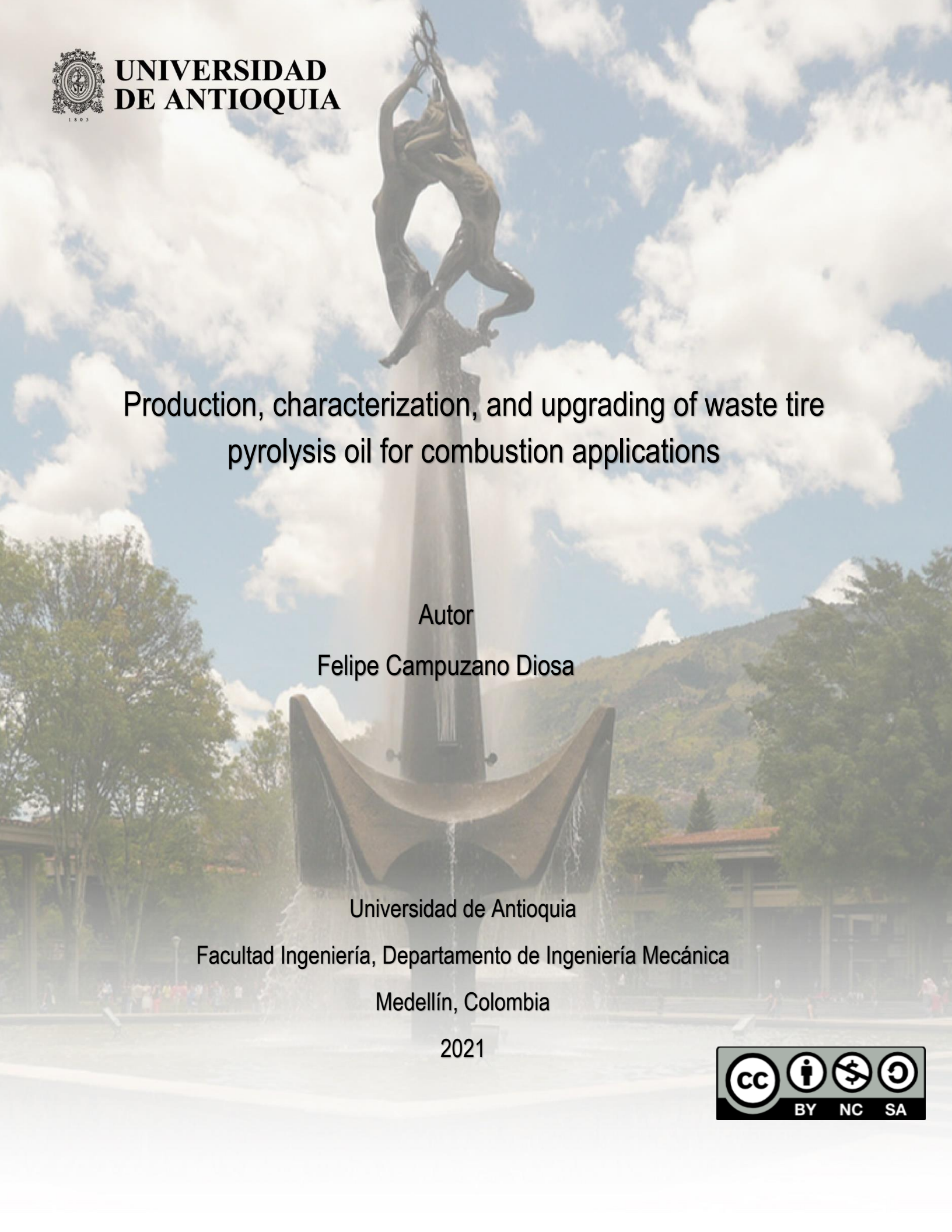

UNIVERSIDAD DE ANTIOQUIA

Production, characterization, and upgrading of waste tire pyrolysis oil for combustion applications

Autor

Felipe Campuzano Diosa

Universidad de Antioquia

Facultad Ingeniería, Departamento de Ingeniería Mecánica

Medellín, Colombia

2021

Production, characterization, and upgrading of waste tire pyrolysis oil for combustion applications

Felipe Campuzano Diosa

Tesis presentada como requisito parcial para optar al título de:

Doctor en Ingeniería de Materiales

Asesores:

Dr. Andrés Felipe Agudelo Santamaría

Dr. John Ramiro Agudelo Santamaria

Asesor Externo:

Dr. Juan Daniel Martínez Ángel

Línea de Investigación:

Maquinas Térmicas y Biocombustibles

Grupo de Investigación:

Grupo de Manejo Eficiente de la Energía (GIMEL)

Universidad de Antioquia

Facultad de Ingeniería, Departamento de Ingeniería Mecánica

Medellín, Colombia

2021

PRODUCTION, CHARACTERIZATION, AND UPGRADING OF WASTE TIRE PYROLYSIS OIL FOR COMBUSTION APPLICATIONS

By

Felipe Campuzano Diosa

A thesis submitted in conformity with the requirements for the degree of Doctor of Philosophy in Materials Engineering

Graduate Department of the Engineering Faculty

University of Antioquia

Advisors

Dr. Andrés Felipe Agudelo Santamaría

Dr. John Ramiro Agudelo Santamaria

External Advisor

Dr. Juan Daniel Martinez Angel

Universidad de Antioquia

Medellín, 2021

To my family and friends for

their unconditional support

Acknowledgement

I would like to express my acknowledgements to the people and institutions that gave me their unconditional support during my doctoral studies at University of Antioquia.

First, I want to express my most sincere gratitude to my research advisors: Dr. Juan D. Martinez, Dr. Andrés F. Agudelo, and Dr. John R. Agudelo for their magnificent directions. Thanks a ton for your encouragement, enthusiasm, and patient not only during my doctoral studies, but also along my entire formation process at both University of Antioquia (UdeA) and Pontificia Bolivariana University (UPB).

Second, I would like to thank my friends and co-workers in the *Grupo de Investigaciones Ambientales* (GIA) (Cindy Arenas, Cristian Ortiz, Natalia Cardona, Lina Castaneda, etc.) and the *Grupo de Manejo Eficiente de la Energía* (GIMEL) (Andres Felipe Lopez, Jackeline Saldarriaga, Cristian Avila, etc.) of UPB and UdeA, respectively, for their worthy friendship and unconditional support along these years. In particular, I would like to thank Dr. Mariluz Bentancur, coordinator of GIA-UPB, for trusting me from the very beginning and giving me the great opportunity to be part of her research team.

Third, I express special acknowledgements to Prof. Dr. Mani Sarathy, Prof. Dr. Willian Roberts for all their support and for making possible my doctoral internship in the *Clean Combustion Research Center* (CCRC) at Kind Abdullah University of Science and Technology in the Kingdom of Saudi Arabia. I also thank all the people in the *Combustion and Pyrolysis Chemistry Group* (CPC) and the *Heavy Fuel Oil Research Team* of CCRC for their guidance and friendship during my internship at KAUST.

In general, I express all my most sincere gratitude to all the staff in GIA, GIMEL, and CCRC for their valuable contributions in my doctoral journey.

Last but not least, I want to thank the *Administrative Department of Science, Technology, and Innovation* (COLCIENCIAS) for my doctoral scholarship (757-2016), as well as for providing the resources needed to conduct the first part of this research through the project 1210-715-51742.

Abstract

Waste tire (WT) valorization has gained significant impetus due to the rise in their pernicious disposal and subsequent environmental harm, coupled with the possibility of recovering both energy and materials. Rubber from WT (a mix of natural and synthetic rubber) exhibits high energy density (HHV 35 - 40 MJ/kg), high volatile matter content (55 - 65 wt.%), and a significant amount of carbon black (35 - 40 wt. %). Based on this composition, pyrolysis has been regarded as one of the pathways with a greater potential to recover both liquid and gaseous hydrocarbons, as well as valuable solid materials from WT. Hence, this thermochemical process has been perceived as a roadmap towards a circular and sustainable economy for WT management.

In this scenario, this dissertation presents a comprehensive analysis, which starts highlighting the environmental and social issues related to WT, outlines their transformation into a valuable liquid fuel (tire pyrolysis oil) via pyrolysis in a twin-auger reactor using low-cost catalytic materials (CaO), and assesses distillation as an alternative for tire pyrolysis oil upgrading. In addition, the fuel and chemical properties of tire pyrolysis oil and its distillate fractions are studied from a fundamental point of view in order to provide new insights for their implementation in practical combustion applications, as well as for formulating further upgrading strategies. Finally, a model industrial pyrolysis plant is propose based on several experimental studies conducted at lab-scale and a thermoeconomic approach is taken in order to identify the benefits of scaling and modifying the process, as well as the potentials for improvement.

In order to carried out this investigation, the initial part of this dissertation considered the study of the operational characteristics of a novel twin-auger reactor to transform WT by intermediate pyrolysis into tire pyrolysis oil (TPO), recovery carbon black (rCB), and tire pyrolysis gas (TPG). The influence of four operating parameters: reactor temperature (X_1), WT mass flow rate (X_2), solid residence time (X_3) and N_2 volumetric flow rate (X_4), was assessed in order to maximize the TPO yield (Y_1), while keeping the rCB one (Y_2) as low as possible. The experimental campaign (thirty runs) was established according to the response surface methodology (RSM) based on a previously defined central composite design (CCD). The analysis of variance (ANOVA) showed that X_1 and X_2 exhibit the highest statistical influence on both Y_1 and Y_2. An optimization of both responses resulted in TPO, rCB, and TPG yields of 45, 40 and 15 wt.%, respectively, when the pyrolyzer is operated at 475 °C, 1.16 kg/h, 3.5 min and 300 mL/min. Furthermore, based on the optimum experimental conditions obtained by means of the RSM analysis, the repeatability of the experimental facility in terms of TPO, rCB, and TPG yields, as well as the consistency of the properties of the derived products were also assessed and discussed. Here, results of the ANOVA test aided at demonstrating that the experimental facility is repeatable in terms of TPO, rCB, and TPG yields. Moreover, the standard deviation calculated from the characterization of different product samples suggested that the physicochemical properties of TPO, rCB, and TPG obtained at given experimental conditions are also consistent.

Thereafter, and going towards the upgrading of TPO, at the optimum experimental conditions, the effect of adding CaO during the pyrolysis of WT on the physiochemical properties of TPO, in particular sulfur content was assessed. As such, CaO was continuously fed at 10, 15, and 20 wt.%, based on a fixed WT mass flow rate (1.16 kg/h). The resulting TPO samples were

initially characterized in terms of sulfur content. Then, the sample presenting the lowest sulfur content (TPO[CaO]) was further studied, along with the rCB and TPG related to TPO[CaO], named in this work rCB[CaO] and TPG[CaO], respectively. By adding CaO during the pyrolysis of WT, a maximum sulfur reduction in TPO of 26.40 wt.% was found. Moreover, CaO addition was also reflected on other physiochemical properties such as a reduction in the viscosity (from 2.6 to 1.9 cSt). Although the ash content of rCB[CaO] was significantly high after pyrolysis (57.5 wt.%), an acid demineralization step was effective at removing 80 wt.% of its inorganic content; in turn, this process improved rCB[CaO] surface area and porosity. Regarding TPG[CaO], an increase in the concentrations of H_2 and some CxHy compounds (*i.e.* C_3H_8, C_2H_6, and C_2H_4), while a decrease in CO_2, CO, and H_2S ones confirmed the participation of CaO in several reactions during the pyrolysis of WT.

Subsequently, this work pursued a comprehensive understanding of the structural characteristics of TPO and TPO[CaO]. Thereby, advanced analytical techniques such as Fourier Transform - Ion Cyclotron Resonance Mass Spectrometry (FT-ICR MS), and ^{1}H and ^{13}C Nuclear Magnetic Resonance (NMR) spectroscopy were utilized. FT-ICR MS results revealed the significant presence of pure hydrocarbons (HC) and hydrocarbons containing one sulfur atom (S_1) in both fuels. HC compounds were found mainly in the form of tri-aromatics, tetra-aromatics, and penta-aromatics, while S_1 compounds in the form of dibenzothiophene and benzonaphthothiophene (34 %). ^{1}H and ^{13}C NMR analysis showed that hydrogen atoms in methylene (CH_2), methyl (CH_3), and naphthenic groups, as well as hydrogen atoms in aromatic structures make up more than 80 % of both fuels. Similarly, carbon atoms in paraffinic groups (both CH_2 and CH_3) and protonated carbons in aromatic rings together form more than 50 % of the carbon atoms in TPO and TPO[CaO]. According to this characterization and considering the chemical complexity and wide boiling point range of TPO and TPO[CaO], distillation was perceived as an interesting alternative to group compounds with similar properties to be further refined and/or used in specific applications. Thus, the reduced sulfur TPO (TPO[CaO]) was further fractionated by distilled at atmospheric pressure into different fractions, named here light, low-middle, high-middle, and heavy. The structural characteristics of each fraction were also studied in-depth utilizing FT-ICR MS and NMR. Among others, fractionation by distillation resulted in concentration of both sulfur and highly aromatic compounds in the heaviest fraction.

In addition to illustrating the structural features, the oxidation characteristics of TPO and TPO[CaO] as whole were investigated using non-isothermal thermogravimetric analysis. The thermogravimetric analyzer used in this study was coupled with a Fourier Transform Infrared (FT-IR) spectrometer, which allowed for obtaining valuable information regarding the real-time compositional changes of the evolved gases during the oxidation processes of both fuels, giving special attention to pollutants such as CO_2, CO, SO_2, NO. Furthermore, a comprehensive study into the oxidation characteristics of only the light fraction of TPO[CaO] obtained by distillation (named $TPO[CaO]_{Light}$) was carried out by conducting combustion experiments in a jet stirred reactor (JSR) under a wide range of experimental conditions (*i.e*. temperatures and equivalence ratios). $TPO[CaO]_{Light}$ was chosen since it was the most abundant (40 vol.%) and it presented the lowest sulfur content among all of the distillate fractions. A surrogate fuel for $TPO[CaO]_{Light}$ was also formulated to facilitate future research into its combustion chemistry. Likewise, this surrogate fuel was tested in the JSR under the same experimental conditions used for $TPO[CaO]_{Light}$ in order to compare the reaction tendencies (*i.e.* fuel consumption rate) and the formation of main intermediate species. In this manner, it was possible

to confirm if the proposed surrogate was a proper representation of TPO[CaO]$_{Light}$. Roughly speaking, the information presented in this part of the research is fundamental for future investigations, for instance the development/adjustment of detailed kinetic mechanisms needed to model the combustion chemistry of the studied fuels.

Finally, a thermoeconomic approach of a model WT pyrolysis plant at industrial scale with a nominal capacity of 1,000 kg/h was taken. This plant was proposed based on an exhaustive experimental campaign in a lab-scale twin auger reactor. Here, an exergy analysis was combined with the thermoeconomic principles to estimate the exergy and exergoeconomic cost of every stream in the process. Through this analysis, it was found that scaling and modifying the process can result in an increase in the plant's exergy efficiency of around 20%, in contrast to the process conducted at lab-scale. In terms of monetary units, the production cost of TPO, rCB, and TPG was found to be 0.054 – 0.095 $/L, 0.035 – 0.062 $/kg, and 0.0082 – 0.012 $/kWh, respectively, depending on the feedstock (WT) price. Finally, an exergy decomposition analysis confirmed that 47 % of the exergy of TPO and TPG comes from renewable resources, namely NR. Therefore, their use as fuels is in line with the worldwide guidelines regarding the promotion of renewable energy, *e.g.* the 2009/28/EC European directive. In addition, 47 % of the energy of the combustion gases released into the atmosphere come from renewable resources, which implies reduced net carbon emissions. This could give rise to several benefits for this project, *i.e.* in terms of carbon credits.

Graphical abstract

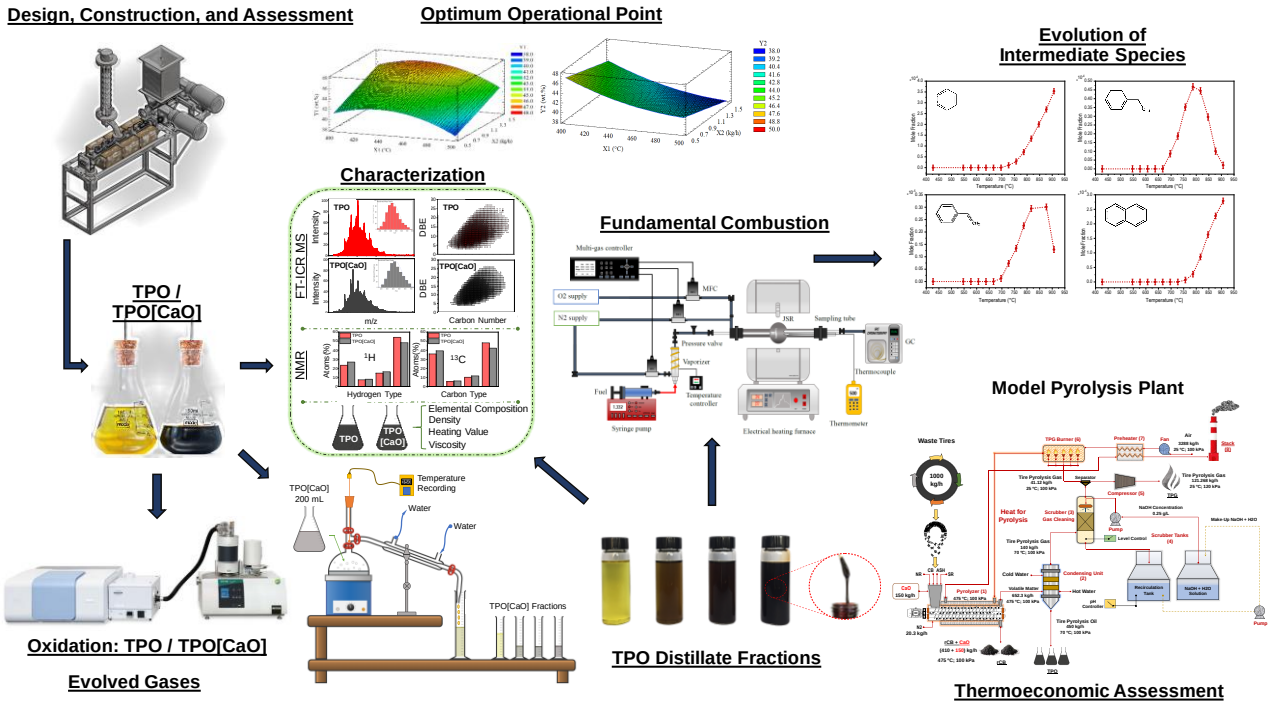

Content

Chapter 1. Introduction

Waste management is one of the core issues for the sustainable development of societies, given the large generation of waste per capita, of which more than a quarter is municipal solid waste (MSW). In particular, the accelerated increase of rubber waste, derived mainly from waste tires (WT), has become a serious concern due to their complex structure and composition (*i.e.* vulcanized rubber cured by sulfur, carbon black, zinc oxide, and silica). The pursuit of recycling and recovery of such materials is difficult because WT are insoluble, infusible, and cannot be retreated in simple processes like those used for thermoplastics. By nature, tires are designed to withstand harsh mechanical and weather conditions such as ozone, light, and bacteria, thus impeding their further processing [1,2]. In addition, the logistics is expensive because of the toroidal shape of WT (around 75 % of its volume is empty space), which complicates their final disposal. Even though WT do not present an imminent danger, their mass production coupled with inappropriate disposal methods, have exhibited detrimental effects on both the environment and public health [3].

There are several factors that have shifted the attention of environmental authorities and research entities to develop strategies towards the sustainable management and valorization of WT. These factors include, among others: (i) the high amount of tires discarded every year (estimated to be around 17 million tons per year [4]), (ii) the environmental damage caused by their uncontrolled disposal, (iii) their non-biodegradable character, (iv) the increasing demand for recycling hydrocarbons, and (v) the growing desire to develop sustainable methods to valorize WT within the framework of circular economy (Figure 1.1) [5,6]. A number of reports published by the most important associations of producers and recyclers of tires worldwide have revealed the ongoing progress towards this scope [7–10]. This progress has been the result of the continuous establishment of restrictive regulations banning stockpiling and landfilling of WT. Also, these regulations enforce the reuse, recycling, and recovery of these materials as mandatory procedures, in agreement with the waste hierarchy (Figure 1.1).

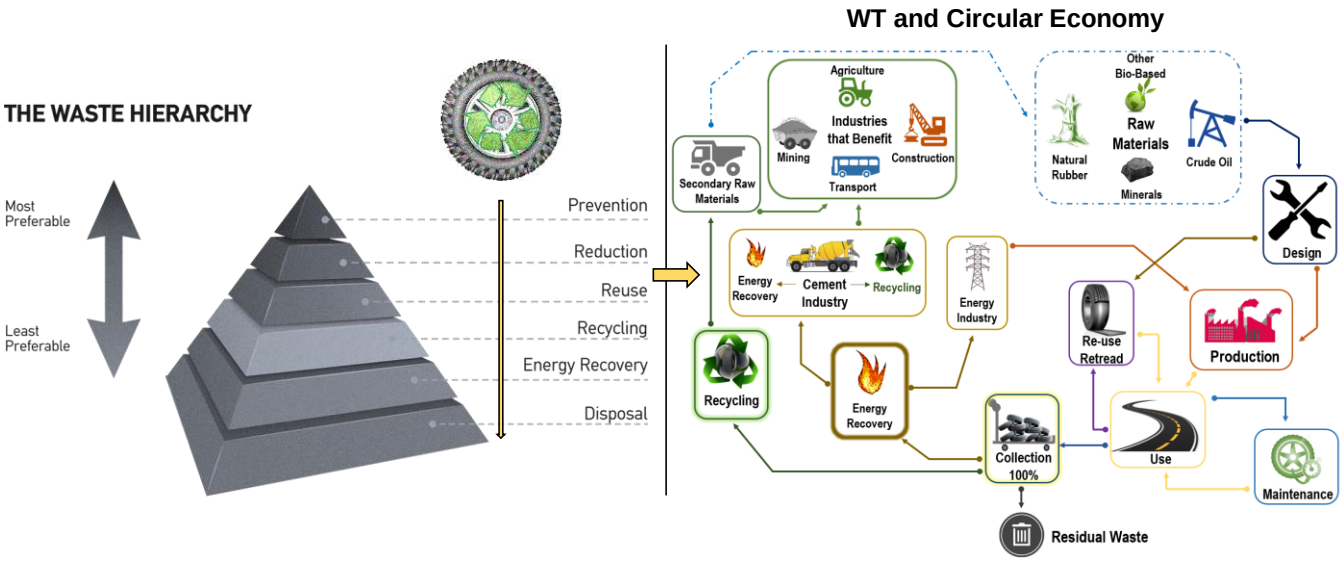

Figure 1.1. The waste hierarchy and the circular economy

Accordingly, developed economies have implemented effective management strategies to deal with the WT generated. For instance, around 28% of the WT generated in the EU is being used for cement production [3], while in the USA the cement kilns and other energy demanding processes account for 43% of the total amount generated [7,9]. Similarly, in Japan, around 63 % of the recovered WT are used in thermal processes such as cement kilns, gasification facilities, and paper manufacturing, among others [9]. The remaining amount is often used for retreating, reuse or as a raw material (granulated or powder rubber) in other productive processes and engineering applications, being landfilling the least desirable practice.

Latin American (LA) countries such as Brazil, Mexico, Chile, and Colombia have implemented the extended producer responsibility (EPR) for end-of-life products, including WT. After collection, the most common practice is the use of WT in combustion processes for cement production. Nevertheless, waste management has historically been hampered by weak infrastructure in LA. Therefore, these initiatives have not been satisfactory enough to guarantee proper waste disposal. The collection of WT in LA faces many challenges, given the lack of joint actions among the final consumers, the government, and private companies [11]. In the Colombian case, the establishment of regulations 1457 (2010) and 1326 (2017), regarding selective collection systems and the environmental management of WT, is expected to accelerate the progress towards a more sustainable management of WT.

Even so, the improvement made in recent years concerning the management of plastic waste, especially in developed economies, has rendered WT as a potential resource to obtain products with wide applicability in diverse productive sectors, including energy, materials, petrochemicals, etc., [12]. In this context, pyrolysis is a thermochemical process that provides a sustainable solution, because it allows the transformation of WT into useful products, instead of heat and CO_2, as occurs in combustion. The pyrolysis of WT produces: (i) a liquid fraction (tire pyrolysis oil: TPO) containing valuable chemicals and exhibiting appealing fuel properties, (ii) a gas fraction (tire pyrolysis gas: TPG) containing significant amounts of H_2 and CH_4, that lead to a heating value similar to that of natural gas (>30 MJ/Nm^3), and (iii), a recovered carbon black (rCB) which groups all the carbon blacks and the inorganic compounds used in tire manufacture [13–16].

From an environmental point of view, and in contrast to other conversion pathways implemented for the valorization of this waste (*i.e.* combustion and gasification), pyrolysis is able to minimize the emissions of hazardous contaminants and pollutants such as dioxins, furans, and particulate matter, given that it is performed under an inert atmosphere (usually N_2) and at lower temperatures (250 – 550 ºC). All these facts have rendered pyrolysis as a suitable process for the WT management/valorization within the framework of circular economy [17]. Therefore, research and development activities on the field of WT pyrolysis remains an open topic worldwide.

In particular, TPO is one of the most abundant and promising products obtained from this process [13]. It can be used as a feedstock in petroleum refineries or as a source for the production of refined chemicals, such as BTX (benzene, toluene, and xylene) [18]. Due to its potential in different economic sectors, TPO is currently studied considering its production, characterization, upgrading, and implementation [16,18–20]. Among all of the alternatives, combustion seems to be the most

straightforward pathway to use TPO, as a result of its high energy density (HHV~43 MJ/kg), along with some physical and chemical properties similar to those of conventional petroleum-derived fuels [5,13,14,21,22]. In fact, TPO is often compared in the literature to petroleum derived fuels such as fuel oil (FO), which is widely used in thermal energy facilities [23].

Considering its renewable characteristics (around 50% of the rubber used in tire manufacture comes from natural resources) and its compatibility with conventional crude oil (completely miscible), TPO is fully aligned with the definition of *drop-in-biofuels* established by Task 39 of the International Energy Agency (IEA): "*Drop-in biofuels are liquid hydrocarbons that are functionally equivalent to petroleum fuels and are fully compatible with existing petroleum infrastructure".* The use of TPO as fuel is also in accordance with worldwide guidelines regarding the promotion of renewable energy, *e.g.* the 2009/28/EC European directive. All these facts suggest that TPO could be considered as a suitable choice to be part of the variety of alternative hydrocarbon feedstocks needed to supply the upcoming energy demand.

Accordingly, this dissertation presents a comprehensive analysis, which starts highlighting the environmental and social issues related to WT, outlines their transformation into a valuable liquid fuel (TPO) via pyrolysis in a novel twin-auger reactor using low-cost catalytic materials (CaO), and assesses distillation as an alternative for TPO upgrading. In addition, the fuel and chemical properties of TPO and its distillate fractions are studied from a fundamental point of view in order to provide new insights for their implementation in practical combustion applications. Finally, a model industrial pyrolysis plant is propose based on several experimental studies conducted at lab-scale. Based on this model plant, a thermoeconomic approach is taken to allocate energy, exergy, and economic costs associated with the production of the derived-pyrolysis products and exergy losses.

In this regard, the main goals of this investigation are: (i) to study the potential of pyrolysis and the twin-auger technology for the valorization of WT within the framework of the circular economy, (ii) to explore *in-situ* (desulfurization using CaO) and *ex-situ* (fractionation by distillation) upgrading strategies for TPO, (iii) to develop a deep understanding of the properties affecting the combustion characteristics of TPO and its distillate fractions, and (iv) to identify the benefits of scaling and modifying the pyrolysis process, as well as the assessment of improvement potentials by applying the thermoeconomic principles.

This introductory chapter provides a brief but fundamental survey regarding pyrolysis as a method for the valorization of WT. Likewise, the main physicochemical and combustion characteristics, as well as applications and challenges of TPO (the focus of this dissertation) are discussed. Finally, a general overview of the thermoeconomic approach and its potential for assessing the WT pyrolysis process is presented. In accordance with this literature survey, the motivation, research questions, and objectives for this work are formulated. This chapter is therefore divided into four main parts:

I. The first part (*Section 1.1*) contains general information regarding the fundamentals of WT pyrolysis, the mechanisms related to the process, and a general description of the reactors used for pyrolysis giving special attention to the auger technology (twin-auger configuration).

II. The second part (*Section 1.2*) discusses the main fuel and chemical properties of TPO, highlighting the main potentials and challenges for TPO implementation in combustion systems, as well as possible upgrading strategies. In addition, the progress on understanding its combustion behavior from a fundamental standpoint.

III. The third part (*Section 1.3*) provides a general description of the thermodynamic methodology, and its potential in gaining in-depth understanding of the pyrolysis process in order to identify exergy and economic costs of products and losses.

IV. The fourth part (*Section 1.4*) presents the motivation for conducting this investigation. In turn, this motivation provides a solid criterion to stablish the research questions, the objectives, and the structure of this dissertation, which are also presented in this section.

1.1 Fundamentals of waste tire pyrolysis

The pyrolysis of WT can be regarded as an endothermic process performed in an oxygen-free atmosphere at temperatures between 250 °C and 550 °C (although some works have reported up to 1,000 °C [24,25]). Conditions for the process depend on the feedstock characteristics (composition, particle size, etc.) and on the main target: to maximize the liquid (TPO), the gas (TPG) or the solid (rCB) fractions. Pyrolysis is essentially a molecular breakdown process, usually conducted in an inert gas environment at atmospheric or slightly high pressures, even though vacuum conditions [26] or pressurized hydrogen are also employed [27,28]. Pyrolysis requires heat supply to the reactor (known as the heat for pyrolysis) in order to drive the thermal decomposition of the feedstock into products [29], as shown in Figure 1.2. In general, yield ratios and physicochemical properties of these products are closely related to the feedstock composition, to reactor technology, and to the main pyrolysis-governing variables (*i.e.* temperature, pressure, heating rate, residence time, etc.). Several works reported in the literature associated with the pyrolysis of WT have aimed at developing a deep understanding of how these factors influence the characteristics of the final products [13–16].

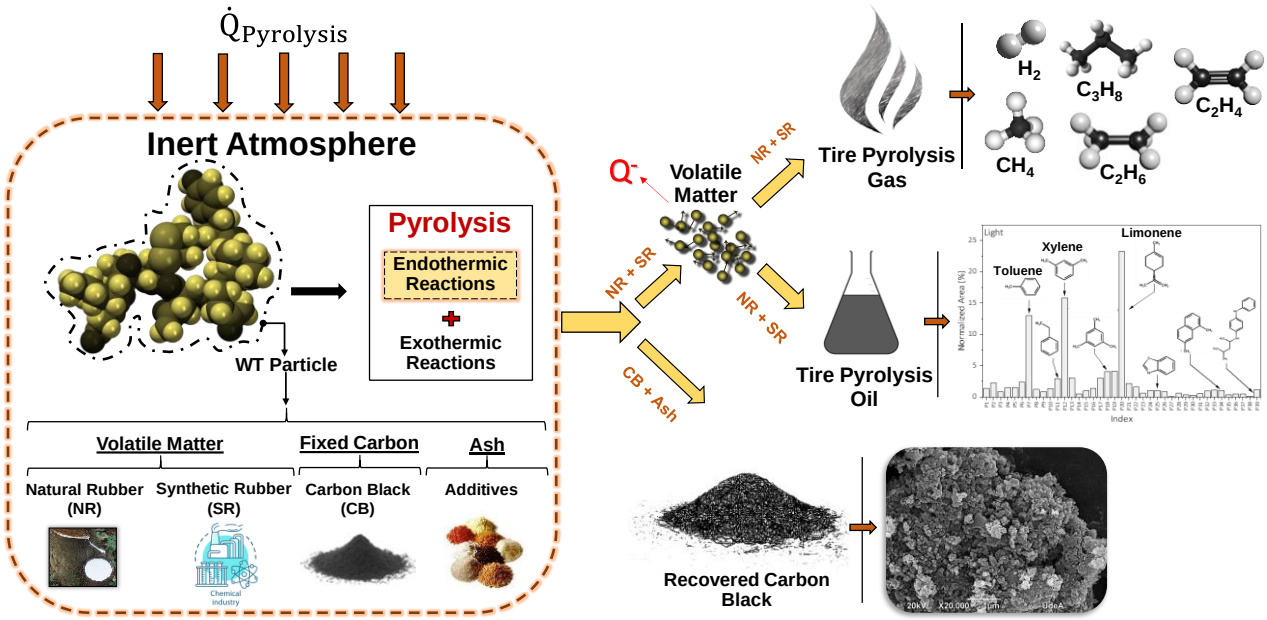

Figure 1.2. Schematic representation of the pyrolysis of WT

WT particles are a mixture of natural (NR) and synthetic (SR) rubber, as well as carbon black (CB) and inorganic materials (Ash). At conditions of high temperatures (600 °C - 700 °C) in an environment with no or very little oxygen, these particles release volatile matter (a mixture of different hydrocarbons). These products then encounter secondary reactions such as thermal and catalyst-cracking, repolymerization, recondensation, oxidation and reduction, etc. [30]. The pyrolysis of WT follows complex routes (*i.e.* random chain scission, end chain scission, chain stripping, and cross-linking [30]) that cannot be easily described by accurate reaction mechanisms. The reason for this is that reaction pathways are highly sensitive to the experimental system: temperature, feedstock composition, particle size, and thermal regime (heat transfer or kinetic control) [31]. Multiple reaction mechanisms have been proposed in the literature for the pyrolysis of WT [32–36]. A recent work published by Menares *et al.* [31] presents a summarized reaction mechanism of this process (Figure 1.3), which is based on the results obtained by the integration of thermogravimetric analysis (TGA), kinetic modelling, and an analytical pyrolysis reactor coupled to a gas chromatography/mass spectrometry (Py-GC/MS) device. The TGA results showed by Menares *et al.* [31] indicate that WT pyrolysis is ruled by devolatilization/condensation and propagation reactions, up to 482 °C. At higher temperatures, the cyclization and aromatization of primary products take place to form mostly monoaromatic compounds such as BTX that are then found in the resulting TPO.

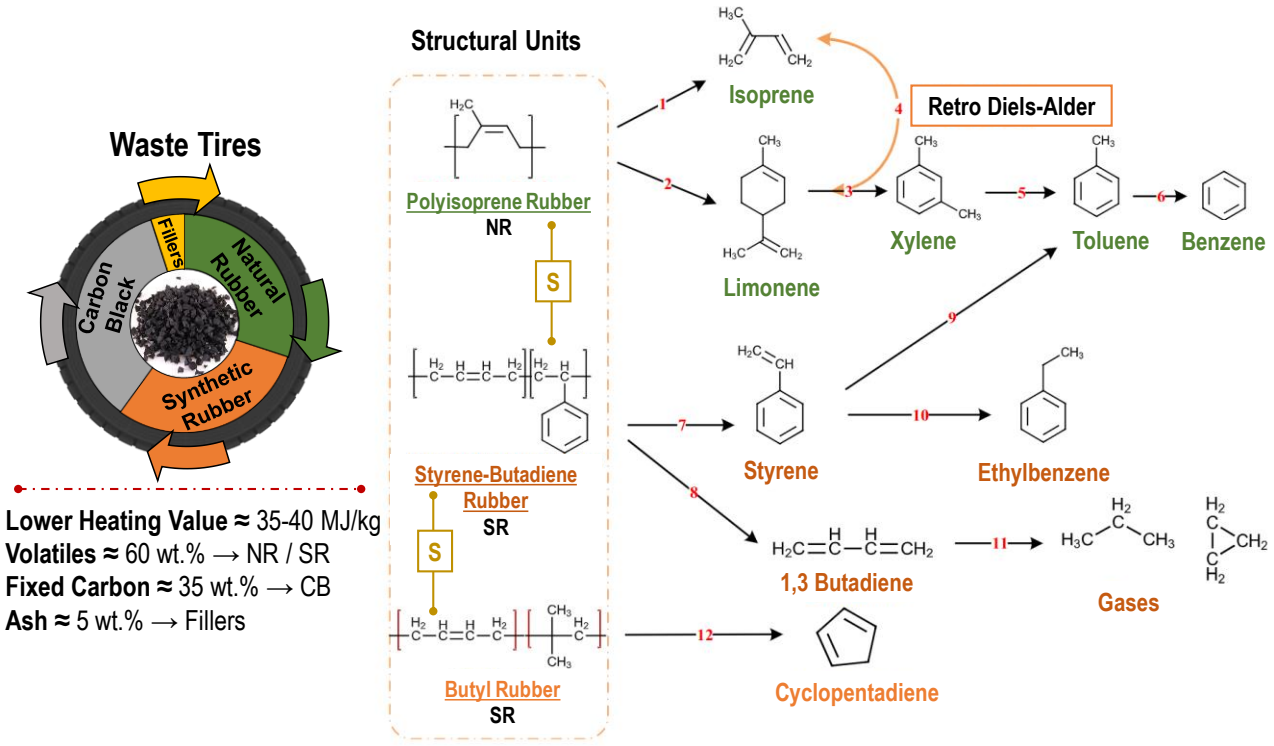

Figure 1.3. Proposed reaction mechanism of WT pyrolysis (adjusted from [31]).

Several types pyrolyzers have been used to assess the pyrolysis of WT at lab-scale, including fixed bed reactors [37], rotary kilns [38], fluidized bed reactors [39], and auger reactors [40], among others [5,13,14]. All of these reactors/configurations have exhibited advantages and disadvantages in terms of technical and economic parameters. They have also been used for different

energy applications, depending on the feedstock characteristics and the final target (TPO, TPG or rCB). Recently, auger reactors have received special attention due to their potential to transform a wide range of feedstocks by means of a continuous process, and because they allow an accurate control of the solid/vapor residence time. The advantages of using an auger reactor also include low specific size and portability, which imply a reduction of the costs associated with transportation, management, and logistics of the feedstock. Furthermore, auger reactors, in particular the twin-auger configuration, offer a high degree of mixing and heat transfer, which favors the conversion of the feedstock during pyrolysis. These characteristics have rendered the twin-auger configuration suitable for conducting processes such as co-pyrolysis and catalytic pyrolysis. A work derived from this dissertation presents a comprehensive description of the auger technology, including heat supply methods, design recommendations, scaling up considerations and examples of commercial/demonstration-scale auger pyrolysis plants operated around the world [41].

For the pyrolysis of WT, the auger reactor is still considered as a new technology in comparison to other well-developed ones such as rotary kilns, and fixed bed reactors that are in a more mature stage. Nonetheless, previous works reported in the literature have highlighted the advantages of the auger technology in this field, including both single and twin configuration [40,42–49]. In particular, Martínez *et al*. [40] demonstrated the suitability of the single-auger technology for the pyrolysis of WT on a pilot scale, and the potential to scale it up to a commercial level. This was supported by the reproducibility and stability of the process during more than 100 hours of operation. Similarly, the appeal of this technology is also attributed to the possibility of maximizing the TPO yield, while reducing rCB (low content of volatile matter), which is achievable via an accurate control of the operating conditions, particularly solid residence time, as mentioned previously.

It is worth to highlight in this point that the Environmental Research Group (GIA), at Universidad Pontificia Bolivariana (Medellin-Colombia), has been studying the auger technology, in particular the twin configuration, for the pyrolysis and co-pyrolysis of different feedstock including WT on a pilot–scale. This experience has supported to a great extent the development of the present work in the design, construction, and assessment of the operational features of a twin-auger pyrolysis plant at lab-scale, as well as the production of the TPO used in the characterization trials and the fundamental combustion studies conducted in this investigation [17,41,50].

1.2 Tire pyrolysis oil

1.2.1 General characteristics of tire pyrolysis oil

TPO is a dark-brown liquid containing a complex mixture of several hydrocarbon families with a wide carbon number range (C_5–C_{50}), some heteroatoms including sulfur and nitrogen, as well as oxygen to a minor extent. Its H/C atomic ratio is around 1.5, which indicates the presence of both aliphatic (paraffins) and aromatic compounds [16,51]. This oil has high energy density (HHV: 40-44 MJ/kg), and physical and chemical properties comparable to those of crude oils, such as kinematic viscosity (1.70-17.80 cSt) and density (871-995 kg/m^3) [5,13,14,21,22]. Elemental bulk carbon, hydrogen, nitrogen, sulfur, and oxygen contents depend on both feedstock composition and pyrolysis conditions (temperature, residence time, etc.), and are usually in the ranges

of 83-87 wt.%, 9-11 wt.%, 0.4-1 wt.%, 0.6-1.4 wt.%, 0.2-2.1 wt.%, respectively. [13]. TPO contains different types of hydrocarbons with boiling points ranging from 70 ºC to 450 ºC, or higher. Hita *et al*. [5] reported that TPO could be fractionated into 25.7 wt.% naphtha (boiling point 36 - 216 ºC), 44.5 wt.% diesel (boiling point 216 - 343 ºC) and 29.8 wt.% gasoil (> 343 ºC). This suggests that TPO can be considered as an unrefined hydrocarbon source [13]. Light aromatic hydrocarbons (BTX), polyaromatic hydrocarbons (naphthalene), aliphatic hydrocarbons (dodecane, tridecane), and monoterpenes (limonene) seem to represent some of the major compounds in the mixture [52–55]. In general, a complete understanding of these characteristics is an important and fundamental step in identifying and improving application and upgrading strategies for TPO.

Lately, several works reported in the literature have aimed at providing comprehensive insights into the chemical properties of TPO [56–59]. However, the extent of knowledge regarding TPO's molecular structure is rather limited due to its complexity, which renders molecular resolution with conventional analytical techniques quite difficult. For instance, Fourier Transform Infrared (FT-IR) spectroscopy [57,58] and gas chromatography coupled to mass spectroscopy (GC-MS) [60] have been widely used to identify the types of bonds in the molecules, as well as to analyze individual components in TPO. Nonetheless, due to the limitation of these techniques, it has been challenging to obtain a complete picture of TPO. Nowadays, higher-resolution analytical techniques, including Fourier Transform Ion Cyclotron Resonance Mass Spectrometry (FT-ICR MS) [61–65] and Nuclear Magnetic Resonance (NMR) [66] would be ideally suited to characterize complex and high molecular weight fuels such as TPO which possess high molecular weight molecules with the presence of some heteroatoms.

1.2.2 Tire pyrolysis oil as alternative fuel

TPO has a strong potential to be a partial substitute of petroleum-derived fuels in several industrial processes where thermal systems such as boilers, furnaces, and internal combustion engines are used [67–69]. For instance, the use of TPO in compression ignition engines has been reported in a number of studies [45,67,70–75]. Current approaches to operate diesel engines with TPO have mainly relied on the following strategies: (i) blending TPO with conventional fuels (diesel) [45,67,70,72,75–77], or with methyl esters [73,78,79], (ii) increasing intake air temperature above threshold [80], and (iii) increasing the compression ratio [74]. As a general conclusion, all these studies show acceptable performance up to 70 v/v % of TPO blended with diesel fuel. Even so, Bascovic *et al.* [81] demonstrated the possibility of using pure TPO in a common rail diesel engine by adding one pilot injection and retarding it in relation to the original ECU injection strategy.

Overall, adding TPO to conventional diesel engines have not represented a remarkable effect on the performance characteristics, but it has caused an increase in some pollutants such as CO, NOx, SO_2, THC, and PM. Despite the potential of partially substituting conventional fuels in diesel engines, the use of TPO faces several challenges under the current regulations (standard fuel specifications and emissions). First, some physicochemical and combustion properties of TPO are out of specification according to the diesel fuel standard [82]. These properties include density, water content, cetane number, distillation characteristics, etc. However, the sulfur content seems to be the main limitation (for diesel, its sulfur must be ≤ 10 ppm). Second, environmental limits related to SO_2, NO_2, and CO emissions levels established by the European Air Quality

Standard (EU2015/2193) have also restricted the use of TPO in automotive engines. Altogether, this suggests that upgrading strategies (in particular deep desulfurization methods) are required to improve the physicochemical properties of TPO before its use in these types of systems.

Alternatively, a more direct approach for the use of TPO could be in industrial burners [68], boilers [83], marine engines [84], and for power generation in large stationary engines [85]. The sulfur limits regarding these applications are considerably more permissive than those established for automotive purposes (*i.e.* 1,000 ppm instead of 10 ppm, according to the Spanish Royal Decree 61/2006 or in the case marine fuels, sulfur should be lower than around 5000 ppm [84]). Even so, all these studies have suggested that certain properties should be improved in order to increase the applicability of TPO from a technical and environmental point of view. These properties usually include a high content of aromatic compounds (up to 65 wt.%), as well as several other elements such as fuel-bound nitrogen (0.40 – 1.05 wt.%), and sulfur (0.6 – 1.4 wt.%). Additional drawbacks of TPO for its used as an alternative fuel include: (i) the significant presence of BTX, and limonene, which tend to increase ignition delay time (IDT); (ii) a high final distillation point (550 °C), affecting its vaporization during combustion; and (iii), a low flash point (up to 30 °C), making it difficult to handle and store [5,13,16]. Table 1.1 summarizes some characteristics of TPO and the related challenges for its application.

Table 1.1. Characteristics of TPO and related challenges for its application.

Property	Characteristics	Issues
Sulfur Content	Usually between 0.6 -1.4 wt.%. Sulfur is added to tires in the vulcanization process. Up to 70 % of initial sulfur in tires remains in recovered carbon black after pyrolysis. The remaining fraction is distributed into pyrolytic gas and TPO [86]. Sulfur compounds in TPO are in the form of thiophene, benzothiazole, benzothiophene, etc.	Sulfur containing compounds are environmental pollutants. During oxidation, SOx are produced and released as gas products. SOx also reaches the lubricant oil, causing corrosion problems in combustion systems like internal combustion engines.
Nitrogen Content	Commonly in the range of 0.4 -1.05 wt.%, depending on initial tire composition and attributable to thermal degradation of accelerators such as N,N-di-isopropyl-2-benzothiazole-sulfenamide, 2-(4-morpholinylthio)-benzothiazole, N,N caprolactamdisulphide, and 2-mercaptobenzothiazole incorporated into tires during formulation. Nitrogen in TPO is commonly found in the form of benzothiazole, also containing sulfur.	High nitrogen levels in the fuel lead to fuel NOx formation during combustion, which may cause acid rain.
Flash Point	Usually lower than 30 °C, this low flash point is due to high fraction of volatile compounds in TPO.	High flash point of a liquid fuel is beneficial for storage. A lower flash point is easier for igniting the fuel/air mixture; liquid is considered flammable if its flash point is less than 60 ºC.
Aromatic Content	As much as 65 wt.% of TPO could be represented by aromatic hydrocarbons, associated with the aromatic nature of rubber (one aromatic ring in the styrene butadiene rubber monomer) and the cyclization of olefin structures, followed by dehydration and Diels-Alder reactions, favored at high temperature in the pyrolysis process.	Aromatic hydrocarbons are associated with incomplete combustion (due to long IDT) and the tendency to form particulate matter (PM) (act as PM precursors).
Final Distillation Point	Final distillation point is usually higher than 550 °C, which is associated with the presence of high molecular weight compounds like polycyclic aromatic hydrocarbons (PAH) and polycyclic aromatic sulfur hydrocarbon (PASH).	Fuel's boiling point affects its vaporization and combustion process. A high final boiling point may decrease the vaporization rate, resulting in incomplete combustion and PM formation.
Ignition Delay Time (IDT)	Significant presence of light aromatic (BTX) and iso-paraffinic (limonene) hydrocarbons tends to increase the IDT of TPO, resulting in a low cetane number. These compounds have stable molecular structures, requiring high temperatures and pressures to ignite.	In diesel engines, fuels with high IDT may increase PM emissions, given that combustion begins later in the expansion stroke, when the temperature inside the chamber decreases. Oxidation rate decreases here, increasing the concentration of unburned hydrocarbons which may further condense on the PM surface. Hence, the PM mass increases [87].

1.2.3 Upgrading strategies for tire pyrolysis oil

Intensive research has been conducted to improve the above-described properties and increase the value and quality of TPO. Techniques such as catalytic pyrolysis (*in-situ* upgrading), or optimization of the pyrolysis conditions, have been conducted to selectively favor the yields of certain compounds during the pyrolysis of WT [88,89]. Regarding the presence of sulfur (the main drawback), various alternatives have been explored in order to reduce its content in TPO, which include *in-situ* and *ex-situ* desulfurization pathways. *In-situ* methods have involved the addition of different catalysts and/or sorbents into the same pyrolyzer [51,90,91]. Within this context, calcium-based materials have been posed as promising alternatives due to their low-cost, high abundance, and desulfurization capability. For instance, previous studies reported the use of calcium hydroxide ($Ca(OH)_2$) [21], natural dolomite ($CaMg(CO_3)_2$) [91], and calcined dolomite (CaO + MgO) [91], among others, during pyrolysis. By using these materials, desulfurization percentages up to 34 wt. % have been achieved in TPO. In general, these alternatives seem to be promising as first hint to improve the properties of TPO since they offer low related cost and simplicity.

On the other hand, e*x-situ* desulfurization processes commonly involve extraction, oxidation/extraction (oxidative desulfurization), distillation (fractionation) and hydrotreating (hydrocracking and hydrodesulfurization). These processes are applied after TPO is produced [20,88,92–98], or the volatile matter released from WT during pyrolysis is directed into a separate upgrading stage [99,100]. In fact, due to the compatibility of TPO with petroleum derived fuels, *ex-situ* upgrading strategies may have several steps in common with those implemented in conventional refineries, usually including oxidative desulfurization (ODS) and hydroprocessing (HP). In this regard, ODS of TPO has been previously assessed in several experimental studies where desulfurization percentages up to 75 wt. % have been achieved [88][92,93]. Moreover, HP has also been widely explored to improve the properties of TPO [20,94–98]. A nearly complete reduction of the sulfur content (99.9 %) has been found, as well as an increase in the paraffinic and iso-paraffinic portions (up to 70 %) in the desulfurized TPO.

Even though these upgrading strategies appear to be adequate in overcoming the compositional barriers of TPO, such processes have been conducted mostly in lab-scale plants under highly controlled conditions, making their applicability for large-scale TPO production uncertain. First, ODS presents significant challenges given that certain oxidant agents tend to reduce the quality of the final product. The use of an incompatible solvent may result in removing desirable compounds, or extracting less sulfur from the fuel, affecting the quality and yield of the final product. In both cases, the consequences are costly [101,102]. Second, HP has been described as an expensive process, unsustainable for small to medium scale pyrolysis plants. A dedicated HP facility for TPO implies the construction of units with a massive supply of H_2, resulting in high operating costs and increasing the price of the final product. These limitations defy the concept of pyrolysis as a relatively simple, widely distributed technology. The WT pyrolysis industry is in its early stages and cannot compete with petroleum refineries in terms of technological capacity and cost, making all these upgrading steps highly challenging from the feasibility point of view in the short run.

As an alternative, Rodriguez *et al*. [103] recently investigated the possibility of using TPO as a feed or co-feed in the cracking of vacuum gasoil in a fluid catalytic cracking unit (FCC). Their results demonstrated that the use of TPO in FCC units leads to

high gasoline-like fuels which frame this option as a viable and economically attractive route for valorizing WT, in agreement with the concept of waste refinery. Similarly, in line with the principles of the waste refinery approach, fractional distillation offers interesting advantages for TPO upgrading [104]. Considering the chemical complexity of TPO regarding the wide range of both carbon number (C_6 – C_{55}) and boiling point (70 – 550 ºC) [50], fractionation by distillation would be an attractive method of grouping similar compounds, based on their volatility. Distillation is by far the most important and widely used separation process in a petroleum refinery. In conventional refineries, crude oils are distilled into groups with similar properties to be further characterized, upgraded, and used in different systems. In an analogous manner, different fractions of TPO could be separated according to their boiling points in order to be refined and used individually. Previous works have reported that separating TPO into distinct fractions by distillation can expand the range of possibilities, making it more suitable for specific applications, rather than using the raw oil directly [105–107]. For instance, high molecular weight sulfur-containing compounds in TPO could be concentrated in the leftover heavy fraction, improving the characteristics of the remaining fractions. In this manner, subsequent severe upgrading steps can be minimized or even avoided for some of the resulting distillate fractions.

Distillation data alone is not conclusive about whether a fraction is suitable for a particular application. Therefore, after fractionation, more detailed knowledge about the characteristics of each fraction is also necessary. Clarification of these features is essential to understand the deployment of each fraction in practical combustion applications, as well as for fuel upgrading strategies. In addition, a comprehensive characterization of TPO distillate fractions by means of advanced analytical techniques such as the ones mentioned before (GC-MS, APPI FT-ICR MS and ^{1}H and ^{13}C NMR) would allow to correlate (and ultimately predict) their properties and behavior in thermal systems. For instance, it would be possible to estimate molecular mass distribution, distillation profile, heavy ends (asphaltenes content), and sulfur distribution, among others [108]. Up until now, just few works have studied the distillation of TPO and the characteristics of the resulting distillate fractions [104].

1.2.4 Fundamental combustion characteristics of tire pyrolysis oil

In addition to investigate the structural characteristics of TPO and its resulting distillate fractions, the study of their combustion behavior is of great importance for their efficient utilization in thermal systems. The cited works along this chapter regarding the application of TPO in thermal systems have mainly aimed at describing basic combustion properties and emissions in internal combustion engines, boilers, and furnaces [22,67–69,83]. Despite the important insights provided by these studies, the extent of knowledge regarding the combustion behavior of TPO from a fundamental point of view is still quite limited. The use of complex configurations to study the combustion of TPO complicates the accurately control of all the experimental parameters. Thereby, the obtained results could be influenced by those variables that are hard to control during the process. Hence, the obtained performance cannot be completely associated with the nature and properties of the fuel [109]. Recently, Muelas *et al*. [109] made some progress on understanding the fundamental combustion characteristics of TPO by conducting single droplet combustion studies of a well characterized TPO sample. Here, combustion characteristics such as droplet and flame size evolution, burning rates, soot shell morphology, microexplosion occurrence, and soot analysis were assessed. According to the authors, this information can be used as the fuel-specific input data required for the simulation of realistic spray flames. Aside

from the study carried out by Muelas *et al*. [109], the knowledge regarding the combustion features of TPO from a fundamental point of view is still scarce.

1.3 Thermoeconomic assessment of the waste tire pyrolysis process

Aside from a comprehensive understanding of the operational features of the pyrolysis process and properties of the derived products, the assessment of its operational efficiency is also a fundamental step. This type of analysis is of great interest for identifying potential improvements when either scaling up the process, improving the performance of exiting pyrolysis facilities or even for comparing, from an energy standpoint, with different WT valorization pathways (*i.e.* gasification or combustion). In this scenario, the thermoeconomic approach is a methodology that combines exergy and economic principles aiming at assessing energy conversion systems [110]. Results from the thermoeconomic analysis provide crucial information regarding the effect of design and operation of the system, which is not possible to obtain with conventional energy and economic analyses. Overall, this methodology is regarded a powerful engineering tool to detect possible malfunctions (irreversibilities) in real processes, allocate them, quantify the influence of system components, understand their causes, and ultimately reduce operating costs [111]. Up to date, beyond some energy and techno-economic studies [40,112], the thermoeconomic methodology has not yet been applied to study the pyrolysis of WT.

1.4 Motivation to conduct this research

Over the last three decades, several studies have been conducted on the pyrolysis of WT using different pyrolyzers and operation modes (batch or continuous). As discussed along this chapter, these studies have aimed at developing a comprehensive understanding of the influence of the pyrolysis technology and operational variables on both yields and characteristics of the products. Lately, auger reactors, in particular the twin-auger configuration, have been recognized as one of the technologies with better strengths for fast, intermediate, and slow pyrolysis, which is not possible with other technologies (Figure 1.4). However, information regarding the use of twin-auger reactors for the pyrolysis of WT in the literature is still scarce.

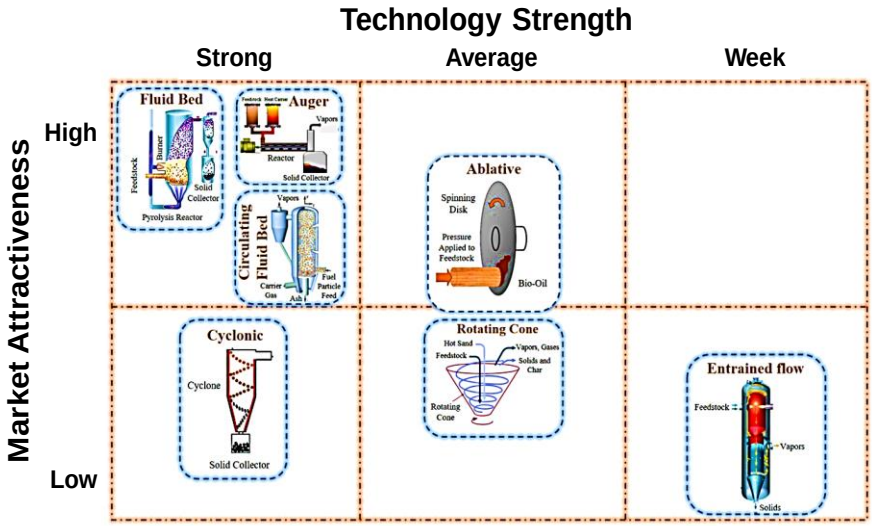

Figure 1.4. Strength and attractiveness of different pyrolysis technologies (adapted from [113])

More research is therefore needed to strengthen the potential of this technology to valorize WT in accordance with the circular economy principles. In addition, due to the intrinsic characteristics of the twin-auger (*i.e.* high degree of mixing and heat transfer), *in-situ* desulfurization using low-cost calcium-based materials such as CaO could be an attractive option as a first hint to improve the properties of TPO. The simultaneous study of WT pyrolysis combined with *in-situ* desulfurization has not yet been investigated in twin-auger pyrolyzers.

The development of auger technology for the pyrolysis of WT can be addressed from the assessment of its reliability in the long-term, as well as on the identification of the proper operational conditions to achieve a balance between a high TPO yield and adequate physicochemical properties of the rCB. These are major key factors that will ultimately define the feasibility of this technology. On the other hand, one of the main challenges in the development of a *waste-to-energy* process is the unpredictable variation of the prices of raw material and oil in the global market. This makes difficult to establish competing prices for new products, especially considering that new technologies will be placed at a commercial scale in the long term. Therefore, in order to maintain a sustainable profile for these new technologies researchers and engineers must ensure that such processes are conducted in an efficient and low-cost manner with minimal process malfunctions and emissions. These points must be carefully considered, and therefore, besides the assessment of the quality of the products, the development of new technologies must be accompanied with the analysis of performance and environmental indicators. Within this context, a thermoeconmic approach (combination of exergy analysis and economic principles) could provide insights into the design and operation of cost-effective systems for this process, which is not possible by means of conventional energy or economic analyses.

Regarding the pyrolysis products, particularly TPO, there is no much information available in the scientific literature regarding its fundamental fuel and chemical properties. Therefore, unraveling structural features of TPO has been a challenging undertaking. Despite its high energy density, there is much to discover about the structural properties influencing its combustion characteristics. Accordingly, a complete understanding of these characteristics is needed in order to provide new insights for its use in practical combustion applications, and for identifying subsequent fuel upgrading strategies. This knowledge will also be key to understand gaseous and particulate matter emissions, as well as to define strategies to reduce TPO impacts on both environment and human health. In this manner, combustion and emission control systems could be either enhanced or modified to make TPO viable as a fuel in different combustion systems from technical, economic, and environmental points of view.

Up to date, the combustion of TPO has been studied using conventional systems such as compression ignition engines, furnaces, and burners, which may hinder the comprehension of what it is really occurring during its oxidation process. This is because the results obtained might be influenced by non-controlled variables, including atomization characteristics, and the fuel-air ratio, among others. Thus, a dependency on the experimental setup is consequently inevitably introduced, being difficult to precisely determine whether certain combustion behaviors are entirely attributable to the tested fuel or, on the contrary, are an indirect result of effects from other related processes.

For all these reasons, this dissertation aims at establishing a WT valorization pathway through the production of a combustible liquid fraction from WT by means of pyrolysis. As such, the operational features of the auger technology, in particular the twin-auger configuration are addressed to aid in demonstrating the suitability of this type of reactor for the pyrolysis of WT. Subsequently, *in-situ* desulfurization using CaO is assessed as a first approach to reduce the sulfur content in TPO (one of its major drawbacks). Thereafter, the main fuel and chemical characteristics of the derived TPO, as well as different fractions obtained by distillation, are elucidated using advanced analytical techniques such as FT-ICR MS and ^{1}H and ^{13}C NMR. In turn, this information allows the development of an improved understanding regarding the properties influencing the combustion performance of TPO. These properties are then used to explain the oxidation behavior of TPO and its distillate fractions by carrying out fundamental oxidation studies using thermogravimetric (TG) and differential thermogravimetric (DTG) analyses for the raw TPO, as well as experiments in jet stirred reactor (JSR) for the distillate fraction. Finally, a thermoecomic approach is taken to study a model pyrolysis plant at industrial-scale, which is proposed based on several experimental studies carried out in the lab-scale twin-auger plant. The same analysis is conducted for the lab-scale plant with the aim of identifying some of the benefits of scaling and modifying the process from an exergy / cost point of view, as well as the potential improvements. In this analysis, the raw matter was disaggregated into the rubber compounds (NR, SBR), CB, and ashes, in order to gain insights about the contribution of fossil (SR and CB) and renewable (NR) resources to the characteristics (in terms of exergy) of the pyrolysis derived products. Among others, the information obtained in this doctoral work serves to pave the bridge towards the design of large-scale plants in a reliable way through the different stages of the Technology Readiness Levels (TRL).

1.5 Research questions

Based on the previous statements, the following research questions are addressed in this dissertation:

- How can the variables governing the pyrolysis- be fine-tuned in a twin-auger reactor to maximize TPO yield?
- What is the effect of adding low-cost materials such as CaO on the physical and chemical properties of TPO?
- Is distillation a feasible upgrading strategy for TPO?
- How do the structural characteristics of upgraded TPO affect its combustion properties?
- How can emission tendencies and energy balances be used to assess the sustainability of this waste-to-energy pathway?

1.6 Objectives

In order to answer these research questions, the following objectives have been established:

1.6.1 General objective

To produce, characterize, and upgrade waste tire pyrolysis oil (TPO) for its assessment for combustion applications.

1.6.2 Specific objectives

- To assess the operational features of a twin-auger pyrolyzer, as well as to evaluate an *in-situ* desulfurization pathway using CaO in order to obtain TPO with reduced sulfur content.
- To identify the main fuel and chemical properties of TPO in order to gain insights into potential applications and upgrading strategies
- To assess distillation as an upgrading method to improve the properties of TPO distillate fractions.
- To study the fundamental combustion characteristics of TPO and its distillate fractions.
- To analyze the sustainability of pyrolysis based on emission tendencies and energy balances.

1.7 Dissertation structure

- **Chapter 1. Introduction**

A general introduction describing the problem statement is presented in this chapter. In addition, a brief literature survey regarding the state-of-the-art of pyrolysis as a WT valorization method is carried out. As such, pyrolysis fundamentals, pyrolysis technologies, and WT pyrolysis in auger reactors, as well as the properties, applications, upgrading strategies, and challenges of TPO are discussed. In addition, a brief description of the thermoeconomic analysis and its applicability to gain comprehensive insight into the efficiency of the pyrolysis process is provided. Finally, the motivation for conducting this research, research questions, objectives, and dissertation structure are established.

- **Chapter 2. Twin-auger pyrolysis plant: Characteristics and assessment of the operational features**

The most important characteristics of the twin-auger pyrolysis plant used in this work are described, as well as the methodology used to assess the operational features influencing the process. The Response Surface Methodology (RSM) is applied to define the optimum pyrolysis operating conditions. In addition, a repeatability study using the analysis of variance (ANOVA) is conducted to demonstrate the reproducibility and stability of the experimental setup, as well as the reliability of the obtained results. Finally, different TPO, rCB, TPG samples are randomly selected to assess the consistency of their physicochemical properties.

- **Chapter 3. Waste tire pyrolysis in a twin- auger reactor: Effect of CaO on the physical and chemical properties of the derived products**

This chapter assesses the addition of CaO during the pyrolysis of WT in the twin-auger reactor, as a first approach to reduce the sulfur content in the TPO. In addition to other physicochemical properties of TPO (*i.e.* density, viscosity, heating value, chemical composition, etc.), the effect of CaO on the chemical composition of TPG and the characteristics of rCB is also discussed.

- **Chapter 4. Fuel and chemical properties of waste tire pyrolysis oil derived from a continuous twin-auger reactor**

Fuel and chemical properties of TPO and its distillate fractions are studied in detail in this chapter. In order to carry out this analysis, advanced high-resolution analytical techniques such as FT-ICR MS, ^{1}H and ^{13}C NMR, and GC-MS are utilized to elucidate the structural characteristics of these fuels. Besides structural features, this analysis is accompanied by the study physicochemical properties, including density, viscosity, heating value, and elemental composition.

- **Chapter 5. Fundamental combustion studies of tire pyrolysis oil**

This chapter is divided into two sections. First, the combustion characteristics of TPO are studied by conducting thermogravimetric (TG) and differential thermogravimetric (DTG) analyses at different heating rates and a wide temperature range. TG and DTG are conducted using non-isothermal conditions to continuously investigate the physical and chemical variations occurring in the fuel. Moreover, the TG analyzer used is coupled with a Fourier Transform Infrared (FT-IR) spectrometer; therefore, it allows obtaining information regarding the real time composition of the evolved gases during the oxidation processes. In the second part, a comprehensive study of the oxidation characteristics of the light fraction of TPO obtained by distillation is carried out by conducting combustion experiments in JSR. Here, reaction tendencies (*i.e.* fuel consumption rate) and the evolution of main intermediate oxidation species are discussed. In addition, a surrogate fuel for this light fraction is formulated to facilitate future research into its combustion chemistry.

- **Chapter 6. Thermoeconomic assessment of the pyrolysis of waste tires in a twin-auger reactor**

This chapter presents a thermoeconmic assessment of a model WT pyrolysis plant at industrial-scale, which is proposed based on several experimental studies carried out in the lab-scale twin-auger plant. The Thermoeconmic approach combines exergy analysis and economic principles to provide insights into the cost structure for such systems. In order to conduct this analysis, the mass, energy, and exergy balances of the process are combined with the thermoeconomic approach by means of the Theory of Exergy Cost (TEC). This allows the quantification of the exergy and the monetary costs of the pyrolysis-derived products. The same analysis is conducted for the lab-scale plant with the aim of identifying some of the benefits of scaling and modifying the process from an exergy / cost point of view.

- **Chapter 7. Conclusions and future work**

This closing chapter outlines the final remark and conclusions of this dissertation. In addition, base of the obtained results, future works are discussed.

- **Appendices**

A flowchart representing the structure of this dissertation is shown in Figure 1.5.

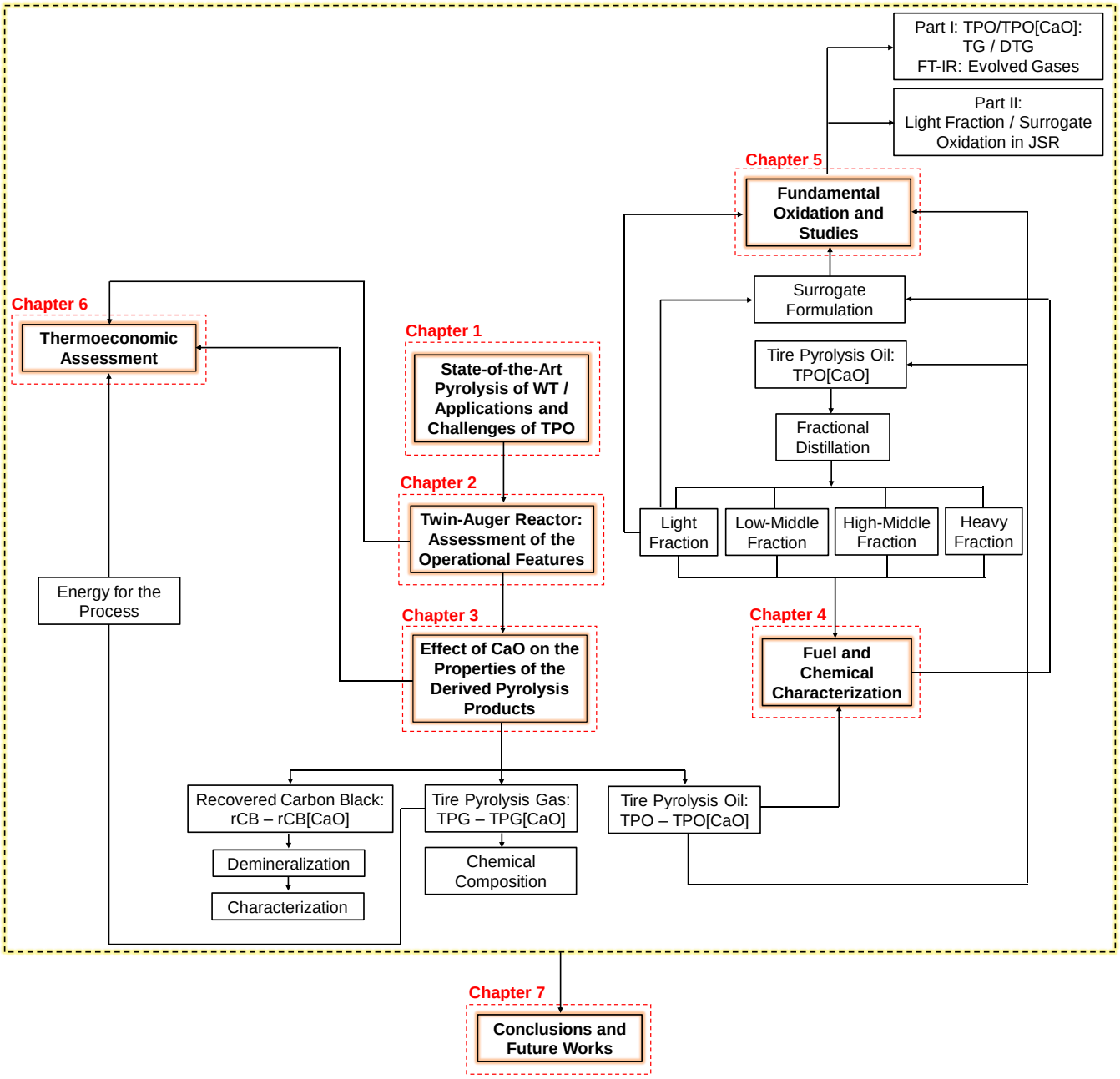

Figure 1.5. Flowchart of the dissertation structure

References

[1] E.B. Machin, D.T. Pedroso, J. Andrade de Carvalho Jr, Energetic valorization of waste tires, Renew. Sustain. Energy Rev. 68 (2017) 306–315.

[2] I. de M. Rodriguez, M.F. Laresgoiti, M.A. Cabrero, A. Torres, M.J. Chomon, B. Caballero, Pyrolysis of scrap tyres, Fuel Process. Technol. 72 (2001) 9–22.

[3] J.G. Penagos, What the fire in Fontibón revealed (in Spanish), El Espectador. (2014). https://www.elespectador.com/noticias/bogota/lo-que-dejo-al-descubierto-el-incendio-en-fontibon/ (accessed

September 7, 2020).

[4] D. Czajzynska, R. Krzyzynska, H. Jouhara, N. Spencer, Use of pyrolytic gas from waste tire as a fuel : A review, Energy. 134 (2017) 1121–1131.

[5] I. Hita, M. Arabiourrutia, M. Olazar, J. Bilbao, J. M. Arandes, and P. Castaño, Opportunities and barriers for producing high quality fuels from the pyrolysis of scrap tires, Renew. Sustain. Energy Rev. 56 (2016) 745–759.

[6] World Business Council for Sustainable Development, Managing end-of-life tires, (2008) 1–15. https://docs.wbcsd.org/2018/02/TIP/End_of_Life_Tires-Full-Report.pdf (accessed January 20, 2020).

[7] U.S. Tire Manufacturers Association, U.S. Scrap tire management summary, (2017). https://www.ustires.org/system/files/scraptire_summ_2015_05_2017_Final_USTMA.pdf (accessed September 7, 2020).

[8] The Japan Automobile Tyre Manufacturers Association (JATMA), Tyre industry of Japan, (2017). http://www.jatma.or.jp/media/pdf/tyre_industry_2017.pdf (accessed September 7, 2020).

[9] European Tyre and Rubber Manufacturers Association (ETRMA), End-of-life tyre report, (2015). http://www.etrma.org/uploads/Modules/Documentsmanager/elt-report-v9a---final.pdf (accessed December 15, 2019).

[10] World Business Council for Sustainable Development (WBCSD), Managing end-of-life tires, 2009. http://www.rubberassociation.ca/files/ELT Full Report, 2008.pdf.

[11] J.D. Martínez, WtE best practices and perspectives in Latin America, in: Munic. Solid Waste Energy Convers. Dev. Ctries., 2019: pp. 107–145.

[12] H. Punkkinen, A. Oasmaa, J. Laatikainen Luntama, M. Nieminen, J. Laine-Ylijoki, Thermal conversion of plastic-containing waste: A review, Research Report Nº D4.1-22 - Helsinki, 2017.

[13] J.D. Martínez, N. Puy, R. Murillo, T. García, M.V. Navarro, A.M. Mastral, Waste tyre pyrolysis - A review, Renew. Sustain. Energy Rev. 23 (2013) 179–213.

[14] P.T. Williams, Pyrolysis of waste tyres: A review, Waste Manag. 33 (2013) 1714–1728.

[15] P. Parthasarathy, H.S. Choi, H.C. Park, J.G. Hwang, H.S. Yoo, B.K. Lee, M. Upadhyay, Influence of process conditions on product yield of waste tyre pyrolysis-A review, Korean J. Chem. Eng. 33 (2016) 2268–2286.

[16] A. Queck, R. Balasubramanian, Liquefaction of waste tires by pyrolysis for oil and chemicals — A review, J. Anal. Appl. Pyrolysis. 101 (2013) 1–16.

[17] J.D. Martínez, F. Campuzano, N. Cardona-uribe, C.N. Arenas, D. Muñoz-lopera, Waste tire valorization by intermediate pyrolysis using a continuous twin-auger reactor : Operational features, Waste Manag. 113 (2020) 404–412.

[18] I. H. del Olmo, Valorization of scrap tires pyrolysis oil (stpo) through a 2-stage hydrotreating hydrocracking strategy. Process variables and kinetic modeling, Doctoral Thesis, University of Basque Country (Spain), 2015.

[19] J. D. Martínez, Waste tire valorization by pyrolysis: production and application of the products, Doctoral Thesis, University of Zaragoza (Spain), 2014.

[20] I. Hita, A. Gutiérrez, M. Olazar, J. Bilbao, J.M. Arandes, P. Castaño, Upgrading model compounds and scrap tires pyrolysis oil (STPO) on hydrotreating NiMo catalysts with tailored supports, Fuel. 145 (2015) 158–169.

[21] J.D. Martínez, M. Lapuerta, R. Garcia-Contreras, R. Murillo, T. García, Fuel properties of tire pyrolysis liquid and its blends with diesel fuel, Energy Fuels. 27 (2013) 3296–3305.

[22] J.D. Martínez, Á. Ramos, O. Armas, R. Murillo, T. García, Potential for using a tire pyrolysis liquid-diesel fuel blend in a light duty engine under transient operation, Appl. Energy. 130 (2014) 437–446.

[23] C. Roy, A. Chaala, H. Darmstadt, The vacuum pyrolysis of used tires end-uses for oil and carbon black products, J. Anal. Appl. Pyrolysis. 51 (1999) 201–221.

[24] S. Luo, Y. Feng, The production of fuel oil and combustible gas by catalytic pyrolysis of waste tire using waste heat of blast-furnace slag, Energy Convers. Manag. 136 (2017) 27–35.

[25] B. Acevedo, C. Barriocanal, The influence of the pyrolysis conditions in a rotary oven on the characteristics of the products, Fuel Process. Technol. 131 (2015) 109–116.

[26] H. Pakdel, D.M. Pantea, C. Roy, Production of dl-limonene by vacuum pyrolysis of used tires, Anal. Appl. Pyrolysis. 57 (2001) 91–107.

[27] A.M. Mastral, M.S. Callen, T. García, M. V. Navarro, Improvement of liquids from coal-tire co-thermolysis. Characterization of the obtained oils, Fuel Process. Technol. 64 (2000) 135–140.

[28] M. Callén, S. Hall, A.M. Mastral, T. Garcia, A. Ross, K.D. Bartle, PAH presence in oils and tars from coal-tyre coprocessing, Fuel Process. Technol. 62 (2000) 53–63.

[29] A. Anca-Couce, Reaction mechanisms and multi-scale modelling of lignocellulosic biomass pyrolysis, Prog. Energy Combust. Sci. 53 (2016) 41–79.

[30] M.Y. Wey, B.H. Liou, S.Y. Wu, and C.H. Zhang, The autothermal pyrolysis of waste tires, J. Air Waste Manag. Assoc. 45 (2014) 855–863.

[31] T. Menares, J. Herrera, R. Romero, P. Osorio, L.E. Arteaga-Pérez, Waste tires pyrolysis kinetics and reaction mechanisms explained by TGA and Py-GC/MS under kinetically-controlled regime, Waste Manag. 102 (2020) 21–29.

[32] J. Han, W. Li, D. Liu, L. Qin, W. Chen, F. Xing, Pyrolysis characteristic and mechanism of waste tyre: A thermogravimetry-mass spectrometry analysis, J. Anal. Appl. Pyrolysis. 129 (2018) 1–5.

[33] D. Irmak Aslan, P. Parthasarathy, J.L. Goldfarb, S. Ceylan, Pyrolysis reaction models of waste tires: Application of Master-Plots method for energy conversion via devolatilization, Waste Manag. 68 (2017) 405–411.

[34] O. Senneca, P. Salatino, R. Chirone, A fast heating-rate thermogravimetric study of the pyrolysis of scrap tyres, Fuel Energy Abstr. 78 (1999) 1575–1581.

[35] D.Y.C. Leung, C.L. Wang, Kinetic study of scrap tyre pyrolysis and combustion, J. Anal. Appl. Pyrolysis. 45 (1998) 153–169.

[36] C. Wang, B. Zhao, X. Tian, K. Wang, Z. Tian, W. Han, H. Bian, Study on the pyrolysis kinetics and mechanisms of the tread compounds of silica-filled discarded car tires, Polymers (Basel). 12 (2020) 1–19.

[37] A. m. M. E. Aylón, A. Fernández-Colino, M. V. Navarro, R. Murillo, T.García, Waste tyre pyrolysis: comparison between fixed bed reactor and moving bed reactor, Ind. Eng. Chem. Res. 47 (2008) 4029–4033.

[38] S.-Q. Li, Q. Yao, Y. Chi, J.-H. Yan, K.-F. Cen, Pilot-Scale Pyrolysis of Scrap Tires in a Continuous Rotary Kiln, Ind. Eng. Chem. Res. 43 (2004) 5133–5145.

[39] X. Dai, X. Yin, C. Wu, W. Zhang, Y. Chen, Pyrolysis of waste tires in a circulating fluidized-bed reactor, Energy. 26 (2001) 385–399.

[40] J.D. Martínez, R. Murillo, T. García, A. Veses, Demonstration of the waste tire pyrolysis process on pilot scale in a continuous auger reactor, J. Hazard. Mater. 261 (2013) 637–645.

[41] F. Campuzano, R.C. Brown, J.D. Martínez, Auger reactors for pyrolysis of biomass and wastes, Renew. Sustain. Energy Rev. 102 (2019) 372–409.

[42] E. Aylón, A. Fernández-Colino, R. Murillo, G. Grasa, M. V. Navarro, T. García, A.M. Mastral, Waste tyre pyrolysis:

Modelling of a moving bed reactor, Waste Manag. 30 (2010) 2530–2536.

[43] E. Aylón, A. Fernández-Colino, R. Murillo, M.V. Navarro, T. García, A.M. Mastral, Valorisation of waste tyre by pyrolysis in a moving bed reactor, Waste Manag. 30 (2010) 1220–1224.

[44] J.D. Martínez, A. Veses, A.M. Mastral, R. Murillo, M.V. Navarro, N. Puy, A. Artigues, J. Bartrolí, T. García, Co-pyrolysis of biomass with waste tyres: Upgrading of liquid bio-fuel, Fuel Process. Technol. 119 (2014) 263–271.

[45] S. Frigo, M. Seggiani, M. Puccini, S. Vitolo, Liquid fuel production from waste tyre pyrolysis and its utilisation in a diesel engine, Fuel. 116 (2014) 399–408.

[46] O. Sanahuja-Parejo, A. Veses, J.M. López, R. Murillo, M.S. Callén, T. García, Ca-based catalysts for the production of high-quality bio-oils from the catalytic co-pyrolysis of grape seeds and waste tyres, Catalysts. 9 (2019) 1–17. doi:10.3390/catal9120992.

[47] H. Raclavská, A. Corsaro, D. Juchelková, V. Sassmanová, J. Frantík, Effect of temperature on the enrichment and volatility of 18 elements during pyrolysis of biomass, coal, and tires, Fuel Process. Technol. 131 (2015) 330–337.

[48] V.A. Kalitko, Steam feed and effect of steam-thermal seal in thermolysis of tire shreds in a screw-type reactor, J. Eng. Phys. Thermophys. 83 (2010) 324–329.

[49] A. V. Lozhechnik, V. V. Savchin, Pyrolysis of Rubber in a Screw Reactor, J. Eng. Phys. Thermophys. 89 (2016) 1482–1486.

[50] F. Campuzano, A.G. Abdul Jameel, W. Zhang, A.-H. Emwas, A.F. Agudelo, J.D. Martínez, M.S. Sarathy, Fuel and chemical properties of waste tire pyrolysis oil derived from a continuous twin-auger reactor, Energy Fuels. 34 (2020) 12688–12702.

[51] G. Choi, S. Oh, J. Kim, Clean pyrolysis oil from a continuous two-stage pyrolysis of scrap tires using in-situ and ex-situ desulfurization, Energy. 141 (2017) 2234–2241.

[52] P.T. Williams, S. Besler, D.T. Taylor, The pyrolysis of scrap automotive and heating rate on product composition, Fuel. 69 (1990) 1474–1482.

[53] J. Alvarez, G. Lopez, M. Amutio, N.M. Mkhize, B. Danon, P. Van Der Gryp, Evaluation of the properties of tyre pyrolysis oils obtained in a conical spouted bed reactor, Energy. 128 (2017) 463–474.

[54] S. Chen, H. Su, J. Chang, W. Lee, K. Huang, L. Hsieh, Y. Huang, W. Lin, C. Lin, Emissions of polycyclic aromatic hydrocarbons (PAHs) from the pyrolysis of scrap tires, Atmos. Environ. 41 (2007) 1209–1220.

[55] S.H. Cho, J.I. Oh, S. Jung, Y.K. Park, Y.F. Tsang, Y.S. Ok, E.E. Kwon, Catalytic pyrolytic platform for scrap tires using CO2 and steel slag, Appl. Energy. 259 (2020) 114164.

[56] R.K. Singh, B. Ruj, A. Jana, S. Mondal, B. Jana, A.K. Sadhukhan, P. Gupta, Pyrolysis of three different categories of automotive tyre wastes: Product yield analysis and characterization, J. Anal. Appl. Pyrolysis. 135 (2018) 379–389.

[57] M. Banar, V. Akyıldız, A. Özkan, Z. Çokaygil, Ö. Onay, Characterization of pyrolytic oil obtained from pyrolysis of TDF (Tire Derived Fuel), Energy Convers. Manag. 62 (2012) 22–30.

[58] A. Mohan, S. Dutta, V. Madav, Characterization and upgradation of crude tire pyrolysis oil (CTPO) obtained from a rotating autoclave reactor, Fuel. 250 (2019) 339–351.

[59] G. López, M. Olazar, R. Aguado, J. Bilbao, Continuous pyrolysis of waste tyres in a conical spouted bed reactor, Fuel. 89 (2010) 1946–1952.

[60] J.D. Martínez, A. Veses, A.M. Mastral, R. Murillo, M.V. Navarro, N. Puy, A. Artigues, J. Bartrolí, T. García, Co-pyrolysis of biomass with waste tyres: Upgrading of liquid bio-fuel, Fuel Process. Technol. 119 (2014) 263–271.

[61] N. Hourani, H. Muller, F.M. Adam, S.K. Panda, M. Witt, A.A. Al-Hajji, S.M. Sarathy, Structural level characterization of base oils using advanced analytical techniques, Energy Fuels. 29 (2015) 2962–2970.

[62] A.M. Elbaz, A. Gani, N. Hourani, A.H. Emwas, S.M. Sarathy, W.L. Roberts, TG/DTG, FT-ICR mass spectrometry, and NMR spectroscopy study of heavy fuel oil, Energy Fuels. 29 (2015) 7825–7835.

[63] H. Chen, R.K. Nelson, R.F. Swarthout, G. Shigenaka, A.H.B. De Oliveira, C.M. Reddy, A.M. Mckenna, Detailed compositional characterization of the 2014 Bangladesh furnace oil released into the world ' s largest mangrove forest, Energy Fuels. 32 (2018) 3232–3242.

[64] Z. Wu, R.P. Rodgers, A.G. Marshall, ESI FT-ICR mass spectral analysis of coal liquefaction products, Fuel. 84 (2005) 1790–1797.

[65] F.J. Liu, G.H. Liu, K.A.M. Gasem, B. Xu, A. Goroncy, M.C. Tang, Z.X. Huang, M. Fan, X.Y. Wei, Green and efficient two-step degradation approach for converting Powder River Basin coal into fuels/chemicals and insights into their chemical compositions, Appl. Energy. 264 (2020) 114739.

[66] A.G. Abdul Jameel, S.M. Sarathy, Lube products: Molecular characterization of base oils, Encycl. Anal. Chem. Appl. Theory Instrum. (2018) 1–14.

[67] J.D. Martínez, J. Rodríguez-Fernández, J. Sánchez-Valdepeñas, R. Murillo, T. García, Performance and emissions of an automotive diesel engine using a tire pyrolysis liquid blend, Fuel. 115 (2014) 490–499.

[68] J. Pilusa and E. Muzenda, Combustion characteristics of waste tyre pyrolysis fuel as industrial burner fuel, in: Dev. Combust. Technol. Chapter 4, 2016: pp. 97–116.

[69] S.T. Kumaravel, A. Murugesan, A. Kumaravel, Tyre pyrolysis oil as an alternative fuel for diesel engines – A review, Renew. Sustain. Energy Rev. 60 (2016) 1678–1685.

[70] İ. Cumali, H. Aydin, Fuel production from waste vehicle tires by catalytic pyrolysis and its application in a diesel engine, Fuel Process. Technol. 92 (2011) 1129–1135.

[71] A.K. Hossain, P.A. Davies, Pyrolysis liquids and gases as alternative fuels in internal combustion engines – A review, Renew. Sustain. Energy Rev. 21 (2013) 165–189.

[72] H. Aydin, C. Ilkilic, Analysis of combustion , performance and emission characteristics of a diesel engine using low sulfur tire fuel, Fuel. 143 (2015) 373–382.

[73] A. Sharma, S. Murugan, Investigation on the behaviour of a DI diesel engine fueled with Jatropha Methyl Ester (JME) and Tyre Pyrolysis Oil (TPO) blends, Fuel. 108 (2013) 699–708.

[74] B. Vand de Beld, E. Holle, J. Florijn, The use of pyrolysis oil and pyrolysis oil derived fuels in diesel engines for CHP applications, Appl. Energy. 102 (2013) 190–197.

[75] R. Vihar, T. Seljak, S.R. Oprešnik, T. Katrasnik, Combustion characteristics of tire pyrolysis oil in turbo charged compression ignition engine, Fuel. 150 (2015) 226–235.

[76] A.B. Koc, M. Abdullah, Performance of a 4-cylinder diesel engine running on tire oil-biodiesel-diesel blend, Fuel Process. Technol. 118 (2014) 264–269.

[77] W.C. Wang, C.J. Bai, C.T. Lin, S. Prakash, Alternative fuel produced from thermal pyrolysis of waste tires and its use in a di diesel engine, Appl. Therm. Eng. 93 (2016) 330–338.

[78] A. Sharma, S. Murugan, Combustion, performance and emission characteristics of a di diesel engine fuelled with non-petroleum fuel: A study on the role of fuel injection timing, J. Energy Inst. 88 (2015) 364–375.

[79] A. Sharma, S. Murugan, Potential for using a tyre pyrolysis oil-biodiesel blend in a diesel engine at different compression

ratios, Energy Convers. Manag. 93 (2015) 289–297.

[80] J. McNeil, P. Day, F. Sirovski, Glycerine from biodiesel: The perfect diesel fuel, Process Saf. Environ. Prot. 90 (2012) 180–188.

[81] U. Žvar Baškovič, R. Vihar, T. Seljak, T. Katrašnik, Feasibility analysis of 100% tire pyrolysis oil in a common rail Diesel engine, Energy. 137 (2017) 980–990.

[82] J.D. Matínez, M. Lapuerta, R. García Contreras, R. Murillo, T. García, Fuel properties of tire pyrolysis liquid and its blends with diesel fuel, Energy Fuels. 27 (2013) 3296–3305.

[83] R. García-contreras, J.D. Martínez, O. Armas, R. Murillo, T. García, Study of a residential boiler under start-transient conditions using a tire pyrolysis liquid (TPL)/diesel fuel blend, Fuel. 158 (2015) 744–752.

[84] Weibold, Tire pyrolysis oil and IMO 2020 regulation for sulphur content in marine fuels, (2019). https://weibold.com/tire-pyrolysis-oil-and-imo-2020-regulations-for-sulphur-content-in-marine-fuels/ (accessed September 18, 2019).

[85] T. Seljak, B. Širok, T. Katrašnik, Advanced fuels for gas turbines: Fuel system corrosion, hot path deposit formation and emissions, Energy Convers. Manag. 125 (2016) 40–50.

[86] H. Hu, Y. Fang, H. Liu, R. Yu, G. Luo, W. Liu, A. Li, H. Yao, The fate of sulfur during rapid pyrolysis of scrap tires, Chemosphere. 97 (2014) 102–107.

[87] R. Cataluña, R. da Silva, Effect of cetane number on specific fuel consumption and particulate matter and unburned hydrocarbon emissions from diesel engines, J. Combust. 2012 (2012) 1–6.

[88] H. Aydin and C. Ilkılıç, Optimization of fuel production from waste vehicle tires by pyrolysis and resembling to diesel fuel by various desulfurization methods, Fuel. 102 (2012) 605–612.

[89] J. Shah, M.R. Jan, F. Mabood, Catalytic conversion of waste tyres into valuable hydrocarbons, J. Polym. Environ. 15 (2007) 207–211. doi:10.1007/s10924-007-0062-7.

[90] R. Miandad, M.A. Barakat, M. Rehan, A.S. Aburiazaiza, J. Gardy, A.S. Nizami, Effect of advanced catalysts on tire waste pyrolysis oil, Process Saf. Environ. Prot. 116 (2018) 542–552.

[91] G.G. Choi, S.J. Oh, J.S. Kim, Scrap tire pyrolysis using a new type two-stage pyrolyzer: Effects of dolomite and olivine on producing a low-sulfur pyrolysis oil, Energy. 114 (2016) 457–464.

[92] O. Dogan, M.B. Celik, B. Ozdalyan, The effect of tire derived fuel/diesel fuel blends utilization on diesel engine performance and emissions, Fuel. 95 (2012) 340–346.

[93] A. Al-lal, D. Bolonio, A. Llamas, M. Lapuerta, L. Canoira, Desulfurization of pyrolysis fuels obtained from waste: Lube oils, tires and plastics, Fuel. 150 (2015) 208–216.

[94] N. Jantaraksa, P. Prasassarakich, P. Reubroycharoen, N. Hinchiranan, Cleaner alternative liquid fuels derived from the hydrodesulfurization of waste tire pyrolysis oil, Energy Convers. Manag. 95 (2015) 424–434.

[95] D. Debek and J. Walendziewski, Hydrorefining of oil from pyrolysis of whole tyres for passenger cars and vans, Fuel. 159 (2015) 659–665.

[96] I. Hita, E. Rodríguez, M. Olazar, J. Bilbao, J.M. Arandes, P. Castaño, Prospects for obtaining high quality fuels from the hydrocracking of a hydrotreated scrap tires pyrolysis oil, Energy Fuels. 29 (2015) 5458–5466.

[97] S. Ucar, S. Karagoz, J. Yanik, M. Yuksel, M. Saglam, Upgrading scrap tire derived oils using activated carbon supported metal catalysts, Energy Sources , Part A. 29 (2007) 425–437.

[98] Y. Han, F. Stankovikj, M. Garcia-Perez, Co-hydrotreatment of tire pyrolysis oil and vegetable oil for the production of transportation fuels, Fuel Process. Technol. 159 (2017) 328–339.

[99] R. Yuwapornpanit, S. Jitkarnka, Cu-doped catalysts and their impacts on tire-derived oil and sulfur removal, J. Anal. Appl. Pyrolysis. 111 (2015) 200–208.

[100] S. Muenpol, S. Jitkarnka, Effects of Fe supported on zeolites on structures of hydrocarbon compounds and petrochemicals in waste tire-derived pyrolysis oils, J. Anal. Appl. Pyrolysis. 117 (2016) 147–156.

[101] R. Serefentse, W. Ruwona, G. Danha, E. Muzenda, A review of the desulphurization methods used for pyrolysis oil A review of the desulphurization methods used for pyrolysis oil, Procedia Manuf. 35 (2019) 762–768.

[102] M.F. Ali, A. Al-Malki, B. El-Ali, G. Martinie, M.N. Siddiqui, Deep desulphurization of gasoline and diesel fuels using non-hydrogen consuming techniques, Fuel. 85 (2006) 1354–1363.

[103] E. Rodríguez, S. Izaddoust, J. Valecillo, J. Bilbao, J.M. Arandes, P. Castaño, E. Epelde, G. Elordi, Lessening coke formation and boosting gasoline yield by incorporating scrap tire pyrolysis oil in the cracking conditions of an FCC unit, 224 (2020) 113327.

[104] G.A. Costa, R.G. dos Santos, Fractionation of tire pyrolysis oil into a light fuel fraction by steam distillation, Fuel. 241 (2019) 558–563.

[105] H.F. Öztop, Y. Varol, Ş. Altun, M. Firat, Using Gasoline-like fuel obtained from waste automobile tires in a spark-ignited engine, Energy Sources , Part A. 36 (2014) 1468–1475.

[106] A. Chaala, C. Roy, Production of coke from scrap tire vacuum pyrolysis oil, Fuel Process. Technol. 46 (1996) 227–239.

[107] M.F. Laresgoiti, B.M. Caballero, I. de Marco, A. Torres, M.A. Cabrero, M.J. Chomón, Characterization of the liquid products obtained in tyre pyrolysis, J. Anal. Appl. Pyrolysis. 71 (2004) 917–934.

[108] A.G. Marshall, R.P. Rodgers, P. Rodgers, Petroleomics: Chemistry of the underworld, Procedings Natl. Acad. Sci. United States Am. 105 (2008) 18090–18095.

[109] Á. Muelas, M.S. Callén, R. Murillo, J. Ballester, Production and droplet combustion characteristics of waste tire pyrolysis oil, Fuel Process. Technol. 196 (2019) 106–149.

[110] A. Valero, S. Usón, C. Torres, W. Stanek, Theory of exergy cost and thermo-ecological, in: Thermodyn. Sustain. Manag. Nat. Resour., Springer, 2017: pp. 167–202.

[111] V. Verda, L. Serra, A. Valero, Thermoeconomic diagnosis : Zooming strategy applied to highly complex energy systems. Part 1 : Detection and localization of anomalies, ASME. 127 (2016).

[112] M.R. Islam, M.U.H. Joardder, S.M. Hasan, K. Takai, H. Haniu, Feasibility study for thermal treatment of solid tire wastes in Bangladesh by using pyrolysis technology, Waste Manag. 31 (2011) 2142–2149. doi:10.1016/j.wasman.2011.04.017.

[113] M. Van de Velden, J. Baeyens, A. Brems, B. Janssens, R. Dewil, Fundamentals, kinetics and endothermicity of the biomass pyrolysis reaction, Renew. Energy. 35 (2010) 232–242.

Chapter 2. Twin-auger pyrolysis plant: Characteristics and assessment of the operational features

As highlighted in Chapter 1, auger reactors have been recognized as one of the most robust technologies for conducting fast, intermediate, and slow pyrolysis, as well as one of the strongest contenders for commercial development [1]. These types of reactors, which use a screw (or double screw) to convey a single feedstock or a blend with solid heat carriers down the length of a tube, have gained attention due to their relatively simple design and the potential to overcome some of the problems of conveying heat for pyrolysis. They also have prospects for small scale, distributed processing of different types of feedstocks [1]. In the case of WT pyrolysis, besides the above-described potentials, the attractiveness of this technology as a pyrolizer is also reflected in the possibility of reaching a balance between a high TPO yield and adequate physicochemical properties of the rCB. This is possible via an accurate control of the operating conditions, which has been more challenging with other well-known technologies such as rotary kiln and fixed bed reactors. Therefore, as a first step to achieve the objectives established for this dissertation regarding the TPO production, this investigation took part in the design, construction, and assessment of the operational features of a novel twin-auger pyrolysis plant at lab-scale with a nominal capacity of 1 kg/h of WT. This initial stage of the research was conducted at the Environmental Research Group (GIA) of Pontificia Bolivariana University (Medellin-Colombia) within the framework of the Colciencias research project (1210-715-51742): "*Design, construction and operation of a novel twin-auger reactor for pyrolysis of solid waste and the production of second generation bio-fuels"*. Likewise, this phase of the work was a continuation of the MSc final project, entitled: *"Basic design of an auger reactor for pyrolysis of municipal solid waste"* [2]. The present chapter provides a general overview of the work conducted during the two first years of the doctoral work. In addition to explaining the main characteristics of the twin-auger pyrolysis plant, this chapter shows the assessment of its operational features by means of a design of experiments and a repeatability analysis for the yields of the resulting products.

2.1 Materials and methods

2.1.1 Twin-auger pyrolysis plant: General characteristics

A scheme of the twin-auger pyrolysis plant designed and constructed is shown in Figure 2.1. Six main parts are identified: (1) feeding system, (2) twin-auger reactor, (3) heating systems, (4) solid collection system, (5) condensing unit, and (6) gas burner. The feeding system (1) consists of two independent hoppers, each one with a feeding screw, an agitator (in order to avoid feedstock accumulation and formation of preferential channels), and a gas carrier inlet port. These hoppers allow feeding different materials (i.e. WT and CaO as will be described in Chapter 3) in an independent and continuous manner during operation. The reactor (2) consists of two intermeshing screws (down-pumped rotation), inside of an omega-shape case, and surrounded by electrical heaters, which supply the required energy to carry out the pyrolysis reactions. In the reactor, the feedstock is conveyed/mixed through the reaction zone, while the volatile matter released is conducted to the condensing unit by a continuous N_2 flow. Six K-type thermocouples are located along the reactor case to record the temperature profile during pyrolysis. The heating system (3) comprises electrical resistances located strategically in three sections of the reactor. Each

section has a K-type thermocouple installed, in order to control the reactor temperature. At the end of the reaction zone, the resulting solid fraction (rCB) falls by gravity into the solid collecting vessel (4).

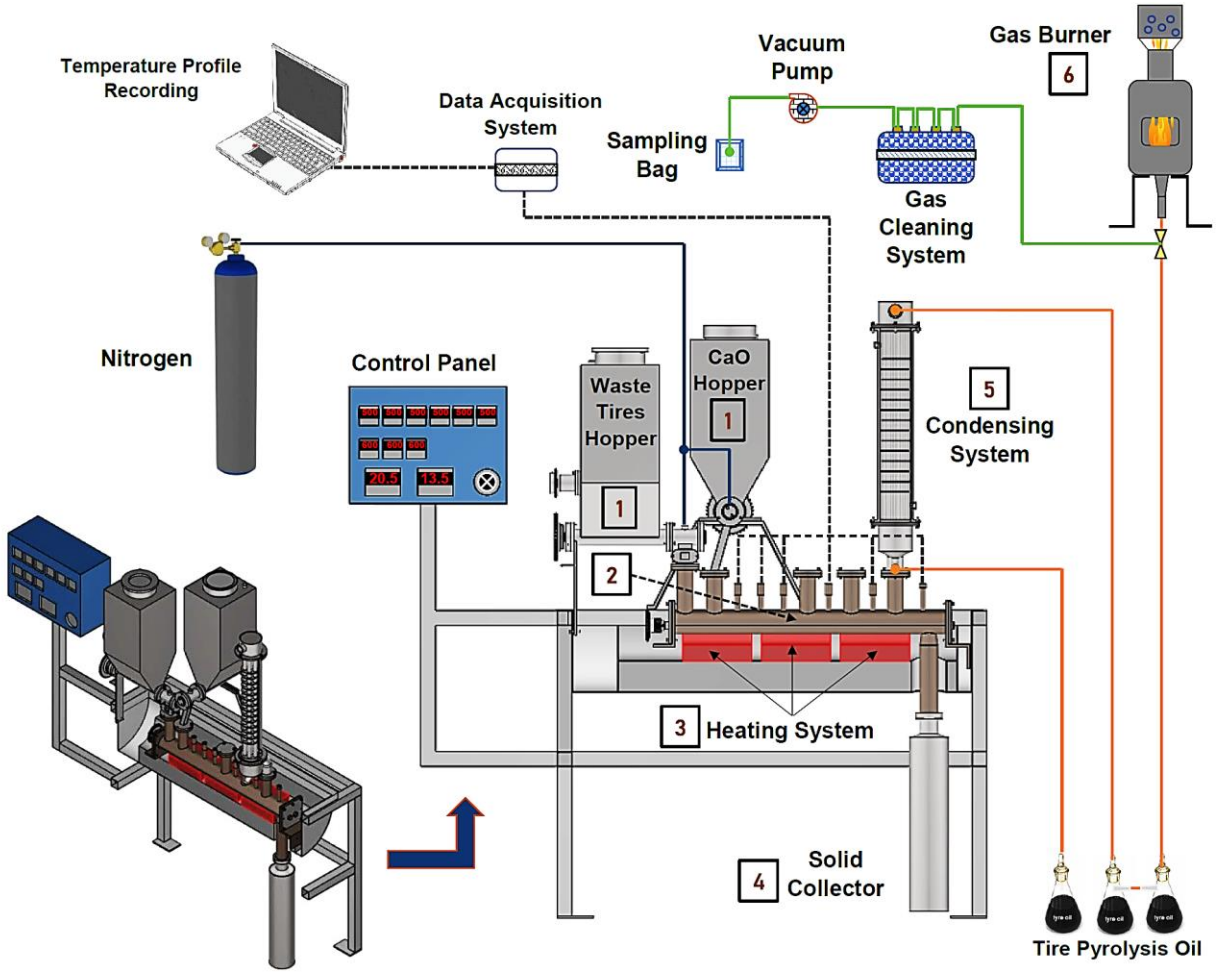

Figure 2.1 Schematic diagram of the twin-auger pyrolysis plant

The fifth system is the condensing unit (5), which receives the volatile matter released during the process. It comprises a shell and tube counter-flow heat exchanger, which uses water as a cold fluid for cooling down the pyrolysis vapors and thus, to recover the liquid fraction. The condensed fraction (TPO) is collected in a glass container located at the bottom of the condensing unit. After the main condensing unit, two additional traps (gas expanders) are installed in order to recover those hydrocarbon compounds that do not condense in the heat exchanger. The non-condensable pyrolysis gases (TPG) continue to a gas burner (6) to be transformed into combustion products, before being released to the atmosphere. Right before the gas burner, a bifurcation with a gas cleaning system coupled to a small vacuum pump is adjusted for TPG sampling. The cleaning step consists in a bubbling system using isopropanol to capture possible condensable compounds, and an impinger with silica gel to remove moisture. This system is submerged into an ice bath, in order to keep the temperature as low as possible. Gas samples are collected in Tedlar bags once the process reaches steady state (verified by the reactor temperature profile) for chromatographic characterization. The reactor (2) and the heating systems (3) are well isolated by a refractory concrete wall, as well as by an

isolation mantle, which covers both systems entirely in order to avoid cold spots. More details about the characteristics of each subsystem, as well as some images associated with their construction process can be found in the Appendix A, Section A1.1 and A1.2.

2.1.2 Waste tires characterization

A non-specified mixture of granulated WT (supplied by a local WT recycling company) with particle size between 2 and 4 mm was used for the pyrolysis experimental campaign. The WT granulate were composed of rubber, without the steel thread and textile netting. These granulate were characterized in terms of higher heating value (HHV), proximate analysis, and elemental composition. The HHV was determined experimentally in an IKA C-2000 calorimetric bomb, following the ASTM 240-09 standard procedure. Its moisture and ash content were measured according to EPA-160.3 SM-2540-G and ASTM D1506, respectively, while the volatile matter was obtained based on ISO-5623-1974 and UNE 32-019-84. The fixed carbon was calculated by difference. Finally, the elemental composition was carried out in a Thermoscientific flash 2000 apparatus, meeting the ASTM-D5622-95 and UNE-EN-15407 standards.

2.1.3 Experimental design: Response surface methodology

The response surface methodology (RSM) was implemented to assess the operational characteristics of the twin-auger pyrolysis plant described before. A such, a set of experiments, whose conditions were defined according to a design of experiments (DOE), were performed in order to identify the operational parameters influencing the yield of both TPO and rCB. The combination of DOE together with the RSM has been proved to be useful for developing, improving, and optimizing different processes [3]. It has been extensively used in analytical [4] and industrial [5] applications, bioprocesses [6], and even thermochemical processes such as pyrolysis [7–9]. This methodology consists of a group of mathematical and statistical techniques used to define the effect of different factors (independent variables) and their interactions on the responses (dependent variables) in a particular process. Regarding data collection, the central composite design (CCD) is a common multilevel experimental design used in RSM. The experimental data is then utilized to develop a second order model of the responses as function of the factors; in turn, this model can be ultimately optimized. CCD requires five factorial levels for each variable, which provides high quality prediction over the entire design space. Taking this into account, for the twin-auger pyrolysis plant, the assessment of its operational features was conducted using the CCD.

In order to carry out this study, many experimental runs and an exhaustive literature survey were initially needed to select the process variables (named here factors) and their operational range (including the particle size of the WT). The aim of this stage was therefore to identify those factors that present statistical influence on the yields of both TPO and rCB (named here responses). Four controllable and independent variables were selected: i) reactor temperature (X_1), ii) WT mass flow rate (X_2), iii) solid residence time (X_3), and iv) N_2 volumetric flow rate (X_4). Table 2.1 shows the identified levels for each of the four factors, including the rotatable circumscribed condition (α), which was calculated according to Equation 2.1. Resultantly, the experimental campaign consisted in a total of thirty experiments (see details in Appendix A, Section A.2). During the

experimental process, temperature was controlled using a PID device, which regulates the electric power consumption inside the pyrolyzer according to the set value. The WT mass flow rate was controlled by means of a variable frequency driver coupled to the hopper screw feeder. An electronic mass flow device Aalborg GFMS controlled the N_2 volumetric flow rate. The solid residence time of the WT inside the reactor was controlled by adjusting the speed of the screws with a second variable frequency driver coupled to the transmission mechanism linked to the intermeshing screws located inside the pyrolyzer.

Table 2.1 Experimental factors and levels selected for the CCD

Factor		Levels				
Symbol	Description	Extreme	Inferior	Central	Superior	Extreme
		$-\alpha = -2$	-1	0	1	$+\alpha = 2$
X_1	Reactor temperature (°C)	400	425	450	475	500
X_2	N_2 volumetric flow rate (mL/min)	0.50	0.75	1.00	1.25	1.50
X_3	Solid residence time (min)	2.50	3.00	3.50	4.00	4.50
X_4	WT mass flow rate (kg/h)	0.10	0.20	0.30	0.40	0.50

$$\alpha = (2^n)^{1/4} = (2^4)^{1/4} = 2 \qquad \textbf{(2.1)}$$

The CCD considers a quadratic regression for X_i variables represented by a second-order model to estimate the response surface [3]. Thus, each response (Y_i) is described by the model shown in Equation 2.2, where Y_i is the value of the response (in this case the yields of TPO and rCB), while X_i and X_j are the values of the factors. In addition, β_o, β_i, β_{ij} and β_{ii} are the coefficients related to the intercept, the main factors, the interaction terms, and the higher order terms, respectively. The ε_i term is the random error component, which represents different sources of variability not accounted for in the model. The ε_i is divided into two parts: the lack of fit and the pure error, both are reported in the analysis of variance (ANOVA) tables for each response.

$$Y_i = \beta_o + \sum_{i=1}^{n} \beta_i \chi_i + \sum_{i=1}^{n} \sum_{j>1}^{n} \beta_{ij} \chi_i \chi_j + \sum_{i=1}^{n} \beta_{ii} \chi_i^2 + \varepsilon_i \qquad \textbf{(2.2)}$$

The main goal of building this model was to identify the value of the factors that maximize the TPO yield (Y_1), while minimizing that of rCB (Y_2). It is important to mention that pyrolysis of WT should result in a high TPO yield and the rCB one must be as close as possible to the resulting sum of the fixed carbon and the ash contained in WT (previously determined by means of the proximate analysis). Therefore, the lower the content of volatile matter in rCB, the higher the conversion level of the WT achieved during the pyrolysis process. This statement was a key aspect to define the optimal operational parameters of the pyrolysis plant. The TPG yield was not subjected to any optimization since it represents the lowest yield among all the WT pyrolysis products (as shown later), and because TPO and rCB retain the highest value. The TPG could be used in a straightforward manner as an energy source for the pyrolysis process itself. In addition, in this case, the TPG yield is a linear combination of the other responses, because it is obtained by means of the global mass balance. As a result, this yield was not included in the optimization process.

Finally, the absolute average deviation (ADD) was used to validate the accuracy of the resulting models to predict the responses. This statistical parameter is more significant for describing the deviations between experimental and predicted data, as compared with the regression coefficient (R^2) [10]. The suitability of the resulting models for predicting the yields of TPO and rCB was also evaluated by performing an ANOVA test, and by verifying homoscedasticity and normality of the residuals. The ANOVA test was conducted for both the TPO and the rCB model in order to assess the mean values of data sets. As this analysis assumes that variances are equal across the populations, homoscedasticity of each factor for each model was verified from the Bartlett test [11,12]. In addition, normality was analyzed for each residual (difference between the experimental value and the one predicted from the model) from the Shapiro-Wilk test [13].

2.1.4 Repeatability assessment of the twin-auger pyrolysis plant

The repeatability of the yields of pyrolysis products was evaluated by carrying out several tests by the same users and the same measurement procedure, yet in different days and time of day [14], based on the optimum experimental conditions obtained in the RSM analysis. Based on the obtained results, an ANOVA test was conducted to assess the repeatability of the experimental facility in terms of TPO, rCB, and TPG yields. This test determines if the mean values of experimental groups range within a pre-determined non-rejection region (repeatable), or if they range within the rejection region (non-repeatable) [15]. If the mean values fall within the non-rejection region (repeatable), then the null hypothesis (which states that all mean values are equal) may be accepted, hence rendering the difference in the mean values as not statistically significant. In turn, the non-significant difference in the mean values extends to the implication that the experimental system is generally repeatable. In the present work, the repeatability of the response variables (TPO, rCB, and TPG yields) in the twin-auger pyrolyzer was verified by means of the P-value found by the ANOVA test, with a confidence level of 95 %. Before conducting the ANOVA test, three main assumptions must be fulfilled: i) each replicate is normally distributed about the replicate mean, ii) there is no relationship among the individuals in one replicate as compared to the others, and iii) the variances of data in different replicates should be the same [16]. In this regard, the normality of the experimental data was assessed by the Kolmogorov-Smirnov (K-S) test [17], while the Bartlett's test was used to corroborate the assumption that variances are homogeneous across the same replicate [18]. After verifying these assumptions and demonstrating the repeatability of the plant in terms of the yields of the products by means of the ANOVA test, six different TPO and rCB samples, as well as three TPG samples, were randomly selected to assess the consistency of their physicochemical properties.

2.1.5 General operational procedure of the twin-auger pyrolysis plant

The pyrolysis process was initiated by heating the reactor to the desired pyrolysis temperature while maintaining a continuous N_2 flow, which provided an inert atmosphere inside the reactor. Once this temperature was reached, the WT were fed according to the experimental conditions defined beforehand. The process reached steady state after 30 min of operation (verified by the reactor temperature profile), and every run lasted for 120 min. The yields of TPO and rCB were directly obtained by weight, while the TPG yield was calculated by means of a mass balance.

2.1.6 Characterization of products

TPO samples were characterized in terms of their elemental composition and HHV according to ASTM D-5373-08 and ASTM D240-17, respectively. The elemental analysis was conducted in a TruSpec Micro apparatus, while the HHV was measured in an IKA C-2000 bomb calorimeter. Furthermore, the water content and the total acid number (TAN) were quantified following the ASTM E203 and ASTM D8032-16 standards, respectively. Likewise, the content of saturates, aromatics, resins, and asphaltenes (SARA) was identified in a thin layer chromatograph with an FID detector (Latroscan MK-6) using the IP 469 method. Likewise, Carbon Conradson (ASTM D 189-06), flash point (ASTM D56-16a), density (ASTM D1217-20), and kinematic viscosity (ASTM D445-12) were also measured. Finally, the distillation characteristics of TPO were found at atmospheric conditions following the UNE EN ISO 3405. The distillation process was conducted in a lab-scale distillation unit from room temperature (25 °C) to 350 °C. The measured temperature values were normalized to standard atmospheric pressure by means of the Sidney−Young correlation, as recommended by the standard.

On the other hand, the rCB samples were analyzed in terms of proximate analysis, elemental composition, and heating value. The standard procedures and apparatus to conduct these analyses are similar to those described previously for WT. Furthermore, morphological characteristics were determined through Scanning Electron Microscopy (SEM) in a JEOL JSM-6490 LV apparatus with an acceleration voltage of 20 kV. Textural properties of rCB, including the surface area (S_{BET}), external area base on the statistical thickness method (STSA) [19], total pore volume (V_T), micropore volume (V_{Min}), and mesopores volume (V_{Meso}) were also identified. For this analysis, samples were degassed at 120 ºC under vacuum conditions for 600 min by means of multi-point N_2 adsorption at 77 K in a Micromeritics ASAP-2020 equipment. S_{BET} was calculated by the Brunauer-Emmett-Teller (BET) equation. V_T and V_{min} were obtained using the N_2 gas adsorbed at a relative pressure of 0.985 with the t-plot equation and the Dubin - Astakhov model, respectively. Finally, V_M was found by subtracting V_{min} from V_T.

Simultaneously, three TPG samples were collected in Tedlar bags for chromatography analysis. The chemical composition of the TPG samples was quantitatively determined in a micro gas chromatograph (GC) Agilent model 3000 with a thermal conductivity detector (TCD). The TCD has a molecular sieve 5A column of 10 m × 0.32 mm with argon as gas carrier and a Plot U column of 8 m × 0.32 mm with helium as gas carrier. The system was configured based on an appropriate analytical method in order to identify the volumetric concentrations of H_2, O_2, N_2, CH_4, CO, CO_2, C_2H_4, C_2H_6, C_3H_8, and H_2S.

2.2 Results and discussion

2.2.1 Waste tires characterization

Table 2.2 lists both the ultimate and proximate analyses, as well as the heating value of the WT used during the experimental campaign. As observed, WT has a high energy density (HHV = 38.69 kJ/kg), which is associated with the high content of carbon (82.4 wt.%) and hydrogen (8.2 wt.%). Due to this high energy content, even greater than that of middle and high-rank coal [20], WT have been used as an alternative energy source (known as Tire Derived Fuel) for energy demanding processes, including cement production, pulp and paper mills, electric utilities, industrial boilers, etc. [21,22]. WT also contain high amounts of volatile

matter (62.2 wt.%) and fixed carbon (29.9 wt.%), which are associated with rubber (natural and synthetic) and several carbon blacks added in the tire manufacturing process, respectively. Sulfur is used as a curing agent for rubber, and it also mediates crosslinks between rubber chains. The sulfur content was found to be 1.9 wt.%, which is within the range reported in literature, between 0.9 and 2.3 wt.% [23]. Another relevant aspect is the minor presence of oxygen (0.8 wt.%), which favors the pyrolysis process of WT, as well as the properties of the derived products (TPO and TPG). Finally, ash (6.9 wt.%) are linked to additives and inorganic fillers used in tire manufacture.

Table 2.2 Elemental composition, proximate analysis and heating value of WT

Proximate analysis (wt. %) (dry basis)		**Ultimate analysis (wt. %) (dry basis)**	
Volatile Matter	63.2	C	82.4
Fixed Carbon	29.9	H	8.2
Ash	6.9	N	< 0.1
Heating Value (MJ/kg)	38.69	S	1.9
		O	0.8

2.2.2 Data collection for the Response Surface Methodology: Central composite design

Table A2 in Appendix A shows the randomized sequence of the thirty experiments carried out, their related experimental conditions, and the derived TPO, rCB, and TPG yields. It is noticed that the obtained yields for the TPO, rCB, and TPG ranged from 40.67 to 46.88 wt.%, 38.75 to 46.55 wt.%, and 9.48 to 19.07 wt.%, respectively. The widest data variation occurred for the TPG, while for the TPO and rCB such variation was narrower. The maximum TPO yield was 46.88 wt.%, which is remarkably high taking into account the pyrolysis conditions used in the experimental campaign. Previous works reported in the literature regarding the pyrolysis of WT in single-auger configurations have shown maximum TPO yields of 41.5 wt.% [24] and 42.6 wt.% [25]. Nonetheless, it is worth mentioning that information in the scientific literature about the pyrolysis of WT in twin-auger reactors is still limited, which makes difficult to compare the obtained results with other works. The heating rate (between 150 and 200 °C/min) and the residence time of vapors (between 10 and 15 s) used in the twin-auger reactor lead to intermediate pyrolysis conditions. Hence, the lower amount of TPO in comparison to that produced under higher heating rates and lower residence times. For instance, continuous flash/fast pyrolysis of WT has been conducted in fluidized beds with maximum TPO yields around 65 wt.% [26] and 45 wt.% [8], as well as in spouted beds, with maximum TPO yields of 66 wt.% [27]. Different to intermediate pyrolysis, fast pyrolysis occurs at higher heating rates, on the order of 1,000 °C/min, and the vapors residence times must be shorter than 2 s. It requires feedstock with small particle sizes and quick removal/cooling of the pyrolysis products.

2.2.3 Influence of the factors on the process: Statistical analysis

2.2.3.1 Tire pyrolysis oil yield

The full regression model for TPO yield (see Table A2 in Appendix A) resulted in low ADD (1.66%), indicating an excellent fit of the data to the second-order model. The results of the ANOVA test revealed that only three terms were statistically significant

based on their F-values: reactor temperature (X_1), WT mass flow rate (X_2), and the second-order term for reactor temperature (X_1^2) in the operational range studied (Table A2 in Appendix A). Solid residence time (X_3) and N_2 volumetric flow rate (X_4), did not exhibit statistical influence within a confidence interval of 95%. This observation should not be understood as these variables are not important in the pyrolysis of WT using the twin-auger reactor; they simply did not significantly affect the TPO yield in the experimental domain defined for the CCD. In addition, it is worth noting that no interaction among the factors had statistical significance (at 95% confidence).

Once the statistically significant factors were identified, a reduced model was proposed, as shown in Equation 2.3. In this model, the negative sign indicates an antagonistic effect, while the positive sign indicates a synergistic effect. The regression model for TPO yield (Y_1) from the reduced model also showed a low ADD (1.85%), suggesting a robust fit. The ANOVA test results for this reduced model is presented in Table 2.3. As a result of the high F-values and low P-values, this model is statistically significant, and there was no significant lack of fit [3]. The low value of lack of fit for the F-value (1.04) also validates that the reduced model is not sensitive to systematic variation. According to the F-values, the WT mass flow rate (X_2) is the most influential factor, followed by the second-order term for reactor temperature (X_1^2) and the reactor temperature (X_1) in the experimental domain considered in this work. Homoscedasticity for the WT mass flow rate (X_2) and the reactor temperature (X_1) exhibited P-values of 0.5186 and 0.8138, respectively, indicating that the homoscedasticity assumption was met within a confidence level of 95%. The normality of residuals for the TPO yield (Y_1) showed a P-value of 0.7458, implying that residuals come from a normal distribution within a confidence level of 95%. Hence, both homoscedasticity and normality consolidate the adequacy of the resulting model for the TPO yield (Y_1) using the twin-auger pyrolyzer.

$$Y_1 = -151.068 + 0.8759\boldsymbol{X_1} + 4.4216\boldsymbol{X_2} - 0.0010\boldsymbol{X_1^2} \quad \textbf{(2.3)}$$

Table 2.3. ANOVA results for the TPO yield according to the reduced model

Source	Sum of squares	Degree of freedom	Mean square	F-value	P-value
X_1	10.3622	1	10.3622	8.70	0.0059
X_2	29.3267	1	29.3267	24.62	0.0000
X_1^2	12.5626	1	12.5626	10.55	0.0027
Residual (total error)	38.1116	32	1.19099	---	---
Lack of fit	6.16034	5	1.23207	1.04	0.414
Pure error	31.9513	27	1.18338	---	---
Correlation total	90.3631	35	---	---	---

Figure 2.2 shows the three-dimensional response surface for the TPO yield (Y_1) in terms of the significant factors: reactor temperature (X_1) and WT mass flow rate (X_2). It can be observed that the WT mass flow rate has a more notorious effect on the TPO yield than reactor temperature, as discussed above. An increase of the WT mass flow rate implies an increase in the TPO yield without any sign of curvature. Hence, the TPO yield reaches the maximum value when the system operates at the extreme condition defined for the WT mass flow rate ($+\alpha = 2 \rightarrow 1.5$ kg/h). In auger pyrolyzers, the mass flow rate controls the residence time of the volatiles released; and in this case, it has a higher influence than the N_2 volumetric flow rate. In this regard, the higher the mass flow rate, the higher the resulting amount of released volatiles; and hence, the shorter the residence time of these

compounds, given that the volume occupied by them is constant. A shorter residence time of volatiles implies less time for the occurrence of secondary thermal cracking reactions, which eventually results in a higher TPO yield, as the regression model suggests.

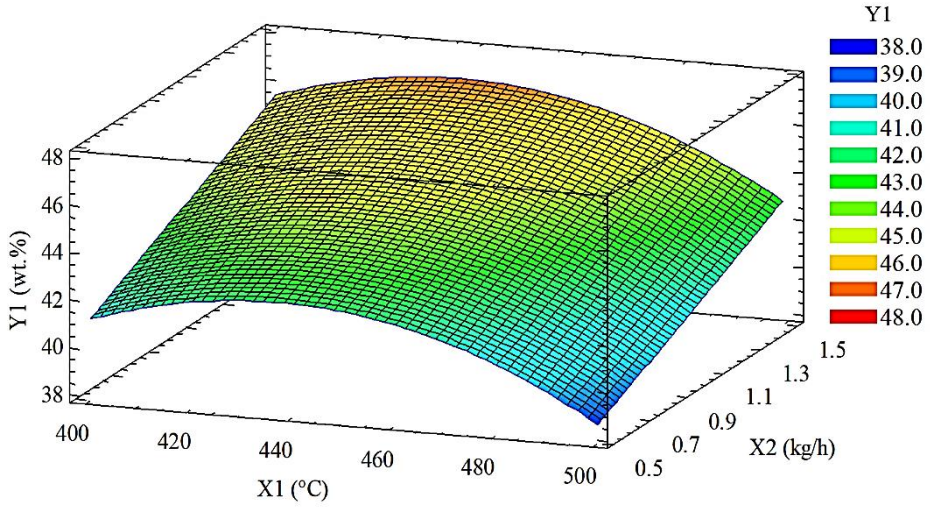

Figure 2.2. Response surface for the TPO yield (X_3 = 3.5 min and X_4 = 300 mL/min)

Regarding the reactor temperature, the response surface indicates a maximum TPO yield around 436 °C, close to the central value (450 °C). Together with other factors such as heating rate and residence time, temperature has a significant effect on the occurrence of secondary reactions associated with the thermal cracking of volatiles. It is observed in Figure 2.2 that the TPO yield decreases when the reactor temperature exceeds 436 °C, likely due to the decomposition of some compounds that eventually end up in the TPG. Overall, the recorded reactor temperature found in the experimental campaign is low in contrast to those reported in other facilities [23,28–30]. Among different reasons, this could be attributed to the rapid movement of the WT particles and their relative high size, which hinders a reliable measurement of the actual temperature. It is worth noting that the temperature is recorded until the particles detach from the thermocouple. Similarly, there are phenomena linked to the exothermic/endothermic reactions involved in the process [31], thus altering the temperature recording as well. Furthermore, there is a high possibility of measuring the "volatile phase" temperature instead of the "solid phase" temperature, which is assumed to be closer to the pyrolysis reaction. As a result, the use of the "reactor temperature" was deemed more appropriate than "pyrolysis temperature". The measurement of the optimum pyrolysis temperature not only for WT, but also for other types of feedstocks, including plastics and even biomass, is very controversial and seems to strongly depend on the reactor characteristics. Overall, ensuring a close contact between the particles and the thermocouple is certainly a hard task [32] and real temperature of the particle is not identical to the surface temperature [33].

2.2.3.2 Recovered carbon black yield

The full regression model describing the rCB yield (see Table A3 in Appendix A) also gave rise to a low ADD (1.42%). The ANOVA test results (Table A3 in Appendix A) showed that reactor temperature (X_1), WT mass flow rate (X_2) and the second-

order term for reactor temperature (X_1^2) are the main factors affecting the rCB yield. As determined for the TPO yield, neither solid residence time (X_3) nor N_2 volumetric flow rate (X_4) had statistical influence within a confidence level of 95%, and no major interactions among the factors were observed. Once again, the trends exhibited by these operational variables on the yields of both TPO and rCB does not suggest they are not important in the pyrolysis process. They just did not influence the yield of the aforementioned products in the experimental domain considered for the experimental campaign. In this regard, either 2.5 or 4.5 min for the solid residence time seems to ensure a very high pyrolysis conversion extent taking into account the other pyrolysis conditions and the WT particle size used. On the other hand, the high amount of volatiles released during the pyrolysis process prevails over the N_2 flow rate (by a factor of 55), affecting directly the residence time of volatiles released, as discussed before. Therefore, the yields of both TPO and rCB are unaffected between 100 and 500 mL/min. Even though, it is worth to point out that the N_2 flow rate allows a positive pressure head at the feedstock feeding point and establishes the trajectory of the volatile matter towards the condensing unit. The low flow rate of N_2 demanded by the process highlights another advantage of using auger pyrolyzers, as discussed in a previous work [1].

The reduced model for rCB yield (Y_2) in terms of the statistical influencing factors is shown in Equation 2.4, while Table 2.4 shows the associated ANOVA test results. High F-values and low P-values were observed; thus, no significant lack of fit was found. Contrary to the results found for the TPO yield (Y_1), reactor temperature (X_1) was more significant than WT mass flow rate (X_2), in the experimental domain considered for the experimental campaign. The homoscedasticity of these factors (P-values of 0.7732 and 0.9253, respectively) confirms the homogeneity of variances, while the normality of residuals showed a p-value of 0.1129. The regression model described by Equation 2.5 also resulted in a low ADD (1.63%). These results imply high accuracy of the resulting model to describe the rCB yield (Y_2) using the twin-auger pyrolyzer.

$$Y_2 = 166.607 - 0.4839\boldsymbol{X_1} - 3.0633\boldsymbol{X_2} + 0.000472333\boldsymbol{X_1^2} \quad \textbf{(2.4)}$$

Table 2.4. ANOVA test results for the rCB yield from the reduced model

Source	Sum of squares	Degree of freedom	Mean square	F-value	P-value
X_1	51.904	1	51.9204	78.09	0.0000
X_2	14.076	1	14.076	21.17	0.0001
X_1^2	2.788	1	2.7887	4.19	0.0504
Residual (total error)	25.76395	32	0.80512	---	---
Lack of fit	7.81245	5	1.56249	2.35	0.0679
Pure error	17.9515	27	0.6648	---	---
Correlation total	94.5492	35	---	---	---

Figure 2.3 shows the three-dimensional response surface for the rCB yield (Y_2) in terms of the influential factors. As observed, the higher the reactor temperature, the lower the rCB yield. Similarly, the higher the WT mass flow rate, the lower the rCB yield, which is linked to the lower amount of carbonaceous compounds onto the rCB surface, as discussed later. The response surface for the rCB shows a slight curvature with reactor temperature (X_1); and the rCB is minimized when the twin-auger pyrolyzer operates at the extreme levels ($+\alpha = 2 \rightarrow$ 500 °C and 1.5 kg/h).

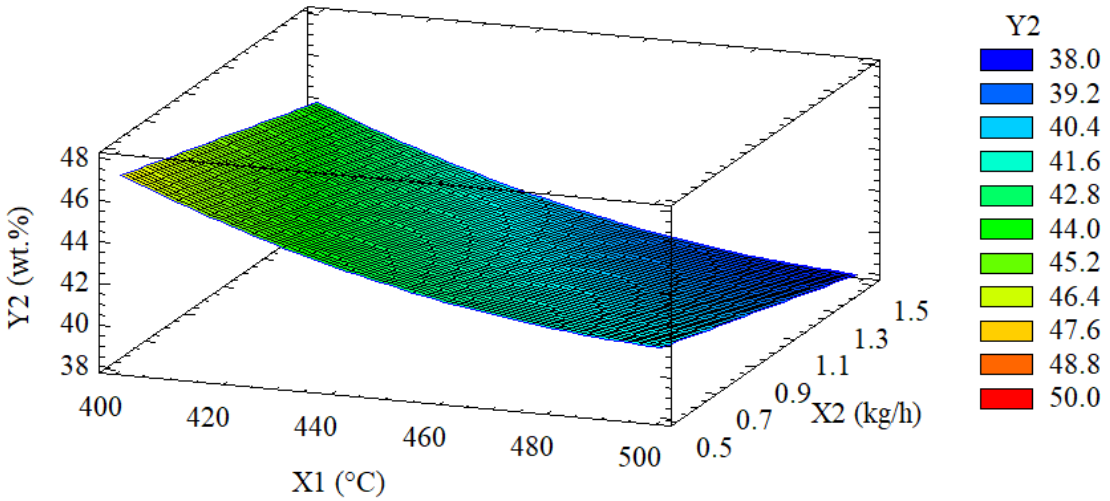

Figure 2.3. Response surface for the rCB yield (X_3 = 3.5 min and X_4 = 300 mL/min)

Several works in the scientific literature have reported the influence of the reactor temperature not only on yield, but also on the quality of the rCB. For instance, different kinds of continuous pyrolizers such as single-auger [24] and fluidized bed [8] have shown that high temperatures cause a reduction of the rCB yield, which is in agreement with the results found in this work. High temperatures strongly promote the devolatilization of both synthetic and natural rubber contained into the WT; hence, the rCB is expected to have high contents of fixed carbon, as well as a very low concentration of volatile compounds. High contents of volatile matter lead to the formation of hard-to-break agglomerated particles, hindering the final use of the rCB as substitute for virgin CB [34]. However, the rCB yield could increase with temperature because of the formation of carbonaceous residues from tarry compounds deposited onto the rCB surface [27,35]. The rCB has catalytic activity that promotes the condensation of polyaromatic compounds on its surface [36].

This extra carbon matter is chemically bonded rather than absorbed [37], and is likely distributed/found as both volatile matter and fixed carbon. The occurrence of these secondary reactions can be explained by the influence of WT mass flow rate, which is in agreement with the arguments given for the TPO yield. As the mass flow rate decreases, the residence time of volatiles released in the process increases, leading to a higher possibility for the occurrence of condensation and char formation reactions; and hence, higher carbonaceous residues onto the rCB surface.

2.2.3.3 Optimization and validation

Maximizing the TPO yield while minimizing the rCB yield (minimal amount of volatile matter) during the WT conversion was the main target during the initial stage of this research. According to the CCD and the optimization process through the RSM, the operating conditions to maximize the TPO yield (47.8 wt.%) are 436 °C, 1.5 kg/h of WT, 3.5 min and 300 mL/min. On the other hand, the rCB yield is minimized (37.15 wt.%) when the twin-auger pyrolyzer operates at 500 °C, 1.5 kg/h of WT, 3.5 min and 300 mL/min. As inferred, the initial target implies very different values of the reactor temperature; thus, further optimization was needed. Therefore, the optimized operating condition was determined by balancing the competing requirements of both yields.

This procedure was conducted using the multiple response optimization (MRO) included in the Statgraphics 18 software package. The resulting contour plot after conducting the MRO is shown in Figure 2.4. As observed, the twin-auger pyrolyzer seems to be able to yield TPO and rCB around 45.3 wt.% and 40.0 wt.% when it operates at 475 °C, 1.5 kg/h, 3.5 min, and 100 mL/min.

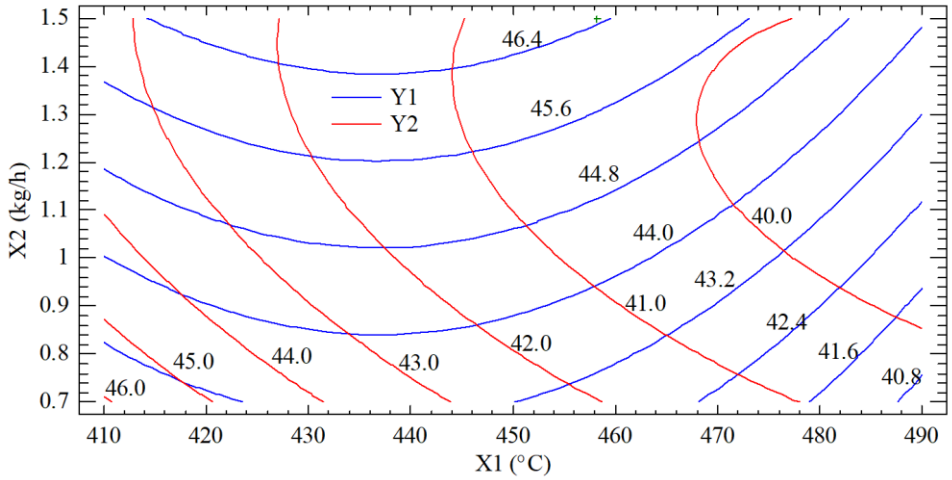

Figure 2.4. Contour plot to find the trade-off between TPO yield and rCB yield (X_3 = 3.5 min and X_4 = 300 mL/min)

The theoretical optimized conditions were validated by carrying out long-term experiments for 240 min in order to verify the equipment's practicalities. However, the optimized WT mass flow rate (1.5 kg/h) led to operational drawbacks after 140 min of operation. Due to the high mass flow rate, the WT granulate accumulated in the inlet tube connecting the feeding screw with the reactor itself, leading to clogging issues. Therefore, taking into account the contour plot shown in Figure 2.4, the WT mass flow rate was decreased to 1.16 kg/h. At this condition, maintaining the values for reactor temperature (475 °C), residence time (3.5 min), and N_2 volumetric flow rate (300 mL/min), the resulting theoretical yields of both TPO and rCB were 44.0 wt.% and 40.3 wt.%, respectively. These yields are very close to those suggested when the WT mass flow rate is 1.5 kg/h. Under these conditions, the twin-auger pyrolyzer operated properly and continuously during 240 min and the TPO, rCB and TPG were 45, 40 and 15 wt.%, respectively. The relative error between theoretical and experimental values for both TPO and rCB was 2.27% and 0.74%, respectively.

2.2.4 Repeatability analysis of the twin-auger pyrolysis plant

The repeatability of the twin-auger pyrolysis plant in terms of TPO, rCB and TPG yields was assessed based on the optimum operational conditions defined through the RSM analysis: 475 °C, 3.5 min of solid residence time, 300 mL/min of N_2 flow, and 1.16 kg/h of WT. A total of twenty-seven experiments were conducted, divided into four replicates, each one separated by a period of reactor maintenance. Each experiment lasted for around 120 min without any technical problem of the twin-auger pyrolyzer. The TPO, rCB, and TPG yields obtained from these experiments are reported in Table A4 in Appendix A. Among all the products, the TPG yield presented the widest variations along the experimental campaign. This can be explained by the fact that the yield of this fraction is obtained by closing the mass balance rather than directly measured as in the case of TPO and

rCB. Based on the information collected from this set of experiments, Table A5 in Appendix A presents the mean value ($\bar{x}$), variance (σ^2), standard deviation (σ), and standard error (σ_x) of the TPO, rCB, and TPG yields for each replicate. The mean values of TPO (44.13 wt.%), rCB (41.28 wt.%), and TPG (14.16 wt.%) yields calculated from the experimental data were very close to the theoretical values obtained through the MRO in Section 2.2.3.3, which demonstrates the agreement between the experimental and the theoretical data; and therefore, the reliability of the results reported so far. A graphical representation of the statistical results previously described is shown in Figure 2.5. Herein, the error bars are associated with the standard deviation, which reveal the variability of the yields from the mean value. The standard deviation was selected in this study over the standard error aiming at identifying the dispersion of the yields from the mean value regardless the sample size (the standard error is inversely proportional to the sample size). It is observed that as the standard deviation bars overlap in all replicates for the TPO, rCB, and TPG yields, it implies that their difference is not statistically significant. This hypothesis will be confirmed by means of the ANOVA test.

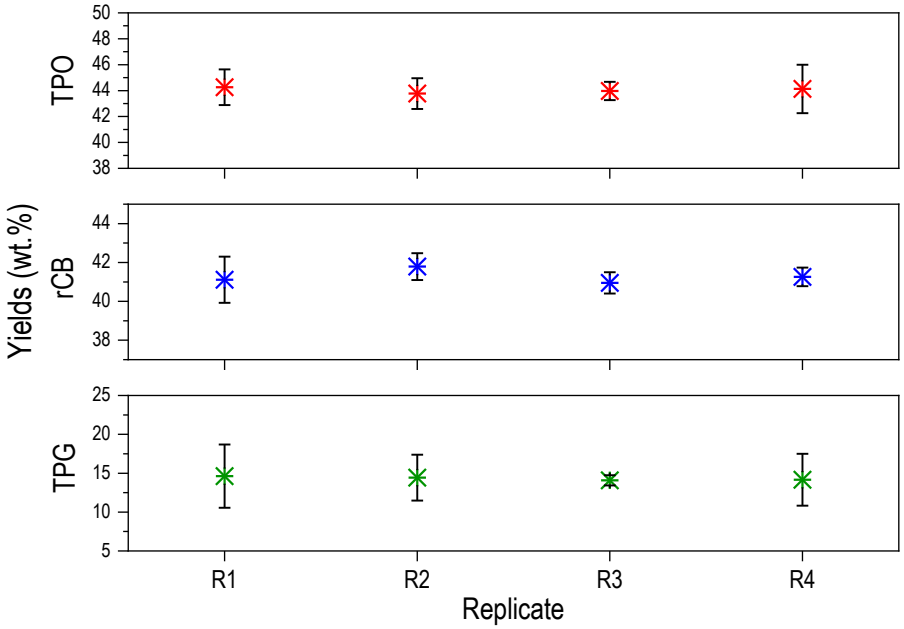

Figure 2.5. Graphical representation of the statistical results for TPO, rCB, and TPG yields

Prior to conducting the ANOVA test, the assumptions described in Section 2.1.4 were corroborated. Table A6 in the Appendix A shows the results obtained from the K-S (normality) and Bartlett's (homogeneous variances) tests. P-values higher than the significance level (0.05) in both tests for all yields imply that the null hypothesis of normal distributed data, as well as homogeneous variance across the replicates, are accepted and the ANOVA test can be performed. Thus, the ANOVA test was carried out between replicates and within replicates for the TPO, rCB, and TPG yields. The summary of the results is reported in Table A7 in the Appendix A. Since all P-values are much greater than the significance level (0.05), the null hypothesis of equal means is accepted; therefore, no statistical difference exists among replicates. Overall, the results reported in Table A7 demonstrate the repeatability of the twin-auger pyrolyzer in terms of TPO, rCB and TPG yields when the plant operates at given experimental conditions.

2.2.5 Characterization of products

After demonstrating the repeatability of the pyrolysis plant in terms of yields, the next step was to corroborate the consistency and reproducibility of some of the physicochemical properties of derived products when the pyrolysis plant operates at the optimum experimental conditions. As such, different samples were randomly selected from different replicates and their main properties were assessed. Based on the obtained results, the standard deviation (σ) and the absolute error (AE) for each property were determined, which were key parameter to define whether the properties of the products were consistent and reproducible or not.

2.2.5.1 Tire pyrolysis oil characterization

TPO was qualitatively observed as a dark-brown colored oil with a strong odor. As mentioned in Chapter 1, TPO is considered as an unrefined hydrocarbon source, containing different hydrocarbon families in the boiling point range between 70 to 450 °C or higher. Figure 2.6 shows the distillation curves obtained at atmospheric conditions for three different samples. In all cases, TPO started boiling at 70 °C and stopped at 350 °C, leaving a heavy end fraction of around 8 vol. % of the starting material.

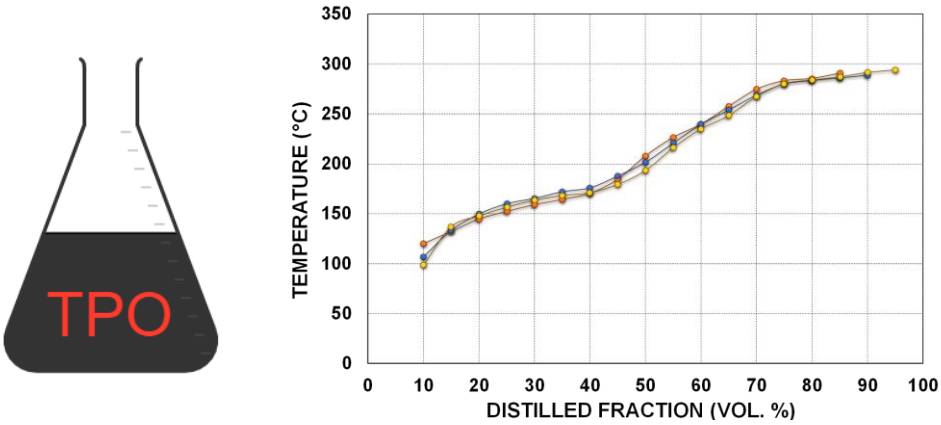

Figure 2.6. Distillation characteristics of TPO

It can be observed that more than 30 vol. % of TPO distillates before 170 °C (upper limit for conventional gasoline), while the remining 90 vol.% distillates before 360 °C (upper limit for conventional diesel). This pattern supports the statement that TPO is an unrefined hydrocarbon mixture. On the other hand, another six samples were randomly selected and their elemental composition (dry basis), higher heating value (HHV), and SARA analysis are reported in Table 2.5. In general, the TPO samples chosen for the analysis exhibited a high HHV (42.76 ± 0.0.38 MJ/kg), which is even higher than that of the initial feedstock (38.69 MJ/kg). These samples also exhibit high contents of carbon (87.95 ± 1.03 wt. %) and hydrogen (10.5 ± 1.02 wt.%). The sulfur content was found to be 0.80 ± 0.06 wt.%, which suggests that further treatments should be applied in order to reduce the environmental impact in terms of SOx emissions. A more detailed discussion regarding the sulfur content in TPO will be presented in Chapter 3. In addition, the SARA analysis revealed that more than 80 wt.% of these samples are characterized by the presence of hydrocarbons in the form of aromatics (38.13 ± 2.16) and resins (53.20 ± 1.97). All these results agree with the information reported in the literature for TPO [23,28,29,38,39].

Table 2.5. Elemental, SARA, and heating value analyses of TPO

Sample	Elemental analysis (wt.%) (as received)					H/C	HHV (MJ/kg)	SARA analysis (wt.%) (as received)			
	C	H[a]	N	S	O			Saturates	Aromatics	Resins	Asphaltenes
1	88.74	9.70	0.76	0.80	<0.1	1.2	42.02	3.37	39.48	52.04	5.11
2	86.83	11.60	0.67	0.90	<0.1	1.4	42.77	3.36	40.59	50.96	5.09
3	88.28	10.20	0.72	0.80	<0.1	1.3	42.98	3.80	35.44	55.62	5.14
4	88.99	9.40	0.81	0.80	<0.1	1.2	43.01	3.50	39.87	51.43	5.20
5	88.34	10.20	0.76	0.70	<0.1	1.3	42.99	3.30	37.44	54.15	5.11
6	86.50	11.90	0.8	0.70	<0.1	1.4	42.80	3.89	35.97	54.96	5.18
$\bar{x}$	87.95	10.50	0.75	0.80	--	1.33	42.76	3.54	38.13	53.2	5.14
σ	1.03	1.02	0.05	0.06	--	0.01	0.38	0.25	2.16	1.97	0.04
AE (±)	0.85	0.83	0.04	0.03	--	0.01	0.25	0.21	1.85	1.72	0.03

H[a] includes de hydrogen from water

Table 2.6 reports other important properties of the TPO samples, including the water content (294 ± 106 ppm), TAN (6.1 ± 0.30 mg_{KOH}/g), carbon Conradson (1.36 ± 1.11 wt.%), viscosity (2.6 ± 0.10 cSt), density (888.3 ± 3.80 kg/m^3), and flash point (< 20.0 °C). It is worth to note that due to the similarity of these properties to those of conventional oil, TPO is often compared in the literature to petroleum derived fuels such as fuel oil (FO), which is widely used in thermal energy facilities [36]. Therefore, similar applications and upgrading strategies can be considered. A more detailed description of the physical, chemical, and structural characteristics of TPO and its distillate fractions will be presented in Chapter 4.

Table 2.6. Water content, TAN, carbon Conradson, viscosity, density, and flash point of TPO

Sample	Water content (ppm)	TAN (mg_{KOH}/g)	Carbon Conradson (wt.%)	Viscosity at 40°C (cSt)	Density at 25°C (kg/m^3)	Flash point (°C)
1	239	5.6	1.40	2.70	888.30	< 20.0
2	279	6.4	3.56	2.60	881.00	< 20.0
3	246	6.4	0.71	2.60	881.10	< 20.0
4	185	6.2	0.88	2.70	880.00	< 20.0
5	324	5.7	0.84	2.50	884.00	< 20.0
6	489	6.2	0.76	2.50	879.10	< 20.0
$\bar{x}$	294	6.1	1.36	2.60	882.40	--
σ	106	0.3	1.11	0.10	3.80	--
AE (±)	75	0.3	0.75	0.10	2.80	--

In general, the σ and AE reported in Tables 2.5 and 2.6 for all the physicochemical properties measured, suggest that the characteristics of the TPO samples derived from the twin-auger pyrolysis plant obtained at the same experimental conditions, and using the same feedstock are consistent and reproducible, which demonstrates the reliability of the experimental data attained.

2.2.5.2 Recovered carbon black characterization

The rCB is known for being a complex mixture containing different grades of carbon blacks (CB) used in the tire manufacture, as well as inorganic materials coming from fillers and accelerators [34]. Similar to TPO, six samples were randomly selected from the experimental campaign to assess their physicochemical properties and textural characteristics. Figure 2.7 shows the

SEM images for the six samples at 20000x. It is observed that the rCB is a porous material with a heterogeneous aggregate size distribution. The bright parts in the images can be associated with inorganic compounds present on the surface.

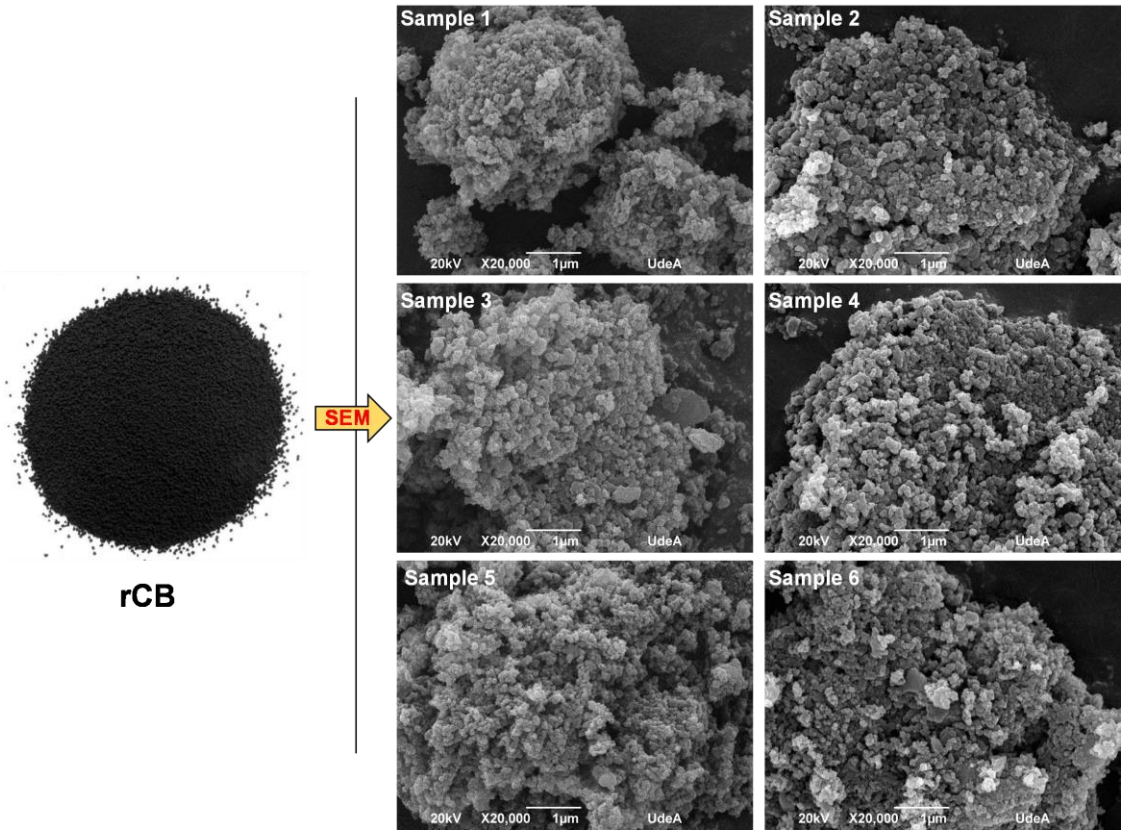

Figure 2.7. SEM images of rCB at 20000x

Table 2.12 shows the elemental composition, as well as proximate, and HHV analyses of all the rCB samples. In this case, these samples were comprised of moisture (M), ash (A), volatile matter (VM), and fixed carbon (FC) of 1.95 ± 0.34, 18.45 ± 1.36, 5.03 ± 0.0.52, 74.57 ± 1.39.

Table 2.12. Proximate, elemental and heating value analyses of rCB

Sample	HHV (MJ/kg)	Elemental analysis (wt.%) (as received)					Proximate analysis (wt.%) (as received)			
		C	H[a]	O	N	S	M	A	VM	FC
1	26.92	75.79	1.37	<0.10	0.28	3.22	2.41	19.34	5.55	72.70
2	25.53	76.42	1.47	<0.10	0.29	3.25	2.18	18.57	5.66	73.58
3	26.62	74.72	1.35	<0.10	0.27	3.21	1.79	20.45	5.16	72.61
4	27.31	78.31	1.32	<0.10	0.28	2.98	1.77	17.11	4.54	76.59
5	26.54	76.02	1.40	<0.10	0.29	3.48	2.08	18.40	4.86	74.67
6	26.74	78.09	1.24	<0.10	0.27	3.57	1.48	16.83	4.41	77.28
$\bar{x}$	26.61	76.56	1.36	--	0.28	3.29	1.95	18.45	5.03	74.57
σ	0.60	1.39	0.08	--	0.01	0.21	0.34	1.36	0.52	1.39
AE (±)	0.38	1.09	0.05	--	0.01	0.16	0.27	1.00	0.43	1.09

H[a] includes de hydrogen from water

In addition, the elemental composition revealed high contents of carbon (76.56 ± 1.39 wt.%) and sulfur (3.29 ± 0.21 wt.%), with low contents of hydrogen (1.36 ± 0.08 wt.%), nitrogen (0.28 ± 0.01 wt.%), and oxygen (< 0.1 wt.%). Interestingly, the low VM content (5.03 ± 0.42 wt.%) in the rCB samples implies a high conversion level of WT in the twin-auger pyrolysis plant. In turn, this low content of VM support the adequacy of the optimum point defined by means of the RSM.

Due to both the high carbon concentration and significant energy density (HHV = 26.61 ± 0.60 MJ/kg), the rCB can be used in combustion or gasification processes. However, the most sustainable and attractive market is its use as substitute for virgin CB in rubber applications. This application, in addition to the environmental advantages related to CO_2 reduction in the production of new CB, it will positively influence the economic feasibility of pyrolysis since it forms a recycling loop for the CB recovered from WT. This is totally in line with the circular economy principles. Taking this into account, the textural characteristics of rCB must be also carefully assessed since they will determine its performance as a reinforcing material.

Table 2.13 shows different textural properties determined for the rCB samples, including S_{BET}, STSA, Vo, V_T, and V_{Meso}. These characteristics are different to those of virgin CB [23], which can be attributed to the presence of inorganic materials (18.45 ± 1.36) and the difference in aggregate size, as discussed previously. It is also important to point out that rCB is a mixture of different references of CB added during tire manufacturing all of them with different properties. Thus, it is challenging to compare the rCB properties with those of a specific reference of commercial CB.

Table 2.13. Textural characteristics of rCB

Sample	S_{BET} (m^2/g)	STSA (m^2/g)	V_o (cm^3/g)	V_T (cm^3/g)	V_{Meso} (cm^3/g)
1	55.0	54.0	0.035	0.400	0.365
2	51.0	50.0	0.028	0.419	0.391
3	48.0	47.0	0.028	0.314	0.286
4	55.0	54.0	0.034	0.285	0.251
5	53.0	50.0	0.031	0.256	0.225
6	57.0	56.0	0.033	0.413	0.380
$\bar{x}$	53.2	51.8	0.032	0.348	0.316
σ	3.3	3.4	0.003	0.071	0.071
AE (±)	2.5	2.8	0.003	0.063	0.032

Even so, a recent work conducted by Martinez *et al*. [34] proved the technical feasibility of rCB as substitute of commercial CB N550 in rubber formulations (Styrene Butadiene Rubber compounding), if it subjected to a prior demineralization step using HCl. Similarly, a study conducted by Norris et al. [37] suggested that based on the properties of rCB, it can be considered as a semi-reinforcing filler in applications occupied by N600 to N700 commercial CB series. Overall, the σ and AE reported in Table 2.12 and Table 2.13 suggests that the characteristics of the rCB derived from the twin-auger pyrolysis plant obtained at the same experimental conditions are consistent and repeatable as well.

2.2.5.3 Tire pyrolysis gas characterization

The TPG covers all the non-condensable compounds contained in the VM released from the pyrolysis of WT. For the repeatability analysis, three different TPG samples were collected in different replicates after the process reached the steady

state (after 30 min of continuous operation). Table 2.14 shows the chemical composition of these samples obtained by means of qualitative gas chromatography. On nitrogen-free basis, the TPG samples were composed mainly of H_2 (23.64 ± 0.35 vol.%), CH_4 (28.22 ± 0.41 vol.%), CO (3.69 ± 0.44 vol.%), CO_2 (3.08 ± 0.43 vol.%), C_2H_4 (4.78 ± 0.06 vol.%), C_2H_6 (6.21 ± 0.14 vol.%), C_3H_8 (5.5 ± 1.22 vol.%) and H_2S (0.54 ± 0.14 vol.%). These species account for 73.6 vol.% of the total TPG, which implies that other species are present in lower amounts. According to this chemical composition, the estimated heating value of TPG is around 27 MJ/Nm^3

Table 2.14. Chemical composition of TPG

Sample	Compound (vol.%)							
	H_2	CH_4	CO	CO_2	C_2H_6	C_2H_4	C_3H_8	H_2S
1	23.69	28.24	3.95	2.47	6.01	4.71	3.88	0.65
2	24.05	27.70	3.07	3.38	6.32	4.85	6.76	0.63
3	23.19	28.71	4.05	3.40	6.31	4.77	6.01	0.34
$\bar{x}$	23.64	28.22	3.69	3.08	6.21	4.78	5.55	0.54
σ	0.35	0.41	0.44	0.43	0.14	0.06	1.22	0.14
AE (±)	0.30	0.34	0.41	0.41	0.14	0.05	1.11	0.13

Despite the presence of H_2S, it has been reported in the literature that due to its high energy density, the combustion of a portion of TPG delivers enough heat to cover the energy demanded by the process (known as the heat for pyrolysis). In addition the remaining TPG can be used to produce electricity, which can be sold for revenue [25,40]. The results shown in Table 2.14 regarding the σ and AE also suggest that the composition of TPG is consistent and reproducible among the replicates.

2.3 Summary

This chapter discusses the operational characteristics of a novel twin-auger reactor to transform WT by intermediate pyrolysis into TPO, rCB, and TPG. The influence of four operating parameters: reactor temperature, WT mass flow rate, solid residence time, and N_2 volumetric flow rate was assessed aiming at maximizing the TPO yield, while minimizing the rCB one. In order to carry out this analysis, an experimental campaign was conducted based on the central composite design (CCD). The analysis of variance (ANOVA) revealed that the reactor temperature and the WT mass flow rate exhibit the highest statistical influence on TPO and rCB yields (responses) in the defined experimental domain. An optimization of both responses resulted in TPO, rCB, and TPG yields of 45, 40, and 15 wt. %, respectively, when the pyrolyzer is operated at 475 °C, 1.16 kg/h, 3.5 min and 300mL/min. Subsequently, based on the optimum experimental conditions obtained in the RSM analysis, the repeatability of the experimental facility in terms of TPO, rCB, and TPG yields, as well as the consistency of the properties of the derived products were also assessed and discussed. Here, results of the ANOVA test demonstrated that the experimental facility is repeatable in terms of TPO, rCB, and TPG yields. Moreover, the standard deviation calculated from the characterization of different products samples suggested that the physicochemical properties of TPO, rCB, and TPG obtained at given experimental conditions are consistent.

References

[1] F. Campuzano, R.C. Brown, J.D. Martínez, Auger reactors for pyrolysis of biomass and wastes, Renew. Sustain. Energy

Rev. 102 (2019) 372–409.

[2] F. Campuzano, Basic design of an auger for pyrolysis of municipal solid waste, Universidad Pontificia Boliavariana, MSc Thesis, 2017.

[3] R.H. Myers, D.C. Montgomery, Response surface methodology: Products and process optimization using design of experiments (Wiley series in probability and statistics), Wiley, New York, 2009.

[4] B. Dejaegher, Y. Vander Heyden, Experimental designs and their recent advances in set-up , data interpretation , and analytical applications, J. Pharm. Biomed. Anal. 56 (2011) 141–158.

[5] J. V Nardi, W. Acchar, D. Hotza, Enhancing the properties of ceramic products through mixture design and response surface analysis, J. Eur. Cern. Soc. 24 (2004) 375–379.

[6] E. Kristo, C.G. Biliaderis, N. Tzanetakis, Modelling of the acidification process and rheological properties of milk fermented with a yogurt starter culture using response surface methodology, Food Chem. 83 (2003) 437–446.

[7] J.N. Brown, R.C. Brown, Process optimization of an auger pyrolyzer with heat carrier using response surface methodology, Bioresour. Technol. 103 (2012) 405–414.

[8] R.E. Raj, Z.R. Kennedy, B.C. Pillai, Optimization of process parameters in flash pyrolysis of waste tyres to liquid and gaseous fuel in a fluidized bed reactor, Energy Convers. Manag. 67 (2013) 145–151.

[9] M. Mathew, L. Muruganandam, Pyrolysis of agricultural biomass using an auger reactor: A parametric optimization, Int. J. Chem. React. Eng. 15 (2017) 1–12. doi:10.1515/ijcre-2016-0133.

[10] D. Bas, I.H. Boyaci, Modeling and optimization I: Usability of response surface methodology, J. Food Eng. 78 (2007) 836–845.

[11] M.S. Bartlett, Properties of sufficiency and statistical test, Procedings R. Soc. a Math. Phys. Eng. Sci. 921 (1937) 268–282.

[12] M.S. Bartlett, D.G. Kendall, The stistical analysis of variance-heterogeneity and the logarithmic transformation, R. Stat. Soc. 8 (1946) 128–138.

[13] S.S. Shapiro, M.B. Wilk, Analysis of variance test for normality (complete samples), Biometrika. 52 (1965) 591–611.

[14] American Socity for Testing and Materials (ASTM), Standard practice for conducting an interlaboratory study to determine the precision of a test method (ASTM E691-19e1), 2019.

[15] Y.A. Lenis, A.F. Agudelo, J.F. Pérez, Analysis of statistical repeatability of a fi xed bed downdraft biomass gasi fi cation facility, Appl. Therm. Eng. 51 (2013) 1006–1016.

[16] NCSS Statistical System, Chapter 210: One way analysis of variance, (n.d.). https://ncss-wpengine.netdna-ssl.com/wp-content/uploads/2012/09/NCSSUG2.pdf (accessed September 7, 2020).

[17] N.M. Razali, Y.B. Wah, Power comparisons of Shapiro-Wilk , Kolmogorov-Smirnov , Lilliefors and Anderson-Darling tests, J. Stat. Model. Anal. 2 (2011) 21–33.

[18] G. V Glass, Testing homogeneity of variances, Am. Educ. Res. J. 3 (1966) 187–190.

[19] ASTM, Standard test method for carbon black—total and external surface area by nitrogen adsorption, 2019.

[20] A.V. Akkaya, Proximate analysis based multiple regression models for higher heating value estimation of low rank coals, Fuel Process. Technol. 90 (2008) 165–170.

[21] R. Feraldi, S. Cashman, M. Huff, L. Raahauge, Comparative LCA of treatment options for US scrap tires: material recycling and tire-derived fuel combustion, Int. J. Life Cycle Assess. 18 (2013) 613–625.

[22] P. Pipilikaki, M. Katsioti, D. Papageorgiou, D. Fragoulis, E. Chaniotakis, Use of tire derived fuel in clinker burning, Cem. Concr. Compos. 27 (2005) 843–847.

[23] J.D. Martínez, N. Puy, R. Murillo, T. García, M.V. Navarro, A.M. Mastral, Waste tyre pyrolysis - A review, Renew. Sustain. Energy Rev. 23 (2013) 179–213.

[24] E. Aylón, A. Fernández-Colino, R. Murillo, M.V. Navarro, T. García, A.M. Mastral, Valorisation of waste tyre by pyrolysis in a moving bed reactor, Waste Manag. 30 (2010) 1220–1224.

[25] J.D. Martínez, R. Murillo, T. García, A. Veses, Demonstration of the waste tire pyrolysis process on pilot scale in a continuous auger reactor, J. Hazard. Mater. 261 (2013) 637–645.

[26] W. Kaminsky, C. Mennerich, Pyrolysis of synthetic tire rubber in a fluidised-bed reactor to yield 1,3-butadiene , styrene and carbon black, J. Aanlytical Appl. Pyrolysis. 58–59 (2001) 803–811.

[27] G. López, M. Olazar, R. Aguado, J. Bilbao, Continuous pyrolysis of waste tyres in a conical spouted bed reactor, Fuel. 89 (2010) 1946–1952.

[28] I. Hita, M. Arabiourrutia, M. Olazar, J. Bilbao, J. M. Arandes, and P. Castaño, Opportunities and barriers for producing high quality fuels from the pyrolysis of scrap tires, Renew. Sustain. Energy Rev. 56 (2016) 745–759.

[29] P.T. Williams, Pyrolysis of waste tyres: A review, Waste Manag. 33 (2013) 1714–1728.

[30] N. Antoniou, A. Zabaniotou, Features of an efficient and environmentally attractive used tyres pyrolysis with energy and material recovery, Renew. Sustain. Energy Rev. 20 (2013) 539–558.

[31] K.Y. Cheung, K.L. Lee, K.L. Lam, T.Y. Chan, C.W. Lee, C.W. Hui, Operation strategy for multi-stage pyrolysis, J. Anal. Appl. Pyrolysis. 91 (2011) 165–182. http://dx.doi.org/10.1016/j.jaap.2011.02.004.

[32] J. Lédé, Biomass Fast pyrolysis reactors: A review of a few scientific challenges and of related recommended research topics, Oil Gas Sci. Technol. – Rev. IFP Energies Nouv. 68 (2013) 801–814.

[33] M.B. Pecha, J.I. Montoya Arbelaez, M. Garcia-Perez, F. Chenjne, P.N. Ciesielski, Progress in understanding the four dominant intra-particle phenomena of lignocellulose pyrolysis: Chemical reactions, heat transfer, mass transfer, and phase change, Green Chem. 21 (2019) 2868–2898. doi:10.1039/c9gc00585d.

[34] J.D. Martínez, N. Cardona-Uribe, R. Murillo, T. García, and J.M. López, Carbon black recovery from waste tire pyrolysis by demineralization : Production and application in rubber compounding, Waste Manag. 85 (2019) 574–584.

[35] S.-Q. Li, Q. Yao, Y. Chi, J.-H. Yan, K.-F. Cen, Pilot-scale pyrolysis of scrap tires in a continuous rotary kiln reactor, Ind. Eng. Chem. Res. 43 (2004) 5133–5145.

[36] C. Roy, A. Chaala, H. Darmstadt, The vacuum pyrolysis of used tires end-uses for oil and carbon black products, J. Anal. Appl. Pyrolysis. 51 (1999) 201–221.

[37] C.J. Norris, M. Hale, M. Bennett, Pyrolytic carbon: Factors controlling in-rubber performance, Plast. Rubber Compos. 43 (2014) 245–256.

[38] J.D. Martínez, M. Lapuerta, R. Garcia-Contreras, R. Murillo, T. García, Fuel properties of tire pyrolysis liquid and its blends with diesel fuel, Energy Fuels. 27 (2013) 3296–3305.

[39] J.D. Martínez, Á. Ramos, O. Armas, R. Murillo, T. García, Potential for using a tire pyrolysis liquid-diesel fuel blend in a light duty engine under transient operation, Appl. Energy. 130 (2014) 437–446.

[40] D. Czajzynska, R. Krzyzynska, H. Jouhara, N. Spencer, Use of pyrolytic gas from waste tire as a fuel : A review, Energy. 134 (2017) 1121–1131.

Chapter 3. Effect of CaO on the physicochemical properties of the pyrolysis derived products

TPO is one of the most abundant and interesting products obtained from the pyrolysis of WT and its use as alternative fuel in thermal systems has been regarded as one of the most straightforward applications. However, TPO still faces several challenges which stand as a bottleneck for its direct deployment in existing combustion facilities. Among others, the high sulfur content (~1.0 wt.%) is one of the main concerns, taking into consideration the associated technical implications and detrimental effects on the environment [1]. Despite its potential as a counterpart of petroleum-derived fuels, its renewable characteristics, as well as compatibility with existing refineries, the use of TPO in combustion applications has been highly disputed based on current fuel standards and emissions normativity, for instance the European Air Quality Standard (EU2015/2193). Thereby, before TPO use in combustion facilities, desulfurization strategies must be explored for its upgrading.

Different approaches have been taken towards this scope, including both *ex-situ* and *in-situ* desulfurization pathways as described in Chapter 1. Among these alternatives, *in-situ* desulfurization seems to offer lower related costs and simplicity, making it attractive as a first attempt to improve the properties of TPO. Within this context, calcium-based materials are posed as promising options due to their low-cost, high abundance, and desulfurization capability. In particular, CaO has been widely used to regulate the sulfur content (H_2S, SO_2, etc.) of products resulting from different thermo-chemical processes (*i.e.* pyrolysis, gasification, and combustion) of several feedstock, including coal, biomass, and plastics [2–7]. In addition, CaO may also adsorb CO_2 and H_2O to produce $CaCO_3$ [8] and $Ca(OH)_2$ [9], respectively, improving the properties of the derived products.

Due to its catalytic activity, CaO has also been used to modify/improve the physicochemical properties of the liquids obtained from the pyrolysis of different types of coals and biomasses [10,11]. For instance, Khan [12] reported a decrease in the viscosity, oxygen content, and Conradson carbon residue in the liquid derived from coal pyrolysis using CaO. Moreover, the composition of the heavy fraction was altered, given the reduction of some aromatic compounds while the aliphatic ones increased [12]. The heavy fraction of the liquid derived from coal pyrolysis usually contains polyphenols, as well as polyfunctional aromatic compounds. The CaO presence during the pyrolysis process seems to promote deoxygenation and cracking reactions resulting in smaller molecules [13–15]. Similarly, in a study conducted by Wang *et al*. [16], the addition of CaO during the co-pyrolysis of bituminous coal and cow dung resulted in a decrease of the relatively amount of polyaromatic hydrocarbons (*i.e.* phenanthrene, pyrene, and retene), while a raise of the relative content of benzene and naphthalene in the derived liquid fraction. These findings were attributed to the catalytic activity of CaO on the decomposition of larger aromatic ring compounds and the repeated bond-forming and bond-breaking process between the Ca species and the carbonaceous matrix. Other works have shown an increase in the liquid yield when calcium-based materials are added during pyrolysis of polyolefin [17,18].

Aside from pyrolysis, several coal and biomass gasification studies reported in the literature have explored the catalytic effects of CaO on tar reforming [19–21]. Results have revealed that the use of CaO during gasification not only reduces the amount of

tar and changes its structural characteristics (modifies aromatic structures), but also enhances the yield of the produced gas and the concentration of H_2 in it.

Up until now, different types of reactor arrangements have been used to carry out the pyrolysis of WT and the upgrading of the resulting products [22–24]. However, auger pyrolyzers, in particular the twin-auger configuration, has not yet been investigated to carry out both processes simultaneously. As highlighted in previous chapters, the twin-auger pyrolyzer offers a high degree of mixing and heat transfer, which favors the conversion of the feedstock during pyrolysis. Therefore, this configuration is promising for conducting *in-situ* desulfurization/catalytic pyrolysis to improve the properties of the derived products using low-cost materials such as CaO. In this regard, this chapter presents a first attempt to reduce the sulfur content in TPO by adding CaO in an independent and continuous manner during the pyrolysis of WT in the twin-auger pyrolizer described in Chapter 2. Besides the sulfur reduction capabilities, the influence of CaO on the main physicochemical properties not only of TPO, but also of the derived rCB and TPG is also addressed.

3.1 Materials and methods

3.1.1 Calcium oxide

CaO was obtained by the thermal decomposition (calcination) of $CaCO_3$. The calcination process was carried out in an electric oven and started by heating the $CaCO_3$ gradually up to 300 ºC at 10 ºC/min, followed by maintaining 300 ºC for 30 min. Thereafter, the temperature was increased to 600 ºC at 10 ºC/min, and sustained again for 30 min. At the same heating rate, the temperature was then increased to 900 °C, and retained for 11 hours (overnight). After calcination, the resulting material was sieved, and the particle size distribution was determined. For the experimental campaign, two particle size ranges were chosen in order to assess the effect of this parameter on the sulfur reduction of TPO. Thus, the selected materials had a particle size distribution between 105 and 149 µm, and between 149 and 841µm. It is worth mentioning that for this study, the particle size distribution of CaO was selected in a wide range, with the intention of industrial applicability; in industrial applications, narrower particle size distributions may be more difficult to achieve. The composition of the obtained CaO was identified by means of an XRF analysis carried out in an Epsilon 1 Panalytical equipment. Likewise, morphological characteristics and surface composition were determined through Scanning Electron Microscopy/Energy Dispersive using X-ray spectroscopy (SEM/EDX) in a JEOL JSM-6490 LV apparatus with an acceleration voltage of 20 kV. Additionally, textural properties namely: BET surface area (S_{BET}), volume of micro pores (V_o), total volume of pores (V_T), and volume of mesopores (V_{Meso}) were determined by multi-point N_2 adsorption in a micrometrics ASAP 2020 Plus apparatus. For characterization purposes, the samples were dried at 110 ºC for 12 h and degassed at 300 ºC for 8 h. Textural parameters were then calculated following the same procedure as described for rCB in Chapter 2.

3.1.2 Experimental procedure

The effect of adding CaO during the pyrolysis of WT on the physicochemical properties of TPO, TPG, and rCB was studied under the optimum operational conditions determined by the RSM, as described in Chapter 2. Thus, CaO was fed into the twin-

auger pyrolyzer in an independent and continuous manner at different feeding rates, ensuring different proportions of CaO/WT (10, 15, and 20 wt.%), based on a fixed WT mass flow rate (1.16 kg/h). The yields of TPO and rCB were determined by weighing the products after pyrolysis, while the yield of TPG was obtained by difference. It is worth mentioning that the final solid fraction considers a mix of rCB, CaO (regenerated or no transformed), and other calcium-containing compounds (*e.g.* CaS, $Ca(OH)_2$, $CaCO_3$). Nonetheless, weight changes in the reacting CaO to form the aforementioned species in contrast to the total weight of the CaO added during the process were considered negligible. Therefore, the rCB yield was obtained by subtracting the total mass of CaO added during the experiments to the total weight of the solids contained in the collecting vessel. In order to have an accurate value of the total amount of CaO fed during operation, the mass flow rate of CaO at different feeder screw velocities was accurately calibrated for both particle size ranges prior to experimentation. The resulting TPO samples were initially characterized in terms of sulfur content (ASTM D 7220-12) in order to estimate the CaO effect on the sulfur reduction. The percentage of the sulfur removal from TPO was calculated according to Equation 3.1. Here, S_{TPO} is the sulfur content of TPO without using CaO and $S_{TPO[CaO]}$ is the sulfur content of TPO when adding CaO during pyrolysis. The sample with the lowest sulfur content, named TPO[CaO], was further characterized as described in the following sections. In addition, the main features of the rCB and TPG linked to TPO[CaO]: rCB[CaO] and TPG[CaO], respectively, were also assessed.

$$\% S_{Reduction} = \frac{S_{TPO} - S_{TPO[CaO]}}{S_{TPO}} \times 100\% \quad \textbf{(3.1)}$$

3.1.3 Demineralization process

One of the major issues behind the WT recycling is the process economics and the commercial value of the obtained products. The profitability of the pyrolysis of WT at industrial or semi-industrial scale depends on the applicability of the major products: TPO and rCB. The addition of CaO during the pyrolysis of WT in this investigation aims at reducing the sulfur content in TPO. Nonetheless, it is clear that this alternative alters the physicochemical properties of rCB, decreasing its suitability, for instance, as a reinforcing material in rubber formulation for substituting of commercial carbon black. In order to decrease this undesirable effect, an acid demineralization process using HCl was assessed to remove the residual/transformed CaO and other inorganic materials contained in the rCB[CaO]. A schematic diagram of the experimental setup is shown in Figure 3.1. This experimental setup consists of a jacketed glass reactor (nominal capacity of 2 L) coupled to a mechanical stirrer. A reflux condenser is adjusted to prevent possible water evaporation and changes in reagent concentrations. Furthermore, a thermocouple is used to monitor the temperature profile during the experiments. The demineralization conditions used in this work were those determined in previous investigations conducted by the GIA research group: *"Experimental evaluation of the demineralization process of the solid fraction produced from the pyrolysis of WT for industrial application"* [25]. A differentiating factor of this process is that no heat is provided to the reactor, which reduces the energy penalties and improves the economic feasibility of demineralization. More details regarding the demineralization system and governing conditions can be found elsewhere [25]. Once the concentration of HCl (5 M) and the volume of reagent (500 mL) were ensured, 100 g of rCB[CaO] was fed into the reactor, and the liquid-solid mixture was stirred for 60 min. The rotation velocity of the mechanical stirrer was fixed at 600 rpm,

since this value guarantees an intimate mixing between reagent and rCB[CaO]. After the mixing period, the obtained solid (drCB[CaO]) was successively washed with distillated water until the pH of the filtrate reached a neutral value.

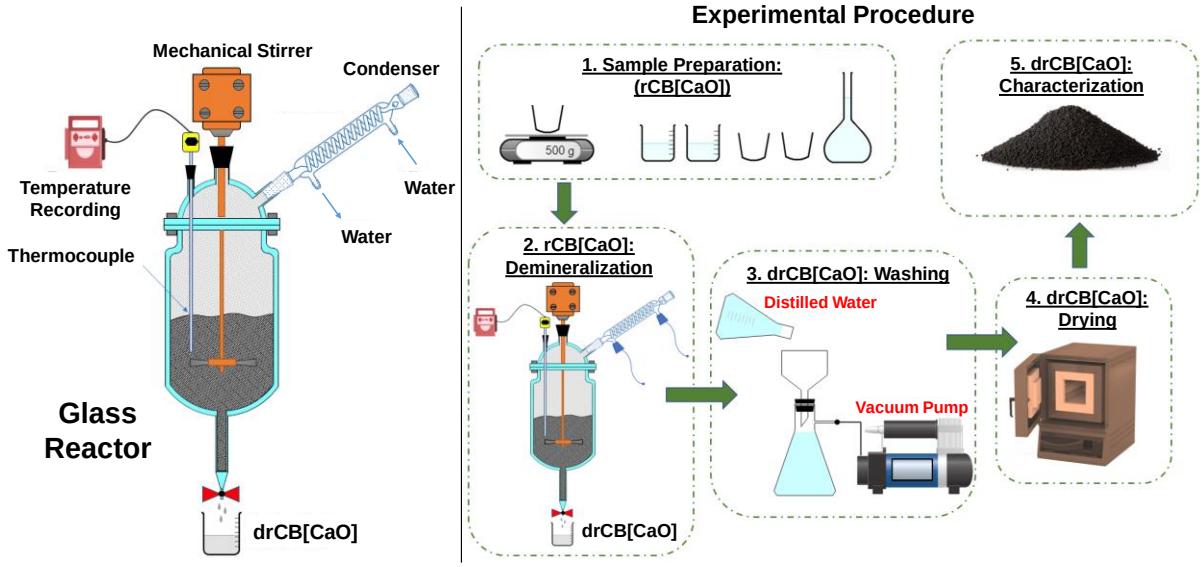

Figure 3.1. Demineralization: Setup and experimental procedure

Then, the drCB[CaO] was dried overnight (8 h) using an electric oven at 105 ºC. Thereafter, the reduction in the presence of inorganic compounds was determined by means of Equation 3.2, where m_3 is the mass of the crucible containing the ashes of the drCB[CaO], m_2 is the mass of the crucible containing the ashes of the rCB[CaO], and m_1 is the mass of the empty crucible. The ashes of each sample were obtained according to ASTM D1506.

$$\%\ Ash_{reduction} = \frac{(m_3 - m_1)}{(m_2 - m_1)} \times 100\% \qquad \textbf{(3.2)}$$

3.1.4 Characterization of products

TPO and TPO[CaO] were initially characterized in terms of elemental composition, higher heating value, density, kinematic viscosity, and water content. The standard procedures to conduct these analyses are similar to the ones described in Chapter 2 for TPO. In addition, the simulated distillation curve was obtained in line with ASTM D7500. Lastly, the main compounds contained in both TPO and TPO[CaO] were identified by means of qualitative gas chromatography mass spectroscopy (GC-MS) in a THERMO Trace GC Ultra with MS DSQ II. The methodology followed to conduct this analysis is presented in Appendix B, Section B2.1. Regarding the rCB[CaO] and drCB[CaO], both samples were initially characterized in terms of ash content, according to ASTM D1506. Then, their chemical composition was determined by XRF in an Epsilon 1 Panalytical apparatus. For the sake of comparison, the ash composition of rCB obtained without adding CaO, as well as the composition of the ashes contained in WT, were measured following the same procedure. Furthermore, textural characteristics such as S_{BET}, V_o, V_T, and V_{Meso}, were determined as well for rCB[CaO], and drCB[CaO]. In order to carry out this analysis, all samples were degassed at 120 ºC under vacuum conditions for 10 h. Textural parameters were calculated following the same procedure as described for

rCB in Chapter 2. Finally, the TPG[CaO] composition was determined by means of gas chromatography following the methodology outlined in Chapter 2 for TPG.

3.2 Results and discussion

3.2.1 Characteristics of calcium oxide

As previously mentioned, CaO was obtained through the calcination of $CaCO_3$ at 900 ºC, resulting in a mass loss of around 44 wt.%. The elemental composition of the resulting CaO identified by XRF revealed that the major species are Ca (81.3 wt. %), followed by Si (1.5 wt. %) and Mg (0.29 wt. %). Other elements such as Al (0.28 wt.%), Fe (0.14 wt.%), Zn (0.006 wt.%), and Sr (0.057 wt.%) were also detected, but in minor quantities. These elements account for 84 wt.% of the total composition of the sample, which implies that traces of other elements might be present. Table 3.1 reports the textural properties of the resulting CaO at the two particle size ranges.

Table 3.1. Textural characteristics of CaO

Sample	S_{BET} (m^2/g)	V_o (cm^3/g)	V_T (cm^3/g)	V_{Meso} (cm^3/g)
CaO [149-841 µm]	9	0.0035	0.035	0.0315
CaO [105-149 µm]	10	0.0041	0.030	0.0259

As observed, both samples exhibit very similar S_{BET}, although V_o is slightly higher (15%) for the CaO [105-149 µm] as compared to that of CaO [149-841 µm]. Nonetheless, CaO [149-841 µm] presents larger V_T (16.7 %) and V_{Meso} (21.6 %) in contrast to CaO [105-149 µm]. Even so, both samples can be regarded as predominantly mesoporous materials, since more than 86 % of total volume of pores corresponds to mesopores (see Figure 3.2). This feature is expected to have a positive effect on the activity of CaO during the pyrolysis of WT, because it facilitates the access and diffusion of reactants (H_2S, COS, H_2O, CO_2, etc.) compounding the volatile matter through the CaO surface of particles.

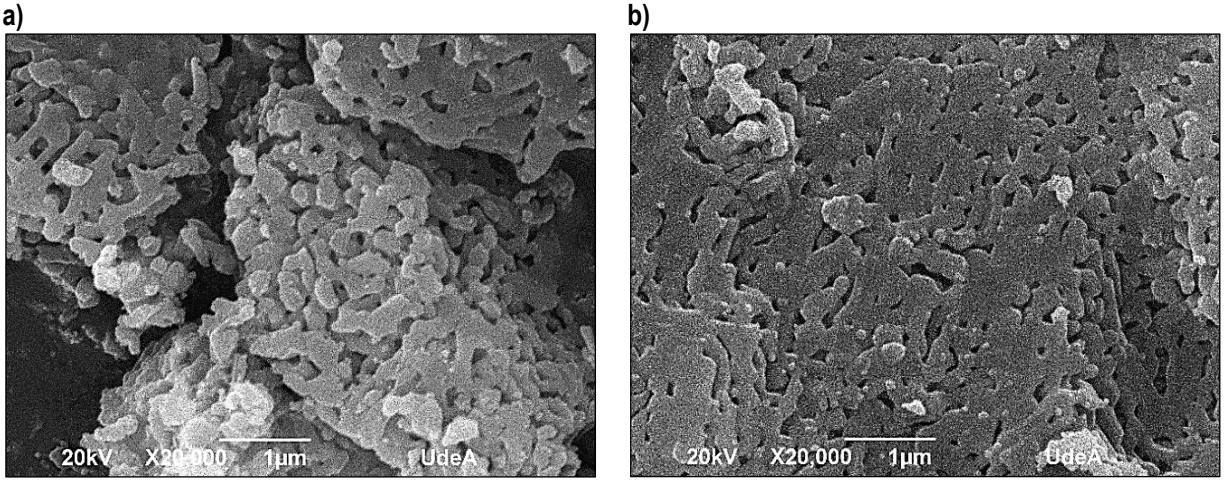

Figure 3.2. SEM images of CaO with a magnification of 20000x: **a)** CaO [105-149 µm] and **b)** CaO [149-841 µm]

The above-described properties are important factors on the rate and degree of reactivity of CaO when used as a catalyst/sorbent in chemical processes [26], and they depend strongly on the characteristics of the base material (particle size,

mineral composition, etc.) and on calcination conditions (temperature, heating rate, and retention time) [27]. For instance, moderate calcination temperatures produce highly porous, highly reactive CaO particles, while high temperatures lead to shrunken, dense CaO particles with low porosity, most likely due to sintering [28]. Due to the strong influence of these parameter on the characteristics of the obtained CaO after calcination, dissimilarities are commonly found when comparing them with the information reported in most of the previous studies [29–31]. Complementary to the information obtained by XRF, Section B1.1 and Section B1.2 in Appendix B show the surface composition of CaO [105-149 µm] and CaO [149-841 µm], respectively, obtained by EDX. These results confirm the predominant presence of Ca, O, and Mg on the surface of the CaO particles.

3.2.2 Influence of calcium oxide addition on the yield of products

Figure 3.3 shows the yields of TPO, TPG, and rCB with the addition of 10, 15, and 20 wt.% of CaO during the pyrolysis of WT. Results obtained without adding CaO are also included for comparison purposes. The associated errors (standard deviations) regarding the TPO, rCB, and TPG yields in the twin-auger pyrolysis plant are ± 1.1 wt.%, ± 0.87 wt.%, and ± 1.6 wt.%, respectively.

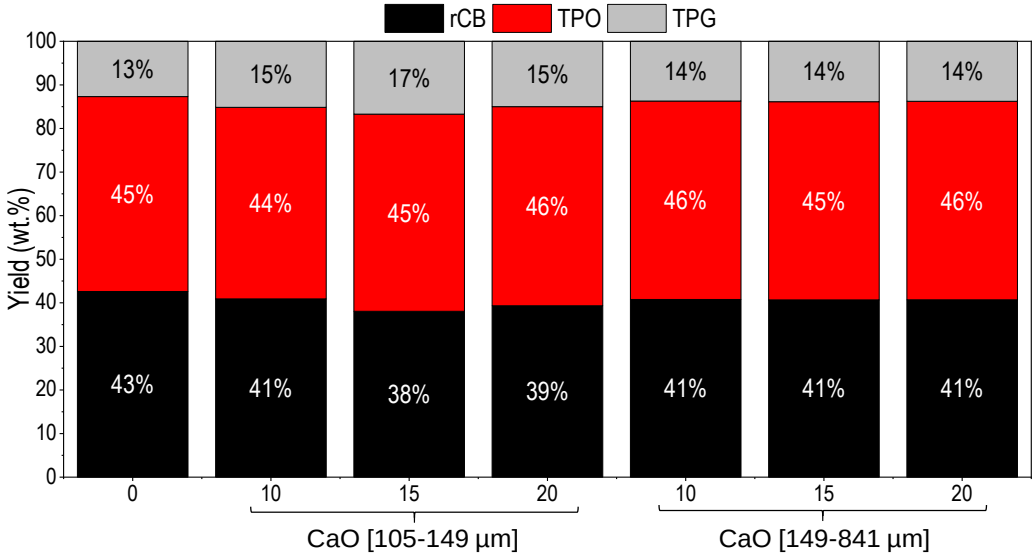

Figure 3.3. Pyrolysis products yields

As observed in Figure 3.3, the addition of CaO has a minor effect on the TPO yield, represented by the slight variation between 44 and 46 wt.%. The effect of CaO was more prominent in the rCB and TPG yields, particularly in the case of CaO [105-149 µm], where the rCB yield decreased from 43 wt. % to 38 wt. %, and TPG yield increased from 13 wt. % to 17 wt.%. Even though these differences may fall within the experimental error, a significant increase in the total volume flow of TPG with the addition of CaO was qualitatively observed during the experiments. Similar results were obtained by Aydin *et al.* [32], using different proportions of $Ca(OH)_2$ in a fixed bed reactor (capacity of 1.15 L), introduced at 5, 10 and 15 wt.% of the WT sample, showing a greater effect in the yields of rCB and TPG, which varied from 48-46 wt.% and 11-14 wt.%, respectively. Also, Choi *et al.* [33] reported small differences on the TPO and rCB yields when calcined dolomite was used in a fluidized bed pyrolyzer. The higher effect was found in the TPG (from 9.1 to 12.3 wt.%), which was attributed to the enhancement of cracking reactions given the

high presence of active sites on the calcined dolomite particles surface. Similarly, more noticeable differences were found by Gabani *et al.* [34] using CaO nanoparticles in a fixed bed reactor. The high S_{BET} (435.54 m^2/g) of the CaO seems to be the main responsible of the wide variation of the TPO, TPG, and rCB yields. The two formers exhibited a significant increase from 34 to 46 wt.% and 28 to 35 wt.%, respectively, while the latter decreased from 38 wt.% to 19 wt.%. Overall, and according to previous investigations, the role of CaO during the pyrolysis of carbonaceous materials seems to be linked to the decomposition/transformation of heavy compounds (*i.e.* large aromatic structures and long alkane chains), which eventually favors the TPG yield [35,36] and to minor extent the yield of TPO. In addition, studies in the field of coal pyrolysis have demonstrated that the catalytic activity CaO enhances the release of volatile matter from the solid particles [37,38]. The combination of all these possible reaction pathways can explain the slight decrease of the rCB yield, while an increase of the TPG yield observed in this study. Nonetheless, this hypothesis may be verified by understanding the compositional changes of the pyrolysis products when adding CaO, in particular those occurring in TPO and TPG. Some insights will be provided in following sections.

3.2.3 Characterization of pyrolysis products

3.2.3.1 Effect of calcium oxide on the tire pyrolysis oil

Figure 3.4 shows the reduction in the sulfur content of TPO when adding CaO during WT pyrolysis. As observed, an increase in the CaO ratio leads to a greater sulfur reduction, especially in the case of coarse particle size. Thus, by adding 20 wt.% of CaO [149-841 µm], a maximum sulfur reduction of 26.40 wt.% was reached. However, it was noticed that between 15 wt.% and 20 wt.% of added CaO, the sulfur reduction was no longer significant. Thereby, it was concluded that adding 15 wt.% of CaO [149-841 µm] is the best option, given that the rCB is less contaminated, thus reducing the need for further severe post-treatments for its recovery. The characterization that will be shown in following section is therefore related to the optimum 15 wt.% of CaO [149-841 µm] addition. The associated error (standard deviation) with the sulfur measurement is ± 0.03 wt.%.

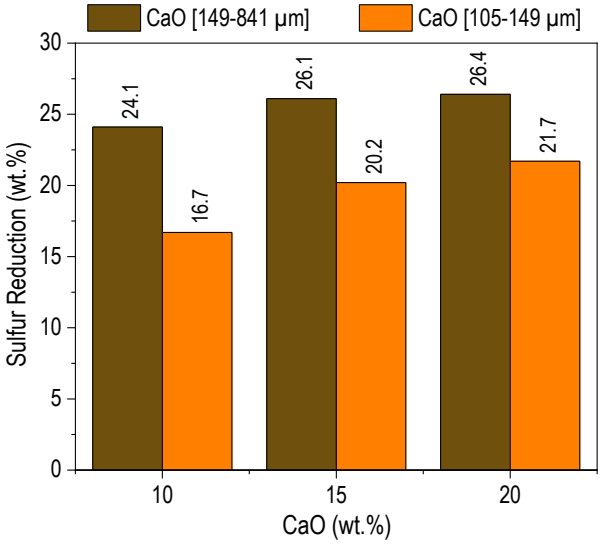

Figure 3.4. Effect of CaO on the sulfur content of TPO

The most abundant sulfur species contained in the volatile matter released during pyrolysis of WT has been reported to be hydrogen sulfide (H_2S), and to a minor extent carbonyl sulfide (COS) [1,32,33,39]. In the presence of CaO, these compounds are likely to react according to Equations 3.3 and 3.4, thus lowering the overall amount of sulfur in both TPO and TPG.

$$CaO + H_2S \leftrightarrow CaS + H_2O \qquad \Delta_r H^{\circ}_{(A)}(298\ K) = -59.44\ kJmol^{-1} \qquad \textbf{(3.3)}$$

$$CaO + COS \rightarrow CaS + CO_2 \qquad \Delta_r H^{\circ}_{(A)}(298\ K) = -94.21\ kJmol^{-1} \qquad \textbf{(3.4)}$$

Several researchers have reported that the occurrence of these reactions is governed by thermodynamic variables such as temperature, pressure, and gas-phase composition (concentration of H_2S and COS in the volatile matter) [40,41]. Furthermore, these works have established that the higher the surface area (S_{BET}) of the CaO particles, the lower the time required to convert the sulfur compound, because reactivity commonly increases with surface area. Interestingly, in this work, CaO [149-841 µm] exhibited a greater capability to remove sulfur in all tested conditions (10, 15, and 20 wt.% of CaO added) than CaO [105-149 µm], although both materials present quite similar S_{BET}. However, it was also found that CaO [149-841 µm] exhibited greater V_{Meso} than CaO [105-149 µm], which is also an important factor that influences this sulfidation reaction. Early studies conducted by Heesink *et al*. [41] found that during the initial reaction stage of the sulfidation pathway, the entire CaO particle surface takes part in the reaction via product layer diffusion of S^{2-} and O^{2-} ions. As the reaction proceeds, the CaO-core surface becomes partially covered by CaS, yet the CaO-core remains porous. In turn, this porosity defines the part of the of the CaO particle that is still available to facilitate the diffusion of the reacting gaseous species.

The sulfur removal percentage achieved in this initial attempt (26.40 wt. %) serves as an important step towards the upgrading of TPO for its use in thermal applications. It is expected that a higher removal could be achieved by improving the textural properties of the CaO particles, as observed by Agnihotri *et al.* [40]. These authors suggested that the sulfidation conversion of CaO particles exposed to a fuel gas containing up to 5000 ppm H_2S can be improved from 15 to 90 % by increasing the S_{BET} from 5.3 to 31.2 m^2/g. Regarding *in-situ* desulfurization in WT pyrolysis, previous studies carried out by Aydin *et al.* [32] reported a maximum sulfur reduction of 34.25 % when adding 5 wt.% of $Ca(OH)_2$ during the process. Nonetheless, the comparison is challenging since the characteristics of $Ca(OH)_2$ were not specified by the authors. Similarly, in the work conducted by Choi *et al*. [33], a maximum sulfur reduction of 35 wt.% was found when using calcined dolomite (CD) with a S_{BET} 9.49 m^2/g, yet in this case, CD was used as a bed material in a fluidized bed reactor. Overall, based on the final sulfur content achieved in this work (0.51 wt.%, shown in Table 3.2), the obtained TPO(TPO[CaO]) can be seen as a potential alternative to partially replace petroleum-derived fuels in the marine sector. In this context, the new regulations, *e.g.*, Regulation 14.1.3, MARPOL Annex 14 have established that by 2020 all ships should burn fuels with a sulfur content of no more than 0.5 wt.% [42].

Aside from the sulfur reduction, the addition of CaO also influences other physical properties of TPO. As observed in Table 3.2, the addition of 15 wt.% of CaO [149-841 µm] resulted in a decrease of 23 % of its kinematic viscosity (from 2.6 to 1.91 cSt). The viscosity reduction without affecting the energy density (TPO[CaO]: HHV = 43.40 MJ/kg and TPO: HHV = 42.76 MJ/kg) is also a noticeable finding of this work. In contrast to the work conducted by Aydin *et al.* [32], the addition of 5 wt.% $Ca(OH)_2$

resulted in a TPO with similar HHV (HHV: 43.34 MJ/kg). Nonetheless, unlike the present study, these authors reported a much higher viscosity (3.8 cSt). A lower viscosity can expand the range of possibilities for TPO implementation in conventional combustion systems, which are commonly designed to operate with low viscosity fuels. The advantages of having a less viscous fuel include ease of transportation and pumping, fuel economy, lower gas and particulate matter emissions (due to the better vaporization of the fuel), etc. Conventional fuels such as diesel used in internal combustion engines have a kinematic viscosity in the range of 2.0 – 5.0 cSt [43]. Accordingly, the obtained TPO[CaO] seems to approach to these applications.

Table 3.2. Physical and chemical properties of TPO and TPO[CaO]

Property/ Sample	Methods	TPO	TPO[CaO]
Density @ 25 °C (kg/m^3)	ASTM D4052-11	888.29	888.67
Kinematic viscosity @ 40 °C (cSt)	ASTM D445-12	2.60	1.91
pH	---	8.65	9.00
C (wt.%)	ThermoScientific 2000 apparatus.	86.64	87.21
H (wt.%)		10.56	10.66
N (wt.%)		1.32	1.23
S (wt.%)		0.70	0.51
O (wt.%)		0.78	0.39
H/C atomic ratio	From elemental composition	1.46	1.47
Water content (ppm)	ASTM E203	294.00	85.00
Higher heating value (MJ/kg)	ASTM D240-17	42.76	43.40
API gravity		29.7	29.7
Initial BP (°C)	ASTM D86	69.00	70.00
50% distillation (°C)	ASTM D7500	253.90	253.90
90% distillation (°C)	ASTM D7500	433.60	429.50
Final BP (°C)	ASTM D7500	558.50	550.90

As mentioned in the introduction, aside from desulfurization capabilities, multiple investigations on the pyrolysis and gasification of different carbonaceous feedstocks have revealed that CaO possesses a cracking effect on poly- and monoaromatic ring structures and long paraffinic chains [36,44]. First, these studies reported that the electron density in the p-orbital active sites of CaO may affect the stability of the π-electron cloud in condensed aromatic structures [36]. Herein, the O^{2-} ions that contain the active sites (electron pairs) of the CaO particles may polarize and subsequently destabilize the resonance structure of aromatic compounds. In turn, this phenomenon may lead to ring splitting, hence forming single aromatic, naphthenes, and/or olefinic compounds [20]. Second, the O^{2-} ions may also abstract H^+ ions from long paraffinic chains that lead to smaller hydrocarbon chains. In addition, these new chains may reorganize to form olefins, cycloparaffins (naphthenes), or even aromatic compounds at high temperatures [45]. The presence of these new compounds in the derived liquid products eventually influences, among other properties, their viscosity, which is sensitive to structural changes in the fuel. However, in order to confirm the occurrence of these reaction paths during the pyrolysis of WT, a comprehensive understanding of the structural changes caused in TPO as a result of the addition of CaO must be developed. This will be discussed in more detail later.

Even though the initial water contained in TPO is not significantly high due to the low moisture content in WT (up to 2 wt. %), the addition of CaO during the pyrolysis of WT also resulted in a decrease of 70 % of the water in TPO[CaO] in regard to TPO. During the pyrolysis of WT, the possible water vapor contained in the volatile matter may reacts with CaO particles to form

$Ca(OH)_2$, according to Equation 3.5 [9]. CaO hydration is a reversible reaction that occurs in the temperature range of 450 - 500 °C [46]. Taking into account that pyrolysis was conducted at 475 °C, CaO particles may not only have reacted with H_2S/COS to form CaS, but they also seem to have reacted with H_2O to form $Ca(OH)_2$; which may explain the reduction of the moisture content in the TPO[CaO]. In addition, H_2O plays an important role in composition of TPG, as will be explained in detail in Section 3.3.3.3.

$$Ca(OH)_2 \leftrightarrow CaO + H_2O \qquad \Delta_r H^{\circ}_{(A)}(298\ K) = -104\ kJmol^{-1} \qquad \textbf{(3.5)}$$

Distillation characteristics of TPO and TPO[CaO] at atmospheric conditions did not show significant differences. Those for TPO are presented in Chapter 2. Nonetheless, the simulated distillation data indicate higher final distillation temperature (558.5 °C and 550.9 °C for TPO and TPO[CaO], respectively) than those found at atmospheric pressure (around 300 °C). Nonetheless, it is worth mentioning that at atmospheric conditions, a heavy end of around 5 % is not evaporated, which is responsible for the significant increase of the final distillation point reported by the simulated data. Furthermore, the distillation temperature at which 50 % of the fuel was evaporated (T50) was 253.9 °C in both samples , while the temperature at which 90 % of the fuel was evaporated (T90) was slightly higher for TPO (433.60 °C) in contrast to TPO[CaO] (429.50 °C) as reported Table 3.2. T50 is a broad indicator of warm-up and acceleration performance under cold starting conditions in internal combustion engines. Thus, the lower the T50, the better the performance. Moreover, when the T90 and the final distillation point are too high, they can cause poor ignition distribution in the combustion chambers. This fact leads to the increase of unburnt hydrocarbon emissions and excessive combustion chamber deposits. The high values of these temperatures for TPO and TPO[CaO] can be associated with the presence of high molecular weight compounds, such as polycyclic aromatic hydrocarbons (PAH) and polycyclic aromatic sulfur hydrocarbon (PASH), as well as with long paraffinic side chains [47–49], which will be addressed in detail in Chapter 4.

On the other hand, API gravity is used to classify an oil as light (> 31.1), medium (22.3 - 31.1), heavy (< 22.3), and extra heavy (< 10). As the “weight” of the oil is the largest determinant of its market value, API gravity is an important parameter [50]. API gravity was found to be 29.7 for both samples. According to this, TPO and TPO[CaO] can be classified as medium weight oils. Finally, the pH was slightly modified due to the basic nature of CaO. Other properties such as density and contents of hydrogen, carbon, and nitrogen were not significantly modified.

The main compounds present in TPO and TPO[CaO] were identified by a qualitative GC-MS analysis. Even though multiple peaks appeared in the resulting spectrums (Appendix B, Section B2.2), which confirms the chemical complexity of both samples, the most representative peaks were chosen (39 compounds in total) in order to simplify the analysis. These compounds, denoted here as *PX* in Figure 3.5, were selected as those presenting the highest intensities in the spectrums. Figure 3.5 illustrates the percentage of the normalized areas of the selected peaks. The main compounds in TPO and TPO[CaO] are toluene (P7; normalized area: 12.2 and 13.0 %), 1,3-dimethyl-benzene or m-Xylene (P12; normalized area: 15.6 and 15.8 %), d-limonene (P20; normalized area: 23.2 and 23 .3 %), totaling to circa 50% of the sample. Other species such as ethylbenzene (P11; normalized area: 2.5 and 2.9 %) and mesitylene (P18; normalized area: 3.9 and 4.1 %) are also representative of both fuels.

Table B3 in Appendix B lists the identified compounds with their related retention times and normalized area percentages. These results are in complete agreement with prior information reported in the literature [22–24].

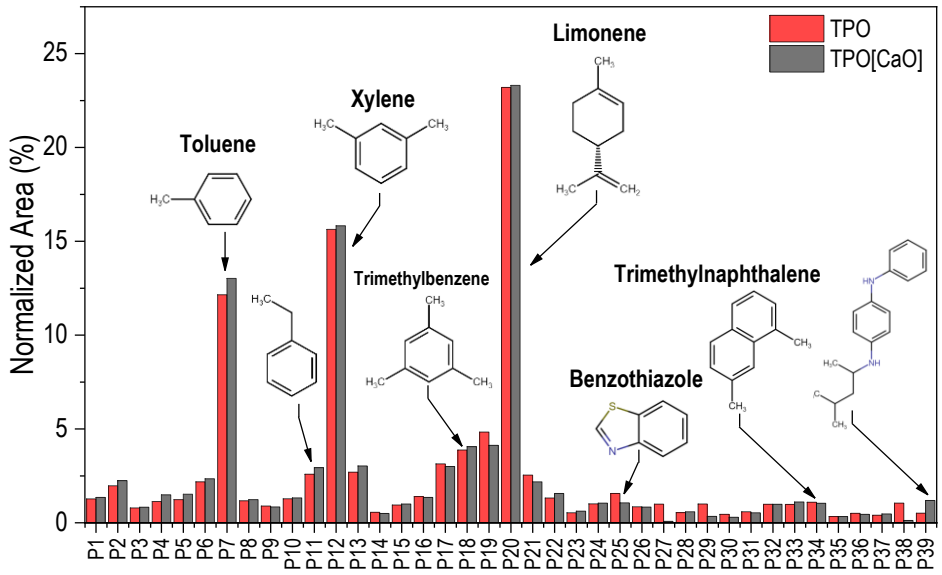

Figure 3.5. GC-MS of TPO and TPO[CaO]

It has been established that TPO contains high-value chemicals such as single aromatic ring compounds, including benzene, toluene, and xylene, as well as aliphatic compounds such as limonene, which was the most abundant compound in both TPO and TPO[CaO]. Most of the identified compounds are found in combinations of paraffinic-aromatic, paraffinic-olefinic, and naphthenic-olefinic structures, including the presence of a few nitrogen-, oxygen-, and sulfur-containing hetero molecules (see Table B.3 in Appendix B). Figure 3.6 illustrates the distribution of the above-described compounds.

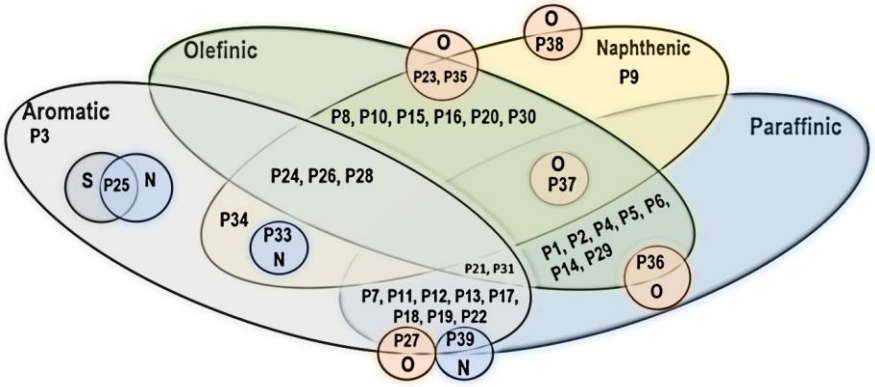

Figure 3.6. Distribution of compounds identified by GC-MS according to hydrocarbon types

Sulfur was found in the form of benzothiazole (P25). As observed in Figure 3.5, benzothiazole is around 31% more abundant in TPO in contrast to TPO[CaO], which agrees with the information reported in Table 3.2, and confirms the desulfurization effect of CaO during WT pyrolysis. Moreover, P7 (toluene) is found to be 7% more abundant in TPO[CaO] in comparison to TPO. Other compounds are similar in both fuels, with some minor deviations. Although these small changes in the abundance of light

aromatic (toluene, xylene, trimethylbenzene, etc.) and aliphatic (limonene) compounds would not independently affect the overall composition of the fuel, the sum of all abundance variations may cause a synergistic transformation, hence modifying the physicochemical properties of the fuel (*i.e.* viscosity). Nonetheless, as the GC-MS method used in this initial characterization stage was only capable of identifying compounds with boiling points up to 250 °C, it would have not elucidated the compositional changes of the heavy fraction of TPO[CaO], as indicated by the decrease in its final distillation point in contrast to TPO. Taking into account all results obtained hitherto, it is not accurate to provide conclusive statements regarding the effect of CaO on the structural characteristics of TPO, and thus on its physicochemical properties. In order to complete this analysis, a broader picture of both fuels is needed. This will be addressed in Chapter 4 by elucidating and contrasting TPO and TPO[CaO] structural characteristics using advanced analytical techniques such as FT-ICR MS and ^{1}H and ^{13}C NMR.

3.2.3.2 Effect of calcium oxide on the recovered carbon black

The solid fraction resulting from the pyrolysis of WT with the addition of CaO (rCB[CaO]) is a mix of rCB, products obtained from the reaction between CaO and volatile mater, and some extra CaO that did not react or was regenerated during the process. Morphological characteristics of rCB and rCB[CaO] can be observed in the SEM images shown in Figure 3.7.

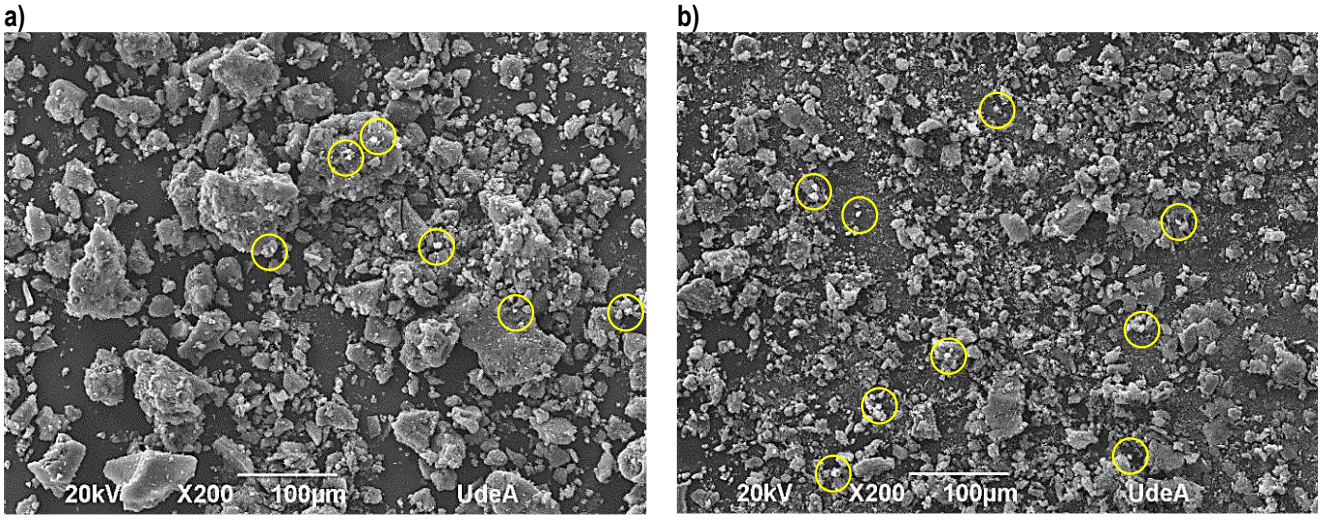

Figure 3.7. SEM images magnification of 200x: **a)** rCB and **b)** rCB[CaO] (CaO [149-841 µm])

It is noticed in Figure 3.7a that rCB exhibits a heterogeneous distribution, ranging from very fine aggregates up to ~100 µm. Nonetheless, in the case of rCB[CaO] (Figure 3.7b), the distribution of aggregate sizes is more uniform, presenting aggregates with smaller sizes in contrast to rCB. The uniformity in the distribution of the rCB[CaO] aggregates can be attributed to the attrition effect of CaO during the pyrolysis process. This is because the addition of CaO leads to a higher material density in the gap located between the reactor screws. Thus, mechanical friction is likely to take place between the rCB aggregates and CaO particles. In turn, this friction breaks apart the larger rCB aggregates. The bright points in the images (marked in circles) can be associated with inorganic compounds on the rCB surface, most likely CaO in the case of rCB[CaO].

In general, rCB differs from the virgin CB used in tire manufacture because it contains almost all of the inorganic compounds (ash content: 18.45 wt. %) present in tires, including reinforcing fillers, processing aids (oils, peptizers, trackfiers), and antidegradants (antioxidants, antiozonant, and waxes), etc., which eventually affect its physicochemical properties and reinforcement potential in rubber [51]. Thereby, among all the pyrolysis products, rCB poses the higher challenges for commercialization and use at industrial scale, thus lowering the overall profitability of WT pyrolysis [51]. Even though the catalytic pyrolysis of WT using CaO presents a positive effect on the physiochemical properties of TPO, particularly on the sulfur content, it is clear that there is a significant increase of the inorganic materials in the rCB fraction, which reduces its quality considerably at least as potential substitute of virgin CB. Other applications for rCB can be more flexible in regard to the CaO content [52]. Even so, in order to enhance the properties and potential applications of rCB[CaO] as partial substitute of CB (most convenient application), post-pyrolysis treatment is needed in order to reduce its inorganic content. Accordingly, rCB[CaO] was subjected to an acid demineralization process, which luckily also improved its textural properties, such as S_{BET} and porosity as will be shown later. The demineralization process decreased the ash content from 57.5 wt.% (rCB[CaO]) to 11.52 wt.% (drCB[CaO]), which represents a total ash reduction of ~ 80 wt.%. In addition, drCB[CaO] reached an ash content 37.57 wt.%, lower than that of rCB (18.45 wt.%), as reported in Chapter 2. Therefore, it can be inferred that the acid demineralization treatment was not only capable to reduce significantly the Ca added during pyrolysis, but also some other inorganic materials initially contained in the WT. Even so, the final ash content achieved (11.52 wt. %) is still high in comparison with that reported in previous investigations obtained after conducting demineralization, which is usually lower than 7.0 wt.% [53].

To understand the characteristics of these compounds in detail, Table 3.3 reports the normalized chemical composition regarding the inorganic compounds present in rCB[CaO] and drCB[CaO] obtained by XRF. For the sake of comparison, the ash composition of rCB and WT is included in Table 3.3 as well. As expected for rCB[CaO], there is a significant presence of CaO (65.38 wt.%), which comes not only from the CaO added during pyrolysis (CaO/WT: 15 wt.%), but also from the initial Ca contained in the inorganic materials (ash) in the WT (3.40 wt.%).

Other elements such as Zn (16.15 wt.%), S (8.78 wt.%), and Si (6.20 wt.%) are also present in significant amounts in rCB[CaO]. Zn and Si are commonly used as accelerators and fillers during the tire manufacturing process [51]. In fact, it is observed in Table 3.3 that the ashes of the WT used in this study contained 59.34 wt.% and 25.80 wt.% of Zn and Si, respectively, which remained similar in the rCB when pyrolysis was conducted without adding CaO. Likewise, the content of sulfur in the inorganic material of WT was found to be 3.09 wt.%, which also did not exhibit any change in the rCB either. Nonetheless, in this case of rCB[CaO], this S content also accounts for the sulfur removed by CaO from the volatile matter; hence, it may be present in the form of CaS. An interesting aspect noticed in Table 3.3 is that the ash composition of that from the WT and that of the rCB is quite similar; in turn, this indicates that the inorganic materials initially contained in the WT are completely trapped in the rCB.

Regarding drCB[CaO], it is observed that Ca was significantly reduced from 65.38 wt.% to 27.89 wt.%, which implies a decrease of 91% (based on the mass balance) in contrast to rCB[CaO]. This agrees with the significant ash loss through the

demineralization process. In addition, and for a better visualization, Table 3.3 shows the reduction percentage of the measured inorganic elements of the drCB[CaO] in comparison with rCB based on the mass balances and the composition determined by means of XRF. In contrast to the initial content of Zn in the ashes of rCB (51.37 wt.%), the acid demineralization step was effective to reduce the presence of this element in almost 78 %. Likewise, other elements, including Fe, K, Al, etc., were significantly reduced as well. However, elements such as S still remain in the drCB[CaO], which can be attributed to the presence of CaS. Altogether, these results suggest that a second demineralization step may be conducted to fine-tune the properties of drCB[CaO] and remove these undesirable elements.

Table 3.3. Elemental composition of inorganic compounds in WT, rCB, rCB[CaO] and drCB[CaO]

Element	WT (wt.%)	rCB (wt.%)	rCB[CaO] (wt.%)	drCB[CaO] (wt.%)	Reduction (%) (drCB[CaO] vs rCB)
Ash Content	6.9	18.45	57.5	11.52	37.57
Zn	59.34	51.37	16.15	17.68	78.51
Si	25.8	23.21	6.2	34.97	5.92
Ca	3.4	2.69	65.38	27.89	--
Fe	3.34	13.91	0.69	0.93	95.83
S	3.09	3.1	8.78	14.34	--
K	1.5	1.29	0	1.15	44.34
Al	1.27	2.21	1.26	1.64	53.67
P	0.88	0.86	0	0.44	68.05
Co	0.72	0.77	0.27	0.41	66.75
Cu	0.27	0.31	0.06	0.23	53.67
Br	0.21	0.14	0.42	0.12	46.48
Ti	0.15	0.15	0	0.19	20.91
Mn	251.3 ppm	918 ppm	0	145.2 ppm	--
Mg	0	0	0.71	0	0
As	0	0	0.01	0	0
Sr	0	0	0.05	0	0

Finally, Table 3.4 shows the textural properties rCB [CaO] and drCB[CaO]. Such properties for rCB (reported in Chapter 2) are also included for the sake of comparison. It is noticed that the S_{BET} of rCB decreases significantly with the addition of CaO. This is expected, since the addition of CaO during pyrolysis considerably increases the ash content of rCB, which eventually affects is textural properties (porosity and surface area). Other characteristics such as V_o, V_T, and V_{Meso} do not present significant changes. Nonetheless, it is worth to point out that, in the case of rCB[CaO], these values cannot be completely attributed to the rCB, since CaO and derived products are also present. Although the drCB[CaO] shows an increase in S_{BET} of 6% respect to that offered by rCB, it is still low in contrast to previous studies, which report a S_{BET} higher than 70 m^2/g in the rCB obtained after

demineralization [53]. An important parameter when considering rCB for rubber formulation is the STSA. This parameter is known as total and external surface area and according to the ASTM D6556, it defines the area that is accessible for rubber. The demineralization step resulted in a slightly increase of the STSA from 52 m^2/g (rCB) to 55 m^2/g (drCB[CaO]).

Table 3.4. Textural characteristics of rCB, rCB[CaO], and drCB[CaO] (CaO [149-841 µm])

Sample	S_{BET} (m^2/g)	STSA (m^2/g)	V_o (cm^3/g)	V_T (cm^3/g)	V_{Meso} (cm^3/g)
rCB	53	52	0.030	0.350	0.32
rCB[CaO]	46	45	0.031	0.361	0.33
drCB[CaO]	59	55	0.038	0.505	0.47

3.3.3.3 Effect of calcium oxide on the tire pyrolysis gas

Figure 3.8 shows the normalized chemical composition of TPG and TPG[CaO] obtained by gas chromatography. The amount of gases quantified represents about 80 % of the total gases in both cases. The composition of TPG exhibits important variations with the addition of CaO (TPG[CaO]). In particular, it is worth to highlight the increase of H_2 (from 31.22 to 38.61 vol.%), as well as some C_xH_y compounds such as C_3H_8 (from 7.33 to 10.73 vol.%), C_2H_6 (from 8.20 to 9.19 vol.%), C_2H_4 (from 6.31 to 7.77 vol.%), while a decrease of CO_2 (from 4.07 to 1.97 vol. %), CO (from 4.87 to 4.07 vol. %), and H_2S (from 0.71 to 0.50 vol.%). The related experimental errors (standard deviation) regarding the measurement of the chemical composition of TPG and TPG[CaO] are H_2 (± 0.35 vol.%), CH_4 (± 0.41vol.%), CO (± 0.44 vol.%), CO_2 (± 0.43 vol.%), C_2H_4 (± 0.06 vol.%), C_2H_6 (± 0.14 vol.%), C_3H_8 (± 1.22 vol.%), and H_2S (± 0.14 vol.%).

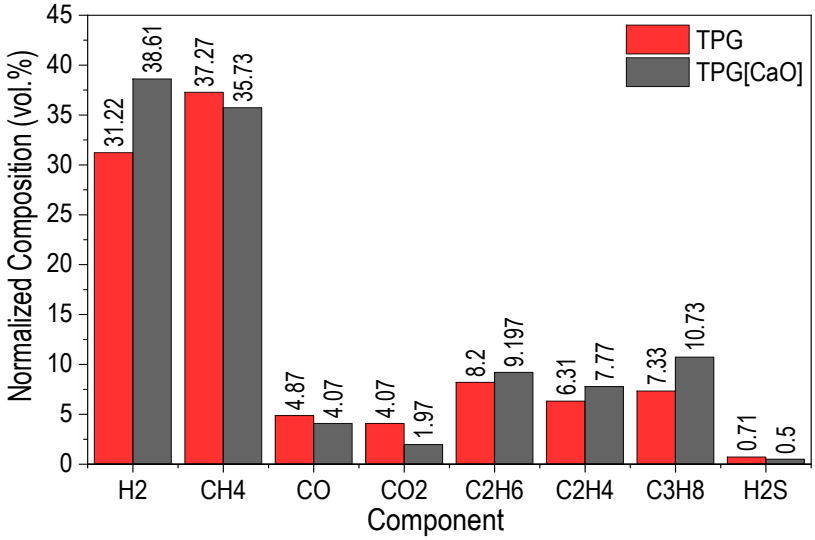

Figure 3.8. Chemical composition of TPO and TPG[CaO] (CaO [149-841 µm])

The possible decomposition of oxygen-containing compounds, for example in aromatic structures via catalytic cracking (CaO as the catalyst), may lead to an increase in the concentration of CO in TPG [44]. Nonetheless, the water vapor contained in the volatile matter along with the produced CO may be likely consumed in the water-gas shift reaction (Equation 3.6), resulting in

an increase of H_2. The water-gas shift is an exothermic reaction; thus, it is thermodynamically favorable at the tested pyrolysis conditions. Although CO_2 is also expected, the presence of CaO in the system possibly led to the production of $CaCO_3$ as shown in Equation 3.7 [44], which is also thermodynamically favorable at the tested conditions. This hypothesis is in agreement with the observed decrease of CO_2 in TPG[CaO] in Figure 3.8.

$$CO + H_2O \leftrightarrow CO_2 + H_2 \qquad \Delta_r H^{\circ}_{(A)}(298\ K) = -41.1\ kJmol^{-1} \qquad \textbf{(3.6)}$$

$$CaO + CO_2 \leftrightarrow +CaCO_3 \qquad \Delta_r H^{\circ}_{(A)}(298\ K) = -178\ kJmol^{-1} \qquad \textbf{(3.7)}$$

Furthermore, and similar to the explanation given for TPO, the O^{2-} in the CaO contains a full p-orbital available for electron pair donation. In turn, the full p-orbital on the O^{2-} may destabilize the π-electron cloud responsible for resonance stabilization in aromatic structures. Thus, electron cloud polarization and subsequent unequal charge distribution across the aromatic ring, coupled with the high temperatures of pyrolysis, may lead to the cracking of aromatic structures. The presence of Ca^{2+} may aid various cracking pathways by stabilizing anionic intermediates, while O^{2-} can abstract H^+. In this regard, the cracking of aromatic structures present in the volatile matter can yield H_2, as well as short chain hydrocarbons, which was also evidenced in Figure 3.8 with the slight increase of C_2H_6, C_2H_4, and C_3H_8. Similar pathways have been reported in the literature in previous catalytic pyrolysis studies of coal and biomass using calcium-based materials [7,35,36]. For instance, Tingyu *et al*. [8] suggested that during the initial stages of coal pyrolysis (volatilization), primary products are released, which are known for containing condensed aromatic compounds. Due to the above-describe characteristics of CaO, it may catalyze secondary reactions of these primary products to increase the gas yield and the concentration of C_1 - C_5 hydrocarbons in it.

Finally, the desulfurization capabilities of CaO in the pyrolysis of WT were evidenced in a reduction of 38 % of the H_2S contained in TPG. Overall, the results found suggest that not only the physicochemical properties of TPO were upgraded, but also those of TPG. Aside from a reduction in the concentration of H_2S, CO, and CO_2, the addition of CaO promoted a rise in the concentration of gaseous hydrocarbons in TPG, which ultimately influence its energy density. Indeed, the addition of CaO resulted in an increase of 7% in the HHV, from 26 MJ/Nm^3 in TPG to 28 MJ/Nm^3 in TPG[CaO].

In summary, the participation of CaO in the pyrolysis of WT has several effects on the properties of TPO, TPG, and rCB. During pyrolysis, CaO could have acted as an adsorbent (physical absorption), reactant, and catalyst. Nonetheless, and as mentioned before, in order to confirm this hypothesis, a more detailed characterization of the pyrolysis products is required, in particular for TPO and TPO[CaO] in order to elucidate their structural differences. This will be addressed in the following chapter.

3.4 Summary

The effect of adding CaO during the pyrolysis of WT on the physicochemical properties of the pyrolysis products was assessed and discussed. Pyrolysis was conducted in a lab-scale twin-auger reactor at 475 °C, 3.5 min of solid residence time, 1.16 kg/h of WT, and 300 mL/h of N_2. CaO was continuously fed at 10, 15, and 20 wt.%, based on the WT mass flow rate, and using two particle size ranges. The resulting TPO samples were initially characterized in terms of sulfur content. Then, the sample obtained

by adding 15 wt.% of CaO (TPO[CaO]) was further studied by means of elemental composition (CHNSO), chemical composition (GC-MS), viscosity, density, high heating value, etc. Furthermore, the rCB and TPG related to TPO[CaO] (rCB[CaO] and TPG[CaO], respectively) were also characterized. All these properties were contrasted with those of the pyrolysis products obtained without using CaO (TPO, TPG, rCB). Finally, an acid-demineralization process was carried out to remove the inorganic elements from the rCB[CaO] as well as to upgrade its textural characteristics (surface area and porosity). By adding CaO during the pyrolysis of WT, a maximum sulfur reduction in TPO of 26.40 % was found. Moreover, CaO addition also influenced other physicochemical properties such as viscosity and water content. The GC-MS analysis of TPO revealed a significant presence of benzene, toluene, xylene, as well as limonene. A slight increase of these compounds was noticed in the liquid fraction (TPO[CaO]) with the addition of CaO during pyrolysis, which was associated with the possible catalytic activity of CaO. However, conclusive statements were not provided due to the lack of sufficient information to confirm this hypothesis. Although the ash content of rCB[CaO] was significantly high after pyrolysis (57.5 wt.%), the acid demineralization process was effective at removing 80 % of its inorganic content, also improving surface area and porosity. Regarding TPG[CaO], an increase in the amount of H_2 and some CxHy compounds (*i.e.* C_3H_8, C_2H_6, and C_2H_4), while a decrease in CO_2, CO, and H_2S was also found. The results obtained represent significant findings regarding the advancement of upgrading strategies, not only for TPO, but also for TPG.

References

[1] H. Hu, Y. Fang, H. Liu, R. Yu, G. Luo, W. Liu, A. Li, H. Yao, The fate of sulfur during rapid pyrolysis of scrap tires, Chemosphere. 97 (2014) 102–107.

[2] T. Hlincik, P. Buryan, Desulfurization of boiler flue gas by means of activated calcium oxide, Fuel Process. Technol. 111 (2013) 62–67.

[3] H. Fan, K. Xie, J. Shangguan, F. Shen, C. Li, Effect of calcium oxide additive on the performance of iron oxide sorbent for high-temperature coal gas desulfurization, J. Nat. Gas Chem. 16 (2007) 404–408.

[4] A. Abad, J. Adánez, F. Garcia-Labiano, L.F. Diego, P. Gayán, Hot coal-gas desulfurization with calcium-based sorbents in a pressurized moving-bed reactor, Energy Fuels. 18 (2004) 1543–1554.

[5] R. Guan, W. Li, B. Li, Effects of Ca-based additives on desulfurization during coal pyrolysis, Fuel. 82 (2003) 1961–1966.

[6] L. Lin, S.J. Khang, T.C. Keener, Coal desulfurization by mild pyrolysis in a dual-auger coal feeder, Fuel Process. Technol. 53 (1997) 15–29.

[7] A. Veses, M. Aznar, I. Martínez, J.D. Martínez, J.M. López, M.V. Navarro, M.S. Callén, R. Murillo, T. García, Catalytic pyrolysis of wood biomass in an auger reactor using calcium-based catalysts, Bioresour. Technol. 162 (2014) 250–258.

[8] Z. Tingyu, Z. Shouyu, H. Jiejie, W. Yang, Effect of calcium oxide on pyrolysis of coal in a fluidized bed, Fuel Process. Technol. 64 (2000) 271–284.

[9] E. Serris, L. Favergeon, M. Pijolat, M. Soustelle, P. Nortier, R. S. Gartner, T. Chopin, Z. Habib, Study of the hydration of CaO powder by gas–solid reaction, Cem. Concr. Res. 41 (2011) 1078–1084.

[10] Y. Lin, C. Zhang, M. Zhang, J. Zhang, Deoxygenation of bio-oil during pyrolysis of biomass in the presence of CaO in a fluidized-bed reactor, 19 (2010) 5686–5695.

[11] L. Yan, Y. Bai, X. Kong, F. Li, Effects of alkali and alkaline earth metals on the formation of light aromatic hydrocarbons during coal pyrolysis, Anal. Appl. Pyrolysis. 122 (2016) 169–174.

[12] M. R. Khan, Production of high quality liquid fuels from coal by mild pyrolysis of coal-lime mixtures, Fuel Sci. Technol. Int. 5 (1987) 185–231.

[13] M.R. Khan, Compositional changes in the mild gasification liquids produced in the presence of calcium compounds, Fuel Process. Technol. 27 (1991) 83–94.

[14] H. D. Franklin, W. A. Peters, and J. B. Howard, Mineral matter effects on the rapid pyrolysis and hydropyrolysis of a bituminous coal. 1 . Effects on yields of char, tar and light gaseous volatiles, Fuel. 61 (1982) 155–160.

[15] C.-K.S. Lai, P. Chen, J.P. Longwell, W.A. Peters, Thermal reaction of m-cresol over calcium oxide between 350 and 600 ^{o}C, Fuel. 66 (1987) 525–531.

[16] J. Wang, M. Ma, Y. Bai, W. Su, X. Song, G. Yu, Effect of CaO additive on co-pyrolysis behavior of bituminous coal and cow dung, Fuel. 265 (2020) 116911.

[17] M. Brebu, T. Bhaskar, K. Murai, A. Muto, Y. Sakata, M. Azhar Uddin, Removal of nitrogen, bromine, and chlorine from PP/PE/PS/PV/ABS-Br pyrolysis liquid products using Fe- and Ca-based catalysts, Polym. Degrad. Stab. 87 (2005) 225–230.

[18] T. Yoshioka, T. Handa, G. Grause, Z. Lei, H. Inomata, T. Mizoguchi, Effects of metal oxides on the pyrolysis of poly(ethylene terephthalate), J. Anal. Appl. Pyrolysis. 73 (2005) 139–144.

[19] C. Zhou, T. Stuermer, R. Gunarathne, W. Yang, Effect of calcium oxide on high-temperature steam gasification of municipal solid waste, Fuel. 122 (2014) 36–46.

[20] J. Udomsirichakorn, P. Basu, P.A. Salam, B. Acharya, Effect of CaO on tar reforming to hydrogen-enriched gas with in-process CO2 capture in a bubbling fluidized bed biomass steam gasifier, Int. J. Hydrogen Energy. 38 (2013) 14495–14504.

[21] L. Han, Q. Wang, Y. Yang, C. Yu, M. Fang, Z. Luo, Hydrogen production via CaO sorption enhanced anaerobic gasification of sawdust in a bubbling fluidized bed, Int. J. Hydrogen Energy. 36 (2011) 4820–4829. doi:10.1016/j.ijhydene.2010.12.086.

[22] I. Hita, M. Arabiourrutia, M. Olazar, J. Bilbao, J. M. Arandes, and P. Castaño, Opportunities and barriers for producing high quality fuels from the pyrolysis of scrap tires, Renew. Sustain. Energy Rev. 56 (2016) 745–759.

[23] J.D. Martínez, N. Puy, R. Murillo, T. García, M.V. Navarro, A.M. Mastral, Waste tyre pyrolysis - A review, Renew. Sustain. Energy Rev. 23 (2013) 179–213.

[24] P.T. Williams, Pyrolysis of waste tyres: A review, Waste Manag. 33 (2013) 1714–1728.

[25] N. Cardona-Uribe, Experimental investigation of the demineralization process to the recovery carbon black produced in the pyrolysis of waste tires aiming at its industrial application, MSc Dissertation (in Spanish), Universidad Pontificia Bolivariana, Colombia, 2018.

[26] E.S.P.B. V, K. Gullett, U.S.E.P. Agency, N. Carolina, A. Blom, T. Cunningham, N. Carolina, Porosity, surface area, and particle size effects of CaO reacting with SO2 at 1100 ^{o}C, React. Solids. 6 (1988) 263–275.

[27] A.M. Mohamed Soltan, Petrographic modelling of Egyptian limestones for quicklime manufacture, Arab. J. Geosci. 4 (2011) 803–815.

[28] J.L. Eades, P.A. Sandberg, Characterization of the properties of commercial lime by surface area measurements and scanning electron microscopy, in: React. Parameters Lime, ASTM International, 1970: pp. 4–24.

[29] D.M. Marinkovic, M. V Stankovic, A. V Velickovic, J.M. Avramovic, M.R. Miladinovic, O.O. Stamenkovic, V.B. Veljkovic, D.M. Jovanovic, Calcium oxide as a promising heterogeneous catalyst for biodiesel production: Current state and perspectives, Renew. Sustain. Energy Rev. 56 (2016) 1387–1408.

[30] L. Zhang, B. Zhang, Z. Yang, Y. Yan, Pyrolysis behavior of biomass with different Ca-based additives, RSC Adv. 4 (2014) 39145–39155.

[31] M. Hartman, R.W. Coughlin, Reaction of sulfur dioxide with limestone and the influence of pore structure, Ind. Eng. Chem. Process Desing Dev. 13 (1974) 248–253.

[32] H. Aydin and C. Ilkılıç, Optimization of fuel production from waste vehicle tires by pyrolysis and resembling to diesel fuel by various desulfurization methods, Fuel. 102 (2012) 605–612.

[33] G.G. Choi, S.J. Oh, J.S. Kim, Scrap tire pyrolysis using a new type two-stage pyrolyzer: Effects of dolomite and olivine on producing a low-sulfur pyrolysis oil, Energy. 114 (2016) 457–464.

[34] C. Gabani, Y. Ranchh, R. Borodia, P. Sivakumar, Chapter 27. Tyre pyrolysis by using nano-catalyst to improve energy efficiency and fuel quality, in: Int. Conf. Nano Energy Water, 2017: pp. 201–206.

[35] D. Wu, S. Zhang, Q. Zheng, X. Zhao, W. Liu, X. Xue, The influence of CaO on the pyrolysis behavior and kinetics characteristics of low rank coal, Energy Procedia. 105 (2017) 2039–2046.

[36] J. Yongbin, H. Jiejie, W. Yang, Effects of calcium oxide on the cracking of coal tar in the freeboard of a fluidized bed, Energy Fuels. 18 (2004) 1625–1632.

[37] S. Lin, M. Harada, Y. Suzuki, H. Hatano, Comparison of pyrolysis products between coal, coal/CaO, and coal/Ca(OH)2 materials, Energy Fuels. 17 (2003) 602–607.

[38] Y. Fu, Y. Guo, K. Zhang, Effect of three different catalysts (KCl, CaO, and Fe2O3) on the reactivity and mechanism of low-rank coal pyrolysis, Energy Fuel. 30 (2016) 2428–2433.

[39] G.G. Choi, S.J. Oh, J.S. Kim, Non-catalytic pyrolysis of scrap tires using a newly developed two-stage pyrolyzer for the production of a pyrolysis oil with a low sulfur content, Appl. Energy. 170 (2016) 140–147.

[40] R. Agnihotri, S.S. Chauk, S.K. Mahuli, L. Fan, Mechanism of CaO reaction with H2S : Diffusion through CaS product layer, Chem. Eng. Sci. 54 (1999) 3443–3453.

[41] A.B.M. Heesink, W.P.M. Van Swaaij, The sulphidation of calcined limestone with hydrogen sulphide and carbonyl sulphide, Chem. Eng. Sci. 50 (1995) 2983–2996.

[42] The Marine Environmental Commite, Resolution MEPC.320(74)-Annex 14, (2019) 1–19.

[43] R. Miandad, M.A. Barakat, M. Rehan, A.S. Aburiazaiza, J. Gardy, A.S. Nizami, Effect of advanced catalysts on tire waste pyrolysis oil, Process Saf. Environ. Prot. 116 (2018) 542–552.

[44] Q. Wang, X. Zhang, S. Sun, Z. Wang, D. Cui, Effect of CaO on pyrolysis products and reaction mechanisms of a corn stover, ACS Omega. 5 (2020) 10276–10287.

[45] B.S. Greensfelder, H.H. Voge, G.M. Good, Catalytic and thermal cracking of pure hydrocarbons: Mechanisms of reaction, Ind. Eng. Chem. 41 (1949) 2573–2584.

[46] Y.A. Criado, M. Alonso, J.C. Abanades, Kinetics of the CaO/Ca(OH)2 hydration/dehydration reaction for thermochemical energy storage applications, Ind. Eng. Chem. Res. 53 (2014) 12594–12601.

[47] J. Alvarez, G. Lopez, M. Amutio, N.M. Mkhize, B. Danon, P. Van Der Gryp, Evaluation of the properties of tyre pyrolysis oils obtained in a conical spouted bed reactor, Energy. 128 (2017) 463–474.

[48] A. Mohan, S. Dutta, V. Madav, Characterization and upgradation of crude tire pyrolysis oil (CTPO) obtained from a

rotating autoclave reactor, Fuel. 250 (2019) 339–351.

[49] P.T. Williams, P. Bottrill, Sulfur-polycyclic aromatic hydrocarbons in tyre pyrolysis oil, Fuel. 74 (1995) 736–742.

[50] Petroleum, API gravity, (2015). http://www.petroleum.co.uk/api (accessed November 8, 2019).

[51] J. D. Martínez, Waste tire valorization by pyrolysis: production and application of the products, Doctoral Thesis, University of Zaragoza (Spain), 2014.

[52] M. Betandur, Obtaining activated carbon from WT by incorporating calcium and its application in the adsorption process (in Spanish), PhD thesis, Universidad Pontificia Boliavariana, Colombia, 2010.

[53] J.D. Martínez, N. Cardona-Uribe, R. Murillo, T. García, and J.M. López, Carbon black recovery from waste tire pyrolysis by demineralization : Production and application in rubber compounding, Waste Manag. 85 (2019) 574–584.

Chapter 4. Fuel and chemical properties of tire pyrolysis oil and its fractions

As has been pointed out along this dissertation, TPO exhibits an important potential to substitute petroleum-derived fuels in several combustion processes [1–3]. Nonetheless, the fundamental fuel characteristics and combustion properties of TPO are still unexplored, which stand as an impediment to define the best manner to use it in thermal systems. A complete understanding of these characteristics is therefore needed in order to provide new insights for its deployment in practical combustion applications, and for defining fuel upgrading strategies. This knowledge will be fundamental, for instance, for understanding gaseous and particulate matter emissions [4], as well as to define strategies to reduce TPO impacts on the environment and on human health. Hence, combustion and emission control systems could be either enhanced or modified to make TPO viable as a fuel for road transportation, marine transportation (low sulfur fuel oil), power generation (gas turbines/stationary diesel engines), or industrial applications (boilers) from a technical, economic, and environmental point of view. Thereby, this stage of the research pursues a complete understanding of the structural characteristics of TPO and its distillate fractions as a first approach towards defining further upgrading strategies and applications. The molecular analysis of non-conventional fuels such as TPO is also valuable for the advancement of scientific knowledge, and for obtaining accurate predictions of their combustion behavior [5–7]. Up to now, the extent of knowledge regarding TPO's structure is rather limited due to its complexity, which renders molecular resolution quite difficult. Therefore, in this chapter, the combination of advanced analytical techniques such as Fourier Transform - Ion Cyclotron Resonance Mass Spectrometry (FT-ICR MS), and ^{1}H and ^{13}C Nuclear Magnetic Resonance (NMR) spectroscopy allowed elucidating the main structural characteristics of TPO and its distillate fractions.

This chapter is divided into two main parts. The first one is dedicated to understanding the fuel and chemical properties of TPO and TPO[CaO], which were briefly described in Chapter 3. Here, their structural characteristics are compared and contrasted between them. The second part presents the structural features of different distillate fractions obtained from the low sulfur TPO, *i.e*, that obtained using CaO during the pyrolysis process (TPO[CaO]). As such, TPO[CaO] was separated into four distillate volume fractions, named here light, low middle, high middle, and heavy fractions, and each of them was then studied in detail. Distillation is by far the most important and widely used separation process in a petroleum refinery. In conventional refineries, crude oils are distilled into groups with similar properties to be further characterized, upgraded, and used in different systems. In an analogous manner and considering that TPO[CaO] is an unrefined hydrocarbon source [8], different fractions of TPO[CaO] could be separated according to their boiling points in order to be refined and used individually. Separating TPO[CaO] into distinct fractions by distillation can expand the range of possibilities, making it more suitable for specific applications, rather than using the raw oil directly [9–11]. Thus, this chapter aims to provide some insights towards this scope.

4.1 Material and methods

4.1.1 Tire pyrolysis oil separation

A schematic representation of the experimental setup used to conduct the distillation of TPO[CaO] is shown in Figure 4.1. Initially, a round-bottomed flask was filled with 200 mL of feedstock and gradually heated from room temperature (25 ºC) to 350

ºC using a heating mantle. A thermocouple recorded the temperature of the vapor phase in the takeoff position, before the cooling system. As the temperature increased, condensed vapors were collected in different containers according to the recovered volume. Thus, TPO[CaO] was divided into four distillate volume fractions: (i) light (recovered volume: 40 %), (ii) low-middle (recovered volume: 20 %), (iii) high-middle (recovered volume: 20 %), and (iv) heavy (recovered volume: 20 %). The related temperature range to each fraction is specified in Figure 4.1. The recovered volume percentages of these fractions were selected based on the profile of the distillation curve of TPO[CaO], while aiming at overlapping with the boiling point ranges of commercial petroleum derived fuels. The methodology for the distillation procedure is based on the ASTM D86.

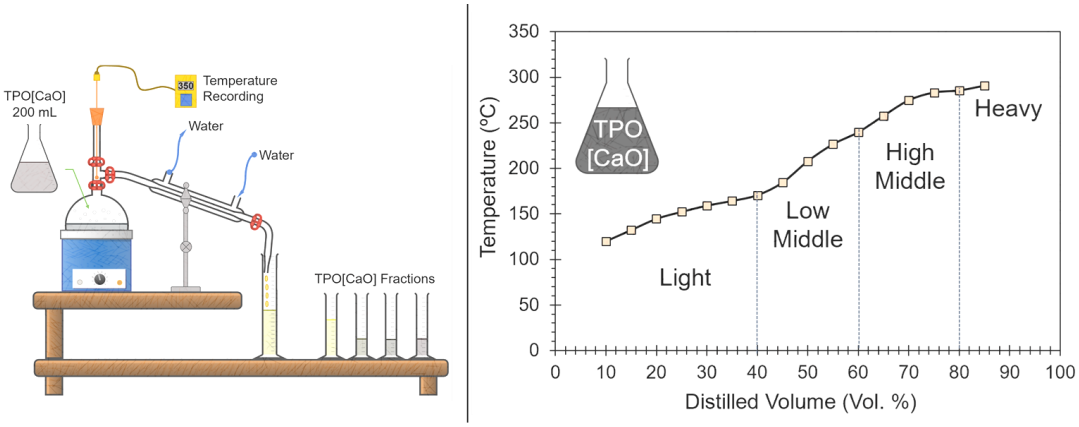

Figure 4.1 Distillation process

4.1.1 Characterization of test fuels

Figure 4.2 gives a general overview of the analytical procedure followed to characterize TPO and TPO[CaO], as well as the obtained distillate fractions from TPO[CaO].

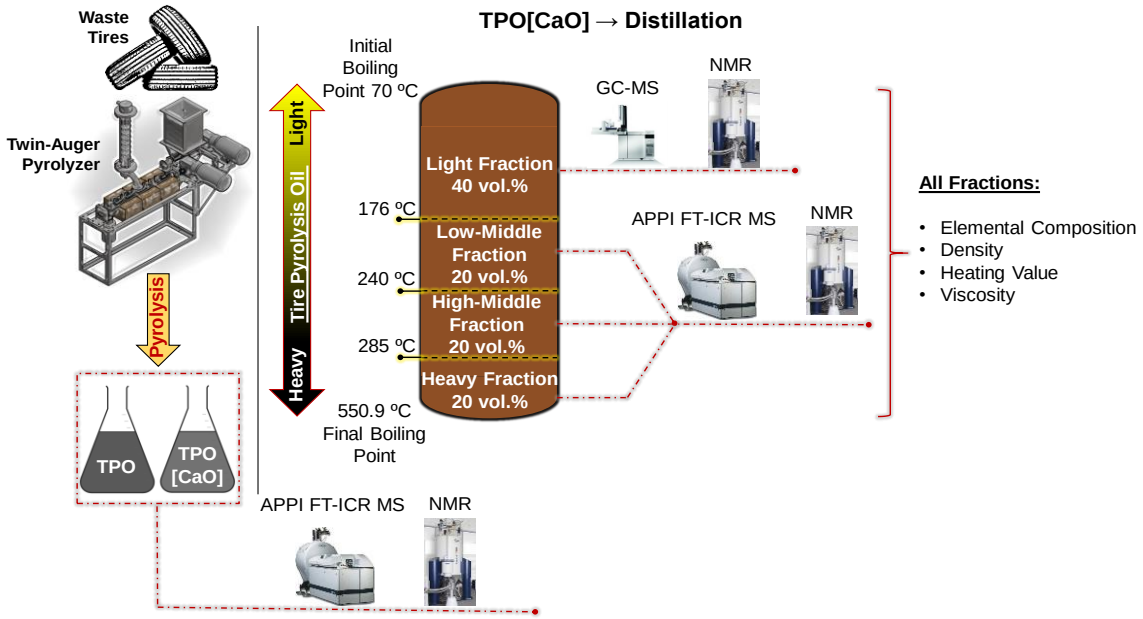

Figure 4.2. Overview of the characterization process

A complete description of the of the procedure followed to conduct GC-MS, APPI FT-ICR MS, ^{1}H and ^{13}C NMR is presented in Appendix C. The elemental composition, density, heating value, and viscosity of the obtained distillated fraction were measured in line with the standard procedure considered for TPO and TPO[CaO] as reported in Chapter 3.

4.2. Results and discussions

4.2.1 Structural characterization of tire pyrolysis oil

4.2.1.1 Atmospheric pressure photoionization Fourier transform ion cyclotron resonance mass spectrometry

APPI FT-ICR MS was used to study the chemical composition and molecular structure of TPO and TPO[CaO]. Based on the unsaturation degree (DBE: double bond equivalence) and carbon range distribution, structural parameters were elucidated. Even though there are different ionization modes, APPI mode was chosen as it is more effective in ionizing high aromatic and sulfur containing compounds [12]. Figure 4.3 shows the mass spectra obtained for each sample. The mass spectra of TPO and TPO[CaO] exhibit a mass to charge ratio (*m/z*) ranging from 200 to 800, and from 200 to 750, respectively. Herein, 2,448 and 1,473 mass peaks were resolved for TPO and TPO[CaO], respectively, and a unique molecular formula was assigned to each mass peak detected. Due to the high complexity of TPO, the possible structural isomers with identical chemical formulas and molecular weights cannot be distinguished by FT-ICR MS technique alone [13]. Nevertheless, comparing with other classic analytical methods, such as FTIR, NMR, etc., the FT-ICR MS technique can provide the most detailed compositional and structural information of complex oil samples at the molecular level. The inserted graphs (histograms) in Figure 4.3 show the frequency at which the resolved compounds for either TPO or TPO[CaO] fall in a specific *m/z* range. As such, it can be observed that in both cases, the highest frequency is found in a *m/z* range between 400 and 450. Moreover, the symmetrical shape of the continuous lines shows values clustering around the central range (normal distribution); thus, the MW_{avg} was calculated to lie in this range as shown later.

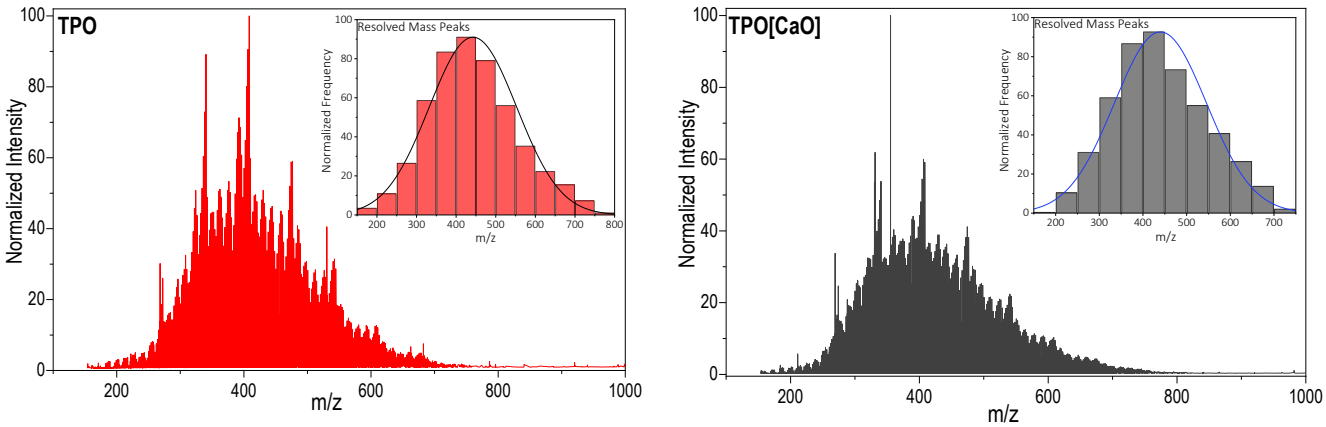

Figure 4.3. APPI FT-ICR mass spectra of TPO and TPO[CaO]

Table 4.1 presents some molecular parameters for TPO and TPO[CaO], derived from the assigned chemical formulas. The following values were calculated: MW_{avg}, the average number of carbon atoms (C_{avg}), and the average DBE number (DBE_{avg}).

The MW_{avg} was found to be 430 and 427 g/mol for TPO and TPO[CaO], respectively. These values, along with the average number of carbon atoms (31.6) agree with the high final boiling points (558.5 and 550.9 °C) of TPO and TPO[CaO], previously reported in Chapter 3. It is important to point out that the oil obtained from WT presents a significant content of low molecular weight hydrocarbons such as benzene (C_6), toluene (C_7), xylene (C_8), limonene (C_{10}), etc., which explains the low initial boiling point (69 and 70 °C for TPO and TPO[CaO], respectively) [14,15]. However, these compounds are not detected by the present technique. Light hydrocarbons have low molecular weight, which makes them travel very fast in the ICR cell with possible interference of signals making accurate determination difficult [16]. These compounds are more suitable to be detected by GC-MS, which has been reported in Chapter 3.

Table 4.1. Average molecular parameters

Parameter	TPO	TPO[CaO]
MW_{avg} (g/mol)	430	427
Carbon number range	12 - 56	14 - 53
C_{avg}	31.6	31.6
DBE number range	0.5 - 27	4 - 26
DBE_{avg}	11.3	12.2
H/C	1.46	1.46

The DBE number is a well-established tool in mass spectrometry, especially for the analysis of complex mixtures, such as petroleum and dissolved organic matter. It represents the sum of unsaturated bonds plus rings in a molecule. The DBE_{avg} for TPO and TPO[CaO] were found to be 11.3 and 12.2, respectively. Taking into account the high aromatic and low olefin content of TPO (Chapter 2), the high DBE_{avg} values can be an indicator of the significant presence of condensed aromatic structures [17]. This hypothesis will be verified by the NMR results in the following section. Table 4.1 also shows the H/C ratio found by means of APPI FT-ICR MS for both TPO and TPO[CaO]. The H/C gives a general idea about the molecular diversity of the sample (relative content of paraffins, aromatics, olefins, and naphthenes), as well as of the amount of heat released during combustion. For instance, aromatic rings have H/C ratios close to unity, while paraffins have H/C ratios closer to two [18]. This ratio also constrains the identity and population of the radical pool, which is a fundamental driver for the occurrence of chemical kinetic phenomena such as induction time, flame velocity, and diffusive extinction limit [19]. An H/C ratio of 1.46 in both samples reveals the presence of aliphatic and aromatic compounds, as reported previously in literature [14,20–22]. It is worth to note that the H/C ratio shown in Table 4.1 is similar to the one calculated from elemental composition, as reported in Chapter 3. These results confirm the reliability of the information at both the macroscopic (elemental analysis) and microscopic (molecular characterization by FT-ICR MS) standpoints.

The most abundant molecular classes observed in both samples (Figure 4.4) were pure hydrocarbons (HC) and hydrocarbons containing one sulfur atom (S_1). The relative abundance of the HC compound class was higher in TPO[CaO] than in TPO. The S_1 class was slightly more abundant in TPO than in TPO[CaO]. Very low levels of hydrocarbon compounds containing two sulfur atoms (S_2) were detected in TPO, whereas none were detected in TPO[CaO]. The proportion of hydrocarbons with oxygen atoms (O_1) is slightly higher in TPO than in TPO[CaO].

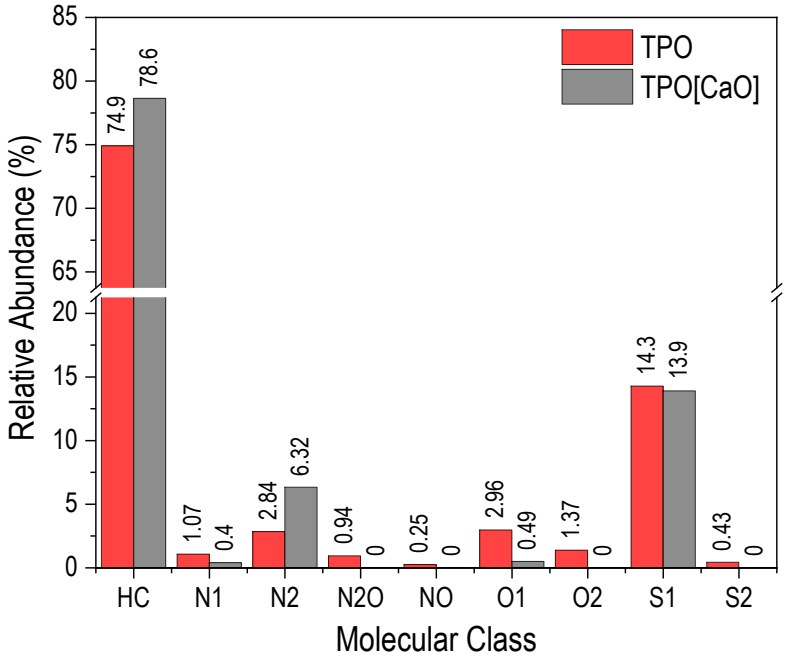

Figure 4.4. Compound class distribution determined by APPI FT-ICR MS

The high abundance of HC species, the low quantities of O_1, and the absence of the S_2 molecular class in TPO[CaO] might be associated with the reactivity of CaO during the pyrolysis. Namely, it is likely that CaO captures/transforms these heteroatoms contained in the volatile matter before they become part of the liquid compounds. As discussed in Chapter 3, the most abundant sulfur species contained in the volatile matter released from WT during pyrolysis are hydrogen sulfide (H_2S) and carbonyl sulfide (COS) [23]. In the presence of CaO, these compounds react to form CaS, which is found in the rCB. Consequently, a reduction of the sulfur concentration of TPO is found. Regarding O_1, the possible decomposition of oxygenated compounds in the volatile matter via catalytic cracking (CaO as the catalyst) may lead to an increase in the concentration of CO [24]. In turn, CO might be involved in further reactions — water-gas shift reaction — along with H_2O to produce H_2 and CO_2. Although CO_2 is produced during the water-gas shift reaction, the presence of CaO in the system could react with it to produce $CaCO_3$ (contained in the rCB). This has been addressed in detail in Chapter 3. The significant presence of S_1 compounds suggest that the core skeletal structures of the molecules might be thiophenic or thiolic in nature. Understanding the nature of sulfur atoms in these fuels is fundamental in choosing proper desulfurization techniques, as will be discussed later [25]. Furthermore, there is a great interest for studying the structure of the PASH present in fuels, because some of them can have carcinogenic and mutagenic effects on humans. Therefore, knowledge of the structure of the sulfur-containing compounds allows for a more precise assessment of the health hazards associated with new fuels such as TPO [22].

Given that HC and S_1 are the most abundant molecular classes, both were divided into subfamilies with respect to their DBE number. The utilization of DBE values allows for the distinction of molecular structures according to their unsaturation degree (presence of both double bonds and rings in the molecule) [13]. For instance, DBE numbers between 10 and 12 could be related to tri-aromatics and naphtheno-aromatics (TrA), while values between 13 and 14 are related to tetra-aromatics and to tetra-

aromatics with naphthenic rings (TeA) [12]. Finally, DBE values higher than 16 could be associated with penta and higher aromatics, including naphthenic rings (PA+) [12]. Table 4.2 provides the minimum and maximum number of carbon atoms for each subfamily.

Table 4.2. Range of the DBE number of carbon atoms per subfamily of pure hydrocarbons (HC) class

DBE	Compound family	TPO		TPO[CaO]	
		Min	Max	Min	Max
0	P	-	-	-	-
1	N	-	-	-	-
2 - 3	DN	12	35	-	-
4 - 6	MA	12	45	14	39
7 - 9	DA+	13	50	16	46
10 - 12	TrA+	17	56	18	51
13 - 14	TeA+	20	56	21	53
16+	PA+	22	56	22	53

P: Normal Paraffins and Isoparaffins; **N:** Naphthenes; **DN**: Dinaphthenes; **MA:** Monoaromatics, **DA+:** Diaromatics and Naphtheno-Aromatics; **TrA+:** Triaromatics and Naphtheno-Aromatics; **TeA+:** Tetraaromatics and tetraaromatics with Naphthenic Rings; **PA+:** Pentaaromatics and higher, including Naphthenic Rings.

The distribution of compounds contained in the HC molecular class as a function of DBE and carbon number are illustrated in Figure 4.5. The bubble size denotes the magnitude (relative abundance) of the recorded mass peaks. As observed, the most abundant compounds in both samples are in the carbon number range between 20 and 45, and DBE numbers between 5 and 20. A wider carbon range is noticed in TPO (C_{15}-C_{58}) than in TPO[CaO] (C_{15}-C_{53}), which is in agreement with the MW_{avg} and final distillation boiling points discussed above. The high final boiling point found in both samples (Chapter 3) could be explained by the presence of heavy compounds with large DBE values (>20), likely linked to condensed aromatic structures [26].

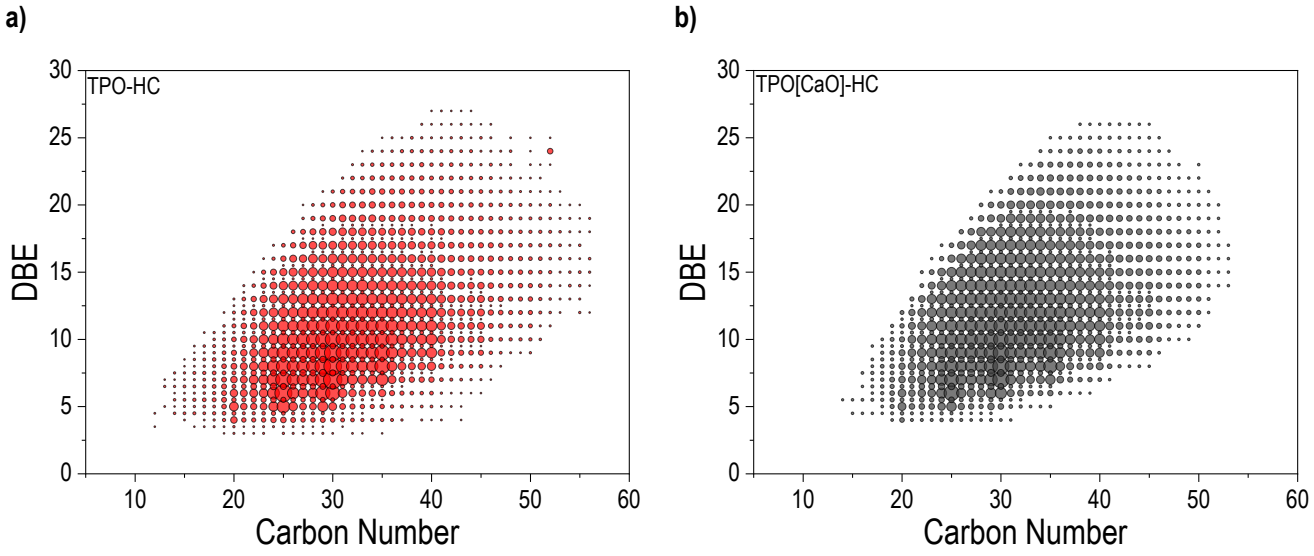

Figure 4.5. Abundance of pure hydrocarbon (HC) compounds: **a)** TPO; **b)** TPO [CaO]

Similarly, for the S_1 molecular class, Table 4.3 reports the carbon number distribution for each subfamily. Subfamilies are also classified according to the DBE number. In this regard, S_1 subfamilies are divided into mono-sulfur containing species like

sulfides (SD) and PASH structures such as thiophene (DBE: 3), benzothiophenes (DBE: 6), dibenzothiophene (DBE: 9), benzonaphthothiophene (DBE: 12) and their related naphthenic derivatives (DBE number ranges 4 - 5, 7 - 8, 10 - 11, and 13 - 15). Herein, the carbon range number for TPO and TPO[CaO] is between 13 and 20; and, 19 and 45, respectively.

Table 4.3. Range of the DBE number of carbon atoms per subfamily of S_1 molecular class

DBE	Compound family	TPO		TPO[CaO]	
		min	max	min	max
0 - 2	SD	-	-	-	-
3 - 5	Th	13	35	19	30
6 - 8	BT	18	45	19	41
9 - 11	DBT	19	50	19	45
12+	BNT	19	50	20	45

SD: Sulfide; **Th:** Thiophene; **BT:** Benzothiophenes; **DBT:** Dibenzothiophene; **BNT:** Benzonaphthothiophene

Figure 4.6 shows the distribution of compounds contained in the S_1 molecular class as a function of DBE and carbon number. As observed, compounds with carbon numbers between 25 and 35 and DBE numbers between 5 and 10 are the most abundant in this molecular class. PASH in TPO and TPO[CaO] show the presence of molecules with carbon numbers up to 50 and 45, respectively; which can be associated with long or multiple short alkyl chains connected to the aromatic rings [17].

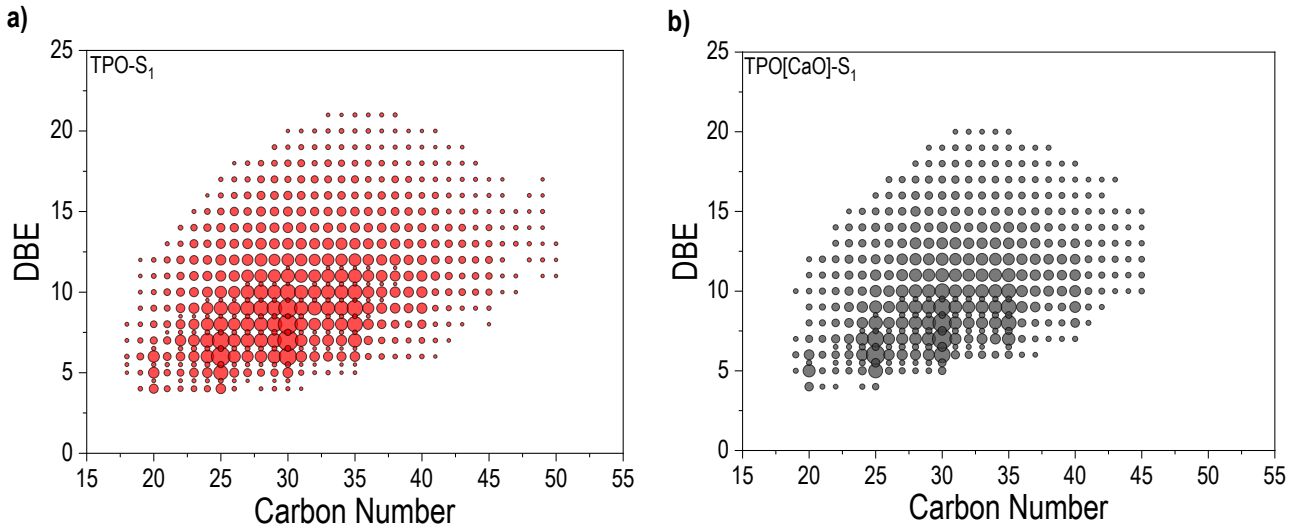

Figure 4.6. Abundance of Mono-sulfur (S_1) compounds: **a)** TPO; **b)** TPO [CaO]

The HC and S_1 compound distributions according to the subfamilies previously described, and their cumulative abundances are plotted in Figures 4.7a and 4.7b, respectively. As observed in Figure 4.7a, 61% and 71% of the HC compounds in TPO and TPO[CaO] are found in the form of TrA, TeA and PA+, respectively. The HC distribution does not show any fully saturated hydrocarbon species (DBE numbers between 0 and 3), which could be due to their absence, or to the inability of alkanes to form stabilized ions using APPI ionization [27]. On the other hand, Figure 4.7b shows that more than 60 % of the sulfur-containing compounds are in the form of dibenzothiophene (DBT) and benzonaphthothiophene (BNT).

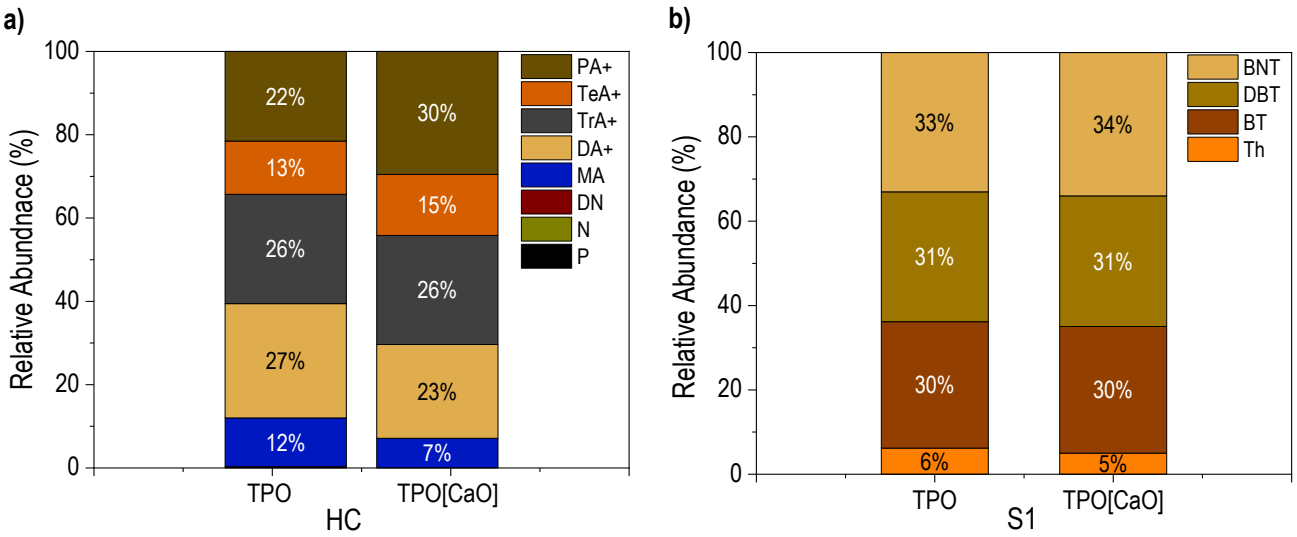

Figure 4.7. Compound subfamilies according to their DBE number and cumulative abundance

Similar results were found by Williams and Bottrill [22], who reported that the PASH present in TPO consist mainly of DBT, alkylated DBT, and naphthothiophenes, along with their methyl derivatives. However, due to the limitations of the analytical techniques used in that work (GC-MS), a large portion of the PASH, particularly high molecular weight compounds, could not be identified. It has been reported that highly condensed aromatic compounds of high molecular weight are formed in the pyrolysis of WT, and heteroatoms are incorporated [22]. These compounds could be formed during pyrolysis or after vapor condensation.

A proper understanding of the molecular characteristics of the compounds present in TPO helps to select and optimize upgrading strategies (e.g. desulfurization steps). Different sulfur-containing compounds behave in a different manner when exposed to diverse desulfurization processes (i.e. oxidative desulfurization, hydrodesulfurization, extractive desulfurization, etc.) [28]. For example, hydrodesulfurization is not effective for removing heterocyclic sulfur compounds such as DBT, and its derivatives (4,6-dimethyldibenzothiophene) [29,30]. Previous hydrodesulfurization studies of diesel fuel have revealed that alkyl dibenzothiophene remains at a level of 1000 ppm, given that these kinds of compounds have low reactivity during hydrodesulfurization [25]. The major cause of low reactivity has been attributed to the steric hindrance presented by bulky sulfur containing aromatics. Alternatively, techniques such as oxidative desulfurization present higher reactivity when sulfur compounds are in the form of BT and DBT [31]. An attractive aspect of this technique is the higher reactivity of aromatic sulfur species with three or more aromatic rings, which is associated with the increase in electron density when sulfur atoms are set in a larger aromatic scheme. This electron density is also improved with the presence of alkyl groups in the aromatic rings. All these facts favor the electrophilic attack by oxidants [32]. In this regard, and according to the APPI FT-ICR results, oxidative desulfurization could be a promising pathway for TPO upgrading.

The high abundance of PAH in TPO and TPO[CaO] is attributed to the aromatic nature of rubber (one aromatic ring is present in the styrene butadiene rubber monomer) and the cyclisation of olefin structures, followed by dehydration and Diels-Alder

reactions [14]. Such aromatization reactions are enhanced at high pyrolysis temperatures, as well as prolong residence times of the volatiles inside the reactor. Likewise, previous studies have shown the formation of aromatics in TPO from the thermal decomposition of limonene (one of the major components of TPO) [28]. Ding *et al*. [33] reported that such a process can occur in a temperature range between 400°C and 700°C. Herein, limonene isomerizes to form 4-isopropylidene-1-methylcyclohexene at temperatures below 500°C. At 600°C, this compound then undergoes carbon-carbon bond cleavage, which is followed by an intramolecular hydrogen transfer to form an alkatriene. Consequently, intramolecular diene synthesis, followed by dehydration, leads to the formation of aromatics such as xylene and toluene. When the temperature reaches 700°C, aromatization reactions can initiate further PAH formation. Similarly, the formation of PASH in TPO during pyrolysis has been attributed to the combinations of available olefins and free sulfur atoms, the combination of sulfur-containing compounds with olefins via the Diels-Alder reactions, and the direct cracking of WT molecules where sulfur atoms resided. A complete description of the reaction mechanisms for the formation of PASH during the pyrolysis of WT have been presented in a previous work conducted by Dung et al. [34].

Table 4.4 shows different molecular parameters found in TPO and TPO[CaO]. Noteworthy facts are the high MW_{avg} of S_1 (higher than 440 g/mol) and their high DBE number (~10). HC species exhibit a MW_{avg} of 419.97 and 428.82 g/mol, while the average DBE numbers are around 10.20 and 12.38 for TPO and TPO[CaO], respectively. Considering that the S_1 molecular class exhibits a high average molecular weight, another path to remove sulfur-containing compounds contained in TPO and TPO[CaO] could be fractional distillation, which will be addressed in the second part of this chapter. Even though distillation will not remove the sulfur atoms from the fuel, sulfur containing compounds can be concentrated in the leftover heavy fraction.

Table 4.4. Molecular parameters of HC and S_1 compound classes

Parameter	TPO		TPO[CaO]	
	HC	S_1	HC	S_1
MW_{avg} (g/mol)	419.97	447.83	428.82	444.56
Average DBE number	10.20	10.28	12.38	10.33
Average H/C ratio	1.35	1.39	1.29	1.39

4.2.1.2 ^{1}H and ^{13}C nuclear magnetic resonance

Combining the data from ^{1}H NMR, ^{13}C NMR spectra, elemental analysis, and MW_{avg}, it is possible to characterize a complex fuel in terms of its average molecular parameters (AMPs). The average molecular formula of TPO and TPO[CaO] obtained by means of Equation C.3 in the Appendix C are $C_{31.09}H_{45.05}N_{0.41}S_{0.09}O_{0.21}$ and $C_{31.00}H_{45.16}N_{0.37}S_{0.07}O_{0.10}$, respectively. Tables 4.5 and Table 4.6 present the characteristic ^{1}H and ^{13}C NMR chemical shift used to identify and quantify several nuclei, as well as the related AMPs calculated using Equation C.3 (Appendix C). The ^{1}H chemical shift assignments were taken from Abdul Jameel et al. [18] and the ^{13}C NMR assignments were obtained from Poveda and Molina [35]. The formulae and terminology used to denote and calculate the AMPs follows the methodology of Poveda and Molina [35] and from Abdul Jameel et al. [36]. As mentioned in the Appendix C, different nuclei exhibit different shifts. Accordingly, the splitting pattern and position of these shifts are indicative of the underlying molecular structure. Thus, it is possible to determine the relative amount of each molecular

functional group and atomic arrangement, such as aromatic carbons, olefinic carbon, aromatic hydrogen, naphthenic hydrogen, etc.

Table 4.5. ^{1}H NMR chemical shift assignments

Symbol	Hydrogen type	Chemical shift	TPO		TPO[CaO]	
			Mole (%)	Number of atoms	Mole (%)	Number of atoms
H_{Arom}	Aromatics	6.42 - 8.99	9.21	4.15	10.96	4.95
H_{Ole}	Olefinic CH - CH_2 groups	4.50 - 6.42	7.55	3.40	8.04	3.63
$H_{CH\alpha}$	CH group α to aromatic ring	2.88 - 3.40	0.72	0.32	0.85	0.38
$H_{CH2\alpha}$	CH_2 group α to aromatic ring	2.64 - 2.88	1.03	0.46	1.45	0.65
$H_{CH3\alpha}$	CH_3 group α to aromatic ring	2.04 - 2.64	12.49	5.63	13.8	6.23
H_{Naph}	Naphthenic CH - CH_2 groups	1.57 - 1.96	14.8	6.67	16.45	7.43
H_{Par-CH}	Paraffinic CH groups	1.39 - 1.57	3.52	1.59	2.67	1.21
$H_{Par-CH2}$	Paraffinic CH_2 groups	0.94 - 1.39	22.83	10.28	19.96	9.01
$H_{Par-CH3}$	Paraffinic CH_3 groups	0.25 - 0.94	27.85	12.55	25.82	11.66
Total			100.00	40.05	100.00	45.16

Table 4.6. ^{13}C NMR chemical shift assignments

Symbol	Carbon type	Chemical shift	TPO		TPO[CaO]	
			Mole (%)	Number of atoms	Mole (%)	Number of atoms
C_{Ar}	Aromatic quaternary C	140.5 - 160.0	3.81	1.18	4.25	1.32
$C_{Ar\alpha-S}$	Aromatic quaternary C α to S atom	137.0 - 140.5	2.04	0.63	1.82	0.56
$C_{Ar\alpha-CH3}$	Aromatic C α to position CH_3 group	131.7 - 137.0	6.8	2.11	7.08	2.19
C_{AA}	Aromatic C bridging 2 aromatic rings	129.2 - 131.7	6.95	2.16	7.1	2.20
C_{AAA}	Aromatic C bridging 3 rings		1.92	0.60	2.04	0.63
C_{Ole}	Olefinic CH - CH_2	85.0 - 129.2	5.51	1.71	6.29	1.95
C_{Ar-H}	Aromatic protonated C		14.5	4.51	17.23	5.34
C_{Par-C}	Paraffinic quaternary C	50.0 - 60.0	0.4	0.12	0	0.00
C_{Naph}	Naphthenic CH - CH_2	40.5 - 50.0	10.2	3.17	11.85	3.67
C_{Par-CH}	Paraffinic CH	35.0 - 40.5	2.67	0.83	2.48	0.77
$C_{Par-CH2}$	Paraffinic CH_2	21.5 - 35.0	23.74	7.38	20.38	6.32
$C_{Par-CH3\alpha-Ar}$	Paraffinic CH_3 α to aromatic ring	18.5 - 21.5	7.05	2.19	6.76	2.10
$C_{Par-CH3}$	Paraffinic CH_3	3.0 - 18.5	14.41	4.48	12.72	3.94
Total			100.00	31.09	100.00	31.00

Figure 4.8 shows the distribution of hydrogen and carbon types in TPO and TPO[CaO], according to different hydrocarbon subfamilies. NMR data reveals that there is a significant presence of hydrogen and carbon atoms in paraffinic structures for both samples. In contrast to TPO, TPO[CaO] exhibits a higher content of hydrogen and carbon atoms in aromatic, naphthenic, and olefinic structures, while hydrogen and carbon atoms in paraffinic ones are lower. This trend can be associated with the participation of CaO in diverse chemical reactions during WT pyrolysis. In this regard, besides desulfurization capabilities, the above-described results help to confirm the hypothesis established in Chapter 3 regarding the catalytic activity of CaO. As previously discussed, the polarity of the active sites of CaO may affect the stability of the π-electron cloud of PAH present in the primary pyrolysis products (volatiles); thus, catalyzing secondary reactions [24]. This phenomenon may lead to ring splitting and, eventually, more protonated aromatic rings, naphthenes, and/or olefins can be formed [37,38]. In addition, the O^{2-} ions may also abstract H^{+} ions from long paraffinic chains. In turn, smaller hydrocarbon chains could be generated. Nevertheless, in the presence of CaO, coupled with the high temperature of pyrolysis, these new chains may reorganize to form olefins, cycloparaffins (naphthenes), or even new aromatics [39].

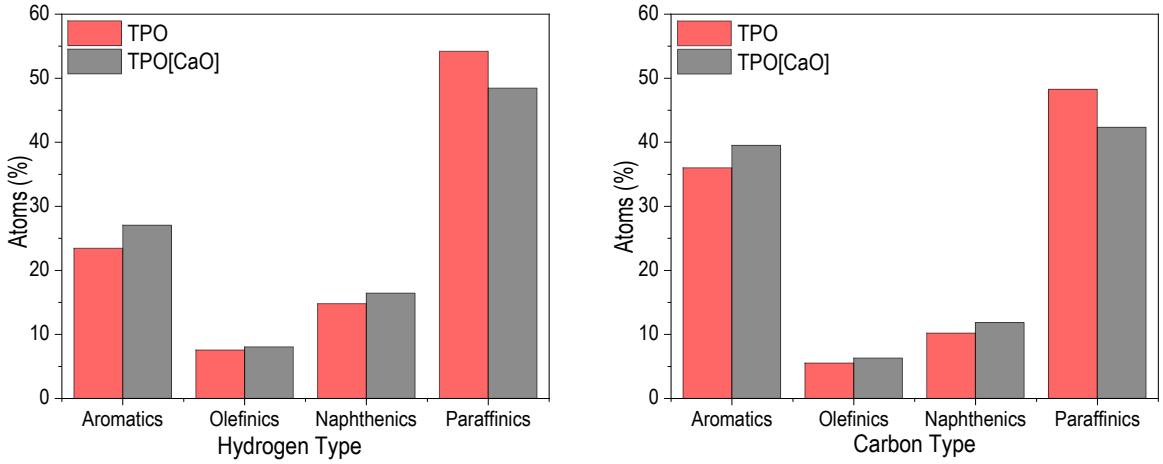

Figure 4.8. Atomic distribution by hydrocarbon families

Figure 4.9 shows the distribution of hydrogen atoms along with their cumulative frequency for TPO and TPO[CaO]. Hydrogen atoms in methylene (CH_2), methyl (CH_3), and naphthenic groups, as well as hydrogen atoms in aromatic rings make up more than 80 % of both samples. This can be associated with the presence of multiple shorter paraffinic chains instead of longer ones attached to aromatic structures [36].

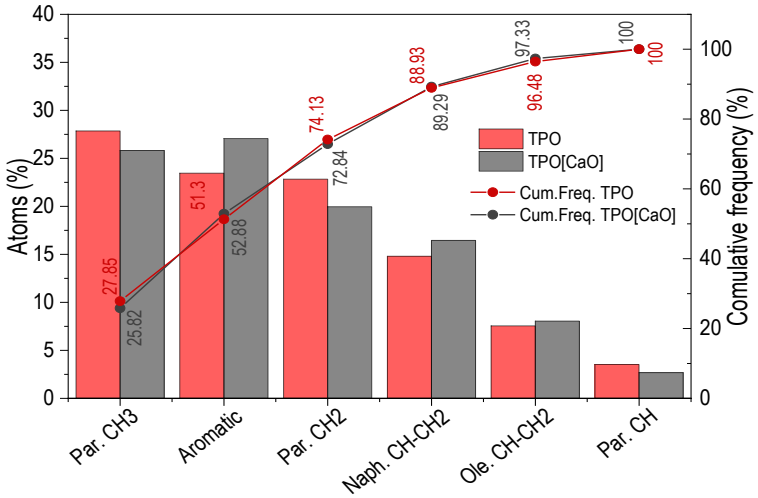

Figure 4.9. Hydrogen environment distribution

On the other hand, carbon atoms in paraffins such as methylene (CH_2) and methyl (CH_3) groups, and protonated carbon atoms in aromatic structures, make up around 50 % of both TPO and TPO[CaO], as shown in Figure 4.10. The number of carbon atoms in aromatic structures is higher than the number of hydrogen atoms, which means that some carbon atoms are non-protonated [17]. This suggests that the carbon atoms in aromatic compounds are either present in condensed structures or connected to paraffinic side chains, as aforementioned. Based on the hydrogen and carbon type distributions obtained from ^{1}H and ^{13}C NMR reported in Table 4.5 and Table 4.6, the derived AMPs for both samples were calculated. Derived AMPs are a group of dimensionless quantities obtained by re-arranging the AMPs, which provide an overall understanding of the structure of complex mixtures.

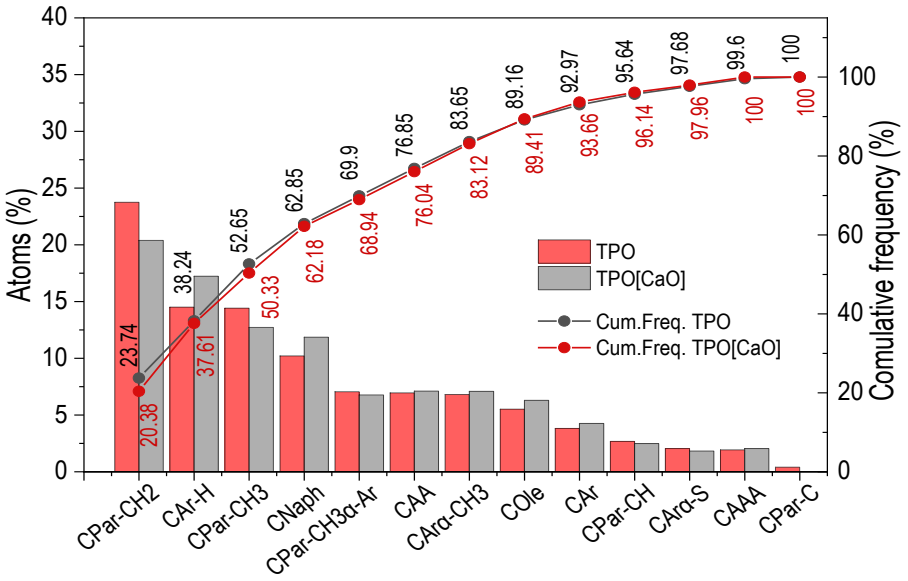

Figure 4.10. Carbon environment distribution

The formulae used to calculate these derived AMPs were taken from Poveda and Molina [35]. The derived AMPs calculated for TPO and TPO[CaO] are listed in Table 4.7. Herein, f_a is related to the aromatic content, and it is defined as the ratio of carbon atoms in aromatic compounds to total carbon atoms in the sample. In this regard, TPO[CaO] was found to be 11% more aromatic (f_a=0.40*)* than TPO (f_a=0.36). C/H is the ratio of the number of carbon atoms to the number of hydrogen atoms in the fuel. Values of 0.68 (H/C =1.47) for this parameter confirms the presence of both paraffinic and aromatic structures in the fuels.

Table 4.7. Derived AMPs for TPO and TPO[CaO]

Derived AMP	Description	TPO	TPO[CaO]
Aromaticity factor (f_a)	Ratio of the number of aromatic C atoms to total number of C atoms in the sample	0.36	0.40
$(C/H)_{Paraffinic}$	Ratio of number of C atoms to H atoms in the paraffinic content of the sample	0.61	0.60
$(C/H)_{Aromatic}$	Ratio of number of C atoms to H atoms in the aromatic content of the sample	2.48	2.70
C/H	Ratio of number of C atoms to H atoms in the sample	0.69	0.69
n_{acl}	Average number of C atoms in paraffinic chains connected with aromatic rings	5.15	2.78
R_N	Total number of naphthenic rings in an average molecule	1.22	1.41
R_A	Total number of aromatic rings in an average molecule	3.46	7.00
R_T	Total number of rings in an average molecule	4.69	4.88
φ	Ratio of total number of aromatic C in poly-condensed structures to number of aromatic C atoms	0.25	0.23

Likewise, a value of $(C/H)_{aromatic}$ of around 3, which indicates that 3 out of 6 aromatic carbons are non-protonated. Therefore, the aromatic rings are present in condensed structures (cata- or peri-condensed) or have multiple side chains connected to them. This confirms the hypothesis previously established according to the results of APPI FT-ICR MS. The average number of C atoms in paraffinic chains connected with aromatic rings (n_{acl}) exhibits a significant difference between TPO (n_{acl}=5.57) and TPO[CaO] (n_{acl}=2.78). The smaller chain length of TPO[CaO] is explained by the possible cracking effect of CaO on long hydrocarbon chains. The phenomenon can also be noticed by the higher R_N and R_A of TPO[CaO], in contrast to TPO. In the case of $(C/H)_{Paraffinic}$, a value of ~ 0.6 in TPO[CaO] and implies that most paraffinic structures are straight-chained, with a slight presence of paraffinic structures with branched chains.

The condensation index (φ) helps to establish the relationship between the total number of aromatic carbon atoms and the aromatic carbon atoms that form poly-condensed structures. A value of 0 denotes the absence of a condensation center, while a value of 0.7 accounts for structures that are highly condensed [36]. In this regard, both samples present aromatic structures that are slightly condensed due to their low value of φ. Overall, the presence of this wide variety of functional groups detected by means of ^{1}H and ^{13}C NMR will significantly influence the combustion properties of TPO and TPO[CaO] and eventually, their gaseous and particulate matter emissions. For instance, paraffinic CH_2 groups seem to have a positive effect on derived cetane number (DCN) [40]. Likewise, aromatic rings tend to reduce the DCN more than other functional groups [41].

Considering the chemical complexity of TPO and TPO[CaO], the wide carbon number (C_6 – C_{55}) and boiling point (70 – 550 ºC) range [8], fractionation by distillation seems to be an attractive method of grouping similar compounds, based on their volatility. In addition, distillation can concentrate sulfur-containing compounds in the leftover heavy fraction, improving the characteristic of the other ones. Thus, distillation of TPO[CaO] will be addressed in the following section.

As a closing remark of this part of the chapter, and based on the obtained results, Figure 4.11 shows possible pathways in regard to the destabilizing effect of CaO on aromatic structures and the cracking of long paraffinic chains, hence forming new compounds. Figure 4.11 also shows how the activity of CaO during pyrolysis favors the formation of light gas hydrocarbons that eventually influence the TPG yield and composition as found and described in Chapter 3. In summary, CaO may chemically react with H_2S/COS, CO_2, and H_2O to form CaS, $CaCO_3$, and $Ca(OH)_2$, respectively, during WT volatilization. At the same time, it possesses catalytic activity associated with its electron-pair donating capability, which facilitates the reaction pathways .

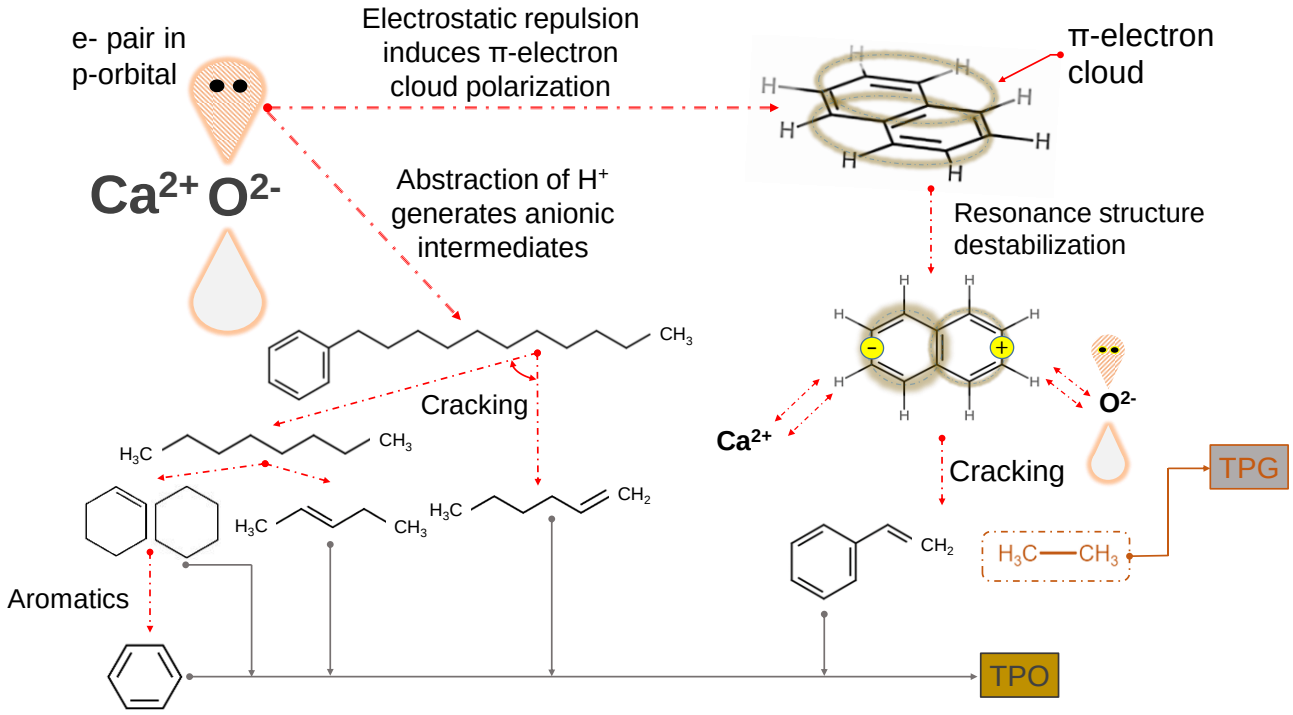

Figure 4.11. Possible cracking pathways of a poly-aromatic structure and paraffinic chains in the presence of CaO during WT pyrolysis

4.2.2 Distillation of tire pyrolysis oil: Structural characteristics of the derived fraction

Figure 4.12 shows the appearance of the fractions obtained after the distillation of TPO[CaO]. As noted, the light fraction (boiling point range: 70 – 176 ºC) has a yellowish appearance, with low viscosity, resembling gasoline fuel. The low-middle (boiling point range: 176 – 240 ºC) and high-middle (boiling point range: 240 – 285 ºC) fractions exhibit a dark brownish color, and were slightly more viscous than the light fraction, in particular the high-middle fraction. These characteristics may indicate compatibility with diesel or distillate marine fuels. Lastly, the heavy fraction (boiling point range: 280 – 550.9 ºC) looks black, with high viscosity at room temperature (barely flowing), resembling bitumen. In addition to a comparison of their properties with those of the petroleum-derived fuels, a detailed characterization of these fractions is presented in the following sections.

Figure 4.12. TPO fractions appearance, from left to right: light, low-middle, high-middle, heavy

4.2.2.1 Physical and chemical characteristics of the distillate fractions

Physical and chemical characteristics of light, low-middle, high-middle, and heavy fractions are listed in Table 4.8. As understood in the first part of this chapter, TPO[CaO] is a complex mixture containing valuable hydrocarbon fractions within a wide boiling point range (70 to 550.9 ºC). The aim of distillation is to generate fractions whose boiling point range coincides with those of conventional fuels, including for instance, gasoline (boiling point range: 35 – 200 ºC), diesel (boiling point range: 150 – 338 ºC), and heavy fuel oil (boiling point range: 350 – 650 ºC). In this manner, the properties of the fractions obtained could be compared with those of conventional fuels, in order to propose similar applications.

Table 4.8. Physicochemical properties of TPO distillate fractions

Property	Fractions				
	Light	Low-middle	High-middle	Heavy	TPO[CaO]
Boiling point range (ºC)	70 – 176	176 – 240	240 – 285	280 – 550.9	70 – 550.9
C (wt.%)	86.16	86.75	87.76	87.43	87.21
H (wt.%)	12.24	10.33	10.49	9.70	10.66
N (wt.%)	0.80	0.50	0.91	0.82	1.23
S (wt.%)	0.06	0.53	0.82	0.89	0.51
O (wt.%)	0.64	1.86	0.02	1.16	0.39
H/C	1.70	1.43	1.43	1.33	1.47
Density @ 25 ºC (kg/m^3)	795.47	873.6	913.3	1050	888.67
Kinematic viscosity (cSt) @ 40 ºC	0.66	2.01	6.96	-	1.9
High heating value (MJ/kg)	41.91	43.37	43.22	42.48	43.4

Density is an important property of fuels, which is fundamental in applications such as internal combustion engines, given that fuel injection systems operate on a volume basis. The density of a fuel changes depending on the carbon number and compound

classes present on it (i.e. paraffins, naphthenes, aromatics). For compounds of the same class, density increases with the carbon number. For compounds with the same carbon number, the order of increasing density is paraffins, naphthenes, and aromatics [42]. This property was found to vary among the TPO[CaO] fractions between 795.47 kg/m^3 (light fraction) and 1050 kg/m^3 (heavy fraction). Comparing these values to those of conventional gasoline (720 – 775 kg/m^3) [42], diesel (820 – 845 kg/m^3) [42], distillate marine fuels (890 – 900 kg/m^3) [43], residual marine fuels (920 – 1010 kg/m^3) [43], and bitumen (1010 – 1060) [44], the light fraction (795.47 kg/m^3) seemed comparable to conventional gasoline, while the low-middle (873.6 kg/m^3) was within the range suggested for conventional diesel fuel. On the other hand, high-middle (913.3 kg/m^3) and heavy (1050 kg/m^3) fractions seemed to be more like distillate marine fuels/residual marine fuels and bitumen, respectively.

Viscosity is another important property that determines the fluidity of the fuel at certain temperature conditions. Like density, it is dependent on temperature, and it decreases as the temperature increases. In thermal systems such as internal combustion engines, this property is very important in the lubrication of the injection systems and on the spray pattern [43]. If viscosity is not within the prescribed limits established by the engine manufacturer, it may result in poor combustion, deposit formation, and energy losses [43]. Viscosity for TPO[CaO] fractions was found to be in the range of 0.66 cSt (light fraction) and 6.96 cSt (high-middle fraction). The heavy fraction was highly viscous at room temperature (no flow) and therefore difficult to measure. Relating these values to conventional petroleum-derived fuels, the light fraction (0.66 cSt), the low-middle (2.01 cSt), and the high-middle (6.96 cSt) can be compared to gasoline (0.4 – 0.7 cSt), diesel (2.0 – 4.5 cSt) [42], and distillate marine fuel grade DMZ (3 – 6 cSt) [43] fuels, respectively.

Another important property to consider in a fuel is the energy density. A common aspect among all fractions is their high heating value, which can be linked to their high carbon (85 – 88 wt.%) and hydrogen (9.72 – 13.47 wt.%) contents, as shown in Table 4.8. The high heating value of the TPO[CaO] distillate fractions was found to be in the range of 41.91 – 43.37 MJ/kg; these values were close to those reported for conventional gasoline (46.5 MJ/kg) [42], diesel (45.13.0 MJ/kg) [45], and heavy fuel oil (43.0 MJ/kg) [46]. These values also agreed with those specified for marine fuels. For instance, the heating value for ship fuels is expected to be at least 30 MJ/kg for ideal economical operation [46].

After distillation, the sulfur content was found to gradually increase from the light (0.06 wt.%) to the heavy fraction (0.89 wt.%), confirming the benefits of distillation to enrich sulfur-containing compounds in the heavy leftover fraction. Now, further desulfurization strategies can be applied to this heavy fraction, depending on the specific application. Sulfur distribution among the fractions will be corroborated with the FT-ICR MS data in Section 4.2.2.3. The H/C ratio was found to decrease from 1.70 (light fraction) to 1.33 (heaviest fraction). In this manner, as the boiling point increases (as the distillate TPO fraction becomes heavier), it tends to be more aromatic in nature. As mentioned before, high molecular weight compounds (high carbon number) contained in TPO exhibited a large DBE number (> 20), and hence, a high degree of unsaturation. These compounds can be linked to highly condensed aromatic structures, which tend to stay in the heaviest fraction [26]. This tendency will be corroborated by FT-ICR MS and NMR results.

4.2.2.2 GC-MS: Light fraction

The composition of this fraction was determined by means of GC-MS; however, the obtained results are quite similar to the ones discussed in Chapter 3 for TPO[CaO]. Therefore, for the sake of brevity, such results have not been included in the presents chapter. It is clear that the light fraction of TPO contains single aromatic rings (benzene, toluene, xylene) and aliphatic compounds such as limonene (one of the major compounds listed above) [14,15,47]. In particular, limonene is a cyclic terpene ($C_{10}H_{16}$) that exists in its d- and l- forms, as d-limonene and l-limonene [48]. It is a high-value chemical used in the formulation of industrial solvents, resins, adhesives and fragrances, among others [14]. Due to the occurrence of secondary reactions -especially dehydrogenation -to form aromatics, high pyrolysis temperatures lead to lower limonene yield; therefore, yields of some aromatic compounds like benzene, toluene, and xylene (BTX) are inversely proportional to limonene yields [48]. According to the information derived from GC-MS, the light fraction differs from petroleum gasoline since it contains a greater amount of aromatic and olefinic compounds [49]. Also, petroleum gasoline contains compounds in the carbon number range between C_4-C_{12}, while the carbon number of the light fraction of TPO ranges from approximately C_6-C_{18}. Despite these compositional differences, the light fraction of TPO exhibits physicochemical properties comparable to those of petroleum gasoline, as discussed above (Table 4.8). In addition, the average molecular weight of this fraction (MW_{LF}) was found to be 156.4 g/mol, which is close to the gasoline range (60-150 g/mol) [50]. Taking this into account, similar applications can be considered. More information related to the molecular characteristics of this fraction will be given in later (^{1}H and ^{13}C NMR).

4.2.2.3 APPI FT-ICR: low-middle, high-middle, and heavy fractions

Figure 4.13 shows the mass spectra obtained for each fraction. The spectra obtained for the low-middle and high-middle fractions shows that most of the compounds contained in these two fractions are in *m/z* ratio ranging from 100 to 700. On the other hand, the heavy fraction exhibits a wider distribution, containing compounds in the *m/z* ratio range between 100 and 1000.

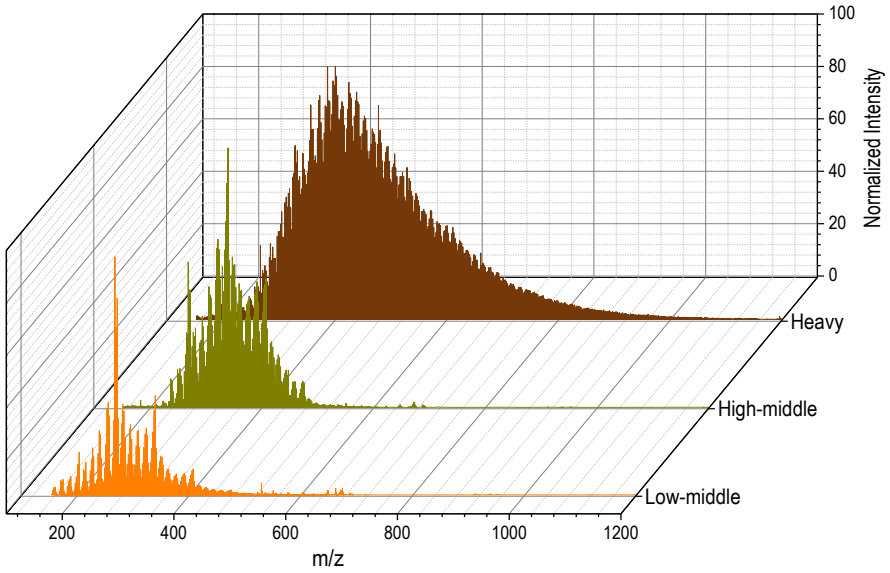

Figure 4.13 APPI FT-ICR mass spectra of low-middle, high-middle, and heavy fractions

Approximately 413, 813 and 3768 mass peaks were resolved for the low-middle, high-middle, and heavy fractions, respectively, and a unique chemical formula was assigned to each mass peak. It is important to note that the molecular formulas assigned to each mass peak may cover several isomers. Figure 4.13 also shows how peaks with the highest intensities are shifted to the right of the *m/z* axis as the boiling point increases, in other words, as the distillate TPO fraction becomes heavier.

From the assigned molecular formulas, different structural parameters, including MW_{avg}, C_{avg}, H_{avg}, DBE_{avg}, etc., were deduced for these three fractions and listed in Table 4.9. As aforementioned, light hydrocarbons have low molecular weight, which makes them travel very fast in the ICR cell with possible interference of signals that make accurate determination difficult [16]. These compounds are more suitable to be detected by GC-MS. In this regard, FT-ICR MS data for the light fraction is not discussed in this work.

Table 4.9. Several structural parameters obtained from FT-ICR MS

Parameter	Fraction		
	Low-middle	**High-middle**	**Heavy**
MW_{avg} (g/mol)	299.94	353.86	498.43
Carbon number range	12 – 36	12 – 42	13 – 74
C_{avg}	22.17	26.05	37.05
Hydrogen number range	12 – 58	14 – 66	12 – 106
H_{avg}	31.52	36.58	48.39
DBE number range	3 – 14	3 – 17	0.5 – 35
DBE_{avg}	7.33	8.79	13.85
H/C	1.417	1.399	1.305

As expected, MW_{avg} increased as the boiling point range also increased. The MW_{avg} was found to be 299.94 g/mol, 353.86 g/mol, and 498.43 g/mol for the low-middle, high-middle, and heavy fractions, respectively. These values aligned well with the carbon and hydrogen number range found for each fraction. The unsaturation level of each sample was identified by means of the DBE_{avg} number, which was found to be 7.33, 8.79, and 13.85 for low-middle, high-middle and heavy fractions, respectively. These values, along with the H/C ratios reported in Table 4.9**,** revealed that the heavy fraction tended to be more aromatic in nature (H/C = 1.305), followed by the high-middle (H/C = 1.39) and finally the low-middle (H/C = 1.42). The H/C values presented the same trend as those calculated from the elemental analysis and reported in Table 4.8.

Combining the elemental composition with the MW_{avg}, and the MW_{LF}, the number of C, H, S, N and O atoms in an average molecular formula for all fractions were calculated and listed in Table 4.10. It can be seen that the number of hydrogen and carbon atoms agrees with the number of atoms for these two elements as shown in Table 4.9. Once again, these results confirm the data reliability from both the macroscopic (elemental analysis) and at the microscopic (molecular characterization by FT-ICR MS) standpoints.

Table 4.10. Number of atoms in average molecular formula

Fraction	C	H	N	S	O
Light	11.23	19.37	0.09	0.00	0.06
Low-middle	25.64	36.75	0.13	0.06	0.41
High-middle	25.40	36.43	0.23	0.09	0.00
Heavy	38.36	51.06	0.31	0.15	0.38

It can be seen in Figure 4.14 that the most abundant molecular classes present in all the fractions were HC and S_1. The relative abundance of the HC molecular class was found to be 92.94 %, 85.81 %, and 82.12 % for low-middle, high-middle and the heavy fraction, respectively. Molecules containing S_1 were more abundant in the heavy fraction (10.37 %), followed by the high-middle fraction (8.02 %), and finally the low-middle fraction (4.99 %).

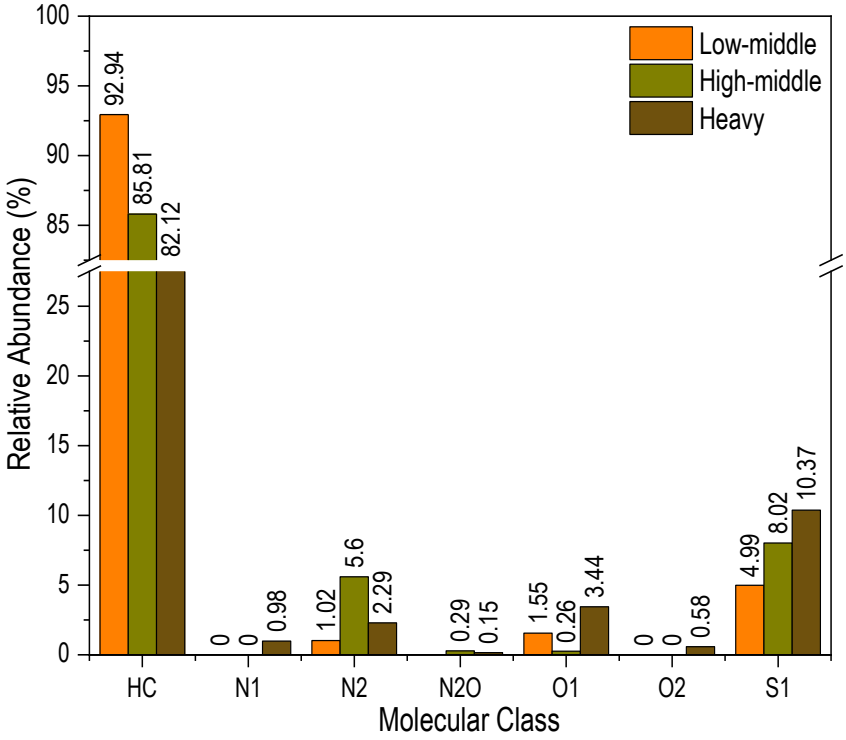

Figure 4.14 Compound class distribution of low-middle, high-middle and heavy fractions

According to these results, sulfur containing compounds (S_1) tended to stay in the heaviest fractions (high-middle and heavy), rather than in the lightest fractions (low-middle). These results are coherent with the elemental composition reported in Table 4.8 and confirm the benefits of distillation to concentrate sulfur containing compounds in the heaviest fraction, while improving the properties of the lightest fractions. As found for the TPO, and taking into consideration that sulfur containing compounds in the heaviest TPO fractions are mainly in the form of S_1 molecules, the core skeletal structures are likely to be thiophenic, or thiolic in nature [17].

Since HC and S_1 were the most abundant molecular classes among all fractions, they were classified further into different sub-families, according to their degree of unsaturation (DBE number) as shown in Table 4.11 [12]. The HC subfamilies have been defined as previously described for TPO and TPO[CaO]. Table 4.11 also displays minimum and maximum carbon atoms for each sub-family, including the low-middle, high-middle, and heavy fractions. Figure 4.15 illustrates the distribution of compounds present in the HC molecular class as a function of the carbon and DBE values. As observed in Figure 4.15, the most abundant compounds were identified in the carbon number range between 20 and 30 (DBE numbers between 5 and 15), for the low-middle and high-middle fractions, respectively. A wider distribution was found for the heavy fraction, presenting carbon and DBE

values in the range of 20 – 50 and 5 – 25, respectively. The high DBE numbers (BDE > 20) in the heavy fraction can be related to condensed aromatic structures [26].

Table 4.11. Range of DBE number of carbon atoms per sub-family of pure hydrocarbons (HC) class

DBE	Sub-family	Carbon number range					
		Min			Max		
		Low-middle	High-middle	Heavy	Low-middle	High-middle	Heavy
0	P	-	-	-	-	-	-
1	N	-	-	-	-	-	-
2 - 3	DN	12	20	17	21	29	44
4 - 6	MA	12	12	13	31	36	54
7 - 9	DA	13	14	13	36	40	58
10 - 12	TrA	17	17	17	36	42	62
13 - 14	TeA	22	21	19	35	42	64
16+	PA+	-	23	21	-	41	74

P: Normal paraffins and isoparaffins; **N:** Naphthenes; **DN**: Dinaphthenes; **MA:** Monoaromatics, **DA+:** Diaromatics and naphtheno-aromatics; **TrA+:** Triaromatics and naphtheno-aromatics; **TeA+:** Tetra-aromatics and tetra-aromatics with naphthenic rings; **PA+:** Penta-aromatics and higher, including naphthenic rings

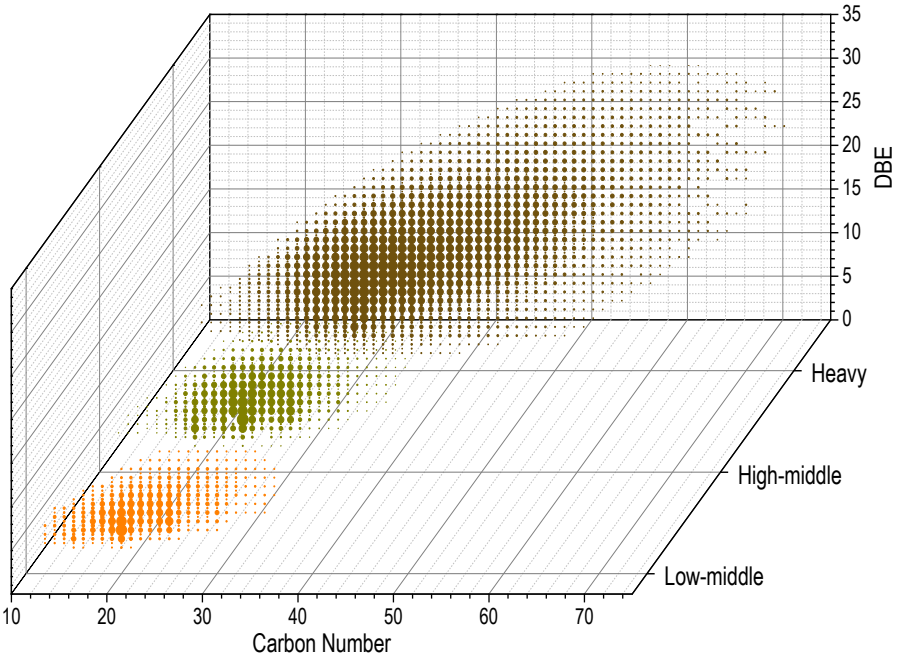

Figure 4.15 Abundance of pure hydrocarbon (HC) compounds: low-middle, high-middle, and heavy fractions

After distillation, light aromatic hydrocarbons were found in the lightest fractions, while more complex aromatic structures were mainly distributed in the heavier fractions. This trend is more easily visualized by means of the sub-families summed abundance plots, which are presented later.

Similarly, for the S_1 molecular class, Table 4.12 reports the carbon number distributions for each sub-family, also sorted according to their respective DBE numbers. S_1 subfamilies have also been defined as described for TPO and TPO[CaO] in previous sections. As a result, a DBE number higher than three in this molecular class suggests that the core skeletal structures of sulfur-containing compounds in TPO were thiophenic or thiolic in nature.

Table 4.12. Range of DBE number of carbon atoms per sub-family of S_1 molecular class

DBE	Sub-family	Carbon number range					
		Min			Max		
		Low-middle	High-middle	Heavy	Low-middle	High-middle	Heavy
0 - 2	SD	-	-	-	-	-	-
3 - 5	TH	15	18	20	25	30	35
4 - 7	BTH	16	16	17	30	35	48
8 - 11	DBT	18	18	17	30	35	51
12+	BNT	-	20	19	-	34	60

SD: sulfide; **Th:** thiophene; **BT:** benzothiophene; **DBT:** dibenzothiphene; **BNT:** benzonaphthothiophene

Figure 4.16 shows the distribution of compounds contained in the S_1 molecular class as a function of the carbon and DBE numbers. The most abundant S_1 identified compounds, in the low and high-middle fractions, were found in the carbon number range of 20 to 30 and DBE numbers between 3 and 10. In the heavy fraction, these compounds were found in the carbon number range of 20 to 50, and DBE number between 5 and 20. Accordingly, the high DBE numbers (DBE > 20) of the S_1 molecular class in the heavy fraction suggest the presence of sulfur atoms in condensed aromatic structures (i.e. benzonaphthothiophene). This will be also illustrated in the summed abundance plots.

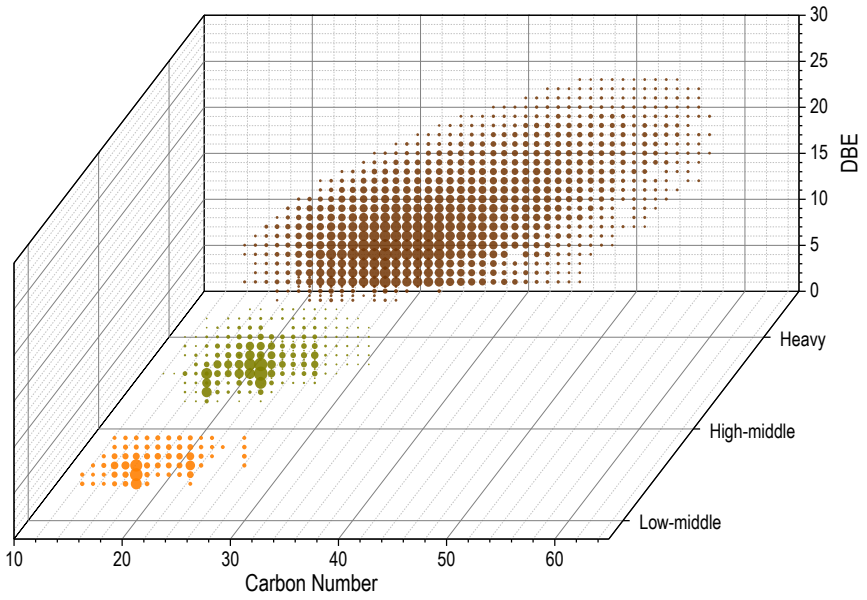

Figure 4.16. S_1 compounds abundance: low-middle, high-middle, and heavy fractions

According to the sub-families previously defined, the HC and S_1 compound distributions and their summed abundances are plotted in Figures 4.17a and 4.17b**,** respectively. The HC molecules present in low-middle and high-middle fractions were mainly in the form of mono-aromatics (MA: 40% and 19%) and diaromatics and naphtheno-aromatics (DA+: 44% and 46%). However, the heavy fraction showed more complex structures, so they were found in the form of tri-aromatics and naphtheno-aromatics (TrA+: 21%), tetra-aromatics and tetra-aromatics with naphthenic rings (TeA+: 14 %), and penta-aromatics and higher (PA+: 42 %). This hypothesis is corroborated with the NMR results in the following section. In Figure 4.16b**,** S_1 containing compounds in the low-middle and high-middle fractions were mainly present in the form of benzothiophenes (BT), while in the heavy fraction, these monosulfur compounds had a major presence in the form of benzonaphthothiophene (BNT).

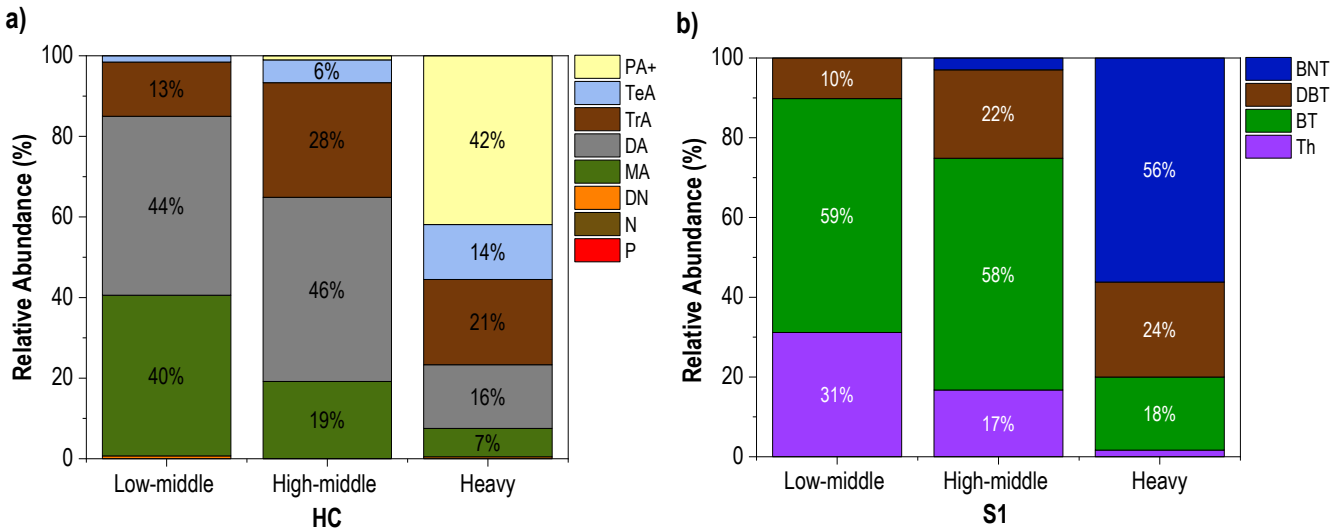

Figure 4.17 Compound sub-families according to DBE number and summed abundance

4.2.2.4 ^{1}H and ^{13}C nuclear magnetic resonance: light, low-middle, high-middle, and heavy fractions

The number of hydrogen and carbon atoms in an average molecule contained in aromatic, paraffinic, olefinic, and naphthenic structures for the light, low-middle, high-middle, and heavy fractions are reported in Tables 4.13 and Table 4.14, respectively. The ^{1}H and ^{13}C NMR assignments, as well as the formulae and terminology used to denote and calculate the AMPs for this fraction follows the same methodology as described for TPO and TPO[CaO]. Accordingly**,** Figure 4.18 and Figure 4.19 illustrate the distribution of hydrogen and carbon atoms for each fraction, respectively. A significant amount of hydrogen atoms in aromatic structures was observed for the light fraction, which is linked to the important presence of protonated single aromatic rings such as benzene, toluene, xylene, etc., in agreement with the information obtained by GC-MS. In addition, the existence of hydrogen and carbon atoms in olefinic and naphthenic structures is associated with the presence of limonene. As the boiling point increased, fewer aromatic rings were protonated, and hydrogen atoms were mainly found in paraffinic structures such as paraffinic CH_3 and paraffinic CH_2. This could be attributed to two possible reasons: (i) the aromatic rings were fused, or (ii) the presence of multiple alkyl side chains.

Table 4.13. ^{1}H NMR chemical shift assignments

Symbol	Hydrogen type	Chemical shift	Number of hydrogen atoms (NA_H)			
			Light	Low-middle	High-middle	Heavy
H_{Arma}	Aromatics	6.42-8.99	2.92	5.61	3.75	2.69
H_{ole}	olefinic CH-CH_2 groups	4.50-6.42	2.79	3.00	2.22	0.63
$H_{CH\alpha}$	CH group α to aromatic ring	2.88-3.40	0.12	0.82	0.52	0.14
$H_{CH2\alpha}$	CH_2 group α to aromatic ring	2.64-2.88	0.25	0.55	1.20	0.14
$H_{CH3\alpha}$	CH_3 group α to aromatic ring	2.04-2.64	2.83	6.26	4.66	1.65
H_{Naph}	naphthenic CH-CH_2 groups	1.57-1.96	5.40	8.13	5.25	0.65
H_{Par-CH}	Paraffinic CH groups	1.39-1.57	0.77	0.71	0.70	0.55
$H_{Par-CH2}$	Paraffinic CH_2 groups	0.94-1.39	2.69	7.24	8.11	28.21
$H_{Par-CH3}$	Paraffinic CH_3 groups	0.25-0.94	1.59	4.43	10.01	16.40
Total			19.37	36.75	36.43	51.06

Table 4.14. ^{13}C NMR chemical shift assignments

Symbol	Carbon type	Chemical shift	Number of carbon atoms (NA_C)			
			Light	Low-middle	High-middle	Heavy
C_{Ar}	Aromatic quaternary C	140.5-160.0	0.53	1.82	1.88	3.26
$C_{Ar\alpha\text{-}S}$	Aromatic quaternary C α to S atom	137.0-140.5	0.47	1.47	1.44	2.66
$C_{Ar\alpha\text{-}CH3}$	Aromatic C α to position CH_3 group	131.7-137.0	0.65	1.54	1.39	0.70
$C_{Ar,\ AA}$	Aromatic C bridging 2 aromatic rings	129.2-131.7	0.53	0.92	0.37	0.28
$C_{Ar,\ AAA}$	Aromatic C bridging 3 rings		0.94	2.60	3.30	8.54
C_{ole}	Olefinic CH - CH_2	85.0-129.2	0.68	1.20	0.77	0.39
$C_{ar\text{-}H}$	Aromatic protonated C		1.79	4.43	3.57	1.97
$C_{Par\text{-}C}$	Paraffinic quaternary C	50.0-60.0	0.08	0.10	0.03	0.02
C_{Naph}	Naphthenic CH and CH_2	40.5-50.0	0.43	0.59	0.28	0.16
$C_{Par\text{-}CH}$	Paraffinic CH	35.0-40.5	0.62	0.75	0.73	0.82
$C_{Par\text{-}CH2}$	Paraffinic CH_2	21.5-35.0	2.28	5.96	6.77	13.01
$C_{Par\text{-}CH3\alpha\text{-}Ar}$	Paraffinic CH_3 α to aromatic ring	18.5-21.5	1.05	2.21	1.92	1.89
$C_{Par\text{-}CH3}$	Paraffinic CH_3	3.0-18.5	1.19	2.06	2.93	4.67
Total			11.23	25.64	25.40	38.36

Indeed, the distribution of carbon atoms showed that there was an increase of the aromatic carbons bridging three rings together ($C_{Ar,\ AAA}$) and aromatic quaternary carbons, while a decrease of the aromatic protonated carbons ($C_{ar\text{-}H}$), from the light to the heavy fractions. Regarding sulfur, the heavier fractions exhibited higher concentrations of aromatic quaternary carbons α to sulfur atoms, in contrast to lighter fractions, in accordance with the results found by elemental analysis and FT-ICR MS. Hydrogen and carbon atoms in paraffinic CH structures can be related to a higher degree of branching. The degree of branching decreases with an increase in boiling point, as evidenced by the decrease of paraffinic CH groups, as seen in Figures 4.18 – 4.19**.** The inverse relationship between degree of branching and boiling point is due to weaker Van Der Waals forces between the branched structures, since there is less surface area for intermolecular interactions, in contrast to straight chains [51]. In addition, naphthenic and olefinic hydrogen and carbon atoms showed a gradual decrease from the light to the heavy fraction.

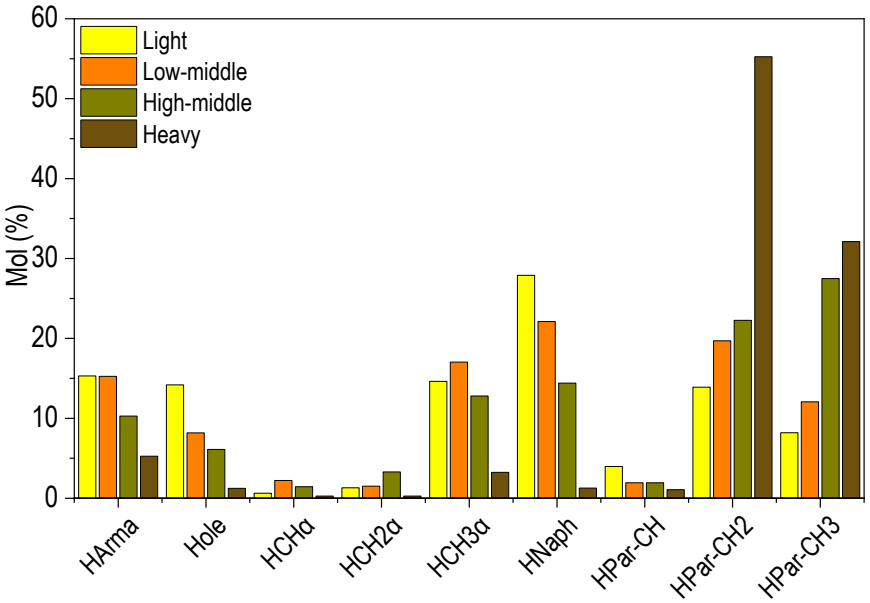

Figure 4.18. Hydrogen environment distribution in the distillate fractions

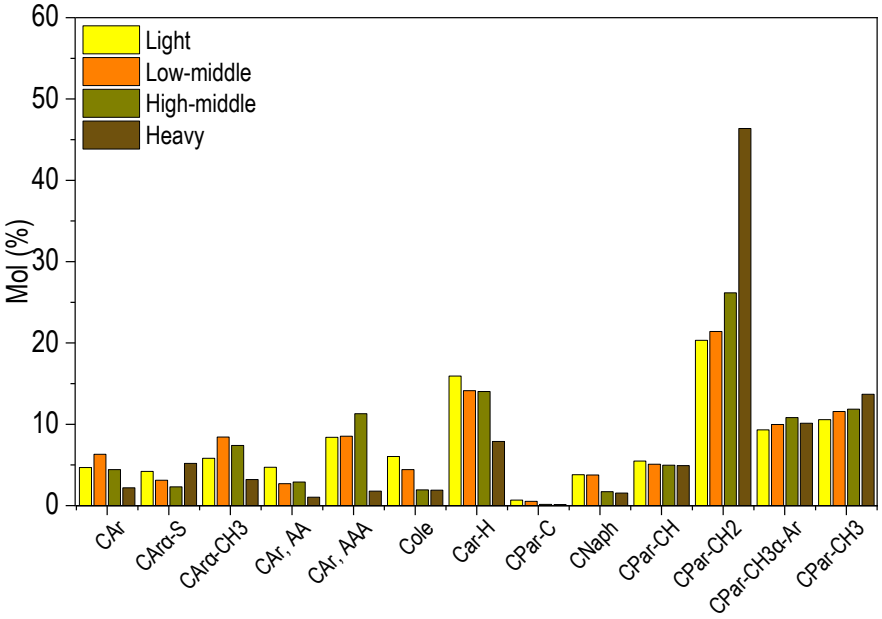

Figure 4.19. Carbon environment distribution in the distillate fractions

Based on the information obtained by means of ^{1}H and ^{13}C NMR, different AMPs were determined and listed in Table 4.15.

Table 4.15. Derived average molecular parameters

AMPs	Description	Light	Low-middle	High-middle	Heavy
Aromaticity Factor (*fa*)	Ratio of the number of aromatic C atoms to total number of C atoms in the sample	0.44	0.49	0.47	0.44
$(C/H)_{Paraffinic}$	Ratio of number of C atoms to H atoms in the paraffinic content of the sample	0.58	0.55	0.49	0.43
$(C/H)_{Aromatic}$	Ratio of number of C atoms to H atoms in the aromatic content of the sample	1.55	2.28	3.19	6.48
C/H	Ratio of number of C atoms to H atoms in the sample	0.53	0.70	0.70	0.75
R_N	Total number of naphthenic rings in an average molecule	0.28	0.45	0.26	0.14
R_A	Total number of aromatic rings in an average molecule	2.26	3.86	3.80	6.35
R_T	Total number of rings in an average molecule	2.54	4.31	4.06	6.49
φ	Ratio of total number of aromatic C in poly-condensed structures to number of aromatic C atoms	0.30	0.28	0.31	0.51

Significant differences can be seen in parameters such as $(C/H)_{Aromatic}$, which increased from the lightest to the heaviest fraction. For instance, a value of 6.48 in the heavy fraction indicates that in an aromatic structure, six of the carbon atoms were non-protonated. In contrast, a value of 1.55 in the light fraction indicates that most of the aromatic carbons were protonated. In the case of $(C/H)_{Paraffinic}$, a value of ~ 0.5 implied that most of the paraffinic structures were straight-chained. Two other important parameters that varied between the different fractions were R_A and R_N, which increased from 2.26 to 6.35, and decreased from 0.28 to 0.14, respectively. Therefore, as a general trend, the number of aromatic rings increased, while the number of naphthenic rings decreased as the fractions became heavier. Finally, the condensation index (φ) changed from 0.30 in the light fraction to 0.51 in the heavy fraction. The high condensation index of the heavy fraction agreed with the information previously reported from the FT-ICR MS analysis, which also revealed the presence of condensed aromatic structures in this fraction.

4.3 Summary

This stage of the research pursued a comprehensive understanding of the structural characteristics of a TPO produced in a lab-scale twin-auger reactor as a first step towards defining applications and upgrading strategies. Therefore, advanced analytical techniques such as Fourier Transform - Ion Cyclotron Resonance Mass Spectrometry (FT-ICR MS), and ^{1}H and ^{13}C Nuclear Magnetic Resonance (NMR) spectroscopy were utilized. In addition, the characterization of a TPO obtained from adding CaO to WT, as a low-cost catalytic material for its *in-situ* upgrading, herein named TPO[CaO], is presented. FT-ICR MS results revealed the significant presence of pure hydrocarbons (HC) ($HC_{(TPO)}$ = 74.9 % and $HC_{(TPO[CaO])}$ = 78.6 %) and hydrocarbons containing one sulfur atom (S_1) ($S_{1(TPO)}$ = 14.3 % and $S_{1(TPO[CaO])}$ = 13.9 %). HC compounds were found mainly in the form of tri-aromatics (26 %), tetra-aromatics (13 and 15 %), and penta-aromatics (22 and 30 %), while S_1 compounds in the form of dibenzothiophene (31 %) and benzonaphthothiophene (34 %). The resolved compounds by means of FT-ICR MS exhibited an average double bond equivalent (DBE) number of 11.3 and 12.2 for TPO and TPO[CaO], respectively. These high DBE values serve as indicators of the significant presence of condensed aromatic structures. ^{1}H NMR analysis showed that hydrogen atoms in methylene (CH_2), methyl (CH_3), and naphthenic groups, as well as hydrogen atoms in aromatic structures make up more than 80 % of both fuels. Similarly, carbon atoms in paraffinic groups (both CH_2 and CH_3) and protonated carbons in aromatic rings together form more than 50 % of the carbon atoms in TPO and TPO[CaO]. In addition, TPO[CaO] was distilled at atmospheric pressure into different fractions (light, low-middle, high-middle, and heavy), and the structural characteristics of each fraction were explored. Fractionation by distillation resulted in concentration of both the sulfur and aromatic compounds in the heaviest fraction. In this manner, effective application and upgrading strategies could be individually designed for each fraction.

References

[1] J.D. Martínez, J. Rodríguez-Fernández, J. Sánchez-Valdepeñas, R. Murillo, T. García, Performance and emissions of an automotive diesel engine using a tire pyrolysis liquid blend, Fuel. 115 (2014) 490–499.

[2] J. Pilusa and E. Muzenda, Combustion characteristics of waste tyre pyrolysis fuel as industrial burner fuel, in: Dev. Combust. Technol. Chapter 4, 2016: pp. 97–116.

[3] S.T. Kumaravel, A. Murugesan, A. Kumaravel, Tyre pyrolysis oil as an alternative fuel for diesel engines – A review, Renew. Sustain. Energy Rev. 60 (2016) 1678–1685.

[4] P. Hellier, M. Talibi, A. Eveleigh, N. Ladommatos, An overview of the effects of fuel molecular structure on the combustion and emissions characteristics of compression ignition engines, J. Automob. Eng. 232 (2018) 90–105.

[5] M. Hechinger, W. Marquardt, Targeted QSPR for the prediction of the laminar burning velocity of biofuels, Comput. Chem. Eng. 34 (2010) 1507–1514.

[6] D.A. Saldana, L. Starck, P. Mougin, B. Rousseau, L. Pidol, N. Jeuland, B. Creton, Flash point and cetane number predictions for fuel compounds using quantitative structure property relationship (QSPR) methods, Energy Fuels. (2011) 3900–3908.

[7] B. Creton, C. Dartiguelongue, T. de Bruin, H. Toulhoat, Prediction of the cetane number of diesel compounds using the quantitative structure property relationship, Energy Fuels. (2010) 5396–5403.

[8] F. Campuzano, A.G. Abdul Jameel, W. Zhang, A.-H. Emwas, A.F. Agudelo, J.D. Martínez, M.S. Sarathy, Fuel and

chemical properties of waste tire pyrolysis oil derived from a continuous twin-auger reactor, Energy Fuels. 34 (2020) 12688–12702.

[9] H.F. Öztop, Y. Varol, Ş. Altun, M. Firat, Using Gasoline-like fuel obtained from waste automobile tires in a spark-ignited engine, Energy Sources , Part A. 36 (2014) 1468–1475.

[10] A. Chaala, C. Roy, Production of coke from scrap tire vacuum pyrolysis oil, Fuel Process. Technol. 46 (1996) 227–239.

[11] M.F. Laresgoiti, B.M. Caballero, I. de Marco, A. Torres, M.A. Cabrero, M.J. Chomón, Characterization of the liquid products obtained in tyre pyrolysis, J. Anal. Appl. Pyrolysis. 71 (2004) 917–934.

[12] N. Hourani, H. Muller, F.M. Adam, S.K. Panda, M. Witt, A.A. Al-Hajji, S.M. Sarathy, Structural level characterization of base oils using advanced analytical techniques, Energy Fuels. 29 (2015) 2962–2970.

[13] P. Rathsack, M. Kroll, A. Rieger, R. Haseneder, D. Gerlach, J. Repke, M. Otto, Analysis of high molecular weight compounds in pyrolysis liquids from scrap tires using Fourier transform ion cyclotron resonance mass spectrometry, J. Anal. Appl. Pyrolysis. 107 (2014) 142–149.

[14] J.D. Martínez, N. Puy, R. Murillo, T. García, M.V. Navarro, A.M. Mastral, Waste tyre pyrolysis - A review, Renew. Sustain. Energy Rev. 23 (2013) 179–213.

[15] I. Hita, M. Arabiourrutia, M. Olazar, J. Bilbao, J. M. Arandes, and P. Castaño, Opportunities and barriers for producing high quality fuels from the pyrolysis of scrap tires, Renew. Sustain. Energy Rev. 56 (2016) 745–759.

[16] H. Wang, X. Chu, Z.-X. Zhao, X.-S. He, Y.-L. Guo, Analysis of low molecular weight compounds by MALDI-FTICR-MS, J. Chromatogr. B. 879 (2011) 1166–1179.

[17] A. Gani, A. Jameel, A. Khateeb, A.M. Elbaz, A. Emwas, Characterization of deasphalted heavy fuel oil using APPI (+) FT-ICR mass spectrometry and NMR spectroscopy, Fuel. 253 (2019) 950–963.

[18] A.G. Abdul Jameel, N. Naser, G. Issayev, J. Touitou, M.K. Ghosh, A.H. Emwas, A. Farooq, S. Dooley, S.M. Sarathy, A minimalist functional group (MFG) approach for surrogate fuel formulation, Combust. Flame. 192 (2018) 250–271.

[19] S. Dooley, S.H. Won, J. Heyne, T.I. Farouk, Y. Ju, F.L. Dryer, K. Kumar, X. Hui, C.J. Sung, H. Wang, M.A. Oehlschlaeger, V. Iyer, S. Iyer, T.A. Litzinger, R.J. Santoro, T. Malewicki, K. Brezinsky, The experimental evaluation of a methodology for surrogate fuel formulation to emulate gas phase combustion kinetic phenomena, Combust. Flame. 159 (2012) 1444–1466.

[20] J. Alvarez, G. Lopez, M. Amutio, N.M. Mkhize, B. Danon, P. Van Der Gryp, Evaluation of the properties of tyre pyrolysis oils obtained in a conical spouted bed reactor, Energy. 128 (2017) 463–474.

[21] A. Mohan, S. Dutta, V. Madav, Characterization and upgradation of crude tire pyrolysis oil (CTPO) obtained from a rotating autoclave reactor, Fuel. 250 (2019) 339–351.

[22] P.T. Williams, P. Bottrill, Sulfur-polycyclic aromatic hydrocarbons in tyre pyrolysis oil, Fuel. 74 (1995) 736–742.

[23] H. Aydin and C. Ilkılıç, Optimization of fuel production from waste vehicle tires by pyrolysis and resembling to diesel fuel by various desulfurization methods, Fuel. 102 (2012) 605–612.

[24] J. Yongbin, H. Jiejie, W. Yang, Effects of calcium oxide on the cracking of coal tar in the freeboard of a fluidized bed, Energy Fuels. 18 (2004) 1625–1632.

[25] P.T. Cherop, S.L. Kiambi, P. Musonge, Modelling and optimisation of oxidative desulphurisation of oil via central central composite design approach, Green Process Synth. 8 (2019) 451–463.

[26] R.L. Ware, S.M. Rowland, R.P. Rodgers, A.G. Marshall, Advanced chemical characterization of pyrolysis oils from land fill waste, recycled plastics, and forestry residue, Energy Fuels. 31 (2017) 8210–8216.

[27] S.E. Bell, R.G. Ewing, G.A. Eiceman, Atmospheric pressure chemical ionization of alkanes, alkenes, and cycloalkanes, J. Am. Soc. Mass Spectrom. 5 (1994) 177–185.

[28] Y. Han, Y. Zhang, C. Xu, C.S. Hsu, Molecular characterization of sulfur-containing compounds in petroleum, Fuel. 221 (2018) 144–158.

[29] R. Serefentse, W. Ruwona, G. Danha, E. Muzenda, A review of the desulphurization methods used for pyrolysis oil A review of the desulphurization methods used for pyrolysis oil, Procedia Manuf. 35 (2019) 762–768.

[30] D.T. Tran, J.M. Palomino, S.R.J. Oliver, Desulfurization of JP-8 jet fuel: Challenges and adsorptive materials, RSC Adv. 8 (2018) 7301–7314.

[31] M.N. Hossain, H.C. Park, H.S. Choi, A comprehensive review on catalytic oxidative desulfurization of liquid fuel oil, Catalysts. 9 (2019) 1–12.

[32] F. Adam, H. Muller, A. Al-Hajji, A. Bourane, O. Koseoglu, Oxidative desulfurization process monitoring using comprehensive two-dimensional gas chromatography and fourier transform ion cyclotron resonance mass spectrometry, Energy Fuels. 29 (2015) 2312–2318.

[33] K. Ding, Z. Zhong, B. Zhang, Z. Song, X. Qian, Pyrolysis characteristics of waste tire in an analytical pyrolyzer coupled with gas chromatography/mass spectrometry, Energy Fuels. 29 (2015) 3181–3187.

[34] N.A. Dung, S. Wongkasemjit, S. Jitkarnka, Effects of pyrolysis temperature and Pt-loaded catalysts on polar-aromatic content in tire-derived oil, Appl. Catal. B Environ. 91 (2009) 300–307.

[35] J.C. Poveda, D.R. Molina, Average molecular parameters of heavy crude oils and their fractions using NMR spectroscopy, J. Pet. Sci. Eng. 84–85 (2012) 1–7.

[36] A.G. Abdul Jameel, A.M. Elbaz, A.H. Emwas, W.L. Roberts, S.M. Sarathy, Calculation of average molecular parameters, functional groups, and a surrogate molecule for heavy fuel oils using 1H and 13C nuclear magnetic resonance spectroscopy, Energy Fuels. 30 (2016) 3894–3905.

[37] Q. Wang, X. Zhang, S. Sun, Z. Wang, D. Cui, Effect of CaO on pyrolysis products and reaction mechanisms of a corn stover, ACS Omega. 5 (2020) 10276–10287.

[38] J. Udomsirichakorn, P. Basu, P.A. Salam, B. Acharya, Effect of CaO on tar reforming to hydrogen-enriched gas with in-process CO2 capture in a bubbling fluidized bed biomass steam gasifier, Int. J. Hydrogen Energy. 38 (2013) 14495–14504.

[39] B.S. Greensfelder, H.H. Voge, G.M. Good, Catalytic and thermal cracking of pure hydrocarbons: Mechanisms of reaction, Ind. Eng. Chem. 41 (1949) 2573–2584.

[40] N. Naser, A. Gani, A.G. Abdul Jameel, A.-H. Emwas, E. Singh, S.H. Chung, S.M. Sarathy, The influence of chemical composition on ignition delay times of gasoline fractions, Combust. Flame. 209 (2019) 418–429.

[41] A.G. Abdul Jameel, N. Naser, A.H. Emwas, S. Dooley, S.M. Sarathy, Predicting fuel ignition quality using 1H NMR spectroscopy and multiple linear regression, Energy Fuels. 30 (2016) 9819–9835.

[42] Chevron, Diesel fuels technical review, (2007). https://www.chevron.com/-/media/chevron/operations/documents/diesel-fuel-tech-review.pdf (accessed July 7, 2020).

[43] Chevron, Everything you need to know about marine fuels, (2012). file:///C:/Users/Felipe Campuzano/Downloads/everything-you-need-to-know-about-marine-fuels.pdf (accessed March 20, 2020).

[44] Bitumen export group, Bitumen: thechnical data sheet, (2020). http://www.bitumen-export.com/datasheets/bitumen-60-70-technical-datasheet.pdf (accessed July 7, 2020).

[45] J.D. Matínez, M. Lapuerta, R. García Contreras, R. Murillo, T. García, Fuel properties of tire pyrolysis liquid and its blends with diesel fuel, Energy Fuels. 27 (2013) 3296–3305.

[46] International Energy Agency Bioenergy, Biofuels for the marine shipping sector, 2017. https://www.ieabioenergy.com/publications/biofuels-for-the-marine-shipping-sector/.

[47] P.T. Williams, Pyrolysis of waste tyres: A review, Waste Manag. 33 (2013) 1714–1728.

[48] I. H. del Olmo, Valorization of scrap tires pyrolysis oil (stpo) through a 2-stage hydrotreating hydrocracking strategy. Process variables and kinetic modeling, Doctoral Thesis, University of Basque Country (Spain), 2015.

[49] S.M. Sarathy, G. Kukkadapu, M. Mehl, T. Javed, A. Ahmed, N. Naser, A. Tekawade, G. Kosiba, M. Alabbad, E. Singh, S. Park, M. Al Rahidi, H.S. Chung, W.L. Roberts, M.A. Oehlschlaeger, C. Sung, A. Farooq, Compositional effects on the ignition of FACE gasolines, Combust. Flame. 169 (2016) 171–193.

[50] IEA Advance Motor Fuels, Diesel and Gasoline, (2019). https://www.iea-amf.org/content/fuel_information/diesel_gasoline (accessed March 25, 2020).

[51] W.H. Brown, T. Poon, Introduction to organic chemistry, 6th ed., Wiley, 2016.

Chapter 5. Combustion characteristics of tire pyrolysis oil and its distillate fractions

In addition to illustrating the structural characteristics of TPO and its resulting distillate fractions, the study of their combustion behavior is of great importance for their efficient utilization in thermal systems. Up until now, the investigations reported in the scientific literature regarding this application have mainly aimed at determining basic combustion properties and emissions in internal combustion engines, boilers, and furnaces [1–5]. Nevertheless, the use of these units to study the combustion features of TPO makes it difficult to accurately control of all the experimental parameters. Thus, the obtained results may be influenced by certain variables which are hard to control during the process. Accordingly, a dependency on the experimental setup is introduced, which presents uncertainty regarding whether the combustion behavior is entirely attributable to the fuel, or to characteristics of the related processes [6].

Therefore, fundamental combustion studies where all the relevant variables can be well-characterized isolating the influence of the thermal device are needed in order to truly understand the combustion features of TPO. In this manner, the obtained combustion performance can be completely associated with the nature and properties of the fuel. The investigation into TPO's (and its resulting distillate fractions') basic combustion properties thus aids in the design/modification of an appropriate combustor, as well as in the emission control system. The acquisition of such fundamental knowledge is key in overcoming the current technical and environmental obstacles involved in the deployment of TPO in commercial combustion applications.

In previous chapters, TPO, along with its distillate factions, were studied in-depth in order to elucidate their complex chemical and fuel properties. However, information concerning the real-time evolution of gases and reaction tendencies (*i.e.* fuel decomposition rates) during combustion has not yet been discussed. Accordingly, the present chapter aims to present novel insights by conducting fundamental combustion studies in order to uncover the combustion features of TPO and its distillate fractions. The obtained information can be used as input experimental data in order to validate oxidation kinetic models needed to design and optimize combustion systems.

In this regard, in the first part of this chapter, the combustion characteristics of the crude TPO and TPO[CaO] were studied by conducting thermogravimetric (TG) and differential thermogravimetric (DTG) analyses at different heating rates and a wide temperature range. TG and DTG were conducted under non-isothermal conditions in order to continually investigate the physical and chemical variations occurring in both samples. The TG analyzer used was coupled to a Fourier Transform Infrared (FT-IR) spectrometer, which allows for the real time observation of the evolved gases' compositional (functional group) variation during the oxidation process. Finally, ignition features of TPO and TPO[CaO] such as the ignition delay time (IDT) and the derived cetane number (DCN) were determined by means of the ignition quality test (IQT).

In the second part of this chapter, a comprehensive study into the oxidation characteristics of the light fraction of TPO[CaO] obtained by distillation (named in this chapter TPO[CaO]$_{Light}$) was carried out by conducting combustion experiments in a jet

stirred reactor (JSR) under a wide range of experimental conditions (*i.e.* temperatures and equivalence ratios). These types of reactors have proven to be well adapted for gas phase kinetic studies [7]. TPO[CaO]$_{Light}$ was chosen since it is the most abundant (40 vol.%) and it presents the lowest sulfur content among all of the distillate fractions. A surrogate fuel for TPO[CaO]$_{Light}$ was also formulated to facilitate future research into its combustion chemistry. Likewise, this surrogate fuel was tested in the JSR under the same experimental conditions used for TPO[CaO]$_{Light}$ in order to compare the reaction tendencies (*i.e.* fuel consumption rate) and the formation of main intermediate species. In this manner, it was possible to confirm if the proposed surrogate was a proper representation of TPO[CaO]$_{Light}$.

5.1 Materials and methods

5.1.1 Thermogravimetric analysis

The TG tests were conducted using TPO and TPO[CaO] at three different heating rates (5, 10, and 20 °C/min) in air atmosphere (50 mL/min) between 30 and 700 °C. The amount of sample used for each experiment varied between 15 and 23 mg. All experiments were conducted in a Netzsch TG 209 F1Iris TG analyzer. Prior to each experiment, a blank test was performed with the same crucibles used during the TG analysis in order to correct the buoyancy effects. Evolved gases from the TG were directed to the IR cell through a heated line at 190 °C. The IR cell was maintained at 200 °C to avoid the condensation of volatiles during the experiments. The FT-IR spectra was acquired with a Thermo Scientific Nicolet iS10 connected to iZ10 interface, equipped with a deuterated triglycine sulfate (DTGS) detector and KBr beamsplitter. The FT-IR was aligned, and the background data was amassed with a resolution of 4 cm^{-1}. A total of 16 spectral lines within the region of 4000–500 cm^{-1} were acquired. During the TG ramp, FT-IR spectra were collected at 25 s interval. The characteristics of the IR bands selected for this study and their assignments may be found in Appendix D, Section D1.

5.1.2 Ignition quality test: Ignition delay time

The ignition quality of the tested fuels was evaluated by measuring their IDT using an IQT (Advanced Engine Technology Ltd., Ontario, Canada). The IQT is a constant volume combustion chamber, which is the standard equipment used to measure the derived cetane number (DCN) of fuels according to the standard procedure ASTM D6890-07b. Here, liquid samples are injected by a pintle nozzle into a pre-heated, pressurized air chamber. Each run involves 32 main injection events, followed by 15 pre-injections, to create a stable environment for the main injection. The time interval between the sample injection and the start of ignition is referred to as the IDT. The average of 32 measurements is denoted as the IDT. The experiments were conducted at two different temperature levels: (*i*) high temperature (548 ºC) and (*ii*) low temperature (478 ºC). The DCN of each fuel was obtained from these experiments. Samples were tested three times to ensure repeatability.

5.1.3 Surrogate fuel formulation for the light fraction of tire pyrolysis oil

In this study, a surrogate fuel for TPO[CaO]$_{Light}$ was formulated following the methodology presented in Figure 5.1. Similar to transportation fuels (gasoline, diesel, etc.), TPO[CaO]$_{Light}$ (named as real fuel) is a complex mixture of hydrocarbons containing

hundreds of individual molecules, as described in Chapter 4. A surrogate fuel (a mixture of two or more pure components) serves to mimic some target fuel physicochemical (*i.e.* density, average molecular weight, distillation characteristics, viscosity, surface tension, H/C ratio, heat of combustion, etc.) and combustion (*i.e.* laminar flame speed, IDT, sooting tendencies, pollutant formation, etc.) properties. The formulation of this surrogate allows for the development/adjustment of detailed kinetic models that help to simulate, design, and optimize combustion systems. In addition, the use of a small number of fuel components in a surrogate fuel ensures that the chemical composition is well-controlled, which in turn helps to increase the reproducibility of experiments and reduce the computational cost associated with numerical modelling [8].

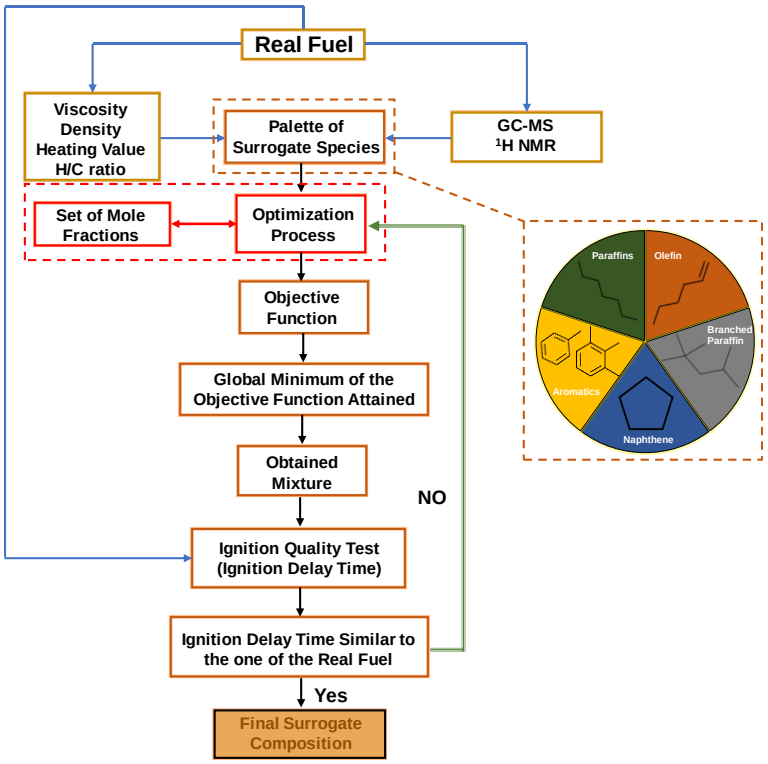

Figure 5.1. Surrogate fuel formulation methodology

According to Violi *et al*. [9], the selection of the molecules that make up the surrogate fuel (*Palette of Surrogate Species*) is based on balancing the three following aspects: (*i*) feasibility (detailed kinetic mechanism available and a limited carbon number), (*ii*) similarity (volatility, sooting tendency, combustion properties, etc.)), and (*iii*) cost. In this work, the *Palette of Surrogate Species* (Figure 5.2) was selected with the aim of fulfilling the following requirements: (*i*) types of hydrocarbon molecules present in TPO[CaO]$_{Light}$ (*i.e.* paraffinic, aromatic, naphthenic, olefinic, branched paraffin molecules), (*ii*) combustion characteristics of TPO[CaO]$_{Light}$ (*i.e.* molecules with similar RON number), and (*iii*), the availability of oxidation kinetic mechanisms in the literature for the selected molecules.

Once the *Palette of Surrogate Species* was established, the next step in the surrogate formulation was to define which target properties of the real fuel it must mimic, as it is harder to mimic all properties in a real fuel. In this regard, the fuel target properties chosen for this particular surrogate formulation were defined as: (*i*) physicochemical properties (density and heating value); (*ii*)

structural properties (type of hydrogen atoms present in the real fuel, which were determined by ^{1}H NMR and the H/C ratio); and (*iii*) combustion properties, namely IDT. Prior to conducting these steps, a complete understanding of the physicochemical properties of the target fuel was required, which was previously accomplished and discussed in Chapter 4. As a result of this process, the molecules selected for the surrogate fuel were: n-heptane (paraffin), toluene and trimethylbenzene (aromatics), 1-hexene (olefin), cyclopentane (naphthene), and isooctane (branched paraffin). Some physical properties for these molecules are listed in Table 5.1. According to GC-MS, aromatics contained in TPO[CaO]$_{Light}$ are mainly in the form of substituted rings, instead of single rings. Thus, toluene and trimethylbenzene were selected for the surrogate, rather than benzene.

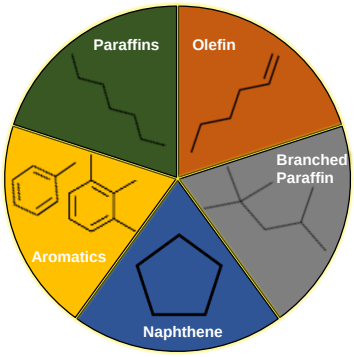

Figure 5.2. *Palette of Surrogate Species*

Table 5.1. Properties of the selected molecules

Molecule	Density kg/m^3	MW g/mol	HHV kJ/kg	Viscosity cSt	H/C	RON	MON
n-Heptane	684.00	100.21	44,566	0.51	2.29	0	0
Toluene	870.00	92.14	42,168	0.55	1.14	118	103
Cyclopentane	751.00	70.10	46,500	0.55	2.00	100	84.9
1-Hexene	673.00	84.16	44,506	0.39	2.00	73.6	64.5
124-TMB	876.10	120.19	42,283	0.64	1.33	110	101
Isooctane	690.00	114.22	47,777	0.60	2.25	100	100
TPO[CaO]$_{Light}$	**795.47**	**156.4**	**41.91**	**0.66**	**1.70**	**99**	**--**

Upon defining a *Palette of Surrogate Species* and the fuel target properties, an optimization process was conducted. The main objective of the optimization process was to define the composition of the overall surrogate fuel (in terms of the mole fraction) based on the molecules presented in the *Palette of Surrogate Species* (see Figure 5.2). The optimization process was carried out via an objective function, which consisted of calculating the sum of errors between real and surrogate fuel properties. Once the minimum of the objective function was found (minimum total error), the IDT of the obtained mixture was measured and compared with that of the real fuel. The IDT of both the real and the surrogate fuels was determined following the same methodology described in Section 5.1.3. The optimization process was run several times until a mixture with a similar IDT to that of the real fuel was achieved, while keeping the total error as low as possible. The physicochemical properties of the final surrogate fuel (density, viscosity, and heating value) were determined following the same experimental procedures specified for the real fuel in Chapter 4.

5.1.4 Oxidation characteristics of the light fraction of tire pyrolysis oil

Oxidation experiments using the jet stirred reactor (JSR) with both the real and the surrogate fuels were performed in a spherical reactor (76 cm^3) made of fused silica (to prevent wall reactions), as shown in Figure 5.3. Four nozzles (i.d. 0.3 mm) acted as the reactor inlets to achieve perfect mixing. The mixing performance was verified experimentally and reported in previous works [10]. A more detailed description regarding the characteristics and the design criteria for the JSR can be found in the literature [11]. The JSR is a type of ideal continuously stirred-tank reactor, and it was chosen for this study due to its suitability for gas kinetic studies.

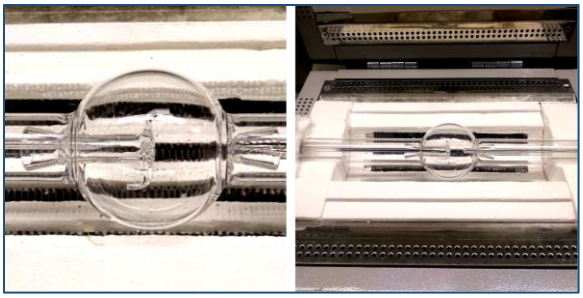

Figure 5.3. Jet stirred reactor

Such studies consist of recording the evolution of reactant species conversions as well as the mole fractions of the reaction products as a function of different parameters, including reaction temperature, residence time, pressure, and composition of the inlet gas. Among others, one of the main advantages of the JSR relies on the efficient mixing of the gas phase, which provides an identical and homogeneous composition of the outlet gas as that of the gas inside the reactor [7]. The experimental results from these types of studies can be used to validate detailed kinetic mechanisms which aim to model the combustion chemistry of real fuels. These detailed mechanisms, which usually include thousands of different reactions, are then reduced (known as reduced mechanisms) to be used in computational fluid dynamics (CFD) for the design/optimization of combustion systems. Such computational studies have not yet been conducted for TPO[CaO]$_{Light}$. Thus, the results of the present investigation may be used as precursors for initiating the development of computational studies aimed at better understanding the combustion mechanism of this fuel.

A schematic diagram of the experimental setup is presented in Figure 5.4. Five main components can be identified: (1) syringe pump, (2) multi-gas controller, (3) electrical heating furnace, (4) the JSR, and (5) gas chromatographs.

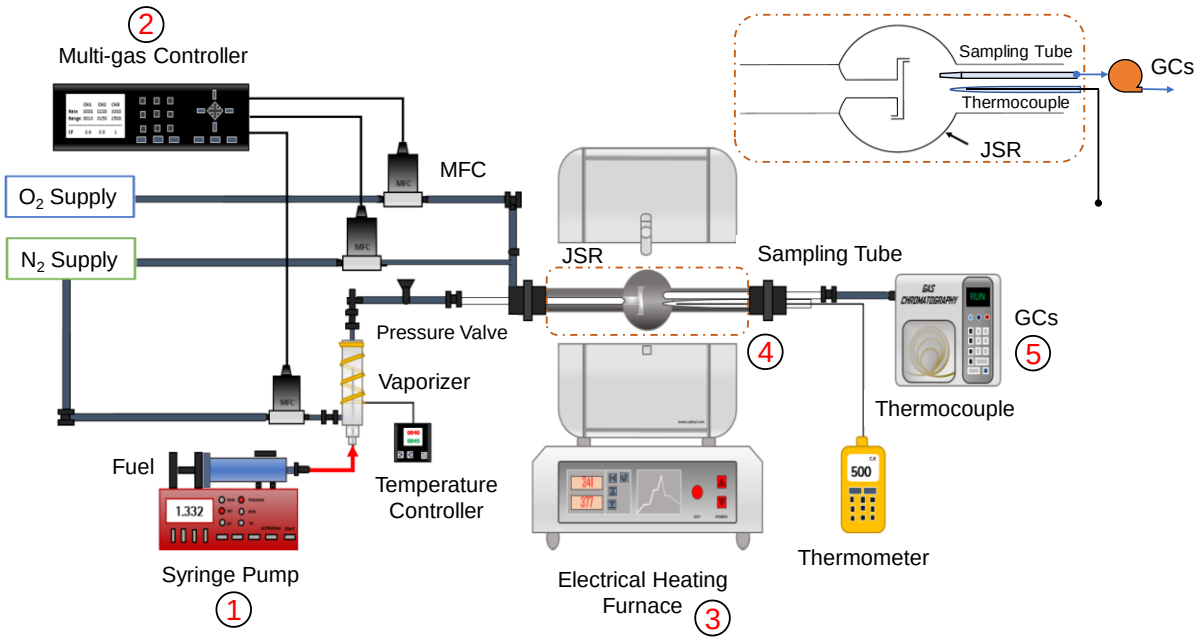

Figure 5.4. JSR experimental setup (Adjusted from [12])

During the experiments, fuel was vaporized at 210 ºC (30 ºC higher than its boiling point) and then diluted with N_2, which also acted as a carrier gas to introduce the fuel in gas phase into the JSR. The syringe pump controlled the mass flow rate of the fuel, depending on the experimental conditions. A K-type thermocouple placed inside the reactor was used to monitor the reaction temperature. The gas flow rates (O_2 and N_2) were controlled with as MKS mass flow controller and adjusted with the reactor temperature to achieve a fixed residence time inside the reactor. The oxidation products were sampled using a sonic-throat gas sampling probe located at the outlet of the reactor and connected to a mechanical pump. The pressure and temperature drop across the orifice was sufficient to quench the reaction in the sample transfer line. The gas sample was analyzed online using two gas chromatographs (GCs): an Agilent Refinery Gas Analysis (RGA) and an Agilent 7890B, which was equipped with an Agilent DB-1 column (15 mm × 0.32 mm) for separation and an FID to detect PAHs. The specific procedures are described in Appendix D.

The experimental setup was initially calibrated by conducting oxidation experiments with pure n-heptane, followed by comparing the reaction tendencies (fuel consumption and species formation) with the information available in the literature [13]. Once the experimental setup was calibrated, oxidation experiments were conducted with the real fuel at lean and stoichiometric conditions (equivalence ratios of 0.2, 0.5, and 1.0). The concentration of the fuel in the mixture and the residence time were fixed at 0.3 vol. % and 1 ms, respectively. It is important to clarify that If the equivalence ratio (ER) is equal to one, the combustion is stoichiometric. If ER is <1, the combustion is lean with excess air, and if ER is >1, the combustion is rich with incomplete combustion. The experiments were conducted in a temperature range between 426.85 °C and 926.85 °C. Thereafter, the surrogate fuel was tested under the same experimental conditions, and the reaction tendencies and formation of intermediate species were compared to those of the real fuel. The experimental conditions are reported in Appendix D.

5.2 Results and discussions

5.2.1 Oxidation characteristics of tire pyrolysis oil

The combustion of TPO and TPO[CaO] is a complex process due to the wide variety of components, as described in previous chapters. Similar to other fuels, the oxidation process involves a large number of parallel reactions at any given moment due to the highly distributed and multicomponent nature of the feedstocks (Chapter 4). Figure 5.5 shows the TG and DTG data obtained for TPO and TPO[CaO] at three different heating rates: 5 °C/min, 10 °C/min, and 20 °C/min.

As observed, the oxidation process starts at 30 °C with the initial degradation/evaporation of low molecular weight hydrocarbons (highly volatile compounds), and finishes at approximately 680 °C, when the heavy compounds (low volatility and highly condensed aromatic structure) are completely oxidized. For both TPO and TPO[CaO], the main decomposition occurs in a temperatures range between 30 and 400 °C. Then, the combustion process may be dominated by the oxidation of heterogeneous carbonaceous residues (*i.e.* coke), which is almost completed at 680 °C, after which there is no noticeable mass loss [14]. It can be seen in Figure 5.5 that, as the heating rate increases, the thermal degradation of both samples is shifted to

a higher temperature. The shift in the mass loss profile to higher temperatures occurs due to a stronger thermal hysteresis effect coupled with an increased difficulty in reaching a thermal equilibrium state [15,16].

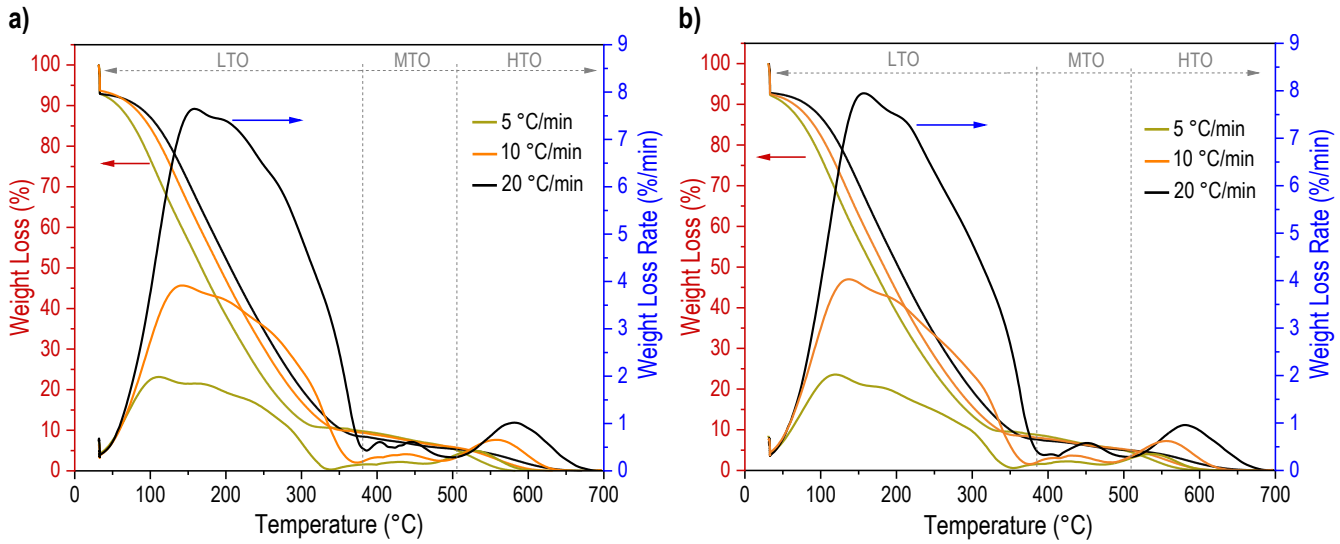

Figure 5.5. Oxidation characteristics at different heating rates; **a)** TPO and **b)** TPO[CaO]

According to the resulting curves, three sequential regions of different reaction mechanisms are identified in the oxidation process of TPO and TPO[CaO]. The first region identified in the DTG curves extents up to ~ 390 °C, which is known as low temperature oxidation (LTO). In this region, more than 90 wt.% of both TPO and TPO[CaO] is oxidized, and the maximum decomposition/devolatilization rate occurs at temperatures around 150 °C, depending on the heating rate. In the LTO oxidation region, the rate of weight loss is similar for both fuels in the experimental domain considered in this study, yet slightly higher for TPO[CaO]. This can be associated with the structural differences caused by the addition of CaO during the pyrolysis of WT as discussed in Chapter 3 and Chapter 4, which can lead to higher transformation/volatilization rates. For instance, it was found that the addition of CaO during pyrolysis decreased the viscosity as well as the final distillation point of the resulting oil (TPO[CaO]). This was linked to the catalytic activity of CaO, which led to compositional and structural changes including, among others, the increase in protonated aromatic compounds, reduction in the average length of paraffinic chains attached to aromatic rings (from 5.15 to 2.78 carbon atoms), etc., as explained in Chapter 4. These compounds could be devolatilized more easily, which was reflected as an increase in the weight loss rate.

In agreement with these results, previous works reported in the literature for heavy fuel oil [17], medium oil [14], light oil [14] combustion have suggested that the LTO region is typically extended up to 380 °C. Despite the complexity of the chemistry involved, the early stage of this region seems to be mainly dominated by hydrocarbon evaporation (which exerts a significant influence on the wight loss rate) and oxygen addition to form hydroperoxides (*ROOH*) [14,17–19]. At the later stage of the LTO, isomerization and decomposition reactions of the formed hydroperoxides are thought to be the main reactions. According to these works, the overall reaction pathways in the LTO region can be seen in Equation 5.1 – 5.2, where RH is any possible aliphatic hydrocarbon or the aliphatic chains attached to naphthenic rings or aromatic rings in the molecule of other components

contained in TPO or TPO[CaO]. The $LTO_{Residue}$ is related to the oxidized products (*i.e.* ketones, alcohols, aldehydes, and carboxylic acids) caused by isomerization and decomposition reactions, along with their possible condensation products. It has been reported that, in this stage, saturates and light aromatics compounds are regarded as the main contributors to the weight loss rate [17].

$$RH + O_2 \rightarrow ROOH \quad \textbf{(5.1)}$$

$$ROOH \rightarrow LTO_{Residue} + CO_2 + CO + H_2O \quad \textbf{(5.2)}$$

After the LTO region, at temperatures higher than 390 °C, the feedstock decomposition continues, and middle-temperature oxidation (MTO) takes place approximately between 400 and 500 °C. In this second zone, around 5 wt.% of both TPO and TPO[CaO] was oxidized and the $LTO_{Residue}$ obtained from the previous oxidation stage (LTO) may have undergone various oxidative cracking reactions to form coke [17,20]. Previous works have reported that such reactions usually include: (*i*) breakage of C-C bonds and C-heteroatoms bonds, (*ii*) rupture of aliphatic and aromatic alkyl side chains, and (*iii*) hydrogenation of aromatic compounds [21]. According to Zhao *et al*. [17], the overall reaction occurring in this region can be written as shown in Equation 5.3, where aromatics and resins seem to be the main contributors to the mass loss rate.

$$LTO_{Residue} + O_2 \rightarrow Coke + CO_2 + H_2O + CO + Hydrocarbons \quad \textbf{(5.3)}$$

Afterwards, the combustion process goes into the high-temperature oxidation (HTO) region and the main reaction which takes place is governed by the combustion of coke to form CO_2 and H_2O (see Equation 5.4) [18]. The HTO roughly occurs in the temperature range between 500 and 680 °C, where the remaining fuel (5 wt.%) is completely oxidized for both TPO and TPO[CaO]. No residual mass left after 680 °C was observable, indicating that all of the compounds present in both samples were completely oxidized. In the HTO region, asphaltenes are the main contributor to the mass loss rate [17].

$$Coke + O_2 \rightarrow CO_2 + CO + H_2O \quad \textbf{(5.4)}$$

Comparing these three oxidation regions, the LTO one may be considered as the main mass loss region. This may be associated with the significant presence of volatile organic compounds (*i.e.* light aromatics) and alkanes (paraffins) in TPO and TPO[CaO] as previously observed by means of ^{1}H and ^{13}C NMR in Chapter 4. These compounds are more vulnerable to evaporation at low temperatures than highly aromatic structures (*i.e.* DBE > 20) as those detected by means of FT-ICR MS (Chapter 4). Comparing this pattern with previous investigations reported in the literature, the thermal degradation of TPO and TPO[CaO] is similar to that of light crude oil [14]. The light crude oil combustion is dominated by a severe evaporation in the LTO interval (mass loss of more than 90 %), and small amount of coke formation in the MTO accounting for a very low mass loss, usually between 2 – 3 %. Already in the HTO zone, the coke combustion process leads to a mass loss of 7 – 8 %. These trends coincide with the ones found in this work for TPO and TPO[CaO]. Light crude oil presents an API gravity between 33 – 53 [22] and a final distillation point around 550 °C [23] (depending on the origin), which are also similar to those of TPO and TPO[CaO] (Chapter 3). Altogether, these properties could imply that TPO and TPO[CaO] may be comparable, to some extent, with this type of oil.

As a general overview, Figure 5.6 provides a possible description of the temperature ranges in which various types of oxidation reactions exert a controlling influence. Here, reactions that are generally restricted to the vapor phase are shown in red. Pyrolysis/coking is also displayed to clarify the temperature at which the liquid-phase tends to disappear. Considering that pyrolysis eventually converts the oil to gaseous or solid phases, the oil oxidation reaction becomes irrelevant above these temperatures [18]. It is worth mentioning that these temperature ranges are approximate, and they can change depending on the hydrocarbon composition. More insights regarding the occurrence of these reaction pathways was obtained with the FT-IR results of the evolved gases, which will be explained later. In Figure 5.6, NTC refers to the Negative Temperature Coefficient.

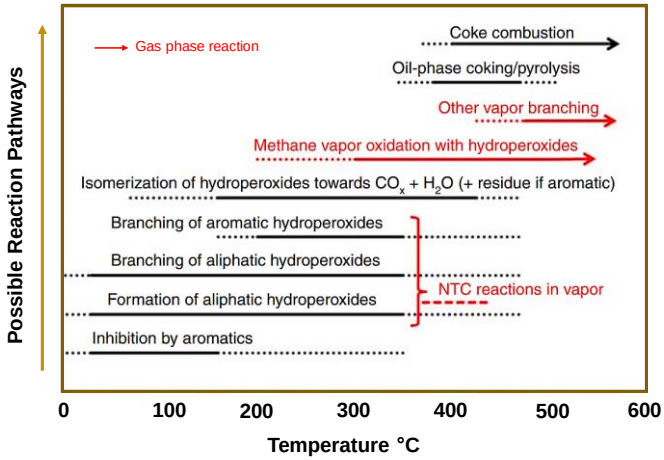

Figure 5.6. Typical temperature ranges over which different reactions may exert control (taken from [18])

Table 5.2 summarizes the combustion characteristics of TPO and TPO[CaO], including the temperature of the decomposition stages described previously, as well as the initial decomposition temperature (T_{in}), peak temperature (T_{max}), and burnout temperature (T_b). T_{in} represents weight loss onset and is defined as the temperature at which the weight loss rate (%/min) reaches 1 %/min. T_{max} is the temperature at which the rate of reaction (weight loss rate) is maximum. T_b denotes the temperature at which the fuel oxidation is completed, as it is taken as the point when the weight loss rate falls to 1 %/min after crossing the T_{max} [24]. As aforementioned, knowledge of these temperatures for TPO and TPO[CaO] helps to identify the different stages related to the combustion process for further combustor design and/or modification [15].

Table 5.2. Combustion characteristics of TPO and TPO[CaO]

Characteristic	Heating rate					
	5 °C/min		10 °C/min		20 °C/min	
	TPO	TPO[CaO]	TPO	TPO[CaO]	TPO	TPO[CaO]
LTO stage (°C)	50 - 340	50 - 350	50 - 375	50 - 375	50 - 390	50 - 390
MTO stage (°C)	340 - 460	350 - 475	375 - 490	375 - 490	390 - 505	390 - 505
HTO stage (°C)	460 - 580	475 - 580	490 - 625	490 - 625	505 - 680	505 - 680
T_{in} (°C)	64	68	63	59	61	59
T_{max} (°C)	112	120	145	138	163	159
T_b (°C)	274	282	337	340	369	372

5.2.2 Evolved gases in the combustion process of tire pyrolysis oil

Aside from the different stages that occur during the oxidation process, information regarding the evolution of intermediate species during the oxidation of TPO and TPO[CaO] provides important insights to understand their combustion process. Figure 5.7 shows three-dimensional FT-IR spectra of the gases evolved during the oxidation of TPO and TPO[CaO] in a temperature range between 50 and 700 °C at 20 °C/min. The spectra are represented in terms of absorbance (associated with the vibrational modes of the various functional groups and bonds present in the oxidation products) versus the wavenumber. Moreover, the temperature axis allows for easily tracking the evolution of certain species with temperature changes. It is observed that, as temperature increases, the intensity of the absorption peaks at different wavenumbers (cm^{-1}) also increases as a result of the higher rate of gas formation. Beyond the maximum peak absorption intensity, a further increase in temperature results in a reduction in the intensity of such peaks, as most of the fuel has been already consumed.

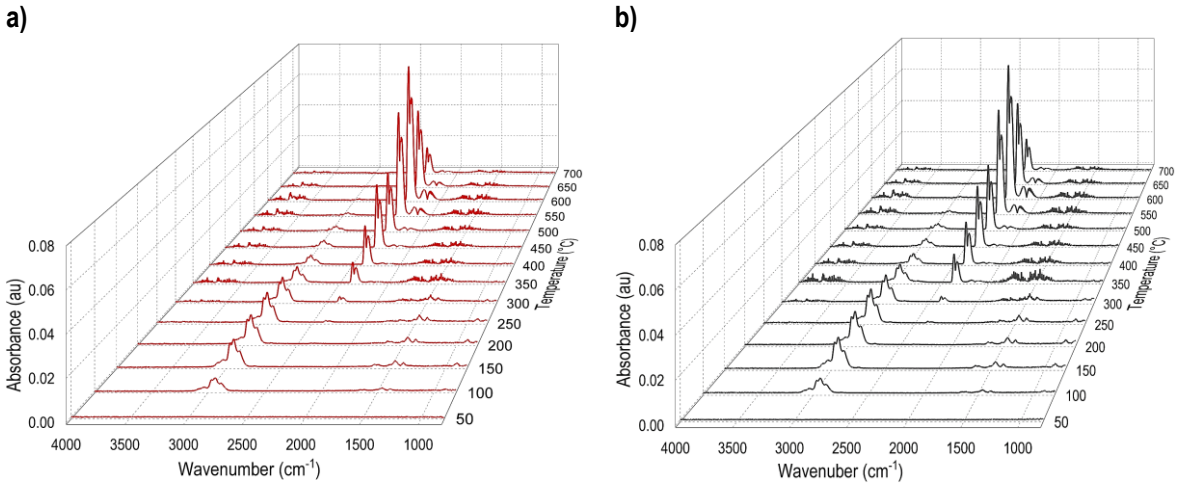

Figure 5.7. FT-IR spectral plot of the gases evolved during the combustion of **a)** TPO and **b)** TPO[CaO], at 20 °C/min

The characteristics of the IR bands selected to interpret the FT-IR data and their assignments have been described in Table D1, Appendix D. Peaks in the band of 4000 – 3500 cm^{-1} were associated with the stretching of O – H bonds, which denote the formation of water vapor (H_2O). Peaks in the region of 2400 - 2224 cm^{-1} and 2180 - 2108 cm^{-1} were linked to the occurrence of asymmetric and symmetric stretching of C = O bonds, respectively, which correspond to the presence of CO and CO_2 in the flue gases. The decomposition of nitrogen- and sulfur-containing compounds was related to the evolution of NO (1762 cm^{-1}) and SO_2 (1342 cm^{-1}) in the flue gases. In addition, peaks arising in the IR spectrum within the 3130 – 2780 cm^{-1} wavenumber range are linked to various hydrocarbon compounds (*i.e.* alkanes, alkenes and aromatics).

The release of these hydrocarbons was initially observed at approximately 100 °C, at which the mass loss appeared. Following that, the absorbance of hydrocarbons exhibited a quick increase and achieved a maximum peak at 250 °C. The signal of H_2O CO_2, CO, NO, and SO_2 appeared at temperature around 300 °C, which suggests the onset of the oxidation process of some hydrocarbons, most likely saturates [17]. It is noticed that, in the temperature range between 50 and 350 °C (LTO interval), the absorbance of hydrocarbons was considerably higher than that of H_2O CO_2, CO, NO, and SO_2. This phenomenon hints the

evaporation of hydrocarbons and the rupture of weak chemical bonds in agreement with the weight loss at the LTO stage, as mentioned before ($ROOH \rightarrow LTO_{Residue} + CO_2 + CO + H_2O$). As the temperature increases, the absorbance of CO_2, H_2O, CO, NO, and SO_2 rises as well, reaching the maximum level at 600 °C corresponding to the HTO region ($Coke + O_2 \rightarrow CO_2 + CO + H_2O$).

In order to illustrate the IR band assignments, Figure 5.8 shows the FT-IR spectra at 600 °C (HTO) and 20 °C/min, where the maximum intensities were observed. As noticed, CO_2 is the main species formed during the combustion process of both TPO and TPO[CaO] at this temperature. The CO_2 intensities are around twenty times higher than that of CO and thirty times higher than the other species (SO_2 and NO). As expected, the coke formed in the LTO and MTO stages is combusted releasing considerable amount of CO_2 (Equation 5.4), as also reported by Yuan *et al*. [14].

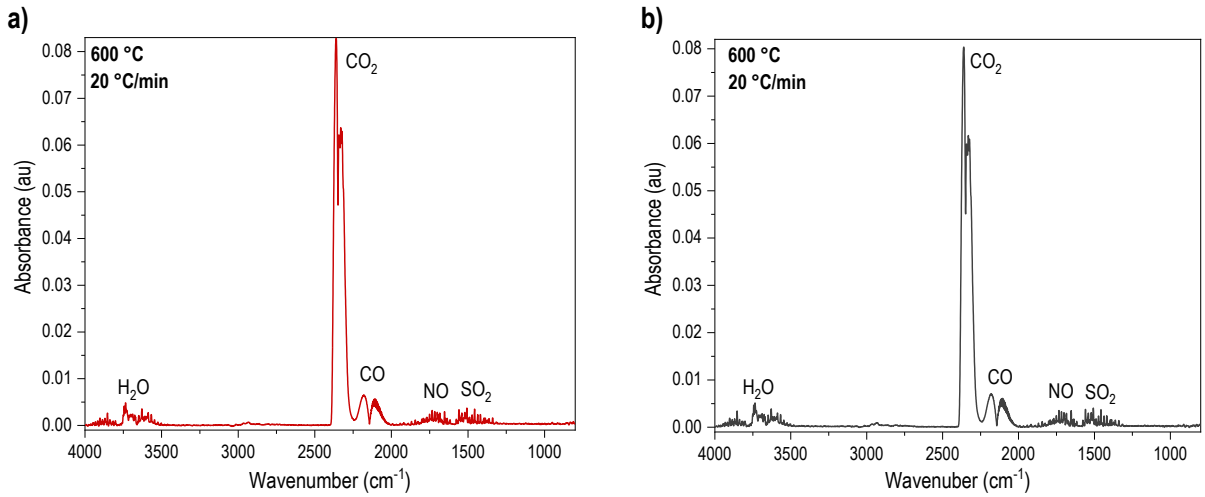

Figure 5.8. FT-IR spectra of the evolved gases showing the various assignments during combustion of **a)** TPO and **b)** TPO[CaO]

For a better visualization, Figure 5.9 shows the evolution of CO_2, CO, SO_2 and NO (considered as main pollutants) during the combustion of TPO and TPO[CaO] at different temperatures and heating rates. The magnitude of the absorbance peaks is reported in terms of relative abundance: absorbance/mg of either TPO or TPO[CaO]. Aside from getting insight for understanding the combustion chemistry of TPO and TPO[CaO], identifying the evaluation of these species contributes to the establishment of operational parameters geared at emission reduction without affecting the efficiency of the combustion process.

For both fuels, the formation of CO_2 gradually increases until around 250 °C (within the LTO), followed by a more rapid increase between 400 and 500 °C (MTO region); this formation phenomenon is likely due to the quick oxidation of aliphatic hydrocarbon or the aliphatic chains attached to naphthenic rings or aromatic rings in the molecule of other components contained in TPO or TPO[CaO]. As reported in previous works these aliphatic chains are more easily oxidized in this temperature interval [20]. The highest peaks are found in the HTO region at 530 °C, 560 °C, and 590 °C at 5 °C/ min, 10 °C/min, 20 °C/min, respectively. Even though the maximum mass loss rate takes place in the LTO and MTO regions, most of the species formed (*i.e.* coke) in these two regions are oxidized in the HTO region, which results in the highest CO_2 formation between 550 and 650 °C, depending

on the heating rate. Thereafter, the CO_2 peak falls rapidly, indicating the end of the combustion process since more than 95 % of the fuel has already been oxidized. These trends in CO_2 formation confirm the reactions occurring in each oxidation region, which were displayed earlier in Equations 5.1 - 5.4.

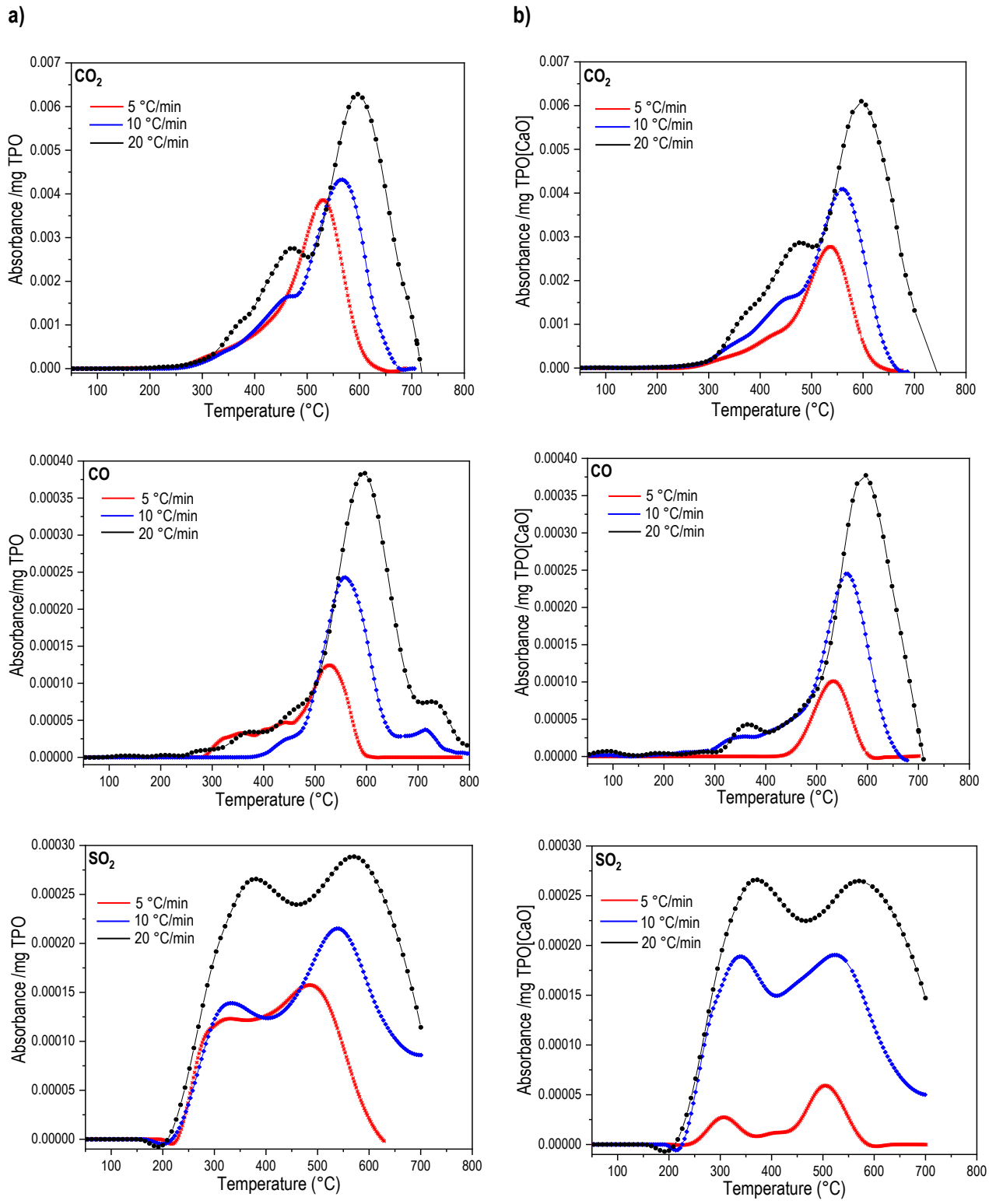

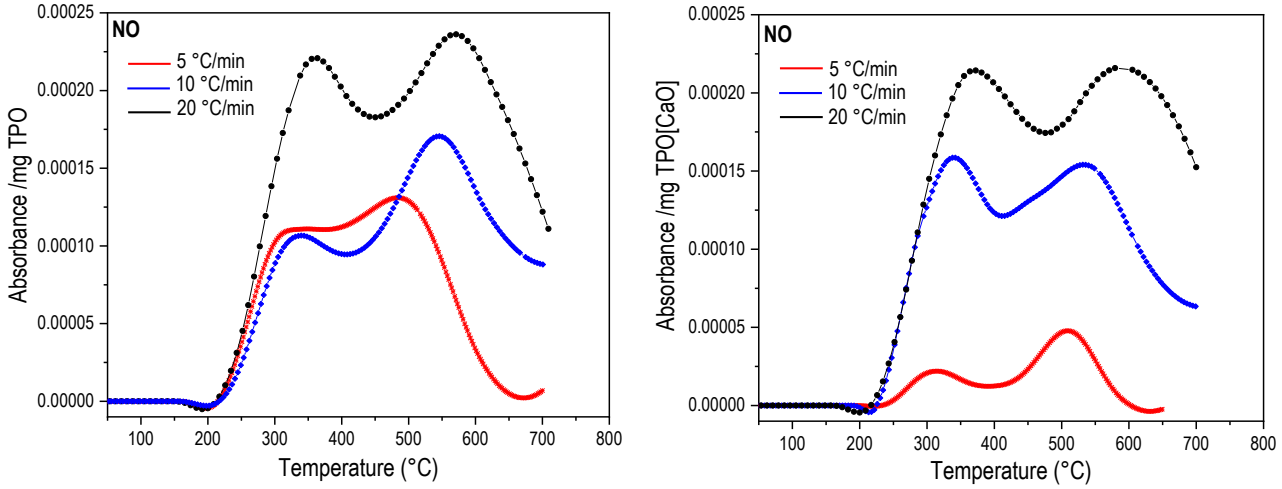

Figure 5.9. Evolution of pollutant gases (CO_2, CO, SO_2, NO) during the combustion process of **a)** TPO, and **b)** TPO[CaO]

In the case of CO, this compound is not clearly detected until the temperature reaches 280 ºC, when the alkyl side chains containing carbonyl groups (–CHO) likely undergo decarboxylation reactions [17]. The CO formation increases drastically beyond 400 ºC, which can be attributed to secondary reactions, including thermal cracking of the heavy compounds released from the fuels in the MTO region as mentioned previously. The maximum peaks of CO are found at 520 °C, 560 °C, and 580 °C at 5 °C/ min, 10 °C/min, 20 °C/min, respectively.

In addition, the formation of SO_2 increases gradually at temperatures around 250 ºC, and two main peaks are observed at 300 – 400 ºC and 490 – 580 ºC, approximately, depending on the heating rate for both TPO and TPO[CaO]. The obtained signal of SO_2 is slightly lower in the case of TPO[CaO] due to its lower sulfur content, as described in previous chapters. In addition, the formation of SO_2 during the combustion process of TPO[CaO] seems to be more sensitive to changes in the heating rate in comparison to TPO. The formation of sulfur-containing species during the combustion of TPO and TPO[CaO] is one of the main limitations of their implementation in practical combustion systems due to their detrimental effect on the environment and human health. As discussed in Chapter 4, sulfur-containing compounds present in TPO and TPO[CaO] are mainly in the form of S_1, which was associated with structures of thiophenic or thiolic nature. As a general rule, 90 % or more of these sulfur-containing compounds are transformed into SO_2 during combustion [25]. A small percentage can be further oxidized to form SO_3. When these compounds are released into atmosphere, they can react to form small particles, which not only contribute to particulate matter pollution, but can also penetrate into the lungs and cause public health problems [26].

As reported in Chapter 3, TPO and TPO[CaO] also present a nitrogen content of 1.32 wt.% and 1.23 wt.%, which may act as a precursor for NO during combustion. Nitrogen-containing compounds are mainly in the form of hydrocarbons containing N, N_2, N_2O, and NO. It has been reported that, during volatilization, organically bonded nitrogen is released as intermediate species, which eventually decompose into radicals such as HCN and NH_3 [27]. Such radicals may react with other species (*i.e.* OH and O) to form NO. In the case of TPO and TPO[CaO], and similar to SO_2, the formation of this compound starts at 250 ºC, and two

maximum peaks are found at 300 – 370 °C and 500 – 600 °C, approximately, depending on the heating rate. It is observed in Figure 5.9 that the absorbance increases as heating rate increases for all evolved gases. This is attributed to the fact that, at higher heating rates, higher rates of gas formation occur. Given the constant IR cell volume and the constant carrier gas flow rate, the higher rates of gas released result in a higher gas occupancy in the cell in a given interval of time. This higher gas volume occupancy finally results in a higher intensity (absorbance) of the peak.

Overall, the knowledge of pollutant formation (CO_2, CO, SO_2, and NO) coupled with the elucidation of the fuel decomposition tendencies described above can be very useful for further investigations. Namely, these insights may be used to formulate TPO/TPO[CaO] surrogate fuels, which may in turn be used to develop detailed chemical kinetic models. An addition to enhancing the understanding of the TPO and TPO[CaO] combustion chemistry, these models may be employed in the modification/design/optimization of practical combustion systems.

5.2.3 Ignition delay time of tire pyrolysis oil

Table 5.3 reports the IDT at high (548 ºC) and low (478 ºC) temperatures, by means of IQT. Ignition quality is defined by the ability of the fuel/air mixture to undergo a series of auto-oxidation reactions that leads to ignition. Fuel ignition quality is affected by several processes which include, among others, fuel spray, vaporization, mixing, and chemical reactivity. All of these parameters ultimately depend on the molecular structure of the fuel. The IDT of a fuel has been reported to be governed by the low temperature combustion chemistry and may define the anti-knock tendency of fuels used in spark-ignition engines or the cetane number of fuels used in compression ignition engines [28].

At low temperature, DCN was found to be 14.3 and 19.9, while at high temperature, such values were found to be 19.2 and 20.6 for TPO and TPO[CaO], respectively. The resulting IDT of both samples suggests a low DCN, in contrast to diesel fuels which exhibit high DCN, commonly found between 48 and 55. Likewise, comparing with marine fuel, their cetane number is in the range of 35 – 45 [29], which is also higher than that determined for TPO and TPO[CaO]. The low DCN of TPO and TPO[CaO] is attributed to the significant presence of light aromatic compounds in both samples, whose IDT is rather high, indicating high octane numbers. If TPO and TPO[CaO] are intended to be used as fuels in internal combustion engines, these parameters must be carefully considered. The IDT value obtained for TPO and TPO[CaO] in this work agrees with those reported in previous works. For instance, in a study conducted by Martinez *et al*. [30], a cetane index of 17.6 was obtained for TPO. Nonetheless, and similar to other properties of the oil derived from WT pyrolysis, this value will vary depending on the feedstock characteristics and the pyrolysis operational parameters.

Table 5.3. Ignition properties of TPO and TPO[CaO]

Sample	Low Temperature		High Temperature	
	IDT (ms)	DCN	IDT (ms)	DCN
TPO	24.3 ± 1.8	14.3 ± 0.6	14.3 ± 0.9	19.2 ± 0.8
TPO[CaO]	13.6 ± 0.9	19.9 ± 0.8	12.8 ± 0.9	20.6 ± 0.9

5.2.4 Surrogate fuel formulation of the light fraction of tire pyrolysis oil

After fine-tuning the mixture several times through the optimization process and comparing its IDT with that of the real fuel, the resulting surrogate fuel consisted of n-heptane (13.0 vol. %), toluene (25.5 vol. %), cyclopentane (21.4 vol. %), 1-hexene (13.5 vol. %), and 1,2,4 trimethylbenzene (26.7 vol. %) as shown in Figure 5.10. This mixture contains all the hydrocarbon classes present in the real fuel (paraffins, aromatics, naphthenes, olefins) and exhibits a similar IDT (20.30 ms) to that of the real fuel (20.80 ms) with a difference of 2.47 %. The minimum total error (objective function) achieved regarding the target fuel properties was 28 %. It is important to mention that although isooctane was included in the *Palette of Surrogate Species*, the optimization process revealed that the participation of this compound in the surrogate mixture was not significant to achieve the target properties. More compounds could have been added to reduce this total error; however, the smaller the number of fuel components involved, the more reproducible the experiments are, thus facilitating deeper insights into the combustion chemistry. It is important to mention that limonene is one of the most abundant compounds in the light fraction of TPO, as discussed in Chapter 4. Including this compound in the surrogate mixture may have enhanced the reproducibility of the properties of the real fuel with the surrogate. However, this hydrocarbon was not included in the *Palette of Surrogate Species* since kinetic mechanisms are not available for it in the scientific literature. The selected compounds included in this surrogate mixture are very common in the formulation of surrogates to study the combustion chemistry of gasoline fuels (*i.e.* Fuels for Advanced Combustion Engines (FACE)); therefore, oxidation kinetic mechanisms are available for all of them in the literature, which strengthen the development of future research [31].

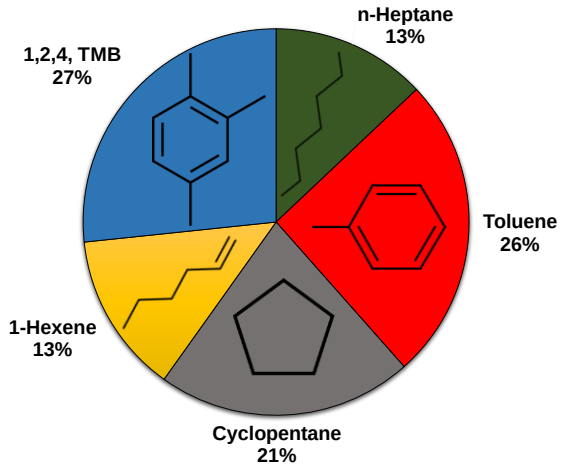

Table 5.4. Properties of the surrogate and real fuels

Properties	Surrogate	TPO[CaO]$_{Light}$	Error (%)
Viscosity @ 40 °C (cSt)	0.50	0.66	24.75
Density (kg/m^3)	795.47	795.47	0.00
HHV (MJ/kg)	43.7	41.91	4.27
H/C	1.60	1.70	5.88
MW (g/mol)	92.30	156.40	41.00
Ignition Delay Time (ms)	20.30	20.80	2.47
Average Molecular Formula	$C_{6.80}H_{10.80}$	$C_{11.23}H_{19.37}N_{0.09}O_{0.06}$	--

Figure 5.10. Final surrogate mixture and related properties

Table 5.4 lists some physicochemical properties of both the surrogate fuel mixture and the real fuel, as well as the related error. It is observed that the main difference between the surrogate and the real fuel is the average molecular weight (real fuel: 156.4 g/mol and surrogate fuel: 92.28 g/mol), which is associated with a lower carbon and hydrogen number in the surrogate fuel. This difference in the average molecular weight is also reflected in the surrogate fuel viscosity, which differs 24.75 % from that of the real fuel. Other properties, including density, HHV, H/C ratio are quite similar for both fuels. It is worth highlighting that the real

fuel contains some heteroatoms such as nitrogen and oxygen; however, they were considered negligible in the surrogate fuel mixture. In addition, the real fuel contains 600 ppm of sulfur, which is not significant in contrast to the carbon and hydrogen atom numbers. For this reason, it was not considered in the surrogate formulation. Nevertheless, in future studies, more refined surrogates should consider the presence of sulfur, due to its environmental implications.

Since the chemical properties of any fuel are linked to its chemical structure, ^{1}H NMR was used in the surrogate formulation since it provides an accurate view of the functional groups present in the studied fuels [32]. Thus, the mole percentage of hydrogen atoms in aromatic, paraffinic, olefinic, and naphthenic structures as determined by ^{1}H NMR (Chapter 4) were used in the optimization process to find the surrogate mixture with similar structural features to those exhibited by the real fuel. According to the ^{1}H NMR (Figure 5.11), 73 % of the structural characteristics of the real fuel can be represented by the final surrogate fuel mixture. Regarding the type of hydrogens detected by ^{1}H NMR, it is noticed that the main structural differences between the real fuel and the final surrogate fuel are related to the hydrogen atoms in paraffinic and olefinic structures. As observed in Figure 5.11, paraffinic hydrogen in the surrogate fuel is 9.45 % units higher than the real fuel, while olefinic hydrogen is 10.51 % units higher in the real fuel. Even though these structural differences may give rise to variations in the combustion behavior, the obtained surrogate fuel can be regarded as a reasonable approximation as a first attempt to study the combustion chemistry of TPO[CaO]$_{Light}$. It must be taken into consideration that no surrogate fuels have been formulated and reported for TPO before.

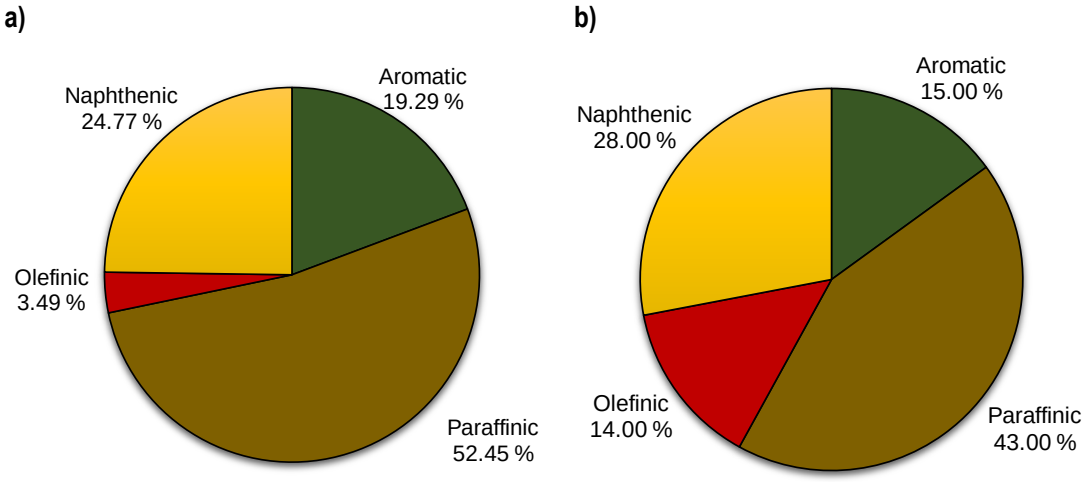

Figure 5.11. Types of hydrogen atoms (mole %) obtained from ^{1}H NMR: a) Surrogate fuel; b) Real fuel

5.2.5 Oxidation of the light fraction of tire pyrolysis oil and the surrogate fuel in jet stirred reactor

As aforementioned, the oxidation characteristics of both the real and the obtained surrogate fuel were assessed and compared by conducting studies in JSR. The fuel consumption rates and evolution of main combustion products (*i.e.* CO_2, CO, CH_4, C_3H_6, etc.) were compared for the real and the surrogate fuels over the assessed temperature range.

It is worth mentioning that, in the combustion of hydrocarbons, two stages of combustion chemistry are typically observed experimentally, which are temperature dependent: low temperature oxidation (230 – 330 ºC) and high temperature oxidation

(>480 ºC). This study was particularly focused on the high temperature oxidation region given its role in the combustion stability in thermal systems, and in the formation of pollutants and soot, among others [28]. Thus, the information obtained through this analysis is expected to provide important insights when the TPO[CaO]$_{Light}$ is intended to be used in combustion systems. Figure 5.12 shows the fuel consumption of both the surrogate and the real fuel during the oxidation experiments. Furthermore, Figures 5.13 – 5.15 show the evolution of different species as a function of temperature for different equivalences ratios (0.2, 0.5, and 1.0). As it can be observed in these figures, fuel transformation starts at ~ 630 ºC and ~ 577 ºC for the surrogate and the real fuel, respectively. At the same temperatures, the formation of different intermediate species is noticed (CH_4, C_2H_4, C_3H_6, etc.), whose mole fractions in the flue gases increase directly with temperature until a maximum is reached. After 730 ºC, the formation of these species decreases gradually, and the rapid formation of CO_2 is observed, which reaches a maximum concentration at temperatures higher than 830 ºC, indicating that most of the fuel has been oxidized.

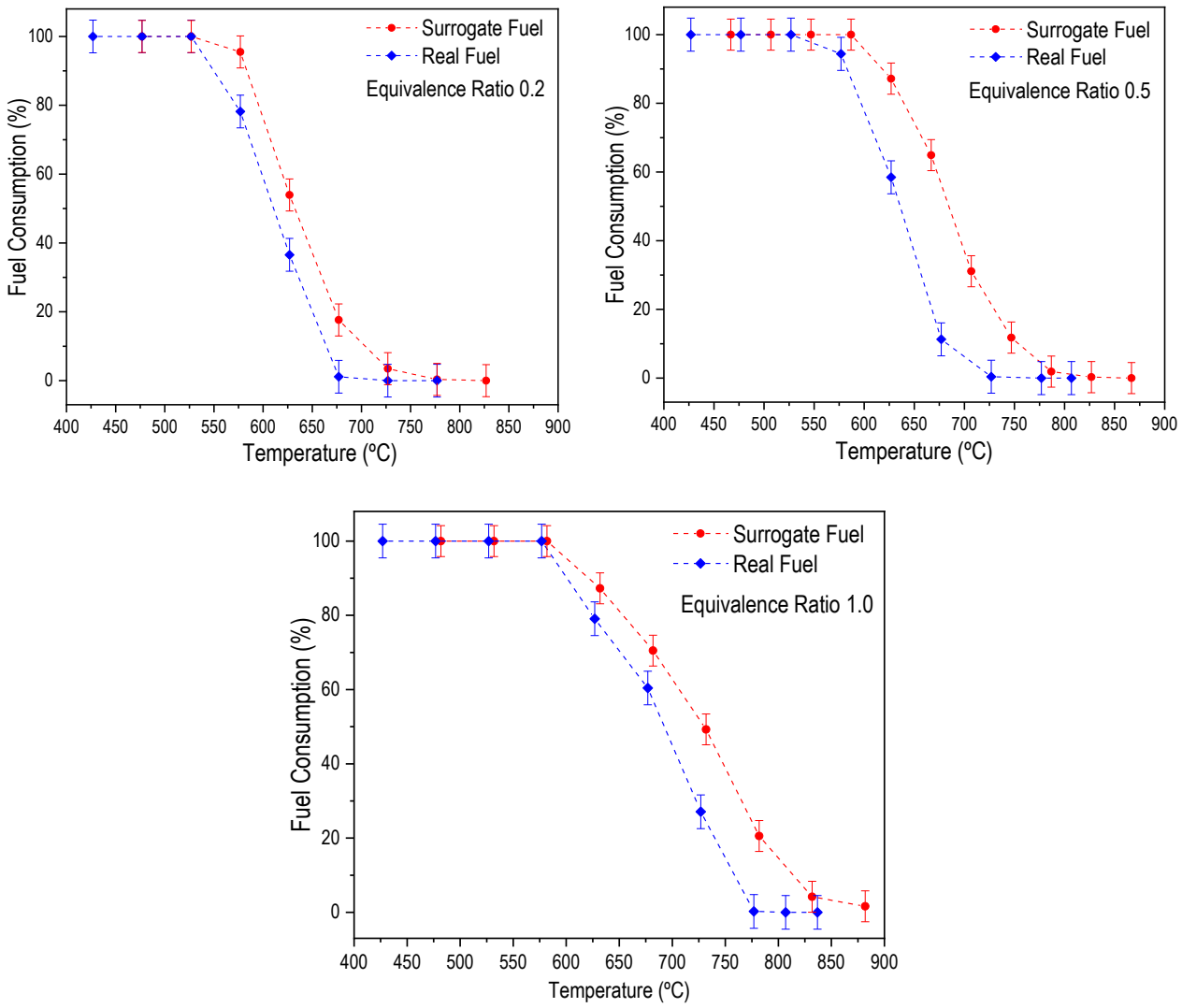

Figure 5.12. Surrogate and real fuel consumption during oxidation at different equivalence ratios

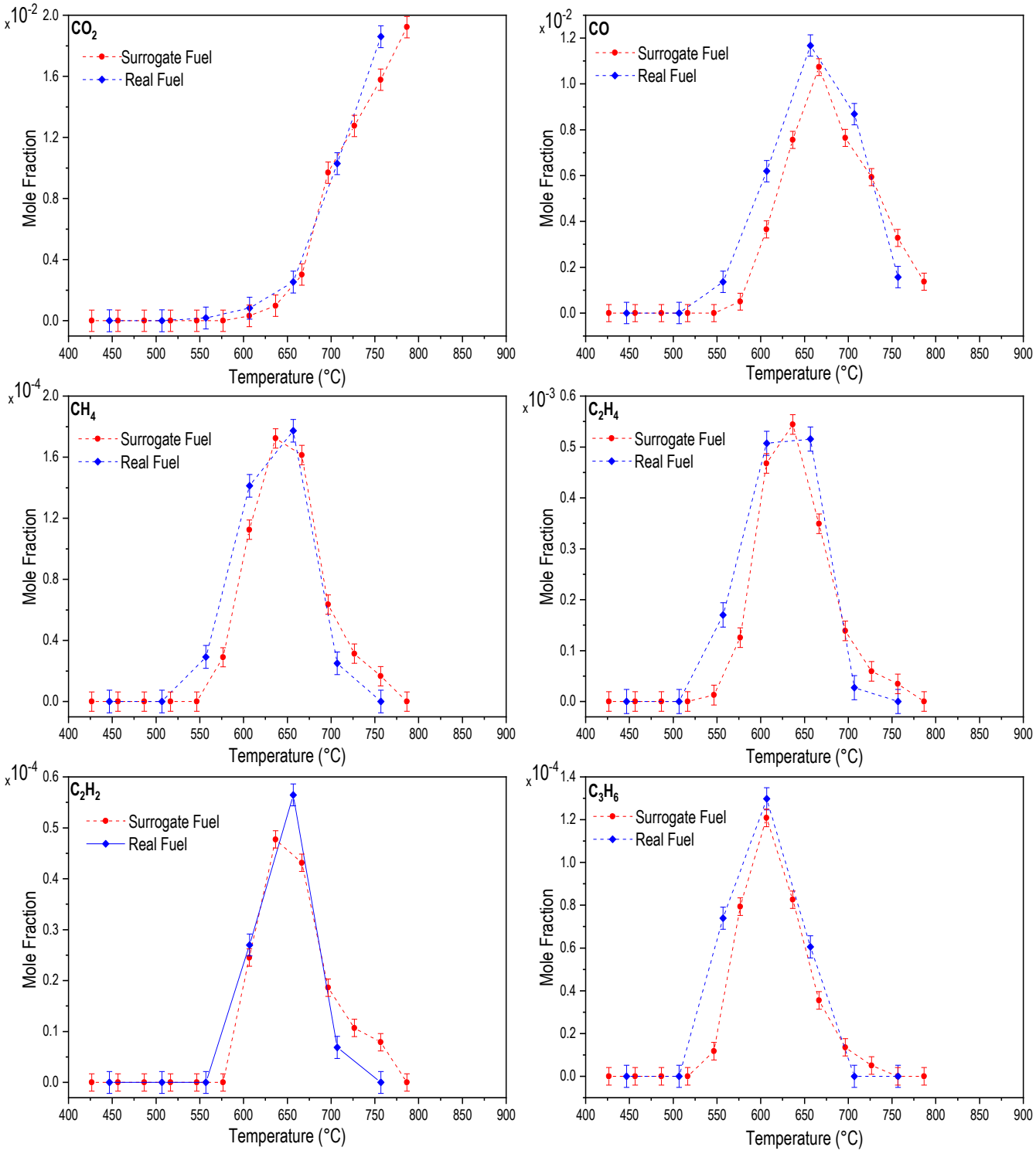

Figure 5.13. Evolution of different species for the surrogate and the real fuels at equivalence ratio of 0.2

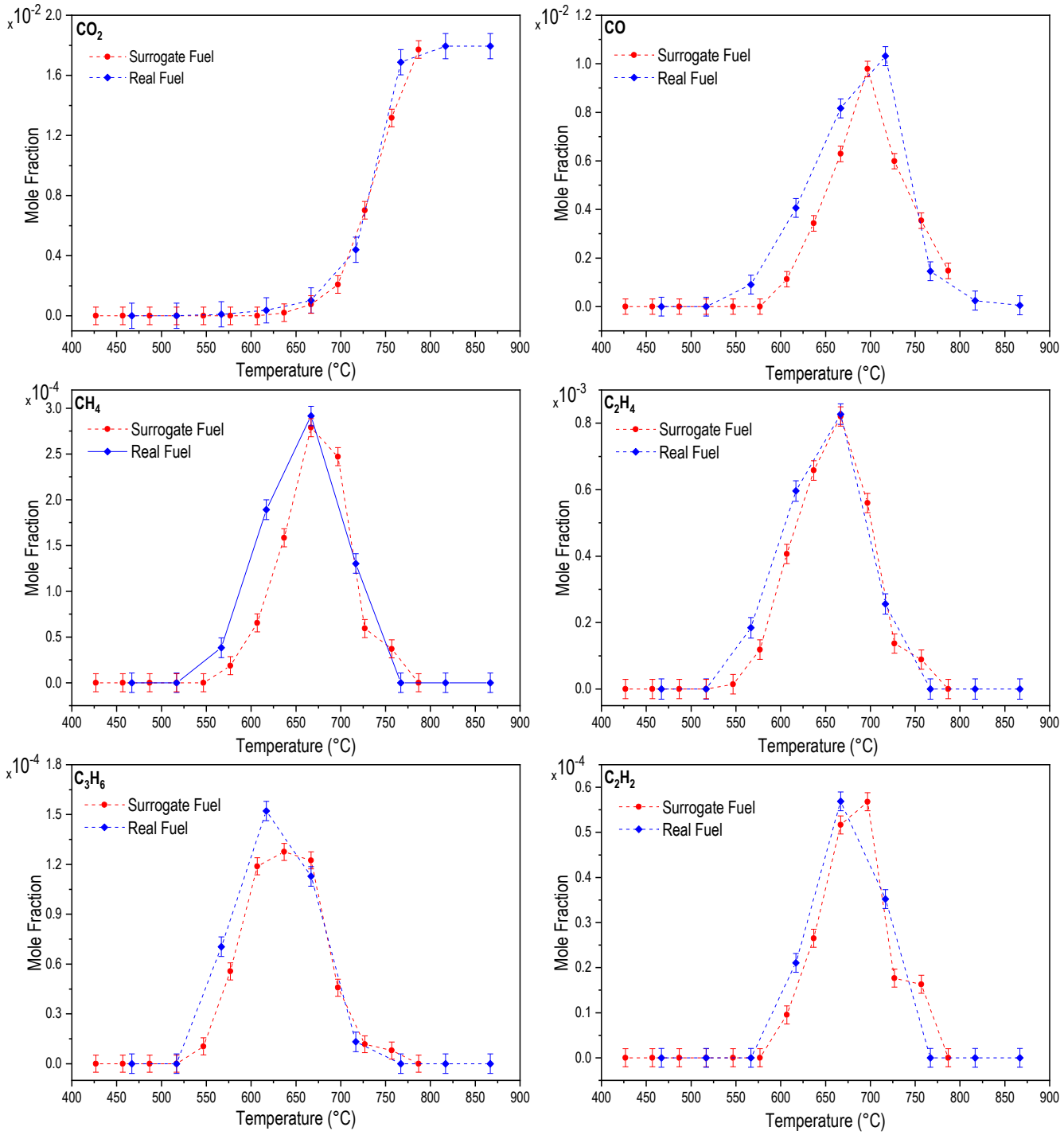

Figure 5.14. Evolution of different species for the surrogate and the real fuels at equivalence ratio of 0.5

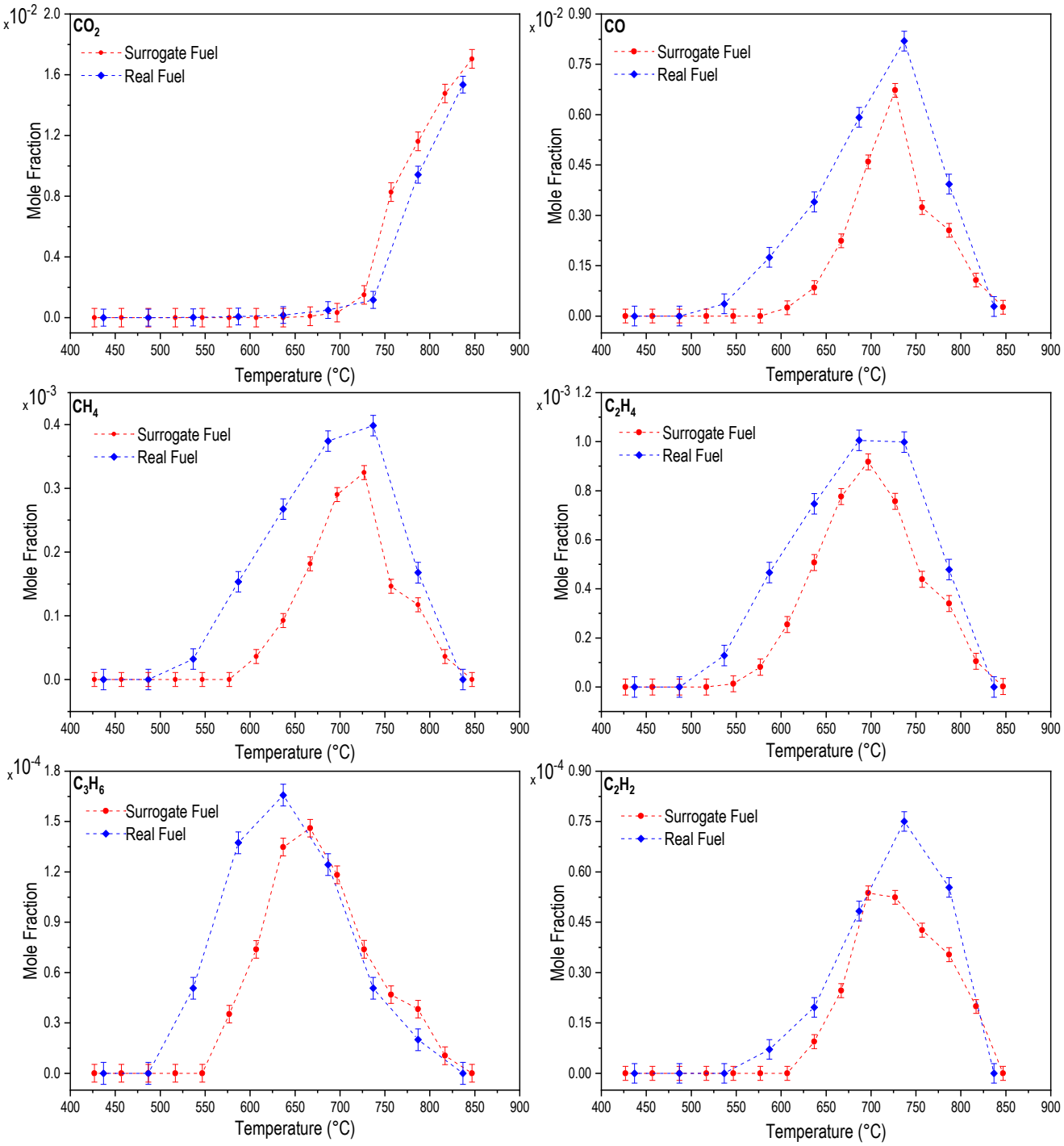

Figure 5.15. Evolution of different species for the surrogate and the real fuels at equivalence ratio of 1.0

Roughly speaking, the combustion reactions of any fuel such as the ones study in this work are driven by the formation of highly reactive radical, such as O, ˙OH, and ˙H. During combustion, fuels are oxidized by a series of chain reactions which can be categorized as one of following (*i*) chain initiating, (*ii*) chain propagating and chain branching, and (*iii*) chain terminating [33]. Chain initiating occurs when radical species are produced by dissociation of the reactants. The chain is propagated and

branched as radicals react with stable compounds to form additional radical species. Finally, the chain terminates when two radicals recombine to form stable species. Even though multiple reaction pathways must occur, as a general overview, Figure 5.16 shows a summarized scheme of the oxidation process of a real fuel within the high temperature oxidation region. It is observed that, in the initial stages (530 – 730 ºC) of this region, intermediate species including CH_4, C_3H_6, C_2H_2 are produced due to the decomposition of large hydrocarbon molecules (*i.e.* paraffins, aromatics, naphthenes, etc.). As temperature increases (> 900 ºC), final products, in particular CO_2 and CO, are produced due to the oxidation of those intermediate species. Along this process, diffusion, mixing, and turbulence are key factors that define the reaction pathways. A Detailed discussion regarding hydrocarbon combustion mechanisms are presented in previous review articles published by Battin-Leclerc [34] and Simmie [35].

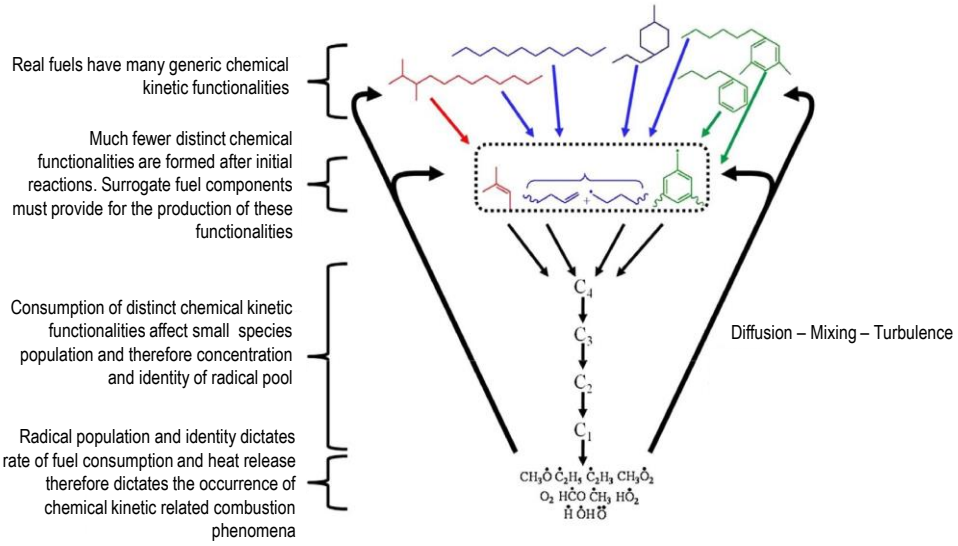

Figure 5.16 High temperature combustion chemistry scheme of complex real fuels (adapted from [36]).

In the case of TPO[CaO]$_{Light}$ and its surrogate fuel, it is noticed that as the process is conducted from leaner to more rich conditions, the formation of above-described intermediate species is slightly shifted to higher temperatures, as expected. In addition, the TPO[CaO]$_{Light}$ seems to be slightly more reactive taking into account that the decomposition process and the formation of intermediate species start earlier than that of the surrogate fuel. This behavior can be associated with the minor presence of light compounds and/or alkyl side chains in the real fuel that start reacting more rapidly. Nonetheless, it is possible to say that the surrogate fuel exhibits similar fuel profiles and reactivity than that of the real fuel within the experimental uncertainty. In this regard, despite differences in composition, comparable behaviors are found in the high temperature oxidation region for both fuels. This similarity in behavior may be attributed to the formation of radical species (so-called "radical pools") in the high temperature oxidation region (>830 ºC), which control the fuel combustion chemistry regardless of the precise structural characteristics of the fuel [36].

According to the results reported hitherto, it is possible to confirm that, aside from representing the physicochemical properties of the real fuel, the surrogate also replicates its reaction tendencies and formation of intermediate species during the combustion

process. Hence, this surrogate can be regarded as an interesting candidate for conducting further research into TPO[CaO]$_{Light}$ combustion chemistry. This information can be used as experimental input data to simulate the oxidation process of TPO[CaO]$_{Light}$ by utilizing detailed kinetic mechanisms currently available in the literature [31], which can further use in CFD to simulate combustion systems.

5.2.6 Pyrolysis of the surrogate fuel of the light fraction of tire pyrolysis oil: Polyaromatic hydrocarbons formation

Aside from oxidation, pyrolysis studies can also be conducted in order to get insights regarding the PAHs formation tendency of TPO[CaO]$_{Light}$. Conducting these types of studies with the real fuel in a JSR is quite complex for two main reasons. Firstly, many compounds are detected by the GC; thus, it is difficult to follow which compounds are being consumed and which ones are being formed as the temperature changes. Secondly, heavy, condensable compounds can be formed, which may lead to technical difficulties in the GC columns. Therefore, in this research, pyrolysis experiments were conducted in the JSR with the surrogate fuel instead.

Pyrolysis studies are fundamental to identify the possible formation of polycyclic aromatic hydrocarbons (PAH), which are known for being soot precursors, hence critical to study in detail. In combustion systems, fuel rich regions and localized high combustion temperatures are commonly found, which eventually promotes the formation of soot [37]. In addition, the released PAHs during the incomplete combustion of hydrocarbons have also been proven to be carcinogenic [38]. Therefore, insights regarding the evolution of PAHs could be used to develop strategies for decreasing their formation and, thus, reducing the production of hazardous pollutants.

In general, in the initial stages of the combustion process, the fuel breaks down to form acetylene (C_2H_2), as observed in Figures 5.13 - 5.16. In the high-temperature regime, soot formation is initiated by the growth of small straight-chain alkenes (acetylene) to small aromatic compounds (*e.g.* benzene). The aromatic hydrocarbons then react sequentially with smaller hydrocarbons (acetylene, in particular) to form larger polyaromatic hydrocarbon (PAHs) species. Gaseous PAH molecules continue to nucleate until the smallest identifiable soot particles appear, with diameters of a few nanometers [33]. Previous studies have also reported that benzyl radicals produced from the abstraction of the methyl site in substituted aromatics play an important role in the formation of these PAHs compounds during pyrolysis or rich fuel oxidation [37]. The important reactions of benzyl radicals towards the growth of large PAHs have been classified into three main categories: decomposition, recombination reactions with radical species, and addition reactions with stable intermediates [37]. Possible formation mechanisms for the formation of these species can be found in the scientific literature [37,39].

Figure 5.17 shows the evolution of some aromatic compounds, including benzene (C_6H_6), ethylbenzene (C_8H_{10}), styrene (C_8H_8), and naphthalene ($C_{10}H_8$) formed during the pyrolysis of the surrogate fuel in a temperature range between 400 and 950 ºC. It is observed that the formation of these compounds increases rapidly at temperatures around 700 ºC. C_8H_{10} and C_8H_8 exhibit similar behaviors, reaching a peak at around 800 ºC after which a sharp decrease is noticed. On the other hand, the formation of C_6H_6 and $C_{10}H_8$ seem to be promoted by an increase in the temperature.

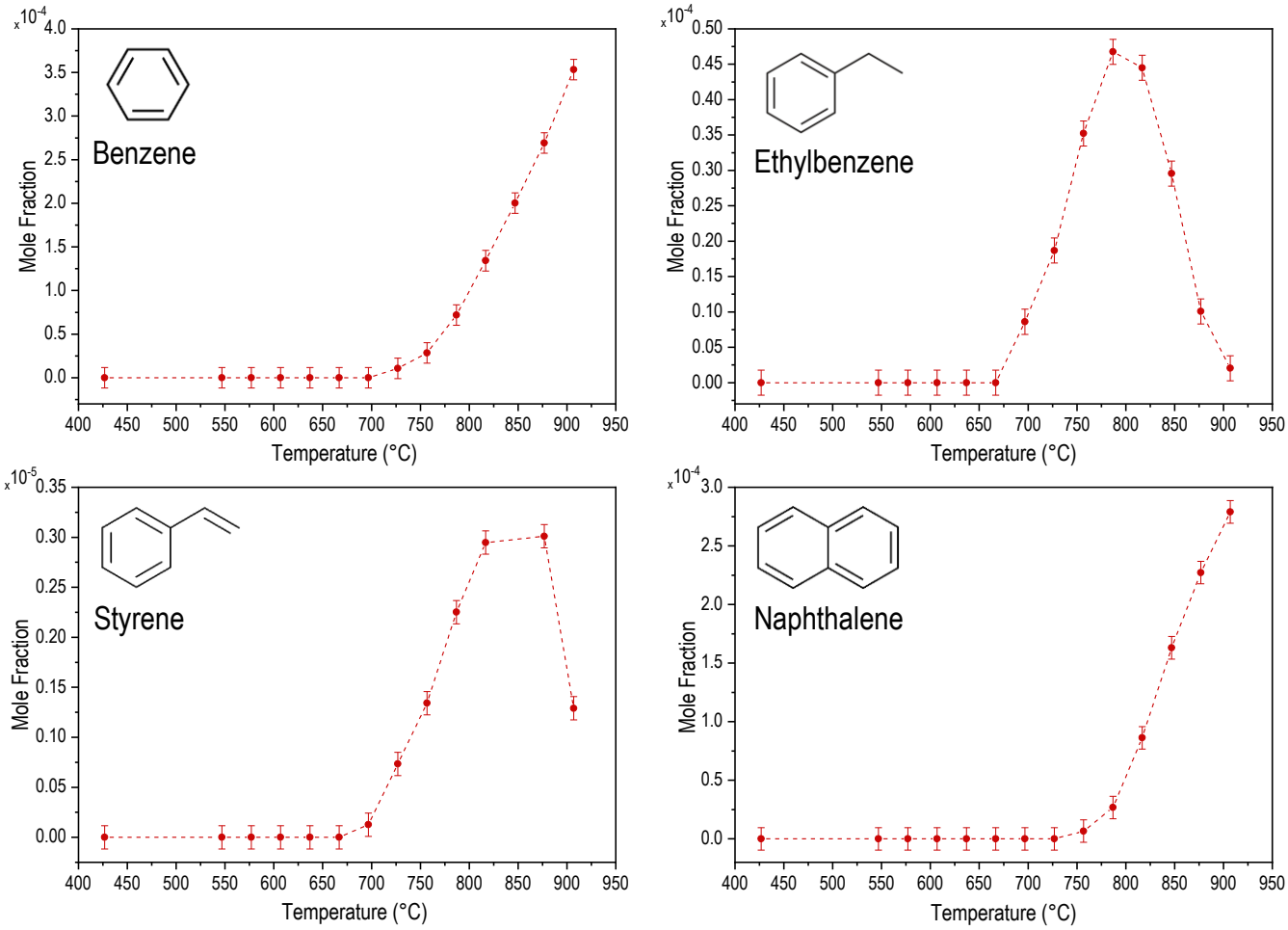

Figure 5.17. Formation of PAHs in the pyrolysis of the surrogate fuel

According to these results and considering that the surrogate fuel is proper representation of the real fuel and that TPO[CaO]$_{Light}$ exhibits similar physicochemical properties to those of conventional gasoline, a possible application could be its use in *Homogenous Charge Compression Ignition* (HCCI) *Engines* [40]. These types of engines have been proven to achieve low emission levels of nitrogen oxides (NOx) and soot, as well as high volumetric efficiency [41]. They operate under lean fuel conditions and low temperatures reducing the possibility of PAHs formation, and thus of soot. It has also been reported that HCCI engines are flexible to operate with different types of fuels, including gasoline, diesel or alternative fuel. In this regard, the HCCI technology can be an interesting option for TPO[CaO]$_{Light}$ implementation. Even so, further research is needed to strengthen these statements.

Overall, the information presented in this chapter aims at contributing to scarcely available data in the scientific literature regarding the fundamental combustion characteristics of TPO and its distillate fractions, which have been deeply characterized in previous chapters. Therefore, this first attempt at describing the combustion behavior of the studied fuel can be considered as a starting point for further investigations aiming to develop a deep understanding of the combustion chemistry of these non-conventional fuels.

On the other hand, the compounds contained in the surrogate fuel are very common in the general formulation of surrogate fuels and have been widely studied to elucidate the combustion chemistry of conventional gasolines. Therefore, their oxidation and pyrolysis kinetic models are available in the literature [31]. In turn, these models can be adjusted to the $TPO[CaO]_{Light}$ surrogate experimental data presented in this work. As such, besides reaching a comprehensive understanding of the combustion chemistry combustors can be further designed, modified or optimized in order to identify the best manner in which to deploy $TPO[CaO]_{Light}$ into practical combustion systems.

5.3 Summary

The present chapter aimed at contributing to the scientific knowledge regarding the combustion features of TPO and its distillate fractions by conducting fundamental combustion studies. In the first part of this chapter, the combustion characteristics of TPO and TPO[CaO] were investigated using non-isothermal thermogravimetric analysis. Thereby, TG and DTG analyses were conducted at different heating rates (5 °C/ min, 10 °C/min, and 20 °C/min) over a temperature range between 30 and 700 °C. Through these analyses, different stages in the combustion process of TPO and TPO[CaO] were identified, including low temperature, middle temperature, and high temperature oxidation regions. In addition, important combustion characteristics such as the initial decomposition temperature, maximum temperature, and burnout temperature were determined for each fuel. The thermogravimetric analyzer used in this study was coupled with a Fourier Transform Infrared (FT-IR) spectrometer, which allowed for obtaining valuable information regarding the real-time compositional changes of the evolved gases during the oxidation processes of these fuels, giving special attention to pollutants such as CO_2, CO, SO_2, NO.

In the second part of this chapter, a surrogate fuel was formulated for the light distillate fraction of TPO[CaO]. Based on the fuel and chemical properties of this fraction (described in previous chapters) a set of pure compounds, including paraffins (n-heptane), aromatics (toluene and trimethylbenzene), olefins (1-hexene), and naphthenes (cyclopentane) was selected. In turn, an optimization process was conducted in order to formulate a surrogate, whose physicochemical and combustion properties mimic certain predetermined target properties of the real fuel. Thereafter, oxidation experiments were conducted in a JSR, and the evolution of different intermediate and final species was identified and compared for both fuels at different experimental conditions (equivalence ratios and temperatures). Pyrolysis experiments with the surrogate fuel were also conducted in order to investigate the formation of highly aromatic compounds (PAHs), which may indicate the formation of such compounds when $TPO[CaO]_{Light}$ is oxidized a more reach condition. The information presented in this chapter is fundamental for further investigations: for instance, for the development/adjustment of detailed kinetic mechanisms needed to model the combustion chemistry of TPO/TPO[CaO].

References

[1] J.D. Martínez, J. Rodríguez-Fernández, J. Sánchez-Valdepeñas, R. Murillo, T. García, Performance and emissions of an automotive diesel engine using a tire pyrolysis liquid blend, Fuel. 115 (2014) 490–499.

[2] J. Pilusa and E. Muzenda, Combustion characteristics of waste tyre pyrolysis fuel as industrial burner fuel, in: Dev.

Combust. Technol. Chapter 4, 2016: pp. 97–116.

[3] S.T. Kumaravel, A. Murugesan, A. Kumaravel, Tyre pyrolysis oil as an alternative fuel for diesel engines – A review, Renew. Sustain. Energy Rev. 60 (2016) 1678–1685.

[4] J.D. Martínez, Á. Ramos, O. Armas, R. Murillo, T. García, Potential for using a tire pyrolysis liquid-diesel fuel blend in a light duty engine under transient operation, Appl. Energy. 130 (2014) 437–446.

[5] R. García-contreras, J.D. Martínez, O. Armas, R. Murillo, T. García, Study of a residential boiler under start-transient conditions using a tire pyrolysis liquid (TPL)/diesel fuel blend, Fuel. 158 (2015) 744–752.

[6] Á. Muelas, M.S. Callén, R. Murillo, J. Ballester, Production and droplet combustion characteristics of waste tire pyrolysis oil, Fuel Process. Technol. 196 (2019) 106–149.

[7] O. Herbinet, G. Dayma, Jet stirred reactors, in: Clean. Combust. Dev. Detail. Chem. Kinet. Model., Springer, 2013: pp. 183–210.

[8] A.G. Abdul Jameel, N. Naser, A.-H. Emwas, S.M. Sarathy, Surrogate formulation for diesel and jet fuels using the minimalist functional group (MFG) approach, Proc. Combust. Inst. 37 (2019) 4663–4671.

[9] A. Violi, S. Yan, E.G. Eddings, A.F. Sarofim, S. Granata, T. Faravelli, E. Ranzi, Experimental formulation and kinetic model for JP-8 surrogate mixtures, Combust. Sci. Technol. 174 (2002) 399–417.

[10] W.W. Ayass, E.F. Nasir, A. Farooq, S.M. Sarathy, Mixing-structure relationship in jet-stirred reactors, Chem. Eng. Res. Des. 111 (2016) 461–464.

[11] J.-Y. Wan, Experimental and kinetic modelling study of ethyl levolinate oxidation in jet stirred reactor, MSc. Thesis, King Abdullah University of Science and Technology, KSA, 2017.

[12] B. Chen, Gasoline combustion chemistry, PhD Thesis, King Abdullah University of Science and Technology, KSA, 2019.

[13] K. Zhang, C. Banyon, J. Bugler, H.J. Curran, A. Rodriguez, O. Herbinet, F. Battin-leclerc, C.B. Chir, K.A. Heufer, An updated experimental and kinetic modeling study of n- heptane oxidation, Combust. Flame. 172 (2016) 116–135.

[14] C. Yuan, D.A. Emelianov, M.A. Varfolomeev, Oxidation behavior and kinetics of light, medium, and heavy crude oils characterized by thermogravimetry coupled with Fourier Transform Infrared Spectroscopy, Energy Fuel. 32 (2018) 5571−5580.

[15] A.M. Elbaz, A. Gani, N. Hourani, A.H. Emwas, S.M. Sarathy, W.L. Roberts, TG/DTG, FT-ICR mass spectrometry, and NMR spectroscopy study of heavy fuel oil, Energy Fuels. 29 (2015) 7825–7835.

[16] M. V Kok, K.G. Gul, Combustion characteristics and kinetic analysis of Turkish crude oils and their SARA fractions by DSC, J. Therm. Anal. Calorim. 114 (2013) 269–275.

[17] S. Zhao, W. Pu, M.A. Varfolomeev, Y. Liu, Z. Liu, Oxidation characteristics of heavy oil and its SARA fractions during combustion using TG-FTIR, J. Pet. Sci. Eng. 192 (2020) 107331.

[18] N.P. Freitag, Chemical reaction mechanisms that govern oxidation rates during in-situ combustion and high-pressure air injection, SPE Int. (2014) 1–16.

[19] W. Pu, C. Yuan, F. Jin, L. Wang, Z. Qian, Y. Li, Low-Temperature Oxidation and Characterization of Heavy Oil via Thermal Analysis, (2015). doi:10.1021/ef502135e.

[20] S. Zhao, W. Pu, X. Peng, J. Zhang, H. Ren, Low-temperature oxidation of heavy crude oil characterized by TG, DSC, GC-MS, and negative ion ESI FT-ICR MS, Energy. 214 (2021) 119004.

[21] D. Liu, L. Chen, L. Chen, R. Zheng, Q. Song, G. Cai, Influence of conversion conditions on heavy-oil coking during in situ combustion process, Energy Fuel. 32 (2018) 2018.

[22] Petroleum, API gravity, (2015). http://www.petroleum.co.uk/api (accessed November 8, 2019).

[23] P. Behrenbruch, T. Dedigama, Classification and characterisation of crude oils based on distillation properties, Pet. Sci. Enegineering. 57 (2007) 166–180.

[24] A.G. Abdul Jameel, Y. Han, O. Brignoli, S. Telalovic, A.M. Elbaz, H.G. Im, W.L. Roberts, M.S. Sarathy, Heavy fuel oil pyrolysis and combustion : Kinetics and evolved gases investigated by TGA-FTIR, J. Anal. Appl. Pyrolysis. 127 (2017) 183–195.

[25] L.H. Coykendall, Formation and control of sulfur oxides in boilers, 12 (1962) 567–591.

[26] Environmental Protection Agency (EPA), Sulfur dioxide (SO2) pollution, (2020). https://www.epa.gov/so2-pollution/sulfur-dioxide-basics (accessed October 21, 2020).

[27] K. Lehtoranta, H. Vesala, S. Korhonen, Selective Catalytic Reduction Operation with Heavy Fuel Oil: NOx, NH3, and particle emissions, Environ. Sci. Technol. 7 (2015) 4735–4741.

[28] S.M. Sarathy, A. Farooq, G.T. Kalghatgi, Recent progress in gasoline surrogate fuels, Prog. Energy Combust. Sci. 65 (2018) 67–108.

[29] Chevron, Everything you need to know about marine fuels, (2012). file:///C:/Users/Felipe Campuzano/Downloads/everything-you-need-to-know-about-marine-fuels.pdf (accessed March 20, 2020).

[30] J.D. Martínez, M. Lapuerta, R. Garcia-Contreras, R. Murillo, T. García, Fuel properties of tire pyrolysis liquid and its blends with diesel fuel, Energy Fuels. 27 (2013) 3296–3305.

[31] S.M. Sarathy, G. Kukkadapu, M. Mehl, T. Javed, A. Ahmed, N. Naser, A. Tekawade, G. Kosiba, M. Alabbad, E. Singh, S. Park, M. Al Rahidi, H.S. Chung, W.L. Roberts, M.A. Oehlschlaeger, C. Sung, A. Farooq, Compositional effects on the ignition of FACE gasolines, Combust. Flame. 169 (2016) 171–193.

[32] A.G. Abdul Jameel, N. Naser, G. Issayev, J. Touitou, M.K. Ghosh, A.H. Emwas, A. Farooq, S. Dooley, S.M. Sarathy, A minimalist functional group (MFG) approach for surrogate fuel formulation, Combust. Flame. 192 (2018) 250–271.

[33] I. Glassman, Combustion, 3rd ed, Academic Press, San Diego, CA, 1996.

[34] F. Battin-Leclerc, Detailed chemical kinetic models for the low-temperature combustion of hydrocarbons with application to gasoline and diesel fuel surrogates, Prog. Energy Combust. Sci. 34 (2008) 440–498.

[35] J.M. Simmie, Detailed chemical kinetic models for the combustion of hydrocarbon fuels, Prog. Energy Combust. Sci. 29 (2003) 599–634.

[36] S. Dooley, H.S. Won, J. Heyne, T.I. Farouk, Y. Ju, F.L. Dryer, K. Kumar, X. Hui, C. Sung, H. Wang, M.A. Oehlschlaeger, V. Iyer, S. Iyer, T.A. Litzinger, R.J. Santoro, T. Malewicki, K. Brezinsky, The experimental evaluation of a methodology for surrogate fuel formulation to emulate gas phase combustion kinetic phenomena, Combust. Flame. 159 (2012) 1444–1466.

[37] C. Shao, G. Kukkadapu, S.W. Wagnon, W.J. Pitz, S.M. Sarathy, PAH formation from jet stirred reactor pyrolysis of gasoline surrogates, Combust. Flame. 219 (2020) 312–326. doi:10.1016/j.combustflame.2020.06.001.

[38] K. Kim, S.A. Jahan, E. Kabir, R.J.C. Brown, A review of airborne polycyclic aromatic hydrocarbons (PAHs) and their human health effects, Environ. Int. 60 (2013) 71–80.

[39] C. Shao, H. Wang, N. Atef, Z. Wang, B. Chen, M. Almalki, Y. Zhang, C. Cao, J. Yang, S.M. Sarathy, Polycyclic aromatic hydrocarbons in pyrolysis of gasoline surrogates (n-heptane/iso-octane/toluene), Proc. Combust. Inst. 37 (2019) 993–1001.

[40] K. Epping, S. Aceves, R. Bechtold, J. Dec, The potential of HCCI combustion for high efficiency and low emissions,

SAE Int. 01–1923 (2002) 1–15.

[41] A.P. Singh, A.K. Agarwal, Combustion characteristics of diesel HCCI engine: An experimental investigation using external mixture formation technique, Appl. Energy. 99 (2012) 116–125.

Chapter 6. Thermoeconomic assessment of a model waste tires pyrolysis plant

The feasibility (technical and economical) of the pyrolysis of WT depends on several factors which often include the cost of products, the production capacity, capital investment, waste processing fee, etc. In the initial stages of development, the key factors that define the feasibility of this new technology are: i) long-term reliability and ii) the identification of the proper operational conditions which yield a balance between high TPO yield and adequate physicochemical properties of the rCB. Aside from ensuring that a competitive product is achieved, researchers and engineers must also guarantee that the pyrolysis process is conducted in an efficient and low-cost manner with low process malfunctions (irreversibilities) and environmental impact. Chapter 2 in this dissertation addressed the operational features of the auger technology, in particular the twin-auger configuration. The results obtained aided in demonstrating the suitability of this type of reactor for the pyrolysis of WT. As a next step in this investigation, the current chapter presents a thermoeconmic assessment of a model WT pyrolysis plant at industrial-scale, which is proposed based on several experimental studies carried out in the lab-scale twin-auger plant described before. The thermoeconmic approach combines exergy analysis and economic principles to provide insights into the cost structure for such systems, which is not possible by means of conventional energy and economic analyses.

In practice, several indicators have been accepted to assess the performance and the environmental impacts of different processes [1–3]. In particular, the exergy analysis is a methodology that helps to identify the thermodynamic irreversibilities in energy conversion systems. Exergy is a magnitude based on the second law of thermodynamics that indicates the maximum work that a system can produce while interacting with the environment [4,5]. Unlike energy, which is conserved (energy quality is not considered), exergy is destroyed in real processes due to thermodynamic irreversibilities (deterioration of energy quality). Therefore, exergy analysis provides valuable information in order to detect where exergy is lost or where resources can be saved [6]. Exergy has been recognized as the confluence of energy, environment, and sustainable development [7]. Hence, this thermodynamic concept presents a valuable tool for the assessment of sustainability since it allows for a rigorous quantification of the loss of availability of resources, hence setting limits to technological development [8]. Exergy analysis reveals the irreversibilities associated with the components of a system, which is a necessary input for increasing energy efficiency. Going one step further, the combination of the exergy concept with the economic concept of cost, by means of methodologies such as the one developed by Valero *et al*. [9] (Theory of Exergy Cost), allows, among others, for the quantification of the amount of exergy / money required to produce a given stream in a system (exergy cost / exergoeconomic cost). The implementation of this analysis for the assessment of a new waste-to-energy pathway, such as the one presented in this dissertation, can help to reach a comprehensive understanding of the process in terms of performance and production cost, which is fundamental for its further implementation and improvement.

As such, this chapter presents a model WT pyrolysis facility with a nominal capacity of 1,000 kg/h, as well as its exergy and thermoeconomic analyses. The mass, energy, and exergy balances of the process are combined with the thermoeconomic approach by means of the Theory of Exergy Cost (TEC), in order to determine both the exergy and the monetary costs of the pyrolysis-derived products. The same analysis is conducted for the lab-scale plant described in previous chapters with the aim

of identifying some of the benefits of scaling and modifying the process from an exergy / cost point of view. Finally, the methodology developed by Agudelo *et al*. [8], which combines TEC and the symbolic exergoeconomic principles [10], is used in order to provide insights regarding the contribution of the external resources (renewable and fossil origin) to the exergy content of the final pyrolysis-derived products.

6.1 Materials and methods

6.1.1 Lab-scale pyrolysis plant

The lab-scale pyrolysis plant studied in this chapter has been described in detail in Chapter 2 (Section 2.1.1). In order to conduct the thermoeconimic analysis, the plant is assumed to operate in accordance with the optimum pyrolysis conditions determined by means of the RSM (Chapter 2). As such, the following conditions were considered for the calculations: (i) pyrolysis temperature of 475 ºC, (ii) solid residence time of 3.5 min, (iii) tire mass flow rate of 1.16 kg/h, and (iv) N_2 flow of 300 mL/min. Characteristics of every stream in the plant were determined based on the experimental data reported in Chapter 2.

6.1.2 Model industrial pyrolysis plant

A model pyrolysis plant based on the twin-auger technology with a capacity of 7,665 ton/year of WT is presented and studied in this chapter (Figure 6.1) as well. This plant is able to produce 3,449.25 ton/year of TPO, 3,142.65 ton/year of rCB, and 1,327,885 m^3/year of TPG. A portion of TPG is used as an energy source in the process to obtain the heat for pyrolysis, which is defined as the sensible energy needed to increase the feedstock temperature from room to the pyrolysis conditions, plus the energy required to transform the feedstock into pyrolysis products (TPO, TPG, and rCB). At industrial scale, two different cases are studied: (i) non-catalytic pyrolysis (reference process) and (ii) catalytic pyrolysis using CaO (alternative process). This model plant is proposed, based on several experimental studies conducted in a lab-scale twin-auger pyrolyzer with a nominal capacity of 1 kg/h of WT (Chapters 2 and 3). The pyrolysis process is assumed to be performed at temperature, solid residence time, and WT mass flow rate of 475 ºC, 3.50 min, and 1,000 kg/h, respectively. In addition, in the alternative process, CaO is fed into the reactor in an independent and continuous manner at a mass flow rate of 150 kg/h. It has been experimentally determined that at these conditions the TPO, rCB, TPG yields are 45 wt.%, 41 wt.%, and 14 wt.%, respectively. Therefore, this is taken as a reference in this analysis.

The pyrolysis plant shown in Figure 6.1 consists of seven main components: (1) twin-auger pyrolyzer, (2) condensation unit, (3) TPG cleaning system (scrubber), (4) TPG compressor, (5) TPG burner, (6) preheater for combustion air, and (7) stack. In both the reference and the alternative processes, pyrolysis is initiated by supplying a continuous N_2 flow and preheating the twin-auger pyrolyzer to the pyrolysis temperature (475 ºC). Once the reactor reaches the desired temperature, WT granulates with a particle size between 2 – 4 mm are fed into the reactor (CaO is also fed in the alternative process) by a screw feeder. While the WT granulates/CaO are mixed and conveyed through the reactor by the rotation of two intermeshing screws, the released volatile matter is directed to the condensing unit by the N_2 flow. The intermeshing screws of the reactor, as well as the screw feeders, are moved by independent electric motors. The rCB falls by gravity into a collecting vessel after the process is

completed. In the alternative process, the solid fraction also holds the CaO added during operation. The condensing unit comprises a shell and tube counter-flow heat exchanger, which receives the volatile matter released during the process. Here, water is used as a cold fluid for cooling down the pyrolysis vapors, thus recovering the liquid fraction (TPO). The non-condensable gases (TPG) are carried to a scrubber where H_2S and CO_2 are removed using a NaOH - H_2O solution. In this component, the liquid phase is dispersed by means of a spray nozzle located at the top of the column, while TPG is sparged at the bottom of the scrubber column in a countercurrent direction. Tanks located downstream the scrubber column are used for storing the scrubbing liquid and controlling its pH. The NaOH and H_2O solution is recirculated through the system using a centrifugal pump. The concentration of the NaOH in the aqueous solution is assumed to be 0.25 g/L [11]. The clean TPG is then separated into two streams. The first stream is used as a fuel in a gas burner with an air/fuel mass ratio of ~ 80. The resulting high temperature combustion gases are used to provide the heat for pyrolysis, as well as to preheat the combustion air before entering the burner. The volumetric flow of the combustion air is controlled with a fan located right before the preheater. The second stream is stored using a reciprocating compressor for its further utilization in other energy related processes, *e.g.* for electricity generation, which can be used to operate compressors, pumps, electric motors, etc., in the plant, as well as being sold for revenue.

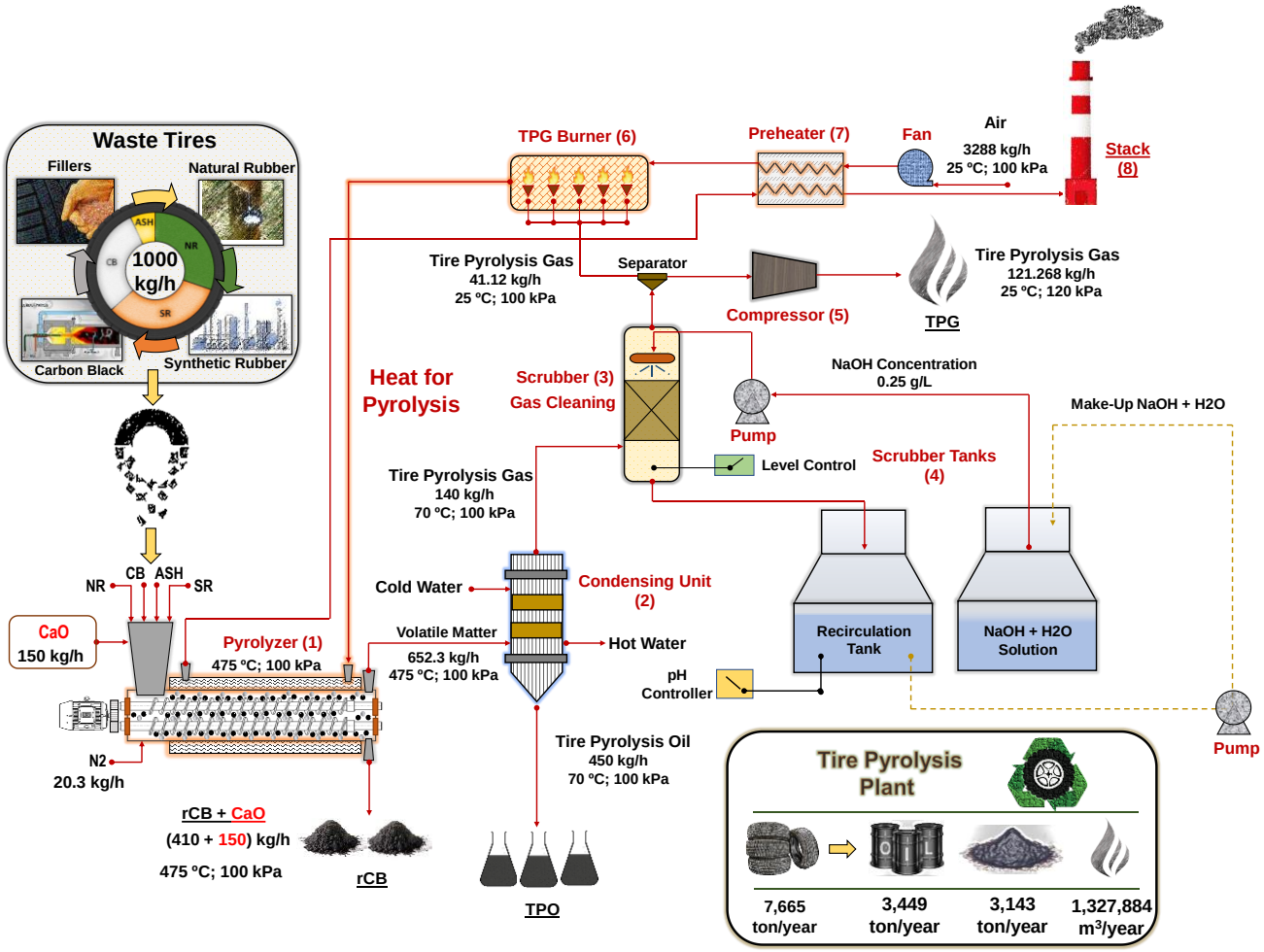

Figure 6.1. Model twin-auger pyrolysis plant at industrial scale

6.2 Implementation of Theory of Exergy Cost to the studied processes

TEC is a matrix-based methodology that integrates thermodynamic and economic analyses using the concept of exergy cost [12]. Its use allows the allocation of energy, exergy, and economic costs associated with both products and energy losses. Thereby, it provides important insights to study complex energy conversion systems. In order to carry out this analysis, the physical structure and the productive structure of the studied process must be defined. First, the physical structure shows the relationships of the components with one another and with the environment by means of the streams of matter and energy. The thermodynamic analysis of an energy conversion system is based on its physical structure. Second, the productive structure is related to the productive purposes of the components in the system, which is established according to the physical structure. A detailed description of these two structures for the systems studied in this chapter is presented in the following sections.

6.2.1 Physical structure: Lab-scale and model industrial plant

A sketch of the twin-auger pyrolysis plant at lab-scale (physical structure) described in Chapter 2 is shown in Figure 6.2. The system has 8 components (numbered inside circles) and 21 streams (numbered inside squares).

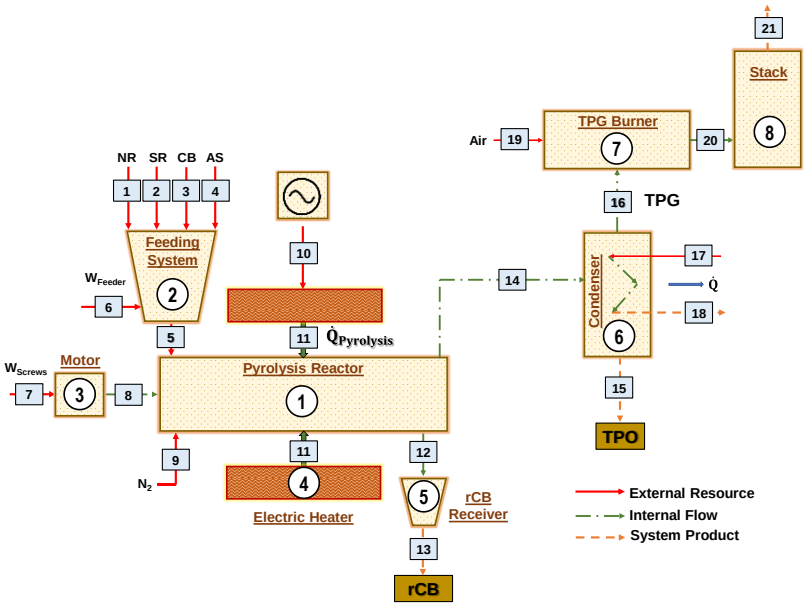

Figure 6.2. Physical structure of the lab-scale twin-auger pyrolysis plant (capacity:1.16 kg/h)

Similarly, the physical structure of the model industrial pyrolysis plant presented in Section 6.1.2 is shown in Figure 6.3. This system has 15 components, numbered inside circles (16 for the case of catalytic process) and 35 streams, numbered inside squares (38 for the case of the catalytic process).

In this study, the WT stream (1,000 kg/h) was divided into four different streams associated with the main components of WT: Natural Rubber (NR), Synthetic Rubber (SR), Carbon Black (CB), and Ashes (AS). In order to simplify the calculations NR, SR, and CB were represented by their main constituents: assumed as isoprene (C_5H_8), butadiene (C_4H_6), and graphite (C), respectively. AS were considered as a standard mixture of inorganic materials. The mass flow rate of these four independent

streams were defined to match the physicochemical properties of the WT reported in Chapter 2, giving especial attention to the proximate analysis (volatile matter, fixed carbon, and ash content) and heating value (HHV).

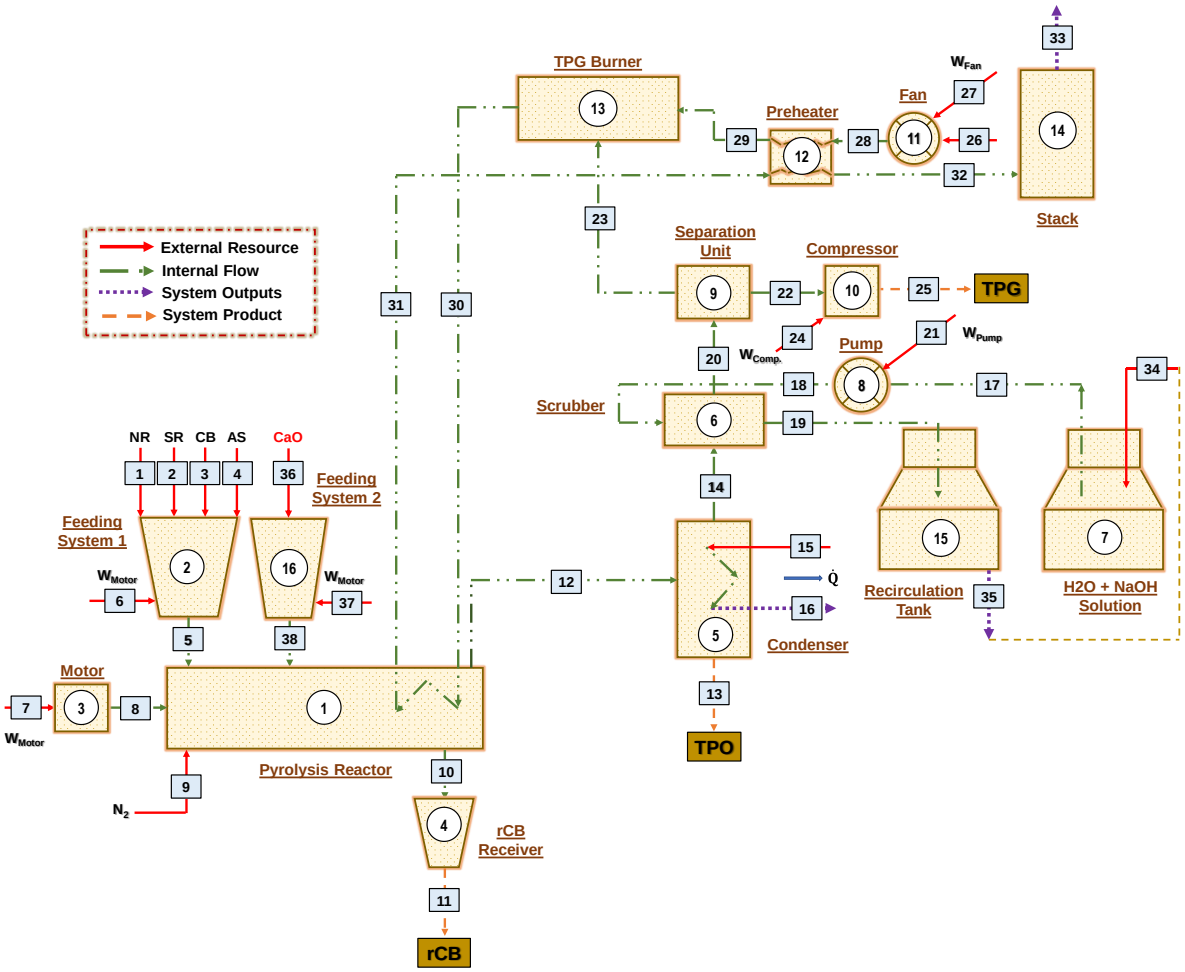

Figure 6.2. Physical structure of the industrial-scale twin-auger pyrolysis plant (capacity: 1,000kg/h)

Thus, the mass flow rate of isoprene (stream 1), butadiene (stream 2), graphite (stream 3), and standard ashes (stream 4) were defined as 303 kg/h, 333 kg/h, 299 kg/h, 68 kg/h, respectively. The separation of the WT stream is proposed in order to discriminate the contribution of fossil (SR and CB) and renewable (NR) sources to the streams of the systems, with emphasis in the final products, by implementing the TEC and the methodology developed by Agudelo *et al.* [8].

Based on the operating conditions (temperature and pressure), as well as on the chemical composition of every stream, specific enthalpies and exergies (physical and chemical) were calculated in both the lab-scale and model industrial plants. Thereafter, this information was used to perform the mass, energy, and exergy balances for every component of the system, as well as for the overall process. The exergy demanded by the pyrolysis process (heat for pyrolysis) was calculated assuming a heat of reaction (the energy needed to transform the feedstock into pyrolysis products) of 907 kJ/kg, as suggested by Martínez *et al.* [13], and a heat capacity at constant pressure for the rubber in tires of 1.9 kJ/kgK [14]. The methodology followed to determine the properties of every stream is described in detail on Appendix E. These calculations were based on the following assumptions:

- The reactor works at steady state (constant 101 kPa and 475 ºC), as well as all the other plant components.
- The composition and properties of resources and products (reported in Chapter 2 and Chapter 3) are constant.
- All gaseous streams are assumed to be ideal gases.
- The fuel used to provide the heat for pyrolysis is TPG. Its chemical composition was assumed as the one reported in Chapter 3.
- The reference or dead state is assumed to be 25 ºC (298.15 K) and 101 kPa.
- External fuel (*i.e.* natural gas) will be necessary to start up the system (transient state); nonetheless, the exergy and monetary cost of this stream was assumed insignificant in the exergy and economic model of the process, in contrast to the total exergy consumption.
- In the case of the alternative process in the model industrial plant, the reaction pathways between CaO and the volatile matter released from the WT particles may involve several endothermic and exothermic reactions. However, the energy required to carry out such reactions was considered negligible in the calculations in order to simplify the analysis.

In order to implement the TEC, the physical structures (Figure 6.2 and Figure 6.3) were mathematically represented by means of the incidence matrix: $\mathrm{A(n \times m)}$. $\mathrm{A(n \times m)}$ shows, in matrix form, how the components and the flows of a system interact [9]. This matrix is made by *n* rows (one for each component) and *m* columns, associated with the physical flows (streams) of the system. Each element $A_{i,j}$ has the information of the relationship of stream *j* with component *i*. The value of $A_{i,j}$ is 1 if stream *j* enters to component *i,* -1 if the stream leaves the component, and 0 if there is no relationship of that stream with the component.

The incidence matrix allows to express the thermodynamic analysis of the system as the solution of systems of linear equations: $\mathrm{A\dot{m} = 0}$, $\mathrm{A\dot{H} = 0}$, and $\mathrm{A\dot{E}} = Irreveribilities$, for mass, energy, exergy balances respectively. The vectors $\mathrm{\dot{m}(m \times 1)}$, $\mathrm{\dot{H}(m \times 1)}$, and $\mathrm{\dot{E}(m \times 1)}$ contain information regarding the mass flow rates, enthalpies, and exergies of every stream in the system, respectively, obtained in the previous step from the thermodynamic analysis. $\mathrm{A(n \times m)}$ for the industrial-scale and lab-scale pyrolysis plants are presented in Appendix E.

6.2.2 Productive structure

Table 6.1 and 6.2 show the productive structure of the lab-scale and the model industrial plants, respectively. In the productive structure, physical inputs and outputs of every component in the system were divided into fuels and products, both in exergy terms. Here, products are related to the purpose of the component, while fuels are linked to the resources used for this purpose. The productive structure can be expressed in a similar manner to $\mathrm{A(n \times m)}$, by means of two additional matrices corresponding to fuels $\mathrm{A_F(n \times m)}$, and products $\mathrm{A_P(n \times m)}$. The fuel of a component is made up by the streams the component requires to meet its purpose on the plant. The products are the streams making up the useful effects of the component. These matrices are built considering only entering and leaving streams to every component, when these are related to its fuel or product, respectively. Then, $\mathrm{A_F}$ and $\mathrm{A_P}$, in combination with $\mathrm{\dot{E}(m \times 1)}$ serve to calculate the total fuel (F), product

(P) for every component in the plant. The difference of F and P vectors results in the irreversibility vector (I). $\mathrm{A_F}$ and $\mathrm{A_P}$ are reported in Appendix E.

Table 6.1. Productive structure: Lab-scale plant

N.	*Component*	*Fuel*	*Product*
1	Reactor	$\dot{E}_5 + \dot{E}_8 + \dot{E}_9 + \dot{E}_{11}$	$\dot{E}_{12} + \dot{E}_{14}$
2	Feeding System	$\dot{E}_1 + \dot{E}_2 + \dot{E}_4 + \dot{E}_6$	$\dot{E}_5$
3	Electric Motor	$\dot{E}_7$	$\dot{E}_8$
4	Electric Heater	$\dot{E}_{10}$	$\dot{E}_{11}$
5	rCB Receiver	$\dot{E}_{12}$	$\dot{E}_{13}$
6	Condenser	$\dot{E}_{14}$	$\dot{E}_{15} + \dot{E}_{16} + (\dot{E}_{18} - \dot{E}_{17})$
7	TPG Burner	$\dot{E}_{16} + \dot{E}_{19}$	$\dot{E}_{20}$
8	Stack	$\dot{E}_{20}$	$\dot{E}_{21}$

Table 6.2. Productive structure: Model industrial plant

N.	*Component*	*Fuel*	*Product*
1	Reactor	$\dot{E}_5 + \dot{E}_8 + \dot{E}_9 + (\dot{E}_{30} - \dot{E}_{31}) + \boldsymbol{\dot{E}_{38}}$	$\dot{E}_{10} + \dot{E}_{12}$
2	Feeding System	$\dot{E}_1 + \dot{E}_2 + \dot{E}_3 + \dot{E}_4 + \dot{E}_6$	$\dot{E}_5$
3	Electric Motor	$\dot{E}_7$	$\dot{E}_8$
4	rCB Receiver	$\dot{E}_{10}$	$\dot{E}_{11}$
5	Condenser	$\dot{E}_{12}$	$\dot{E}_{13} + \dot{E}_{14} + (\dot{E}_{16} - \dot{E}_{15})$
6	Scrubber	$\dot{E}_{14}$	$\dot{E}_{20} + (\dot{E}_{19} - \dot{E}_{18})$
7	Solution Tank	$\dot{E}_{34}$	$\dot{E}_{17}$
8	Pump (Scrubber)	$\dot{E}_{21}$	$\dot{E}_{18} - \dot{E}_{17}$
9	Separation Unit	$\dot{E}_{20}$	$\dot{E}_{22} + \dot{E}_{23}$
10	Compressor TPG	$\dot{E}_{24}$	$\dot{E}_{25} - \dot{E}_{22}$
11	Fan (Burner)	$\dot{E}_{27}$	$\dot{E}_{28} - \dot{E}_{26}$
12	Preheater	$\dot{E}_{31} - \dot{E}_{32}$	$\dot{E}_{29} - \dot{E}_{28}$
13	Burner	$\dot{E}_{23} + \dot{E}_{29}$	$\dot{E}_{30}$
14	Stack	$\dot{E}_{32}$	$\dot{E}_{33}$
15	Recirculation Tank	$\dot{E}_{19}$	$\dot{E}_{36}$
16	Alternative Hopper*	$\boldsymbol{\dot{E}_{36} + \dot{E}_{37}}$	$\boldsymbol{\dot{E}_{38}}$

$\boldsymbol{\dot{E}_{36}, \dot{E}_{37}, \dot{E}_{38}}$ only considered in the alternative process

The main goal of the thermoeconomic approach is to determine the exergy and exergoeconomic costs of every flow in the system [12] , in particular those of the final products (TPO, rCB, and TPG). The exergy cost of a stream is defined as the amount of exergy needed to obtain the given stream inside the system. It serves as an indicator of the thermodynamic efficiency at all the stages of the production process. On the other hand, the exergoeconomic cost is defined as the amount of money consumed to generate a given stream or product. It can be considered as a measure of the economic efficiency of a system, which comprises the economic costs of the fuel consumed, as well as the investment and operation and maintenance costs of the plant. Unit costs are defined as the ratio of the respective cost (exergy or monetary based) and the exergy flow of the stream or product assessed [12]. The productive structure (Tables 6.1 and 6.2) provides *n* equations to calculate the aforementioned costs. Nevertheless, as the system has *m* streams, it is necessary to define *m – n* additional equations, which are stored in a new matrix: $\boldsymbol{\alpha}[(\mathrm{m}-\mathrm{n}) \times \mathrm{m}]$. These equations were obtained following the propositions of the TEC, established by Valero *et al*. [12]. This allows to obtain the cost matrix $\mathbb{A}(\mathrm{m} \times \mathrm{m})$ and the exergy amortization vector $\mathbb{Y}(\mathrm{m} \times 1)$, which make up a

system of linear equations that is solved to obtain the exergy costs of every stream in the system. To determine the exergoeconomic costs of the streams, it is necessary to consider the non-thermodynamic costs of the system, including purchase cost of the equipment (PCE), cost of external resources, etc. The economic model used to calculate the rate of non-thermodynamic costs is shown in Section E9, Appendix E. The parameters used for exergoeconomic analysis are listed in Table 6.3. In this particular case, and for the sake of comparison, the price of the feedstock (WT) was varied from -10 $/ton (most desirable case) and 100 $/ton (least desirable case) in order to assess its influence on the production cost of the pyrolysis products. A negative value in the price of the feedstock means that some revenue is obtained for waste processing, in this case WT.

Table 6.3. Parameters used for the economic model

Parameter	Value	Reference
Plant capacity	7,665 ton/year	Assumed
Effective annual interest rate for debt (*in*)	9 %/year	[15]
Annual inflation rate, (*ri)*[1]	3.51 %/year	[16]
Annual plant operation time, *N*	7920 h/year	Assumed
Plant lifetime, *a*	20 years	[17]
Construction time, *b*	2 years	Assumed
Maintenance factor, ϕ_k	1.1	[17]
Unit cost of electricity	0.12 $/kWh	[18]
Unit cost of WT[2]	-10 up to 100 $/ton	Assumed
Unit cost of powder CaO	0.050 $/kg	[19]

[1]The annual inflation rate is taken as that of 2019 [16]
[2]The unit cost of WT is associated with its pretreatment (granulation/separation)

In addition, information obtained from both manufacturers available online and *Honeywell UnitSim Design R461.1 Cost and Size Analyzer* was considered for defining the PEC of every component in the plant depending on their nominal capacities. The PEC, as well as the non-thermodynamic cost rate ($\dot{Z}_k$) are reported in Table E1 on Appendix E. The exergoeconomic cost balance was then conducted in similar manner to that of the exergy cost, using this time the thermoeconomic amortization vector $\dot{\mathbb{Z}}\,(\mathrm{m} \times 1)$**.** This procedure is also described in detail in Appendix E. At lab-scale, the pyrolysis plant went through several modifications, which were needed to guarantee a proper performance in the long term; thus, an accurate estimation of the final cost of each component in the plant is difficult to define. Accordingly, the exergoeconomic cost was not calculated in this case. However, this procedure was applied for the model industrial pyrolysis plant.

6.2.3 The fate of external resources into the system

The methodology developed by Agudelo *et al*. [8], which combines the TEC and the symbolic exergoeconomics [10], was applied to discriminate the exergy composition of the pyrolysis products (TPO, rCB, and TPG), as a function of the external resources (*i.e.* NR, SR, and CB). This methodology establishes that the exergy of streams is made up of as many types of exergy as the external resources have (Figure 6.4). The implementation of this methodology reveals the fate of energy resources through the streams and components of a system. According to Agudelo *et al*. [8], the above statement can be expressed mathematically

as shown in Equation 4.1. Here, ${}^{k}\dot{E}_i$ is the part of exergy flow *i* that comes from the external resource *k*, while n_f is the number of external resources of different nature the system has.

$$\dot{E}_i = \sum_{k=1}^{n_f} {}^{k}\dot{E}_i \qquad \textbf{(4.1)}$$

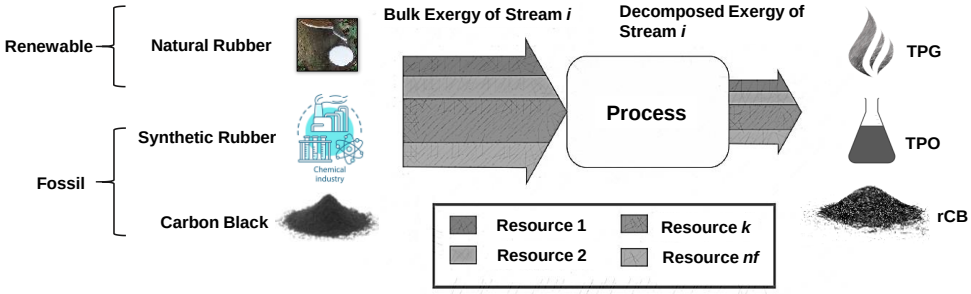

Figure 6.4. Exergy decomposition as a function of external resources: NR, SR, and CB

Similar to the exergy flows in TEC, the composition of exergy flows behaves as the unit exergy cost, which allows to use the complete mathematical structure of TEC and symbolic exergoeconomics [10]. Therefore, the auxiliary equations required in the calculations of exergy decomposition are determined in a similar manner as those for the thermoeconomic analysis. As such, the decomposed exergy flow can be obtained in line with Equation 4.2. In this equation, ${}^{k}\dot{E}_e$ is a vector of length *m* that is made by zeros, except for the flows corresponding to the inputs of external resource *k*. This vector is easily built in accordance with the system inputs. In addition, ${}^{k}P$ is related to the decomposed products. The methodology followed to determine the parameters in this equation is presented in Appendix E, Section E4.

$${}^{k}\dot{E} = A_P^{(-1)}\left({}^{k}P - A_P\,{}^{k}\dot{E}_e\right) + {}^{k}\dot{E}_e \qquad \textbf{(4.2)}$$

6.3 Results and discussion

6.3.1 Thermodynamic analysis of the pyrolysis process: Lab-scale and model industrial plants

Table E3 on Appendix E lists the thermodynamic characteristics of all of the streams in the pyrolysis plant at lab-scale, including temperature (T), pressure (P), mass flow rate ($\dot{m}$), energy ($\dot{H}$), and exergy ($\dot{E}$). At lab-scale level, the energy needed to perform the pyrolysis process (heat for pyrolysis) was found to be 700 Wh. Herein, the sensible and reaction heats represent 48 % and 52 %, respectively, of the total energy demanded by the process. The main differences of this plant, in regard to the proposed model industrial one is the use of electricity (external resource) to obtain the heat for pyrolysis, rather than hot gases produced in the combustion of TPG. Moreover, TPG is transformed into combustion products in a burner, yet these gases are not used in the process. These combustion products are released into the atmosphere, which ultimately results in exergy destruction. In this case TPG cannot be considered as a product of the system, being TPO and rCB the only products. Taking this into account, the exergy efficiency of the process at lab-scale is 75 %, approximately.

Similarly, Table E2 on Appendix E lists the thermodynamic characteristics of all streams in the reference and the alternative processes for the model plant, including temperature (T), pressure (P), mass flow rate ($\dot{m}$), energy ($\dot{H}$), and exergy ($\dot{E}$). The energy needed to conduct the pyrolysis process at industrial level was found to be 611 kWh and 629 kWh for the reference and alternative process, respectively. In the alternative process, the addition of CaO represented a slight increase in exergy demand of 3.0 % in contrast to the reference process. This additional energy is associated with the sensible heat required to rise the CaO temperature from the room (25 ºC) to the pyrolysis conditions (475 ºC). This result suggests that the use of CaO as a low-cost catalytic material in the pyrolysis of WT does not imply significant changes in the process from an energy point of view. Nevertheless, and as discussed in Chapter 3, it has a positive influence on the physicochemical properties of the pyrolysis products, in particular those of TPO (*i.e.* sulfur reduction). According to this energy demand, around 30% of the TPG (stream 20), which is previously cleaned in the scrubber, is needed to supply the heat for pyrolysis. The combustion products of TPG (stream 30) enter the pyrolyzer at 988 ºC and leave the process at 400 ºC. After providing the heat for pyrolysis (stream 31), 137 kW and 158 kW are available to preheat the air used in the combustion process to a temperature of 348 and 330 ºC in the reference and the alternative processes, respectively. Preheating the combustion air significantly reduces the irreversibilities of the combustion system, as will be evidenced when compared with the lab-scale plant where the air enters into the chamber at room conditions. The remaining 70% of the TPG gases (stream 22) is stored to be further used in other energy demanding process. In fact, enough exergy (~ 1500 kW in both cases) is available not only to generate the electricity needed to operate the equipment of the plant (compressor, pumps, motors, etc.), but also extra electrical energy can be sold for revenue. Based on the obtained information, the exergy efficiency is ~ 92 % for the studied cases. This remarkable high efficiency can be attributed to the fact that tires, which represent a significant amount of exergy (chemical exergy) input, are transformed into products (TPO, rCB, and TPG) that also exhibit a high content of chemical exergy. Moreover, it is clear that external inputs (fuels) are needed to initiate the pyrolysis process as mentioned before. However, once the process reaches the steady state, it is autonomous.

Based on the obtained results, it is noticed that the efficiency of the lab-scale plant is almost 20 % lower than that of the proposed model industrial plant. This may indicate the multitude of benefits that would arise from scaling and modifying the process. Figure 6.5 illustrates how the exergy of external resources (mainly WT) is distributed into the pyrolysis derived products (TPO, rCB, and TPG) in both the industrial and the lab-scale plants.

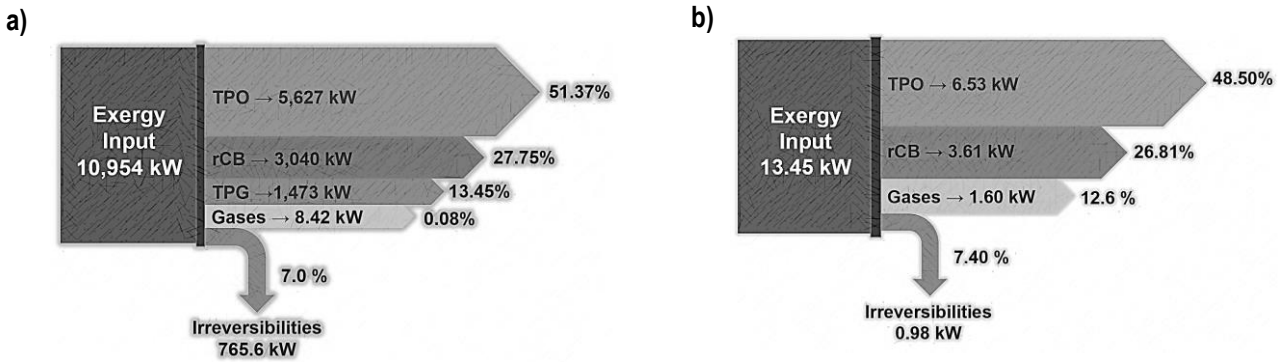

Figure 6.5. Exergy distribution in the pyrolysis plant: **a)** industrial plant, **b)** lab-scale plant

Tables E4 and E5 on Appendix E show the exergy balance by component for the industrial scale and lab-scale plants, respectively. In this tables, the total fuel, products, and exergy destruction rates for every component in both plants are reported. For a better visualization, Figure 6.6 shows the exergy destruction ratio of components, as well as the total exergy destruction rate ($\dot{E}_{d,T}$) of every component in the model industrial and lab-scale plants.

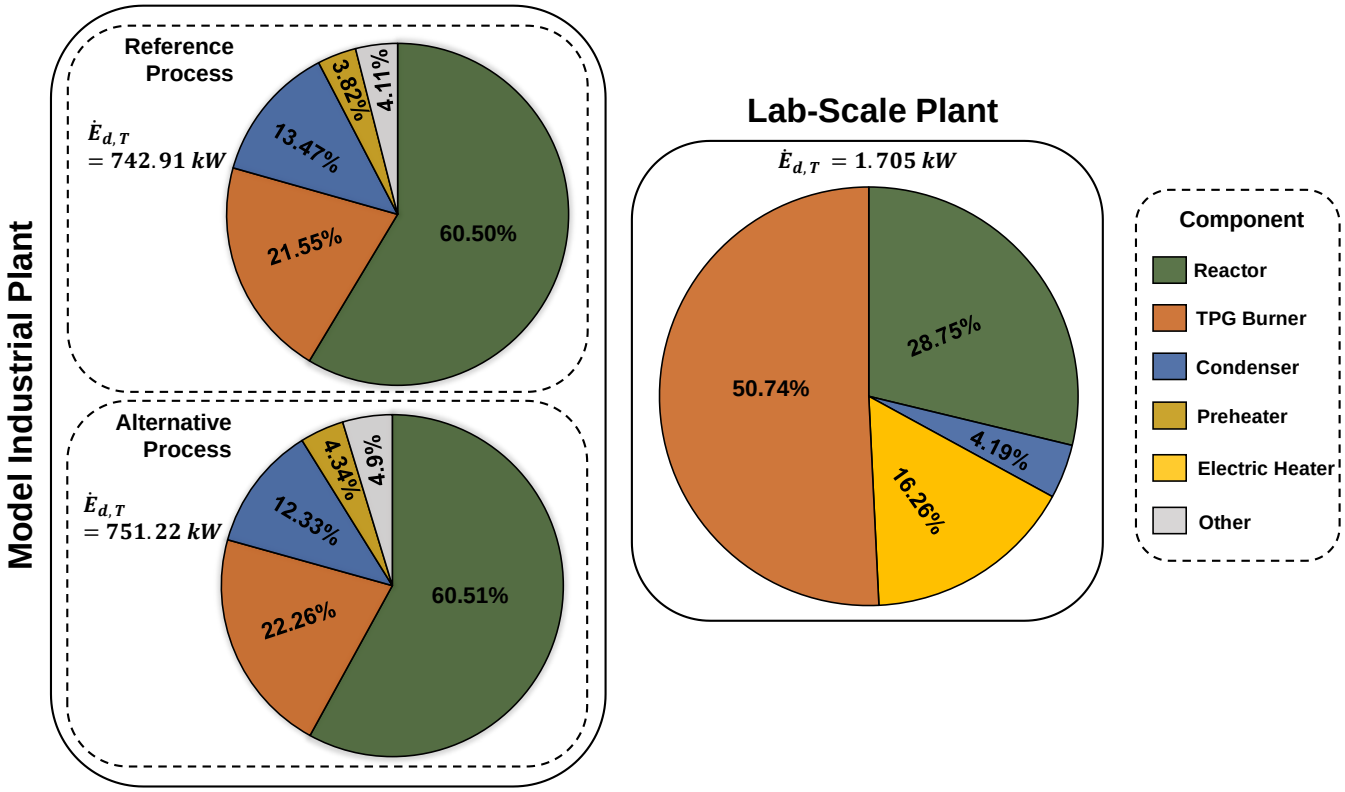

Figure 6.6. Exergy destruction ratio by component

It is observed that the components with higher irreversibilities in the model industrial plant are the pyrolyzer (~ 60%), the burner (~ 22%), and the condenser (~ 13%). In the case of the pyrolyzer and the burner, the high exergy destruction rates are caused by the irreversibilities associated with the pyrolysis reactions (WT to pyrolysis products) and oxidation reactions (to produce thermal energy). In addition, some irreversibilities arise in the burner due to the mixing of high temperature combustion products with colder gases. Thus, the overall irreversibilities of the burner are significantly reduced by preheating the air before entering into the combustion chamber, and in this manner, the fuel consumption to obtain the heat for pyrolysis is reduced. Regarding the condensing unit, heat is removed from stream 12 for TPO recovery. In turn, the exergy that is gained by stream 16 becomes a waste of the system. The addition of CaO in the pyrolysis process does not have a significant effect on the irreversibilities of the pyrolyzer, yet this effect is more notorious in the burner due to slight increase of the exergy demanded to perform the process. In fact, the addition of CaO resulted in an increase of 14% of the fuel (TPG) consumption (from 41 to 47 kg/h). The scrubber does not have a significant influence on the total irreversibilities of the system since the removal of H_2S and CO_2 from TPG has a weak effect on the exergy content of the involved streams. The stack does not present any irreversibilities because this component is only used to release the combustion gases into the atmosphere without changing their exergy. Other

components such as the rCB receiver, the scrubbing tanks, and the TPG separation unit are assumed as reversible components (zero exergy destruction). In the case of the lab-scale plant, and different to the process at industrial scale, the highest exergy destruction rate is found in the TPG burner (50%). This is primarily because the combustion air enters into the combustion chamber at room temperature, along with the inherent irreversibilities that arise from oxidation reactions. Likewise, the electric heater significantly contributes to the irreversibilities of the overall process (16%), which is avoided in the model industrial plant by heating the reactor with the combustion gases. This fact can be attributed to the high amount of external resources (in this case electricity) that has to be consumed to generate a unit of heat in this component. Even though electric heaters are highly energy efficient (above 85 %), their exergy efficiency could be even lower than 10 %, which represents a high exergy destruction rate [20]. This fact reinforces the idea of using non-condensable gases (TPG) to fulfill the energy demand when scaling up the process.

6.3.2 Thermoeconomic analysis of the pyrolysis process

By applying the thermoeconomic principles, the exergy cost, unit exergy cost, and exergoeconomic cost (only calculated for the model industrial plant) were determined for every stream and reported in Table 6.4 and Table 6.5 for the lab-scale and the model industrial plant, respectively. The exergoeconomic cost reported in Table 6.6 is calculated assuming a WT price of 55 $/ton.

Tables 6.4. Exergy cost of streams: Lab-scale plant

Stream	*C (W)*	*c(W/W)*
1	4341	1.00
2	5161	1.00
3	3204	1.00
4	0.00	1.00
5	12707	1.00
6	1.00	1.00
7	1.23	1.00
8	1.23	1.05
9	0.094	1.00
10	747.10	1.00
11	747.10	1.60
12	3827.58	1.06
13	3827.58	1.06
14	9627.84	1.06
15	6979.48	1.07
16	2642.04	1.07
17	0.00	1.00
18	6.33	1.07
19	0.00	1.00
20	2642.04	1.65
21	2642.04	1.65

Tables 6.5 Exergy and exergoeconomic cost of the streams in the pyrolysis industrial plant

Stream	C (kW)		c (kW/kW)		c ($/kWh)	
	Ref.	Alt.	Ref.	Alt.	Ref.	Alt.
1	3742.34	3742.34	1.00	1.00	6.38	6.38
2	4449.34	4449.34	1.00	1.00	7.59	7.59
3	2762.34	2762.34	1.00	1.00	4.71	4.71
4	0.00	0.00	1.00	1.00	0.00	0.00
5	10954.02	10954.02	1.00	1.00	24.32	24.32
6	0.01	0.01	1.00	1.00	0.0012	0.0012
7	0.01	0.01	1.00	1.00	0.0015	0.0015
8	0.01	0.01	1.05	1.05	0.04	0.04
9	0.08	0.08	1.00	1.00	0.00	0.00
10	3230.30	3248.28	1.06	1.06	20.71	20.85
11	3230.30	3248.28	1.06	1.06	20.71	20.85
12	8372.20	8373.38	1.06	1.06	53.68	53.75
13	6056.16	6058.24	1.08	1.08	39.38	39.44
14	2291.37	2292.16	1.08	1.08	14.90	14.92
15	0.00	0.00	1.00	1.00	0.00	0.00
16	24.67	22.98	1.08	1.08	0.16	0.15
17	0.00	0.00	1.00	1.00	1.55	1.55
18	0.00	0.00	2.47	2.47	1.64	1.64
19	0.00	0.00	2.30	2.46	1.64	1.64
20	2291.37	2292.16	1.08	1.08	22.62	22.64
21	0.00	0.00	1.00	1.00	0.00	0.00
22	1629.92	1609.39	1.08	1.08	16.09	15.90
23	661.45	682.78	1.08	1.08	6.53	6.74
24	1.12	1.12	1.00	1.00	0.13	0.13
25	1631.04	1610.50	1.08	1.08	16.35	16.16
26	0.00	0.00	1.00	1.00	0.00	0.00
27	0.02	0.02	1.00	1.00	0.0024	0.0024
28	0.02	0.02	1.45	1.20	0.02	0.02
29	200.52	233.95	1.99	2.02	2.48	2.85
30	861.97	916.73	1.55	1.58	9.86	10.44
31	213.59	249.20	1.55	1.58	2.44	2.84
32	13.09	15.27	1.55	1.58	0.15	0.17
33	13.09	15.27	1.55	1.58	0.15	0.17
34	0.00	0.00	1.00	1.00	0.00	0.00
35	0.00	0.00	2.30	2.46	3.19	3.19
36	--	0.00	--	1.00	--	7.5
37	--	0.01	--	1.00	--	0.0012
38	--	0.01	--	0.01	--	0.02

It is noticed in both cases that the flows with the highest unit exergy cost are those located at the end of the process, because they are affected by the irreversibilities of all components upstream in the system. Nonetheless, in the lab-scale plant, the highest unit exergy cost is found in the heat flow (stream 11) needed to perform the pyrolysis process. In this case, the high unit

exergy cost of this stream is only influenced by the exergy destruction rate caused by the electric heating system. In an electrical resistance space heater, almost all the electricity that enters the unit is dissipated to heat within the space. Thus, the energy efficiency is nearly 100% and there are almost not energy losses. Yet, as mentioned before, the exergy efficiency of such a device is typically less than 10% because it uses pure exergy to produce heat, which has much less exergy [20]. The addition of CaO has a minor influence on the exergy and exergoeconomic cost of every stream.

Tables 6.6 and 6.7 list the exergy and exergoeconomic (only for the model industrial plant) costs of products of every component in the lab-scale and industrial pyrolysis plant, respectively. The exergy cost of products and fuels for each component are equal if the cost balance was correctly conducted. It is noticed that the highest exergy costs of products are found in the pyrolysis reactor and the condenser. This is attributed to the fact that the main products of the plant are formed in these two components.

Table 6.6. Exergy cost of components: Lab-scale plant

Component	***Cost of Product (W)***
Reactor	13455.42
Feeding System	12707.00
Electric Motor	1.23
Electric Heater	747.10
rCB Receiver	3827.58
Condenser	9627.84
TPG Burner	2642.04
Stack	2642.04

Table 6.7. Exergy and thermoeconomic costs of the components: Model industrial pyrolysis plant (WT price: 55 $/ton)

Component	***Cost Product (kW)***		***Cost Fuel ($/kWh)***		***Cost Product ($kW/h)***	
	Ref.	***Alt.***	***Ref.***	***Alt.***	***Ref.***	***Alt.***
Reactor	11602.50	11621.65	31.78	31.97	74.39	74.60
Feeding System	10954.02	10954.02	18.69	18.69	24.32	24.32
Electric Motor	0.01	0.01	0.00	0.00	0.04	0.04
rCB Receiver	3230.30	3248.28	20.71	20.85	20.71	20.85
Condenser	8372.20	8373.38	53.68	53.75	54.44	54.51
Scrubber	2291.37	2292.16	14.90	14.92	22.62	22.64
Solution Tank	0.00	0.00	0.00	0.00	1.55	1.55
Pump (Scrubber)	0.00	0.00	0.00	0.00	0.09	0.09
Separation Unit	2291.37	2292.16	22.62	22.64	22.62	22.64
Compressor TPG	1.12	1.12	0.13	0.13	0.26	0.26
Fan (Burner)	0.02	0.02	0.00	0.00	0.02	0.02
Preheater	200.50	233.93	2.29	2.66	2.46	2.83
Burner	861.97	916.73	9.01	9.59	9.86	10.44
Stack	13.09	15.27	0.15	0.17	0.15	0.17
Recycling Tank	0.00	0.00	1.64	1.64	3.19	3.19
Alternative Hopper		0.01		0.00		0.02

Regarding the exergoeconomic cost of the derived-pyrolysis products, the production costs of TPO, rCB, and TPG were found to be 27.13 – 48.17, 14.18 – 25.40, 13.06 – 18.72 $/h, respectively, when the price of WT vary from -10 to 100 $/ton . Based on this information, and taking into account a TPO production rate of 505 L/h, rCB production rate of 410 kg/h, and TPG production rate of 180 m^3/h, the production cost of TPO, rCB, and TPG is 0.054 – 0.095 $/L, 0.035 – 0.062 $/kg, and 0.0082 – 0.012 $/kWh, respectively, as shown in Figure 6.7. In Figure 6.7, the production costs of TPO, rCB, and TPG are determined for different scenarios in terms of feedstock price. Additional post-treatments (that are not included in this analysis) may influence the final production cost of these products, in particular for TPO and rCB, depending on their practical applications. The cleaning process of TPG has been already included in the analysis. In turn, TPG could be used straight away without further upgrading. It is worth noting that the exergoeconomic analysis only considers the production cost, without including the profits from selling. Nevertheless, the obtained values can be used as reference to assess the economic performance of the pyrolysis plant as a potential alternative for WT valorization. The results provided by the thermoeconomic analysis are of great importance, since it was possible to objectively determine the production cost of the pyrolysis-derived products simultaneously. This would not have been possible with a conventional economic analysis. These results are also fundamental in order to establish the commercial value of TPO, rCB, and TPG, which will define the profitability and competitiveness of the pyrolysis plant in the long term.

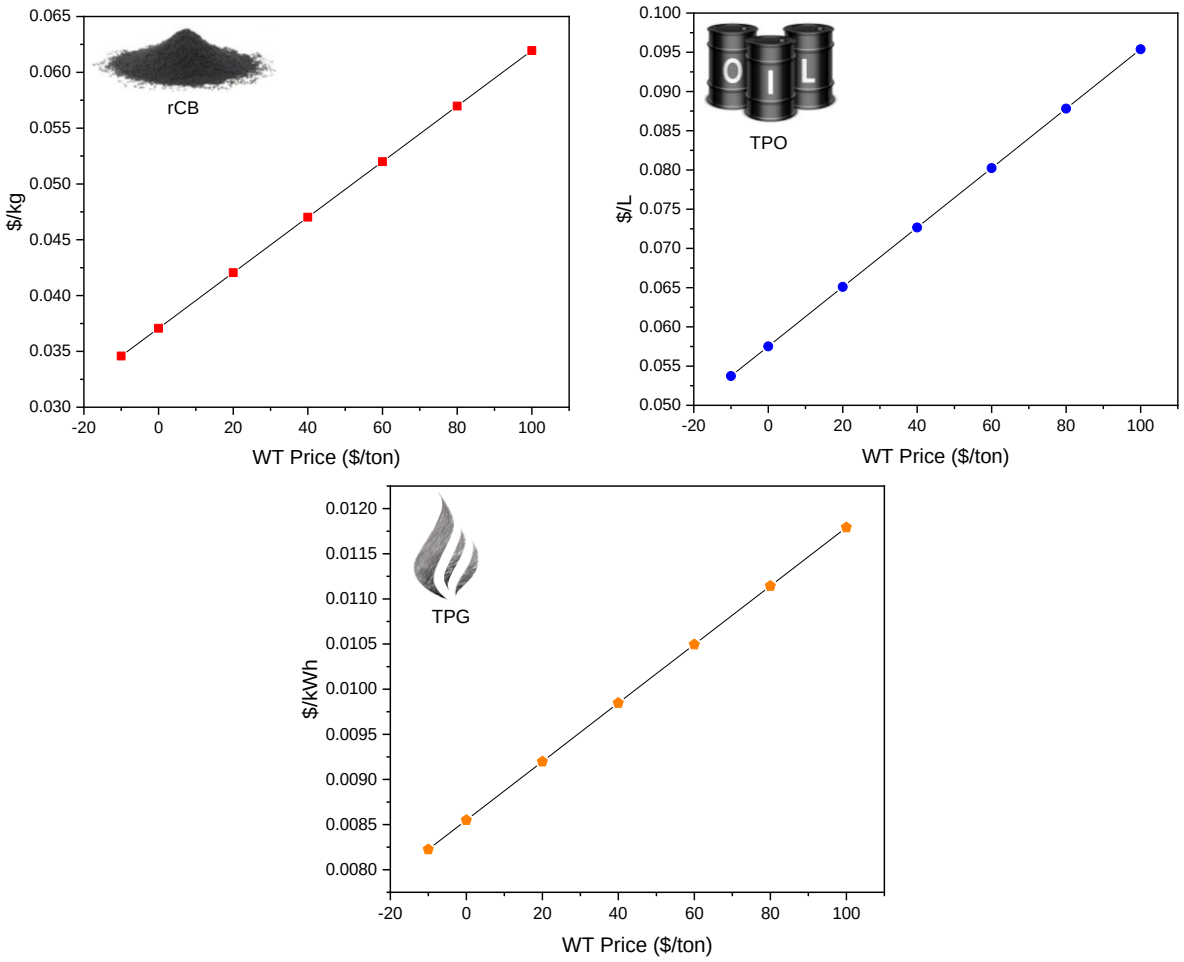

Figure 6.7. Variation in the exergoeconomic cost of the pyrolysis products as a function of the cost of the feedstock (WT)

To put the production cost of TPO (0.054 – 0.095 $/L) into perspective, the cost of fuel oil in Aug 2020 was 0.28 $/L [18]. Despite the additional potential increases in production cost associated with, *i.e.* upgrading steps, transportation, etc., TPO still has a high potential for competitiveness in the fuel oil market, from an economic point of view. Furthermore, this low production cost, along with the compatibility of TPO with existing refineries, and its renewable characteristics (as will be shown later), amplifies its attractiveness and competitiveness. In the case of TPG, its production cost (0.0082 – 0.012 $/kWh) is competitive in comparison to the price of natural gas in Colombia in March 2020 (0.045 $/kWh). Regarding rCB, its value is not dependent on its exergy content; rather, its physicochemical/textural characteristics determine its applicability, and thus its commercial value. As mentioned in Chapter 2, the most straightforward alternative for the use of rCB is as a substitute for commercial carbon black (CB) in rubber formulations. Currently, conventional CB exhibits a high commercial value that varies from $ 700 - 1200 per ton, depending on the grade and market fluctuation. Therefore, given the relatively low production cost of rCB in comparison to that of CB, along with its minimal environmental impact (*i.e.* CO_2 reduction), this material presents a great market attractiveness. Likewise, a work conducted by Martínez *et al*. [21] demonstrated that the acid treatment for rCB demineralization is feasible and applicable at industrial scale.

6.3.3 Assessment of improvement potentials

In general, the above-described results imply that reducing the electricity consumption of the plant is a straightforward way to improve its exergy efficiency. Even though motors and compressors are responsible for some of the irreversibilities of the process, they are usually well-engineered standard components, and the potential for further reducing their electricity consumption (*i.e.*, by more efficient equipment) is linked to high costs. Nonetheless, and as mentioned before, TPG is able to provide both the exergy needed to perform the pyrolysis process and the electrical exergy required to operate these additional pieces of equipment. Therefore, the highest potential of increasing the exergy efficiency when scaling up the process is by modifying the way the pyrolyzer is heated. In addition, it has been established that in fuel-fired industrial processes, one of the most effective ways to improve efficiency and productivity is to preheat the combustion air going into the burner. Extracting thermal exergy from the flue gases leaving the reactor and transferring it to the incoming combustion air will reduce the fuel consumption in the combustor, and thus its irreversibilities. This has been evidenced in this study by contrasting the process at industrial and lab-scale. For the proposed model industrial plant, reducing the fuel consumption of the combustor will be economically favorable, since more exergy coming from the TPG stream will be available to drive other energy related processes, which will be reflected in the total revenue of the plant. The auger pyrolyzer also significantly contributes to the exergy destruction rate of the overall process, as a result of the chemical reactions taking place on it. However, the potential for improving the exergy efficiency in this component is quite limited, because modifying the operating conditions would imply changes in the pyrolysis-derived product yields, in addition to their related physicochemical properties. The pyrolysis conditions have already been fixed to reach a balance between high TPO yields while obtaining rCB with adequate properties. Thereby, this component leaves little room for improving the performance of the overall plant from an exergy point of view.

6.3.4 Exergy discrimination by external resources

Table E6 on Appendix E shows the contribution of the external resources (NR, SR, and CB) to the exergy content of every stream in the model pyrolysis plant. In addition, the distribution percentage of exergy considering both renewable and fossil origin is reported. For simplifying the analysis, Table 6.8 reports the exergy decomposition of TPO, rCB, TPG, and the combustion gases leaving the plant. An important result from distinguishing between the exergy of every stream according to the external resources is to confirm that around 50 % of the exergy content of TPO and TPG comes from the NR, thus highlighting their renewable characteristics. It is also noticed in Table 6.7 that this exergy distribution is then conserved along the process, after the volatile matter stream (stream 12) and the rCB leave the pyrolizer. These results endorse the statement that the use of TPO and TPG as alternative fuels is in line with the worldwide guidelines regarding the promotion of renewable energy, *e.g.* the 2009/28/EC European directive, as discussed before in Chapter 1. In addition, it is also noticed that, similar to TPO and TPG, 47 % of the energy of the combustion gases released into the atmosphere come from renewable resources, which implies reduced net carbon emissions. This gives rise to several benefits for this project, *i.e.* in terms of carbon credits.

Table 6.8. Exergy decomposition

Stream	*Natural Rubber*	*Synthetic Rubber*	*Carbon Black*	*Total*	*Exergy Distribution*	
	E_1 (kW)	*E_2 (kW)*	*E_3 (kW)*	*E_T (kW)*	*Renewable (%)*	*Fossil (%)*
rCB	0.00	0.00	3039.97	3039.97	0.00	100
TPO	2631.88	2995.06	0.00	5626.94	46.77	53.23
TPG	707.67	805.32	0.00	1512.98	46.77	53.23
Stack Gases	3.94	4.48	0.00	8.42	46.77	53.23

6.4 Summary

This chapter presents a thermoeconomic analysis of a model WT pyrolysis plant at industrial scale with a nominal capacity of 1,000 kg/h. This was proposed based on an exhaustive experimental campaign in a lab-scale twin auger reactor, which was described in previous chapters. The characteristics (enthalpies and exergies) of every stream in the plant were determined considering their chemical composition, as well as their operating conditions. Subsequently, this information was utilized to perform mass, energy, and exergy balances not only for each component, but also for the overall process; thus, the exergy efficiency could be calculated. The same methodology was then applied to the process conducted at lab-scale, in order to identify some of the benefits of scaling and modifying the pyrolysis process form an exergy point of view. In addition, the exergy analysis was combined with the thermoeconomic principles to estimate the exergy and exergoeconomic cost of every stream. Through this analysis, it was found that scaling and modifying the process may result in an increase in the plant's exergy efficiency of around 20%, in contrast to the process conducted at lab-scale. This has been attributed to the benefits of using TPG as an exergy source by supplying heat to the pyrolysis process, rather than using external resources, *i.e*. electricity. A high exergy destruction is found in the pyrolizer and the burner, which is mainly associated with the chemical reactions taking place in these two components. The exergy cost balance revealed that those streams located at the end of the process exhibit a higher unit exergy economic cost due to the influence of all component irreversibilities in the plant on their exergy characteristics.

In terms of monetary units, the production cost of TPO, rCB, and TPG was found to be 0.054 – 0.095 $/L, 0.035 – 0.062 $/kg, and 0.0082 – 0.012 $/kWh, respectively, condering a feedstock price variation between -10 $/ton (most desirable case) and 100 $/ton (least desirable of pessimistic case) . Finally, an exergy decomposition analysis confirmed that almost 50 % of the exergy of TPO and TPG comes from renewable resources, namely NR. Therefore, their use as fuels is in line with the worldwide guidelines regarding the promotion of renewable energy, *e.g.* the 2009/28/EC European directive. Furthermore, benefits regarding carbon credits can be obtained for this project, given that 47 % of the energy in the combustion gases leaving the plant come from renewable resources (NR), which implies a reduction of the net carbon emissions.

References

[1] G. Liu, Development of a general sustainability indicator for renewable energy systems: A review, Renew. Sustain. Energy Rev. 31 (2014) 611–621.

[2] A.C. Brent, J.K. Visser, An environmental performance resource impact indicator for life cycle management in the manufacturing industry, J. Clean. Prod. 13 (2005) 557–565.

[3] D. Kourkoumpas, G. Benekos, N. Nikolopoulos, S. Karellas, P. Grammelis, E. Kakaras, A review of key environmental and energy performance indicators for the case of renewable energy systems when integrated with storage solutions, Appl. Energy. 231 (2018) 380–398.

[4] J. Szargut, Exergy method: technical and ecological applications, WIT Press, 2005.

[5] T.J. Kotas, The exergy method of thermal plant analysis, Elsevier, 1985.

[6] S. Usón, A. Valero, A. Agudelo, Thermoeconomics and industrial symbiosis. Effect of by-product integration in cost assessment, Energy. 45 (2012) 43–51.

[7] M.A. Rosen, I. Dincer, Exergy as the confluence of energy , environment and sustainable development, Exergy, an Int. Journall. 1 (2001) 3–13.

[8] A. Agudelo, A. Valero, S. Usón, The fossil trace of CO2 emissions in multi-fuel energy systems, Energy. 58 (2013) 236–246.

[9] M.A. Lozano, A. Valero, Theory of exergy cost, Energy. 18 (1993) 939–960.

[10] C. Torres, A. Valero, C. Cortes, Application of symbolic exergoeconomics to thermal system simulation, Am. Soc. Mech. Eng. Heat Transf. Div. 124 (1989) 75–84.

[11] E. Uresin, H.I. Saraç, A. Sarioglan, F. Akgun, An experimental study for H2S and CO2 removal via caustic scrubbing system, Process Saf. Environ. Prot. 94 (2014) 196–202.

[12] A. Valero, S. Usón, C. Torres, W. Stanek, Theory of exergy cost and thermo-ecological, in: Thermodyn. Sustain. Manag. Nat. Resour., Springer, 2017: pp. 167–202.

[13] J.D. Martínez, R. Murillo, T. García, A. Veses, Demonstration of the waste tire pyrolysis process on pilot scale in a continuous auger reactor, J. Hazard. Mater. 261 (2013) 637–645.

[14] J.D. Martínez, N. Puy, R. Murillo, T. García, M.V. Navarro, A.M. Mastral, Waste tyre pyrolysis - A review, Renew. Sustain. Energy Rev. 23 (2013) 179–213.

[15] P. Badger, S. Badger, M. Puettmann, P. Steele, J. Cooper, Thecno-economic analysis: Preliminary assessment of pyrolysis oil production costs and material energy balance associated with a transportable fast pyrolysis system,

Bioresources. 6 (2011) 34–47.

[16] Banco de la República (Banco de Colombia), Consumer Price Index, 2020.

[17] M.M. Wright, J.A. Satrio, R.C. Brown, D.E. Daugaard, D.D. Hsu, Techno-economic analysis of biomass fast pyrolysis to transportation fuels, Natl. Renew. Energy Lab. (2010) 1–73.

[18] Global Petrol Prices, Electricity prices, (2020). https://www.globalpetrolprices.com/electricity_prices/ (accessed November 12, 2020).

[19] Uthaya Chemicals, Quicklime, (2020). https://www.uthayachemicals.in/ (accessed November 30, 2020).

[20] M.A. Rosen, C.A. Bulucea, Using exergy to understand and improve the efficiency of electrical power technologies, Entropy. 11 (2009) 820–835.

[21] J.D. Martínez, N. Cardona-Uribe, R. Murillo, T. García, and J.M. López, Carbon black recovery from waste tire pyrolysis by demineralization : Production and application in rubber compounding, Waste Manag. 85 (2019) 574–584.

Chapter 7. Conclusions and future works

7.1 Conclusions

This dissertation aimed to (i) study the potential of pyrolysis and the twin-auger technology for the valorization of WT within the framework of the circular economy, (ii) explore *in-situ* and *ex-situ* upgrading strategies for TPO, and (iii) develop a deep understanding of the properties affecting its combustion characteristics. In addition, to put it into perspective, insights regarding the benefits of scaling and modifying the pyrolysis process, as well as the assessment of improvement potentials were possible by applying the thermoeconomic principles. This closing chapter summarizes the main conclusions of this investigation in accordance with the specific objectives established in Chapter 1.

- Regarding the specific objective 1 (addressed in Chapter 2 and Chapter 3)

The analysis presented in Chapter 2 was a fundamental step towards achieving the specific objectives regarding TPO production. The application of the central composite design (CCD) in combination with the ANOVA test revealed that the reactor temperature and the WT mass flow rate exhibited the greatest influence on the yields of both TPO and rCB within the experimental domain considered for this work. In addition, the multiple response optimization showed that the twin-auger pyrolysis plant can satisfactorily transform WT into TPO (45 wt.%), rCB (40 wt.%), and TPG (15 wt.%) when operated at 475 °C, 1.16 kg/h of WT, 3.5 min of solid residence time, and 300 mL/ min of N_2. Likewise, a repeatability analysis based on the ANOVA test aided at demonstrating that the experimental facility is repeatable in terms of TPO, rCB, and TPG yields. The standard deviation and absolute error calculated from the characterization of different product samples also suggested that the physicochemical properties of TPO, rCB, and TPG obtained at the same experimental conditions are consistent. The obtained results are expected to contribute to the development of reliable technology in the circular economy framework. The data provided in this initial phase of the research serves as first step to move forward to larger scales through the different stages of the Technology Readiness Levels (TRL).

Regarding the sulfur content in TPO (one of the main limitations when considered as alternative fuel), the addition of 15 wt. % of CaO during the pyrolysis of WT, resulted in a sulfur reduction of 26.40 wt.%. In addition, the influence of CaO was also evidenced on other physiochemical properties of TPO such as a reduction of the viscosity, which boots its potential as a fuel in combustion facilities. Although the ash content of rCB[CaO] was significantly high after pyrolysis (57.5 wt.%), an acid demineralization step was effective at removing 80 wt.% of its inorganic content; in turn, this process improved its surface area and porosity. Regarding TPG[CaO], an increase in the amount of H_2 and some CxHy compounds (*i.e.* C_3H_8, C_2H_6, and C_2H_4), while a decrease in CO_2, CO, and H_2S ones revealed the participation of CaO in several reactions during the pyrolysis of WT. Based on its energy content (27 MJ/Nm^3), TPG is able to provide not only the heat for pyrolysis, but also an extra amount is available for other energy applications, *e.g.* power generation. Overall, *in-situ* desulfurization using CaO can be considered a promising pathway as a first attempt to improve the properties of TPO and TPG. Nonetheless, the limitations of this alternative

are delineated by the impact on the characteristics of rCB, which must be carefully assessed to guarantee the profitability of the pyrolysis process at larger scale.

- Regarding specific objectives 2 and 3 (addressed in Chapter 4)

This stage the research pursued an in-depth understanding of TPO and TPO[CaO], utilizing advanced analytical techniques such as APPI FT-ICR MS and ^{1}H and ^{13}C NMR. HC compounds in TPO and TPO[CaO] were found mainly in the form of tri-aromatics (26 %), tetra-aromatics (13 and 15 %), and penta-aromatics (22 and 30 %), while S_1 compounds in the form of dibenzothiophene (31 %) and benzonaphthothiophene (34 %), which confirms the aromatic nature of both fuels. According to these results, oxidative desulfurization could be more suitable for TPO, considering its higher selectivity in removing aromatic sulfur compounds compared to other techniques such as hydrodesulfurization. The structural level characterization of TPO and TPO[CaO] aided at confirming the catalytic/cracking effect of CaO during the pyrolysis of WT due to the formation of new compounds in TPO, including olefinic, naphthenic, and protonated aromatic hydrocarbons, among others.

On the other hand, as a result of the complexity of TPO and wide carbon number range (C_6-C_{56}), separating it into distinct fractions by distillation was considered as a promising alternative to expand the range of possibilities and feasibility in specific applications. Indeed, properties such as viscosity, density, and heating value suggested that TPO fractions can be comparable to petroleum-derived fuels such as gasoline (light fraction), diesel (low-middle fraction), distillate marine fuels (high-middle), and bitumen (heavy fraction); for this reason, similar applications to those established for these conventional fuels can be considered. In addition, the use of distillation to divide TPO[CaO] into different fractions allowed concentration of sulfur containing compounds and highly aromatic structures in the heaviest fraction, in turn improving the characteristics of the lightest fractions. In this way, application and upgrading strategies could be established more effectively for each fraction individually, rather than for the raw TPO. For example, according to the characteristics of the sulfur containing compounds in the heavy fraction (obtained with FT-ICR MS), oxidative desulfurization can be also a potential upgrading pathway. In the case of the other fractions, severe post-treatments can be minimized or even avoided (*i.e.* light fraction).

- Regarding first part of the specific objectives 4 (addressed in Chapter 5)

The information presented in this part of the research aimed at contributing to scarcely available data in the scientific literature regarding the fundamental combustion characteristics of TPO and its distillate fractions. Initially, a thermogravimetric analysis of TPO and TPO[CaO] allowed the identification of important combustion characteristics such as the initial decomposition temperature, maximum temperature, and burnout temperature were determined for each fuel. The thermogravimetric analyzer used in this study was coupled with a Fourier Transform Infrared (FT-IR) spectrometer, which allowed for obtaining valuable information regarding the real-time compositional changes of the evolved gases during the oxidation processes of these fuels, giving special attention to pollutants such as CO_2, CO, SO_2, NO. According to the obtained results and contrasting with the information reported in the literature, it was noticed that TPO and TPO[CaO] exhibit similar oxidation behavior to that of light oil.

Regarding the light distillate fraction of TPO[CaO] (TPO[CaO]$_{Light}$), a surrogate fuel was successfully formulated to replicate some of its physical and chemical properties, as well as combustion features. Thus, pyrolysis experiments were further conducted with the surrogate fuel in order to identify the PAHs formation tendency of TPO[CaO]$_{Light}$. Results revealed that there is a high tendency of forming PAHs at temperatures higher than 700 °C. Consequently, and considering that TPO[CaO]$_{Light}$ is a gasoline-like fuel, it was concluded that its use in HCCI engines can be regarded as a potential application since these types of technologies operate under lean air/fuel mixtures and low temperatures avoiding the formation of PAHs during combustion. Overall, the knowledge of pollutant formation coupled with the elucidation of the fuel decomposition tendencies can be very useful for further investigation. Namely, these insights may be used to develop detailed chemical kinetic models. An addition to enhancing the understanding of the combustion chemistry, these models may be employed in the modification/design/optimization of practical combustion systems.

- Regarding first part of the specific objectives 5 (addressed in Chapter 6)

By applying the thermoeconomic principles, it was determined that scaling and modifying the process can result in an increase in the plant's exergy efficiency of around 20%, in contrast to the process conducted at lab-scale. This was attributed to the benefits of using TPG as an exergy source by supplying heat to the pyrolysis process, rather than using external resources, *i.e.* electricity. A high exergy destruction was found in the pyrolyzer and the burner, which was mainly associated with the chemical reactions taking place in these two components. The exergy cost balance revealed that those streams located at the end of the process exhibit a higher unit exergy economic cost due to the influence of all component irreversibilities in the plant on their exergy characteristics. The production cost of TPO, rCB, and TPG was found to be 0.054 – 0.095 $/L, 0.035 – 0.062 $/kg, and 0.0082 – 0.012 $/kWh, respectively, depending on the feedstock (WT) price. Finally, an exergy decomposition analysis confirmed that 47 % of the exergy of TPO and TPG comes from renewable resources, namely NR. Therefore, their use as fuels is in line with the worldwide guidelines regarding the promotion of renewable energy, *e.g.* the 2009/28/EC European directive. In addition, 47 % of the energy of the combustion gases released into the atmosphere come from renewable resources, which implies reduced net carbon emissions. This gives rise to several benefits for this project, *i.e.* in terms of carbon credits.

7.2 Future works

This investigation may pave the path for future research as is highlighted bellow:

- Regarding the use of CaO as a catalytic material during the pyrolysis of WT:

As mentioned in Chapter 3, among all the pyrolysis products, rCB poses the higher challenges for commercialization and use at industrial scale, thus lowering the overall profitability of WT pyrolysis. Previous investigations have suggested that the most straightforward applications for rCB is its use as a partial substitute of commercial CB in rubber formulation. In this scenario, the addition of CaO during pyrolysis as a catalytic material represents a significant increase of the inorganic materials in the rCB fraction, which reduces its quality considerably. Towards minimizing the negative effect of CaO on rCB, an acid demineralization

step was effective on removing around 80 % of the inorganic materials. Nonetheless, the obtained results suggest that further upgrading steps are required to fine-tune the characteristics of rCB if it is intended to be used in rubber formulations. This will be a decisive aspect to define the suitability (technical and economical) of the *in-situ* upgrading using CaO. Taking this into account, further research is needed towards this scope.

Alternatively, aside from the use of rCB as a substitute of commercial CB in rubber formulation, other rCB application can be explore, which may be more flexible regarding the high inorganic materials content. For instance, a previous work conducted in our research group, titled: "*Obtaining activated carbon from WT by incorporating calcium and its application in the adsorption process*" suggested that calcium acts a catalyst in the activation process (gasification) of rCB. In turn, calcium increases the reaction velocity and alters the porous distribution. In this regard, these types of applications can be explored in future investigations to expand the range of possibilities for rCB[CaO] implementation.

- Regarding the oxidation characteristics of TPO and its distillate fraction

As highlighted in Chapter 5, the information presented in that part of the research severs as input data to adjust/develop oxidation kinetic models. Forthcoming works will aim at adjusting detailed kinetic models available in the literature to the experimental data obtained from TG-FT-IR (TPO / TPO[CaO]) and JSR ($TPO[CaO]_{Light}$). This will be important not only to gain a comprehensive understanding regarding the combustion chemistry of the studied fuels, but also to further design and optimize combustion systems for these types of non-conventional fuels.

Furthermore, in the case of the surrogate fuel, its formulation may be improved by considering other aspects such as the presence of sulfur and nitrogen in the real fuel. This will provide more realistic results concerning the oxidation process of $TPO[CaO]_{Light}$ and will pave the path to define potential improvements.

Finally, the present investigation studied the oxidation characteristics of TPO and its distillate fractions, giving special attention to the light distillate fraction ($TPO[CaO]_{Light}$). Nonetheless, the study of the oxidation characteristics of the other fractions (low-middle, high middle, and heavy) is also important and must be covered in future works.

- Regarding the thermoeconomic analysis of the model WT pyrolysis plant

The thermoeconomic analysis presented in Chapter 6 can be expanded by considering different scenarios and configuration of the pyrolysis plant at industrial scale. This can provide a diverse view to define the best alternative when scaling and modifying the WT pyrolysis process. These scenarios can include electricity generation with TPG to be sold for revenue, modification of the reactor heating system, etc.

Publication in peer-reviewed Journals

The development of this doctoral thesis has resulted in some scientific publications in peer-reviewed international journals, as follows:

Paper No. 1

F. Campuzano, R.C. Brown, J.D. Martínez, Auger reactors for pyrolysis of biomass and wastes, Renew. Sustain. Energy Rev. 102 (2019) 372–409.

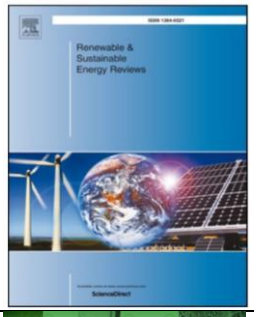

Paper No. 2

F. Campuzano, A.G. Abdul Jameel, W. Zhang, A.-H. Emwas, A.F. Agudelo, J.D. Martínez, M.S. Sarathy, Fuel and chemical properties of waste tire pyrolysis oil, Energy Fuels, 34, 12688−12702, 2020.

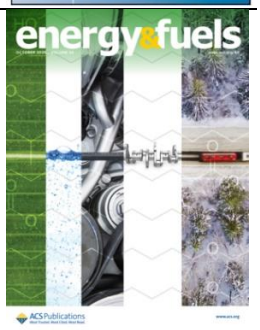

Paper No. 3

F. Campuzano, A.G. Abdul Jameel, W. Zhang, A.-H. Emwas, A.F. Agudelo, J.D. Martínez, M.S. Sarathy, On the distillation of waste tire pyrolysis oil: A structural characterization of the derived fractions, Fuel, 290, 120041, 2021

On the other hand, the author has participated in the following works

J.D. Martínez, **F. Campuzano**, N. Cardona-uribe, C.N. Arenas, D. Muñoz-lopera, Waste tire valorization by intermediate pyrolysis using a continuous twin-auger reactor : Operational features, Waste Manag. 113 (2020) 404–412.

A.G. Abdul Jameel, A.B.S. Alquaity, **F. Campuzano**, S. Saxena, S.M. Sarathy, W.L. Roberts, Surrogate formulation and molecular characterization of sulfur species in vacuum residues using APPI and ESI FT-ICR mass spectrometry, Fuel, **Approved**.

Appendix A: Supplementary information Chapter 2

A1 Twin-auger pyrolysis plant

A1.1 Final design

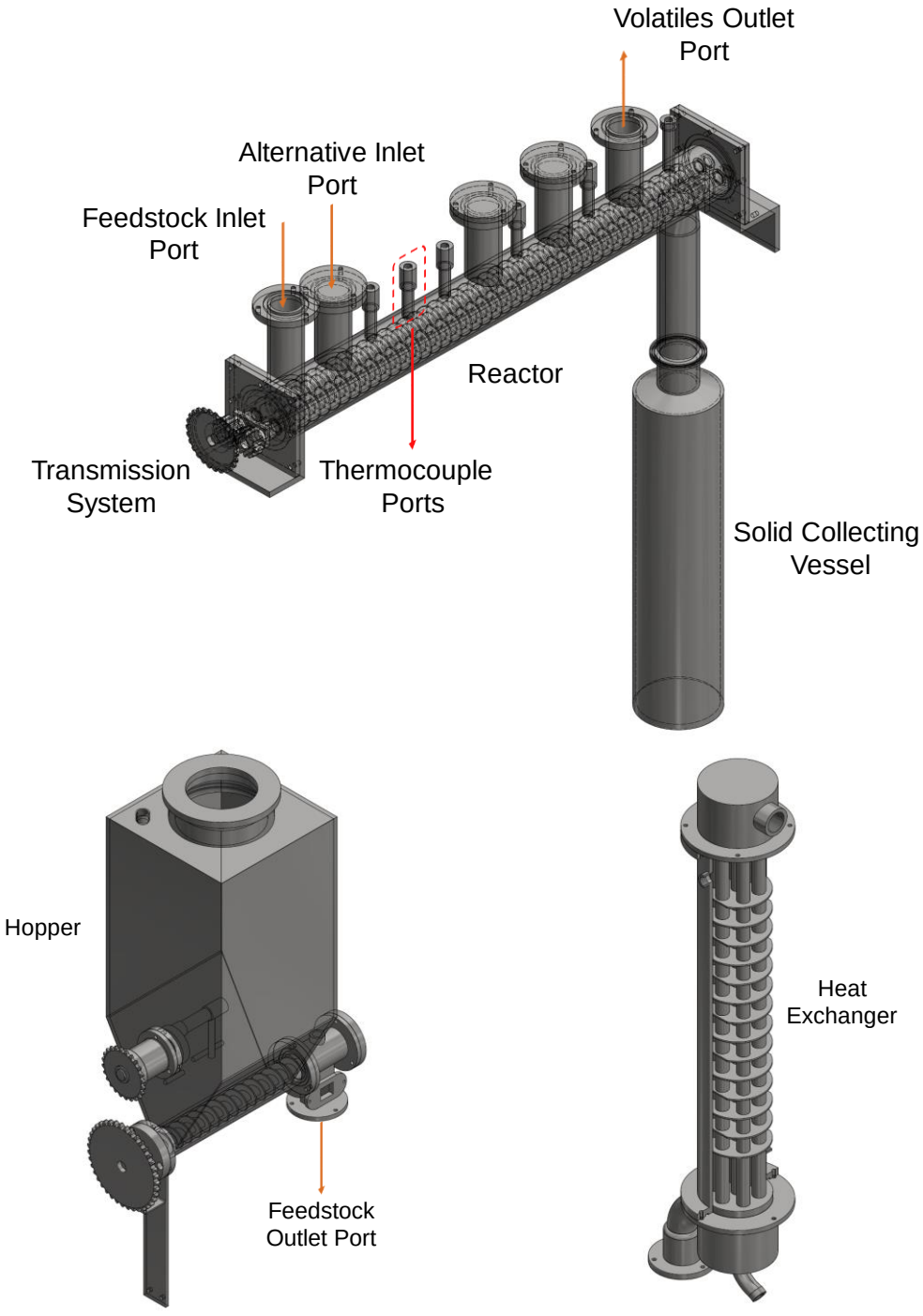

A1.2 Construction process

Feeding System

Twin-Auger Reactor

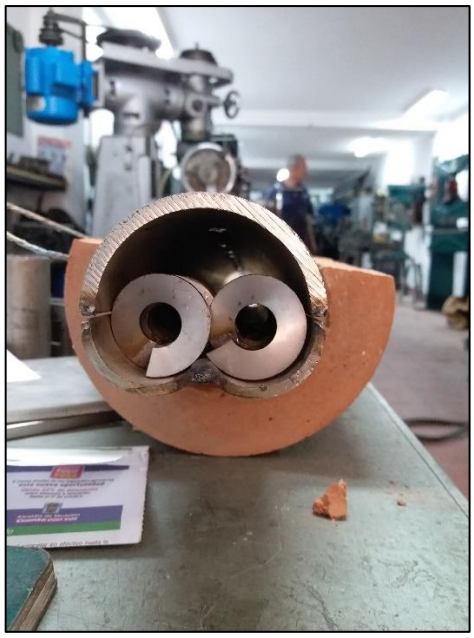

Condensing Unit

Pyrolysis Plant

A2. Design of experiments

Four controllable and independent variables were selected to carry out the design of experiments: i) reactor temperature (X_1), ii) WT mass flow rate (X_2), iii) solid residence time (X_3), and iv) N_2 volumetric flow rate (X_4). Accordingly, the experimental campaign consisted of four factors (n), 2^n factorial experiments, $2.n$ axial experiments, and six center point replicates (m), giving a total of thirty experiments (N), as calculated by Equation A.1.

$$N = 2^n + (2 \times n) + m = 2^4 + (2 \times 4) + 6 = 30 \quad \textbf{(A.1)}$$

Table A.1 shows the randomized sequence of the thirty experiments carried out, their related experimental conditions, and the derived TPO, rCB, and TPG yields.

Table A1 Pyrolysis conditions and product yields

Run	Sequence	X_1 (°C)	X_2 (kg/h)	X_3 (min)	X_4 (mL/min)	TPO (wt.%)	rCB (wt.%)	TPG (wt.%)
1	1	475 (+1)	1.25 (+1)	4.0 (+1)	400 (+1)	43.92	40.20	15.88
2	9	425 (-1)	1.25 (+1)	4.0 (+1)	400 (+1)	45.56	40.88	13.56
3	17	450 (0)	1.0 (0)	3.5 (0)	100 (-2)	45.40	40.20	14.40
4	23	400 (-2)	1.0 (0)	3.5 (0)	300 (0)	42.10	46.55	11.35
5	25	450 (0)	1.0 (0)	3.5 (0)	300 (0)	43.35	41.35	15.30
6	24	500 (+2)	1.0 (0)	3.5 (0)	300 (0)	41.30	38.75	19.95
7	2	475 (+1)	1.25 (+1)	4.0 (+1)	200 (-1)	44.72	39.56	15.72
8	12	425 (-1)	1.25 (+1)	3.0 (-1)	200 (-1)	46.04	41.52	12.44
9	18	450 (0)	1.0 (0)	3.5 (0)	500 (+2)	43.60	41.90	14.50
10	22	450 (0)	1.5 (+2)	3.5 (0)	300 (0)	45.38	40.27	14.36
11	30	450 (0)	1.0 (0)	3.5 (0)	300 (0)	43.60	41.60	14.80
12	8	475 (+1)	0.75 (-1)	3.0 (-1)	200 (-1)	43.00	41.60	15.40
13	10	425 (-1)	1.25 (+1)	4.0 (+1)	200 (-1)	46.88	43.64	9.48
14	13	425 (-1)	0.75 (-1)	4.0 (+1)	400 (+1)	43.20	44.27	12.53
15	19	450 (0)	1.0 (0)	2.5 (-2)	300 (0)	42.20	42.15	15.65
16	26	450 (0)	1.0 (0)	3.5 (0)	300 (0)	46.55	41.95	11.50
17	21	450 (0)	0.5 (-2)	3.5 (0)	300 (0)	42.80	44.80	12.40
18	29	450 (0)	1.0 (0)	3.5 (0)	300 (0)	43.75	39.95	16.30
19	4	475 (+1)	1.25 (+1)	3.0 (-1)	200 (-1)	44.80	39.24	15.96
20	11	425 (-1)	1.25 (+1)	3.0 (-1)	400 (+1)	46.76	42.48	10.76
21	14	425 (-1)	0.75 (-1)	4.0 (+1)	200 (-1)	44.33	43.27	12.40
22	5	475 (+1)	0.75 (-1)	4.0 (+1)	400 (+1)	42.40	41.13	16.47
23	27	450 (0)	1.0 (0)	3.5 (0)	300 (0)	46.05	41.55	12.40
24	16	425 (-1)	0.75 (-1)	3.0 (-1)	200 (-1)	43.67	44.33	12.00
25	6	475 (+1)	0.75 (-1)	4.0 (+1)	200 (-1)	40.67	41.07	18.27
26	20	450 (0)	1.0 (0)	4.5 (+2)	300 (0)	45.25	41.45	13.30
27	15	425 (-1)	0.75 (-1)	3.0 (-1)	400 (+1)	43.20	43.00	13.80
28	28	450 (0)	1.0 (0)	3.5 (0)	300 (0)	44.20	41.15	14.65
29	7	475 (+1)	0.75 (-1)	3.0 (-1)	400 (+1)	41.40	39.53	19.07
30	3	475 (+1)	1.25 (+1)	3.0 (-1)	400 (+1)	44.56	41.36	14.08

A2.2 Statistical analysis: Response surface methodology

A2.2.1 Tire pyrolysis oil

Table A2 Full ANOVA test results for the TPO yield

Source	Sum of squares	Degree of freedom	Mean square	F-value	*p*-value
X_1	10.3622	1	10.3622	6.10	0.0312
X_2	29.3267	1	29.3267	17.25	0.0016
X_3	0.788438	1	0.788438	0.46	0.5099
X_4	1.876	1	1.876	1.10	0.3160
X_1^2	12.5626	1	12.5626	7.39	0.0200
$X_2 X_2$	0.00600625	1	0.00600625	0.00	0.9537
$X_2 X_3$	0.345156	1	0.345156	0.20	0.6610
$X_2 X_4$	0.104006	1	0.104006	0.06	0.8092
X_2^2	0.0270281	1	0.0270281	0.02	0.9019
$X_2 X_3$	0.0105062	1	0.0105062	0.01	0.9387
$X_2 X_4$	0.00180625	1	0.00180625	0.00	0.9746
X_3^2	0.463203	1	0.463203	0.27	0.6120
$X_3 X_4$	0.00030625	1	0.00030625	0.00	0.9895
X_4^2	0.172578	1	0.172578	0.10	0.7560
Lack of fit	**15.6199**	**10**	**1.56199**	**0.92**	**0.5491**
Pure error	**18.6967**	**11**	**1.6997**		
Correlation total	**90.3631**	**35**			

Equation A.2

$$Y_1 = -173.447 + 0.910517X_1 + 7.59167X_2 + 9.1975X_3 - 21.5958X_4 - 0.0010025X_1^2 - 0.0031X_1X_2 - 0.01175X_1X_3 + 0.03225X_1X_4 - 0.465X_2^2 - 0.205X_2X_3 - 0.425X_2X_4 - 0.48125X_3^2 + 0.0875X_3X_4 + 7.34375X_4^2$$

A2.2.2 Recovered carbon black

Table A3 Full ANOVA test results for the rCB yield

Source	Sum of squares	Degree of freedom	Mean square	F-value	*p*-value
X_1	51.9204	1	51.9204	118.39	0.0000
X_2	14.076	1	14.076	32.10	0.0001
X_3	0.00806667	1	0.00806667	0.02	0.8946
X_4	0.170017	1	0.170017	0.39	0.5462
X_1^2	2.78873	1	2.78873	6.36	0.0284
$X_2 X_2$	0.714025	1	0.714025	1.63	0.2282
$X_2 X_3$	0.015625	1	0.015625	0.04	0.8537
$X_2 X_4$	0.5184	1	0.5184	1.18	0.3002
X_2^2	2.272	1	2.272	5.18	0.0438
$X_2 X_3$	0.16	1	0.16	0.36	0.5581
$X_2 X_4$	0.680625	1	0.680625	1.55	0.2387
X_3^2	0.218901	1	0.218901	0.50	0.4946
$X_3 X_4$	0.034225	1	0.034225	0.08	0.7852
X_4^2	0.351401	1	0.351401	0.80	0.3899
Lack of fit	**15.7965**	**10**	**1.57965**	**3.60**	**0.0232**
Pure error	**4.82417**	**11**	**0.438561**		
Correlation total	**94.5492**	**35**			

Equation A.3

$$Y_2 = 193.389 - 0.530583X_1 - 26.475X_2 - 0.15X_3 - 30.2833X_4 + 0.000472333X_1^2 + 0.0338X_1X_2 - 0.0025X_1X_3 + 0.072X_1X_4 + 4.26333X_2^2 - 0.8X_2X_3 + 8.25X_2X_4 + 0.330833X_3^2 - 0.925X_3X_4 - 10.4792X_4^2$$

A3. Repeatability analysis of the TPO, rCB, and TPG yields for the twin-auger pyrolysis plant

Table A4. TPO, rCB, and TPG yields obtained at the optimal operational conditions

Replicate	Exp.	TPO (wt.%)	rCB (wt.%)	TPG (wt.%)
R1	1	44.00	42.05	13.95
	2	43.65	41.85	14.50
	3	44.70	40.19	15.11
	4	43.32	39.64	17.05
	5	44.77	41.68	13.55
	6	42.95	40.09	16.95
	7	46.45	42.27	11.27
R2	8	44.77	42.27	12.95
	9	44.73	42.59	12.68
	10	44.09	42.59	13.32
	11	42.86	41.50	15.64
	12	42.38	41.79	15.83
	13	44.88	41.58	13.54
	14	42.71	40.21	17.08
R3	15	42.58	41.21	16.21
	16	44.13	41.29	14.58
	17	44.17	41.29	14.54
	18	44.67	39.33	16.00
	19	45.13	40.92	13.96
	20	43.75	41.04	15.21
	21	43.38	41.54	15.08
R4	22	43.35	41.35	15.30
	23	46.55	41.95	11.50
	24	46.05	41.55	12.40
	25	44.20	41.15	14.65
	26	43.75	39.95	16.30
	27	43.60	41.60	14.80

Table A5. Data summary regarding the set of experiments conducted in the optimum point

Replicate	TPO				rCB				TPG			
	$\bar{x}_{TPO}$	σ^2_{TPO}	σ_{TPO}	$\sigma_{x\,TPO}$	$\bar{x}_{rCB}$	σ^2_{rCB}	σ_{rCB}	$\sigma_{x\,rCB}$	$\bar{x}_{TPG}$	σ^2_{TPG}	σ_{TPG}	$\sigma_{x\,TPG}$
R1	44.26	1.38	1.18	0.44	41.11	1.19	1.09	0.41	14.63	4.07	2.02	0.76
R2	43.77	1.19	1.09	0.41	41.79	0.69	0.83	0.31	14.43	2.95	1.72	0.65
R3	43.97	0.71	0.84	0.32	40.95	0.55	0.74	0.28	14.08	0.66	0.81	0.31
R4	44.13	1.87	1.37	0.55	41.26	0.48	0.70	0.28	14.16	3.34	1.83	0.75
Total	44.13	1.21	1.10	0.21	41.28	0.76	0.87	0.17	14.60	2.53	1.60	0.31

Table A6. Assessment of the ANOVA test assumptions

Replicate	TPO			rCB			TPG		
	K-S test	Bartlett's test		K-S test	Bartlett's test		K-S test	Bartlett's test	
	P-value	σ^2	P-value	P-value	σ^2	P-value	P-value	σ^2	P-value
R1	0.95	1.38	0.75	0.53	1.19	0.71	0.95	4.07	0.22
R2	0.66	1.19		0.86	0.69		0.53	2.95	
R3	0.99	0.71		0.31	0.55		0.95	0.66	
R4	0.61	1.87		0.70	0.48		0.63	3.34	

Table A7. Summary of ANOVA test results

Source	TPO				rCB				TPG			
	DF	SS	MS	F-Stat	DF	SS	MS	F-Stat	DF	SS	MS	F-Stat
Between replicates	3	2.42	0.81	0.64	3	2.81	0.94	1.27	3	3.00	1.00	0.40
Within replicates	23	29.00	1.26	**P-Value**	23	16.98	0.74	**P-Value**	23	62.80	2.73	**P-Value**
Total	26	31.42	-	1.20	26	19.79	-	1.01	26	65.80	-	1.30

DF: Degree of Freedom; **SS**: Sum of Squares; **MS**: Means of Squares

Appendix B: Supplementary information Chapter 3

B1. Surface composition by energy dispersive X-ray (EDX)

B1.1 CaO [105-149 µm]

Table B1. Surface composition CaO (105-149 µm)

Element	App Conc.	Intensity Corrn.	Weight (%)	Weight (%) Sigma	Atomic (%)
O K	11.42	0.2940	41.42	1.25	63.64
Mg K	0.64	0.6332	1.07	0.22	1.09
Ca K	57.10	1.0588	57.51	1.23	35.28
Total			100.00		

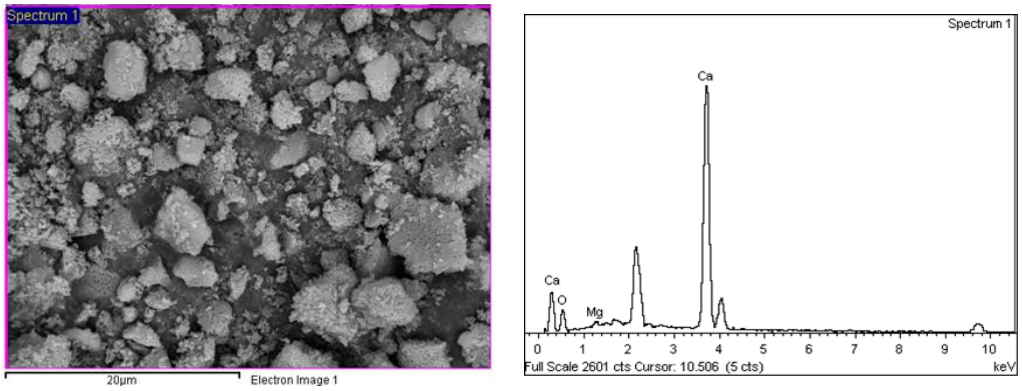

Figure B.1. Surface composition of CaO (105-149 µm)

B1.2 CaO [149-841 µm]

Table B2. Surface composition CaO [149-841 µm]

Element	App Conc.	Intensity Corrn.	Weight (%)	Weight (%) Sigma	Atomic (%)
O K	0.87	0.2173	20.01	2.11	38.53
Ca K	17.38	1.0882	79.99	2.11	61.47
Total			100.00		

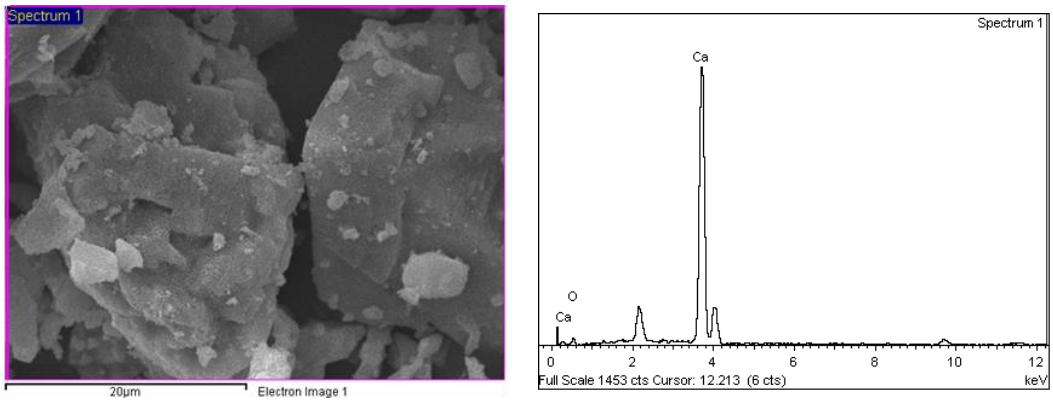

Figure B.2. Surface composition CaO (149-841 µm)

B2. GC-MS of TPO and TPO[CaO]

B2.1 Experimental methodology

TPO and TPO[CaO] were diluted in dichloromethane (1:10) before being injected into the apparatus. A BP-Petro (100m x 0.25 mm ID x 0.5 µm film thickness) capillary column was selected for the tests. He was chosen as a carrier gas with an initial flow of 0.2 mL/min during the first 84 min. Then, the flow rate was increased from 0.2 to 1.8 mL/min and kept at a constant flow rate of 1.8 mL/min during the rest of the analysis. The oven temperature was initially set at 40 ºC (4 min), then gradually heated at different heating rates (1 ºC/min up to 55 ºC, 2 ºC/min up to 185 ºC, and finally 10 ºC/min up to 250 ºC). Once the oven reached 250 ºC, this temperature was kept constant for 60 min. The injector, the ion source, and the transfer line temperatures were maintained constant at 300, 230 and 280 ºC, respectively. A sample volume of 1 µl was injected applying a 1:7 split mode. After a solvent delay of 10.4 min, a full mass spectrum was obtained. The MS was operated in positive electron ionization mode, and an *m/z* range from 30 to 500 was scanned. The voltage applied to the multiplier detector was 1275 V in order to find the total ion chromatograms (TICs) in a full-scan acquisition method. The identification of the peaks was carried out based on computer matching of the mass spectra with the NIST library. Once the identification was accomplished, a Selective Ion Monitoring (SIM) chromatogram of the principal ion of each compound was extracted from the full-scan spectra.

B2.2 Experimental results

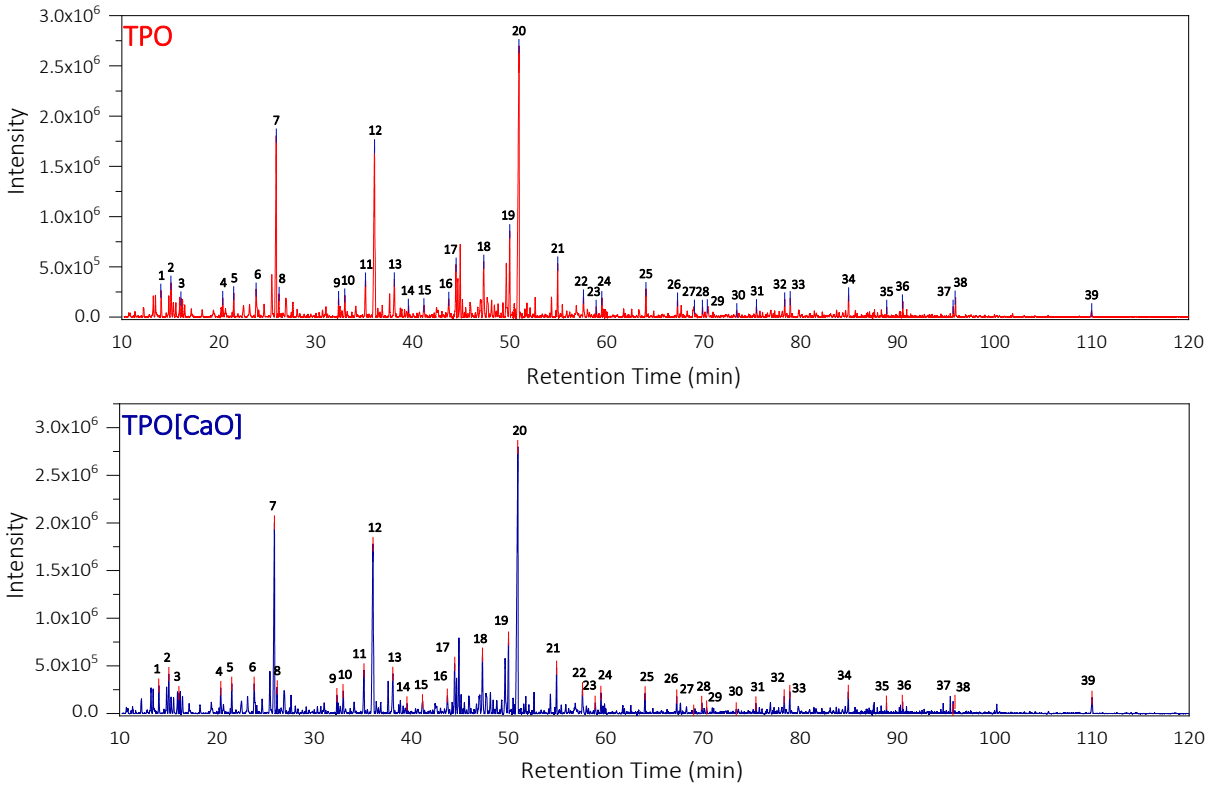

Figure B.3.GC-MS Spectrums

Table B3. Main compounds in TPO and TPO[CaO] (GC-MS)

Index	Retention Time (min)	TPO		TPO[CaO]		Name / Formula	Group(s)
		Area (%)	Normalized Area (%)	Area (%)	Normalized Area (%)		
C1	14	0.64	1.27	0.65	1.34	Name: (Z)-3-methyl-2-Pentene Formula: C_6H_{12}	Paraffin, olefin
C2	15.1	0.99	1.97	1.08	2.23	Name: (Z)-(Z)-2,4-Hexadiene Formula: C_6H_{10}	Paraffin, olefin
C3	16.1	0.39	0.77	0.40	0.83	Name: Benzene Formula: C_6H_6	Aromatic
C4	20.4	0.57	1.13	0.72	1.49	Name: 2,3-dimethyl-1,3-Pentadiene Formula: C_7H_{12}	Paraffin, olefin
C5	21.5	0.62	1.23	0.73	1.51	Name: 4,4-dimethyl-1,2-Pentadiene Formula: C_7H_{12}	Paraffin, olefin
C6	23.8	1.10	2.19	1.13	2.34	Name: (E,E)-1,3,5-Heptatriene Formula: C_7H_{10}	Paraffin, olefin
C7	25.9	6.11	12.14	6.30	13.03	Name: Toluene Formula: C_7H_8	Aromatic, Paraffin
C8	26.2	0.59	1.17	0.59	1.22	Name: 1-methyl-1,4-Cyclohexadiene Formula: C_7H_{10}	Naphthene, Olefin
C9	32.3	0.44	0.87	0.41	0.85	Name: 1,5-dimethyl-Bicyclo [3.1.0] hexane Formula: C_8H_{14}	Naphthene
C10	33	0.64	1.27	0.64	1.32	Name: 4-ethenyl-Cyclohexene Formula: C_8H_{12}	Naphthene, Olefin
C11	35.1	1.30	2.58	1.42	2.94	Name: Ethylbenzene Formula: C_8H_{10}	Aromatic, Paraffin
C12	36.1	7.87	15.64	7.65	15.82	Name: 1,3-dimethyl-Benzene Formula: C_8H_{10}	Aromatic, Paraffin
C13	38.1	1.35	2.68	1.46	3.02	Name: o-Xylene Formula: C_8H_{10}	Aromatic, Paraffin
C14	39.5	0.28	0.56	0.24	0.50	Name: 2,6-Dimethyl-1,3,6-heptatriene Formula: C_9H_{14}	Paraffin, Olefin
C15	41.1	0.47	0.93	0.48	0.99	Name: 1,3,5,5-tetramethyl-1,3-Cyclohexadiene Formula: $C_{10}H_{16}$	Naphthene, Olefin
C16	43.7	0.70	1.39	0.65	1.34	Name: (1R)-2,2-dimethyl-3-methylene-Bicyclo[2.2.1]Heptane Formula: $C_{10}H_{16}$	Naphthene, Olefin
C17	44.5	1.58	3.14	1.45	3.00	Name: 1-ethyl-3-methyl-Benzene Formula: C_9H_{12}	Aromatic, Paraffin
C18	47.3	1.95	3.87	1.96	4.05	Name: Mesitylene Formula: C_9H_{12}	Aromatic, Paraffin
C19	50	2.43	4.83	1.99	4.12	Name: 1-methyl-3-(1-methylethyl)-Benzene Formula: C10H14	Aromatic, Paraffin
C20	50.9	11.67	23.19	11.27	23.31	Name: D-Limonene Formula: $C_{10}H_{16}$	Naphthene, Olefin
C21	54.9	1.28	2.54	1.05	2.17	Name: 1-methyl-4-(1-methylethenyl)-Benzene, Formula: $C_{10}H_{12}$	Aromatic, Paraffin, Olefin
C22	57.6	0.66	1.31	0.75	1.55	Name: 1,2,4,5-tetramethyl-Benzene Formula: $C_{10}H_{14}$	Aromatic, Paraffin
C23	58.9	0.27	0.54	0.30	0.62	Name: 3-Cyclohexen-1-ol, 5-methylene-6-(1-methylethenyl)-, acetate Formula: $C_{12}H_{16}O_2$	Naphthene, Olefin (+ O)
C24	59.5	0.51	1.01	0.50	1.03	Name: 3-methyl-1H-Indene Formula: $C_{10}H_{10}$	Aromatic, Naphthene, Olefin
C25	64	0.78	1.55	0.51	1.05	Name: Benzothiazole Formula: C_7H_5NS	Aromatic (+N, S)

Index	Retention Time (min)	TPO		TPO[CaO]		Name / Formula	Group(s)
		Area (%)	Normalized Area (%)	Area (%)	Normalized Area (%)		
C26	67.3	0.43	0.85	0.40	0.83	Name: 1,2-dihydro-4-methyl-Naphthalene Formula: $C_{11}H_{12}$	Aromatic, Naphthene, Olefin
C27	69	0.50	0.99	0.04	0.08	Name: p-Cymen-7-ol Formula: $C_{10}H_{14}O$	Aromatic, Paraffin (+ O)
C28	69.9	0.27	0.54	0.28	0.58	Name: Benzocycloheptatriene Formula: $C_{11}H_{10}$	Aromatic, Naphthene, Olefin
C29	70.4	0.50	0.99	0.16	0.33	Name: 3-t-butyl-7,7-dimethyl-Oct-3-ene-1,5-diyne Formula: $C_{14}H_{20}$	Paraffin, Olefin
C30	73.4	0.22	0.44	0.14	0.29	Name: cis-1-ethylidene octahydro-7a-methyl-1H-Indene Formula: $C_{12}H_{20}$	Naphthene, Olefin
C31	75.4	0.29	0.58	0.26	0.54	Name: (1-Methylpenta-1,3-dienyl)benzene Formula: $C_{12}H_{14}$	Aromatic, Paraffin, Olefin
C32	78.3	0.49	0.97	0.47	0.97	Name: 1,7-dimethylnaphthalene Formula: $C_{12}H_{12}$	Aromatic, Naphthene
C33	78.9	0.49	0.97	0.53	1.10	Name: 2,4-dimethylQuinoline Formula: $C_{11}H_{11}N$	Aromatic, Naphthene (+ N)
C34	84.9	0.55	1.09	0.50	1.03	Name: 1,6,7-trimethylnaphthalene Formula: $C_{13}H_{14}$	Aromatic, Naphthene
C35	88.9	0.17	0.34	0.16	0.33	Name: Columbin Formula: $C_{20}H_{22}O_6$	Naphthene, Olefin (+ O)
C36	90.5	0.25	0.50	0.22	0.46	Name: 7-Methyl-Z-tetradecen-1-ol acetate Formula: $C_{17}H_{32}O_2$	Paraffin, Olefin (+ O)
C37	95.9	0.20	0.40	0.23	0.48	Name: Retinol Formula: $C_{20}H_{30}O$	Paraffin, Naphthene, Olefin (+ O)
C38	95.7	0.53	1.05	0.06	0.12	Name: (5α)-3-ethyl-3-hydroxy-Androstan-17-one Formula: $C_{21}H_{34}O_2$	Naphthene (+ O)
C39	110	0.25	0.50	0.57	1.18	Name: N-(1,3-dimethylbutyl)-N'-phenyl-1,4-Benzenediamine Formula: $C_{18}H_{24}N_2$	Aromatic, Paraffin (+ N)

Appendices C: Supplementary information Chapter 4

Description of the analytical techniques and the experimental procedure

C1. APPI FT-ICR MS

Mass spectrometry was conducted in a 9.4 Tesla SolariX FT-ICR MS (Bruker GmbH, Germany) equipped with an atmospheric pressure photo ionization (APPI) source. Samples were diluted in pure toluene and directly injected into the APPI source. The FT-ICR mass spectra of the samples were acquired using positive APPI ionization mode with a mass range of 154 – 1200 *m/z*. The APPI source uses a krypton light, which provides 10.6 eV of ionization energy for the analytes; only singly charged ions were observed. The sample molecules were mainly ionized into molecular ions without undergoing fragmentation. The ion accumulation time in the hexapole was 0.01 s, and each spectrum was acquired by accumulating 300 scans with a time domain size of 8 mega-points, and a transient length of 4.4739 s. All mass spectra were externally calibrated using 0.05 mg/ml of a polystyrene solution (from 100 to 1200 *m/z*). Raw data was further recalibrated during data analysis using a set of homologous alkylated compounds for each sample. The mass list with signal to noise ratio > 5 of each mass spectrum was generated by Data Analysis V4.5 and imported into the Composer software (Sierra Analytics, Pasadena, California, USA) for the assignment of chemical formulas [1]. With an error range of 0.5 ppm, the most likely elemental composition of each monoisotopic mass peak was calculated according to the determined accurate mass within the range of $C_{1\text{-}100}H_{1\text{-}200}N_{0\text{-}3}O_{0\text{-}3}S_{0\text{-}3}$. Then, in order to achieve an overview of the compound distributions, all the assigned chemical formulas were divided into molecular classes (i.e. HC, S_1, S_2, O, N, etc.) according to the heteroatom content. The relative abundance of each molecular class was calculated as the total intensity of the particular class divided by the intensity of all assigned peaks. Based on the assigned molecular formula to each mass peak appearing in the spectrum, the double bond equivalent (DBE) number was calculated following Equation C.1. The subscripts c, h, o, n, and s represent the number of carbon, hydrogen, oxygen, nitrogen, and sulfur atoms, respectively, in the assigned molecular formula ($C_cH_hN_nO_oS_s$).

$$\mathrm{DBE} = \mathrm{c} - \frac{\mathrm{h}}{2} + \frac{\mathrm{n}}{2} + 1 \qquad \textbf{(C.1)}$$

The average molecular weight (MW_{avg}) was determined by summing the product of *m/z* (P_i) with the signal intensity (I_i) of each recorded ion, then dividing by the total intensity of all the ions recorded (Equation C.2). Similarly, the average number of carbons and the average DBE number were also calculated.

$$\mathrm{MW_{avg}} = \frac{\sum_{\mathrm{i}=1}^{\mathrm{n}} \mathrm{P_i} \times \mathrm{I_i}}{\sum_{\mathrm{i}=1}^{\mathrm{n}} \mathrm{I_i}} \qquad \textbf{(C.2)}$$

According to the chemical formula assigned to each resolved peak, species were grouped into different molecular classes, depending on their content of heteroatoms. Chemical formulas were classified into different compound classes, including HC (pure hydrocarbons), S_1 (hydrocarbons with one sulfur atom), NS (hydrocarbons with one N atom and one S atom), and S_2

(hydrocarbons with two S atoms), among others. Furthermore, positive APPI mode leads to protonated ions $[M + H]^+$ along with the radical cations $[M^{+\cdot}]$. In the present analysis HC[H], S[H], N_2[H], NO[H], O[H] and O_2[H], were also recorded. However, to reduce the complexity and facilitate the comparison, molecular classes are reported as the sum of both $[M^{+\cdot}]$ and $[M + H]^+$. The relative abundance of each class was calculated as the total intensity of each compound class, divided by the total intensity of all of the assigned signals.

C2. ^{1}H and ^{13}C NMR

The solvent used was deuterated chloroform ($CDCl_3$). 50 µl of the sample were diluted into 600 µl of $CDCl_3$. 0.6 ml of the diluted mixture were transferred into 5 mm NMR tubes. A 700 MHz Bruker AVANCE III spectrometer was used to obtain the spectra at 298 K. The spectrometer was equipped with a Bruker CP TCI multinuclear CryoProbe (from Brukerbiospin, Rheinstetten, Germany). In order to record the ^{1}H NMR spectra, 128 scans were collected with a recycle delay time of 10 s. A standard one-dimensional (1D) 90° pulse sequence was used with standard (zg) program from the Bruker pulse library. Tetramethylsilane (TMS) was used as the internal chemical shift reference for both ^{1}H and ^{13}C spectra. A spectral width of 14,098 Hz was digitized into 64,000 data points to collect the free induction decay (FID). In order to record the ^{13}C NMR spectra, a 1D sequence was used with power gate decoupling, along with a 30° flip angle, using the standard 1D pulse sequence zgig30 program from the Bruker pulse library. Fourier transformation was applied after applying a line broadening of 1 Hz. Bruker Topspin 4.0.4 software (Bruker BioSpin, Rheinstetten, Germany) was used to collect the spectra and MestreNova was used for both spectral post-processing and for data analyses.

C2.1 Average molecular parameters (AMPs)

AMPs enable the structural elucidation of complex hydrocarbon fuels. They are obtained by combining the NMR data with elemental analysis and the average molecular weight (determined from FT-ICR MS or using correlations). This method provides the total distribution of both carbon (from ^{13}C NMR) and hydrogen (^{1}H NMR) atoms in a fictitious average molecule of the fuel (*i.e.,* number of carbon and hydrogen atoms in paraffinic, naphthenic, olefinic, aromatic, etc., compounds) [2]. The NMR spectra is represented in terms of the chemical shifts (usually given in terms of ppm), which is associated with the resonant frequency of the nuclei relative to a magnetic field. Different nuclei exhibit different shifts, and the splitting pattern along with the position of these shifts shed light into the molecular structure. ^{1}H NMR spectra have a typical chemical shift range between 0 and +14 ppm, while ^{13}C NMR spectra have a larger chemical shift range between 0 and +220 ppm. Specific regions within the spectra can be assigned to a group of nuclei. For instance, hydrogen atoms in poly-aromatic compounds give rise to signals between 7.20-8.99 ppm, while hydrogen atoms in paraffinic CH_3 groups lie between 0-0.97 ppm. Similarly, carbon atoms in aromatic quaternary compounds produce peaks between 140.5-160.0 ppm, while paraffinic quaternary carbon atoms do so between 50.0-60.0 ppm [3]. NMR spectroscopy is an inherently quantitative technique, as the area under each peak (integral) is proportional to the concentration level and the number of these nuclei in each molecule existing in the mixture sample. An AMP can be determined by means of Equation 3. X refers to either C or H atoms, I denotes ^{1}H or ^{13}C NMR integral area, and index i

refers to a particular chemical shift interval in the NMR spectra. %X stands for the weight percent of X from the elemental composition.

$$X_i = \frac{I_i}{I_{Total}} \%X \quad \textbf{(C.3)}$$

The average molecular formula of TPO and TPO[CaO] can be obtained in the form of $C_cH_hO_oN_nS_s$, where the subscripts c, h, o, n, and s represent the respective number of atoms (see Equation C.1) in the hypothetical molecule. The number of these atoms can be calculated following Equation C.4:

$$\text{Number of Atoms} = MW_{avg} \times \%X\left(\frac{1}{100 \times a_y}\right) \quad \textbf{(C.4)}$$

MW_{avg} is the average molecular weight of the sample, obtained by means of APPI FT-ICR MS from Equation C.2 (Equation C.5 for the light fraction), %X is the weight percent of the respective element (C, H, N, S, O) obtained from the elemental analysis, and a_y is the atomic mass of the respective element, in grams per mole. The chemical shift assignments and the nomenclature used for denoting the symbols in this work were chosen following the methodology proposed by Poveda and Molina [4]. Derived AMPs, such as aromaticity factor (fa), C/H ratio, average chain length (n_{acl}), naphthenic ring number (R_N), aromatic ring number (R_A), and aromatic condensation index (φ) were also calculated. These derived AMPs provide additional information on the atomic arrangement within TPO and TPO[CaO] structures. The formulae and the procedure to calculate these derived AMPs are described elsewhere [3].

C3. GC-MS: light fraction

The GC-MS analysis of the light fraction was performed in a THERMO Trace GC Ultra with MS DSQ II, to identify its main chemical compounds. This analysis was conducted following the same methodology described in Chapter 3 for TPO and TPO[CaO]. the molecular weight of the light fraction (MW_{LF}) was empirically estimated according to the dependence of this parameter on density (see Equation C.5) [5]. Here, the density (ρ) is in g/cm^3. This equation is valid for $0.780 \leq \rho \leq 0.827$. The MW_{LF}, in g/mol, in combination with the elemental composition, provided an approximation of the average molecular formula (number of carbon, hydrogen, nitrogen, oxygen, and sulfur atoms) of the light fraction, as will be shown later.

$$MW_{LF} = 450.97(\rho)^2 - 422.58(\rho) + 207.4 \quad \textbf{(C.5)}$$

References

[1] W. Zhang, K. Müllen, Analyzing solid fossil-fuel pitches by a combination of Soxhlet extraction and Fourier transform ion cyclotron resonance mass spectrometry, Carbon N. Y. 167 (2020) 414–421.

[2] A. Gani, A. Jameel, A. Khateeb, A.M. Elbaz, A. Emwas, Characterization of deasphalted heavy fuel oil using APPI (+) FT-ICR mass spectrometry and NMR spectroscopy, Fuel. 253 (2019) 950–963.

[3] A.G. Abdul Jameel, A.M. Elbaz, A.H. Emwas, W.L. Roberts, S.M. Sarathy, Calculation of average molecular parameters, functional groups, and a surrogate molecule for heavy fuel oils using 1H and 13C nuclear magnetic resonance spectroscopy, Energy Fuels. 30 (2016) 3894–3905.

[4] J.C. Poveda, D.R. Molina, Average molecular parameters of heavy crude oils and their fractions using NMR spectroscopy, J. Pet. Sci. Eng. 84–85 (2012) 1–7.

[5] C. Saggese, A. V Singh, X. Xue, C. Chu, M.R. Kholghy, T. Zhang, J. Camacho, J. Giaccai, J.H. Miller, M.J. Thomson, C.J. Sung, H. Wang, The distillation curve and sooting propensity of a typical jet fuel, Fuel. 235 (2019) 350–362.

Appendix D: Supplementary information Chapter 5

D1. Characteristics of the IR bands: TG-FTIR experiments (TPO / TPO[CaO])

Table D1. IR bands assignment

Wavenumber range (cm^{-1})	Selected (cm^{-1})	Origin	Assignment
3500–4000	3556	O–H stretching	H_2O
3130–3070	3079	Aromatic C–H bending	Aromatics
1600–1500		Aromatic C=C stretching	
3040–3010	3018	Alkene C–H stretching	Alkenes
1600–1680		Alkene C=C stretching	
2970–2950		Methyl C–H asymmetric stretching	
2880–2860		Methyl C–H symmetric stretching	
1470–1430		Methyl C–H asymmetric bending	
1380–1370	2968, 2920	Methyl C–H symmetric bending	Alkanes or alkyl substituents
2935–2915		Methylene C–H asymmetric stretching	
2865–2845		Methylene C–H symmetric stretching	
1485–1445		Methylene C–H bending	
2400–2224	2361	O=C=O asymmetric stretching	CO_2
2180–2108	2119	C=O stretching	CO
1762			NO
1342			SO_2

D2. Jet stirred reactor experiments: $TPO[CaO]_{Light}$ and surrogate fuel

D2.1 Gas chromatography analyzers: Temperature procedures

The Agilent RGA system is a gas chromatograph configured with three parallel channels that can analyze different species simultaneously. This system follows the ASTM D1945, D1946, and UOP 539 standard procedures and uses TCD (thermal conductivity detector) and FID (flame ionization detector) detectors to quantify CO_2, CO, N_2, O_2 and H_2 and C_1-C_5 hydrocarbons, respectively. Second, the Agilent 7890B system is equipped with an Agilent DB-1 column (15 mm x 0.32 mm) for separation and FID to detect PAHs. The total time of the temperature program in the Agilent 7890B was 17.83 min, with the following oven control: (1) 45 ºC for 6 min, (2) 30 ºC /min to 100 C for 4 min, (3) 30 ºC/min to 280 ºC for 0 min. The mole fractions of each species were calculated by calibrating the system with the standard gas (RGA) and toluene (Agilent 7890B), as well as taking into account the effective carbon numbers.

D2.2 TPO[CaO]$_{Light}$

D2.2.1 Equivalence ratio 0.2: Experimental conditions

Experiment	$T_{react.}$ (°C)	Flow Rates (sccm)					
		Q (Total) sccm	Fuel sccm	Fuel ml/hr	N_2 (Fuel) sccm	N_2 sccm	O_2 sccm
1	527	1557	4.67	2.460	450.0	723	379.5
2	577	1465	4.40	2.316	450.0	654	357.2
3	627	1384	4.15	2.187	450.0	592	337.3
4	677	1311	3.93	2.072	450.0	538	319.6
5	727	1246	3.74	1.968	450.0	488	303.6
6	777	1186	3.56	1.874	450.0	444	289.1
7	827	1132	3.40	1.789	450.0	403	276.0
8	877	1083	3.25	1.711	450.0	366	264.0
9	927	1038	3.11	1.640	450.0	332	253.0

SCCM: Standard cubic centimeters per minute

D2.2.2 Equivalence ratio 0.5: Experimental conditions

Experiment	$T_{react.}$ (°C)	Flow Rates (sccm)					
		Q (Total) sccm	Fuel sccm	Fuel ml/hr	N2 (Fuel) sccm	N2 sccm	O_2 sccm
1	527	1557	4.67	2.460	450.0	950	151.8
2	577	1465	4.40	2.316	450.0	868	142.9
3	627	1384	4.15	2.187	450.0	795	134.9
4	677	1311	3.93	2.072	450.0	729	127.8
5	727	1246	3.74	1.968	450.0	670	121.4
6	777	1186	3.56	1.874	450.0	617	115.7
7	827	1132	3.40	1.789	450.0	569	110.4
8	877	1083	3.25	1.711	450.0	524	105.6
9	927	1038	3.11	1.640	450.0	484	101.2

SCCM: Standard cubic centimeters per minute

D2.2.3 Equivalence ratio 1.0: Experimental conditions

Experiment	$T_{react.}$ (°C)	Flow Rates (sccm)					
		Q (Total) sccm	Fuel sccm	Fuel ml/hr	N_2 (Fuel) sccm	N_2 sccm	O_2 sccm
1	527	1557	4.67	2.460	450.0	950	151.8
2	577	1465	4.40	2.316	450.0	868	142.9
3	627	1384	4.15	2.187	450.0	795	134.9
4	677	1311	3.93	2.072	450.0	729	127.8
5	727	1246	3.74	1.968	450.0	670	121.4
6	777	1186	3.56	1.874	450.0	617	115.7
7	827	1132	3.40	1.789	450.0	569	110.4
8	877	1083	3.25	1.711	450.0	524	105.6
9	927	1038	3.11	1.640	450.0	484	101.2

SCCM: Standard cubic centimeters per minute

D2.3 Surrogate fuel

D2.3.1 Equivalence ratio 0.2: Experimental conditions

Experiment	$T_{react.}$ (°C)	Flow Rates (sccm)					
		Q (Total) sccm	Fuel sccm	Fuel ml/hr	N_2 (Fuel) sccm	N_2 sccm	O_2 sccm
1	427	1779	5.34	1.661	500.0	1020	253.6
2	457	1706	5.12	1.593	500.0	958	243.1
3	487	1639	4.92	1.530	500.0	900	233.5
4	517	1577	4.73	1.472	500.0	847	224.7
5	547	1519	4.56	1.418	500.0	798	216.5
6	577	1465	4.40	1.368	500.0	752	208.8
7	607	1415	4.25	1.322	500.0	709	201.7
8	637	1369	4.11	1.278	500.0	670	195.0
9	667	1325	3.98	1.237	500.0	632	188.8
10	697	1284	3.85	1.199	500.0	597	183.0
11	727	1246	3.74	1.163	500.0	564	177.5
12	757	1209	3.63	1.129	500.0	533	172.3
13	787	1175	3.53	1.097	500.0	504	167.4

SCCM: Standard cubic centimeters per minute

D2.3.2 Equivalence ratio 0.5: Experimental conditions

Experiment	$T_{react.}$ (°C)	Flow Rates (sccm)					
		Q (Total) sccm	Fuel sccm	Fuel ml/hr	N_2 (Fuel) sccm	N_2 sccm	O_2 sccm
1	427	1779	5.34	1.661	500.0	1173	101.4
2	457	1706	5.12	1.593	500.0	1104	97.3
3	487	1639	4.92	1.530	500.0	1041	93.4
4	517	1577	4.73	1.472	500.0	982	89.9
5	547	1519	4.56	1.418	500.0	928	86.6
6	577	1465	4.40	1.368	500.0	877	83.5
7	607	1415	4.25	1.322	500.0	830	80.7
8	637	1369	4.11	1.278	500.0	787	78.0
9	667	1325	3.98	1.237	500.0	746	75.5
10	697	1284	3.85	1.199	500.0	707	73.2
11	727	1246	3.74	1.163	500.0	671	71.0
12	757	1209	3.63	1.129	500.0	637	68.9
13	787	1175	3.53	1.097	500.0	605	67.0
14	817	1143	3.43	1.067	500.0	574	65.1
15	847	1112	3.34	1.038	500.0	545	63.4
16	877	1083	3.25	1.011	500.0	518	61.7
17	907	1056	3.17	0.986	500.0	492	60.2

SCCM: Standard cubic centimeters per minute

D2.3.3 Equivalence ratio 1.0: Experimental conditions

Experiment	$T_{react.}$ (°C)	Flow Rates (sccm)					
		Q (Total) sccm	Fuel sccm	Fuel ml/hr	N_2 (Fuel) sccm	N_2 sccm	O_2 sccm
1	427	1779	5.34	1.661	500.0	1223	50.7
2	457	1706	5.12	1.593	500.0	1153	48.6
3	487	1639	4.92	1.530	500.0	1087	46.7
4	517	1577	4.73	1.472	500.0	1027	44.9
5	547	1519	4.56	1.418	500.0	971	43.3
6	577	1465	4.40	1.368	500.0	919	41.8
7	607	1415	4.25	1.322	500.0	871	40.3
8	637	1369	4.11	1.278	500.0	826	39.0
9	667	1325	3.98	1.237	500.0	783	37.8
10	697	1284	3.85	1.199	500.0	744	36.6
11	727	1246	3.74	1.163	500.0	706	35.5
12	757	1209	3.63	1.129	500.0	671	34.5
13	787	1175	3.53	1.097	500.0	638	33.5
14	817	1143	3.43	1.067	500.0	607	32.6
15	847	1112	3.34	1.038	500.0	577	31.7
16	877	1083	3.25	1.011	500.0	549	30.9
17	907	1056	3.17	0.986	500.0	522	30.1
18	937	1029	3.09	0.961	500.0	497	29.3

SCCM: Standard cubic centimeters per minute

D2.3.4 Pyrolysis: Experimental conditions

Experiment	$T_{react.}$ (°C)	Flow Rates (sccm)					
		Q (Total) sccm	Fuel sccm	Fuel ml/hr	N2 (Fuel) sccm	N2 sccm	O_2 sccm
1	427	1779	5.34	1.661	500.0	1274	0.0
2	457	1706	5.12	1.593	500.0	1201	0.0
3	487	1639	4.92	1.530	500.0	1134	0.0
4	517	1577	4.73	1.472	500.0	1072	0.0
5	547	1519	4.56	1.418	500.0	1014	0.0
6	577	1465	4.40	1.368	500.0	961	0.0
7	607	1415	4.25	1.322	500.0	911	0.0
8	637	1369	4.11	1.278	500.0	865	0.0
9	667	1325	3.98	1.237	500.0	821	0.0
10	697	1284	3.85	1.199	500.0	780	0.0
11	727	1246	3.74	1.163	500.0	742	0.0
12	757	1209	3.63	1.129	500.0	706	0.0
13	787	1175	3.53	1.097	500.0	672	0.0
14	817	1143	3.43	1.067	500.0	639	0.0
15	847	1112	3.34	1.038	500.0	609	0.0
16	877	1083	3.25	1.011	500.0	580	0.0
17	907	1056	3.17	0.986	500.0	552	0.0
18	937	1029	3.09	0.961	500.0	526	0.0

SCCM: Standard cubic centimeters per minute

Appendix E: Supplementary information Chapter 6

E1. Thermodynamic analysis of the pyrolysis process

Based on the operating conditions (temperature and pressure), as well as on the chemical composition of every stream, specific enthalpies and exergies (physical and chemical) were calculated. The energy content (H_i) of each stream was determined by means of Equation E.1. In this equation, $\dot{m}_i$ and HHV_i are related to the mass flow rate (kg/s) and the higher heating value (kJ/kg) of each stream, respectively. Likewise, Cp_i is the heat capacity (kJ/kgK) at constant pressure and ΔT is the temperature difference with respect to the reference state. The C_{pTPGi} of the species contained in the TPG mixture (stream 14), in N_2 free basis, was determined using the empirical correlation shown in Equation E.2 [1]. The coefficients A-E were selected as those reported in Ref. [2]. for each species. Then, the $Cp_{TPGmixture}$ was calculated as shown in Equation E.3, where X_i is the mass fraction of each constituent in the mixture.

$$H_i\ [kW] = \dot{m}_i \times [HHV_i + (Cp_i \times \Delta T)] \qquad \textbf{(E.1)}$$

$$C_{pTPGi}\left[\frac{kJ}{kgK}\right] = A + BT + CT^2 + DT^3 + ET^4 \qquad \textbf{(E.2)}$$

$$C_{pTPGmixture}\left[\frac{kJ}{kgK}\right] = \sum_{i=1}^{n} X_i C_{pTPGi} \qquad \textbf{(E.3)}$$

Similarly, the exergy of every stream in the system was also determined. Exergy is defined as the maximum amount of work that can be produced by a stream of matter or energy (heat, work, etc.) as it comes to equilibrium with a reference environment. In other words, exergy is a measurement of the potential of a flow or a system to cause change [3]. The total exergy of a stream (e_i) is the sum of different types of exergy: (i) kinetic exergy (e_i^k), (ii) potential exergy (e_i^p), (iii) physical exergy (e_i^{ph}), and (iv) chemical exergy (e_i^{ch}) as shown in Equation E.4 [2].

$$e_i\left[\frac{kJ}{kg}\right] = e_i^k + e_i^p + e_i^{ph} + e_i^{ch} \qquad \textbf{(E.4)}$$

The e_i^k is associated with the velocity of a stream with respect to a fixed reference frame. The e_i^p is linked to the position of the stream in a given force field. The e_{xi}^{ph} is the maximum work obtain when bringing a substance from its initial state to the thermodynamic environment by physical processes. The e_i^{ch} represents the maximin that can be obtained when a substance is brought from the reference environment state to the dead state by a process including heat transfer and exchange of substance only with the reference environment [4]. In the present study, the e_i^{ki} and e_i^{po} are relatively small in contrast to the e_i^{ph} and e_i^{ch}; therefore, they were considered negligible in order to simplify the exergy analysis. Thus, Equation E.4 is then rewritten as Equation E.5:

$$e_{xi}\left[\frac{kJ}{kg}\right] = e_i^{ph} + e_i^{ch} \qquad \textbf{(E.5)}$$

The specific physical exergy of each stream was calculated in line with Equation E.6 – 8. Here, h and s are the specific enthalpy (kJ/kg) and specific entropy (kJ/kgK) under the operating conditions, respectively. Likewise, h_o is the specific enthalpy and s_o is the specific entropy at the standard reference state [5].

$$e_{xi}^{ph}\left[\frac{kJ}{kg}\right] = (h - h_o)_i - T_o(s - s_o)_i \qquad \textbf{(E.6)}$$

$$(h - h_o)_i\left[\frac{kJ}{kg}\right] = \int_{T_o}^{T} C_{pi}\,dT \qquad \textbf{(E.7)}$$

$$(s - s_o)_i\left[\frac{kJ}{kg}\right] = \int_{T_o}^{T} \frac{C_{pi}}{T}\,dT \qquad \textbf{(E.8)}$$

The specific chemical exergy of the solid and liquid streams was determined with Equation E.9 and Equation E.10, respectively [6]. In these equations, LHV_i is the lower heating value of either solids or liquids. The coefficients β_o and β_1 were calculated by means of Equation E.11 and Equation E.12. The C, H, N, and O terms are associated with the carbon, hydrogen, nitrogen, and oxygen content, respectively obtained from the elemental analysis and reported in Chapter 3.

$$e_{Solids}^{ch}\left[\frac{kJ}{kg}\right] = (\beta_o LHV_{Solid}) + \frac{S}{100} \qquad \textbf{(E.9)}$$

$$e_{Liquids}^{ch}\left[\frac{kJ}{kg}\right] = \beta_1 LHV_{Liquid} \approx HHV_{Liquid} \qquad \textbf{(E.10)}$$

$$\beta_{o(dry)} = 1.0437 + 0.1882\frac{H}{C} + 0.0610\frac{O}{C} + 0.0404\frac{N}{C} \qquad \textbf{(E.11)}$$

$$\beta_{1(dry)} = 1.0401 + 0.1728\frac{H}{C} + 0.0432\frac{O}{C} + 0.2169\,\frac{S}{C}\left(1 - 2.0628\,\frac{H}{C}\right) \qquad \textbf{(E.12)}$$

Regarding TPG, Equation E.13 [5] was used to calculate its specific chemical exergy based on the chemical composition o reported in Chapter 3:

$$e_{x,gas}^{ch}\left[\frac{kJ}{kg}\right] = \sum y_i e_{ch,i}^{o} + T_o R \sum y_i \ln y_i \qquad \textbf{(E.13)}$$

Finally, when the characteristics of all streams were completely defined, the global exergy efficiency (η) of the process was determined as the ratio between the exergy of the obtained useful products over the exergy provided to the system by the external resources as shown in Equation E.14. Stream 37 (marked in red) is only included in the alternative process.

$$\eta_{\text{Pyrolysis Plant}}(\%) = \left[\frac{\text{Useful Prodcuts}}{\text{External Resources}}\right] \times 100$$
$$= \left[\frac{E_{11} + E_{13} + E_{25}}{E_1 + E_2 + E_3 + E_4 + E_6 + E_7 + E_9 + E_{21} + E_{24} + E_{27} + \mathbf{E_{37}}}\right] \times 100 \quad \textbf{(E.14)}$$

E2. Implementation of the TEC to the pyrolysis process

In order to conduct apply the TEC, the physical structures were mathematically represented by means of the incidence matrix: $A(n \times m)$ [7]. $A(n \times m)$ shows in a matrix form how the components and the flows of a system interact. Each element in the incidence matrix was defined as follows [8].

$$A(n \times m) = \begin{cases} 1, & \text{If stream j enters to the component i} \\ -1, & \text{If stream j leaves the component i} \\ 0, & \text{If stream j is not related to the component i} \end{cases}$$

Based on $A(n \times m)$, the global mass, energy, and exergy balances were expressed in matrix form (Equations E.5 – 17). Here, $\dot{m}(m \times 1)$, $\dot{H}(m \times 1)$, and $\dot{E}(m \times 1)$ are the mass, energy, and exergy column vectors, respectively, which were defined according to the information obtained by means of the thermodynamic analysis.

$$A(n \times m) \times \dot{m}(m \times 1) = \frac{dm}{dt}(n \times 1) = 0 \quad \textbf{(E.15)}$$

$$A(n \times m) \times \dot{H}(m \times 1) = \frac{dH}{dt}(n \times 1) = 0 \quad \textbf{(E.16)}$$

$$[A(n \times m) \times \dot{E}(m \times 1) = \frac{dE}{dt}(n \times 1) + \text{Irreversibilities}]_{CV} \quad \textbf{(E.17)}$$

Considering the productive structure and in a similar manner to $A(n \times m)$, two additional matrices corresponding to fuels $A_F(n \times m)$, and products $A_P(n \times m)$ were built. Then, these matrices were combined with the exergy vector to determine the total fuel (F), product (P), and irreversibilities (I) for every component as shown below.

$$A(n \times m) = A_F(n \times m) - A_P(n \times m) \quad \textbf{(E.18)}$$

$$F(n \times 1) = A_F(n \times m) \times \dot{E}(m \times 1) \quad \textbf{(E.19)}$$

$$P(n \times 1) = A_P(n \times m) \times \dot{E}(m \times 1) \quad \textbf{(E.20)}$$

$$I(n \times 1) = F - P \quad \textbf{(E.21)}$$

Regarding the exergy cost ($\dot{C}$) of the streams, this term is defined as the exergy/money over time that is required to produce it. It can be expressed in either exergy or monetary basis:

$$\dot{C} \equiv \left[\frac{kJ}{s}\right] \qquad \dot{C} \equiv \left[\frac{\$}{s}\right]$$

In order to conduct the exergy cost balance for every component of the system, additional equations must be formulated. These equations can be obtained following the preposition of TEC, developed by Valero *et al*. [8]. As such, another important concept that must be defined is the unit exergy cost (c_i). The c_i is the amount of exergy (or money) needed to produce a unit of exergy of a given flow. The c_i is defined as follows [8].

$$c_i = \frac{\dot{C}}{\dot{E}} \left[\frac{kW}{kW}\right] \vee \left[\frac{\$}{kW}\right] \geq 1 \qquad \textbf{(E.22)}$$

Then, the auxiliary equations needed to conduct the exergy cost balance were established according to the types of fuels and products entering and exiting each component in the system as described below:

E2.1 Industrial-scale twin-auger pyrolysis plant: 20 auxiliary equations are needed (15 components – 35 flows)

- External resources: Preposition 1 from TEC

[1]	Natural Rubber (Stream 1)	$\dot{C}_1 = \dot{E}_1$
[2]	Synthetic Rubber (Stream 2)	$\dot{C}_2 = \dot{E}_2$
[3]	Carbon Black (Stream 3)	$\dot{C}_3 = \dot{E}_3$
[4]	Ash (Stream 4)	$\dot{C}_4 = \dot{E}_4$
[5]	Power (Motor Feeder) (Stream 6)	$\dot{C}_6 = \dot{E}_6$
[6]	Power (Motor Reactor) (Stream 7)	$\dot{C}_7 = \dot{E}_7$
[7]	N_2 (Stream 9)	$\dot{C}_9 = \dot{E}_9$
[8]	Water Condenser (Stream 15)	$\dot{C}_{15} = \dot{E}_{15}$
[9]	Power Pump Scrubber (Stream 21)	$\dot{C}_{21} = \dot{E}_{21}$
[10]	Power Compressor (Stream 24)	$\dot{C}_{24} = \dot{E}_{24}$
[11]	Air Burner (Stream 26)	$\dot{C}_{26} = \dot{E}_{26}$
[12]	Power Fan Burner (Stream 27)	$\dot{C}_{27} = \dot{E}_{27}$
[13]	Make-Up NaOH + H_2O (Stream 34)	$\dot{C}_{34} = \dot{E}_{34}$
[21]	CaO (Stream 36)*	$\dot{C}_{36} = \dot{E}_{36}$
[22]	Power Feeder Alternative Hopper (Stream 37)*	$\dot{C}_{37} = \dot{E}_{37}$

*Equations [22] and [23] are considered only for the alternative process

- Multiple products from one component: Preposition 4 from TEC

[14]	rCB / Volatile Matter (Stream 10/12)	$\frac{\dot{C}_{12}}{\dot{E}_{12}} = \frac{\dot{C}_{10}}{\dot{E}_{10}} \rightarrow \dot{C}_{10} - \frac{\dot{E}_{10}}{\dot{E}_{12}}\dot{C}_{12} = 0$
[15]	TPO / TPG (Stream 13/14)	$\frac{\dot{C}_{13}}{\dot{E}_{13}} = \frac{\dot{C}_{14}}{\dot{E}_{14}} \rightarrow \dot{C}_{13} - \frac{\dot{E}_{13}}{\dot{E}_{14}}\dot{C}_{14} = 0$

[16] TPG/Cold Fluid (Stream 14/16-15) $\frac{\dot{C}_{14}}{\dot{E}_{14}} = \frac{\dot{C}_{16} - \dot{C}_{15}}{\dot{E}_{16} - \dot{E}_{15}} \rightarrow \dot{C}_{14} - \frac{\dot{E}_{14}}{\dot{E}_{16} - \dot{E}_{15}}(\dot{C}_{16} - \dot{C}_{15}) = 0$

[17] TPG 1 / TPG 2 (Stream 22/23) $\frac{\dot{C}_{22}}{\dot{E}_{22}} = \frac{\dot{C}_{23}}{\dot{E}_{23}} \rightarrow \dot{C}_{22} - \frac{\dot{E}_{22}}{\dot{E}_{23}}\dot{C}_{23} = 0$

[18] TPG / Solution (Streams 19-18/20) $\frac{\dot{C}_{19} - \dot{C}_{18}}{\dot{E}_{19} - \dot{E}_{18}} = \frac{\dot{C}_{20}}{\dot{E}_{20}} \rightarrow \dot{C}_{20} - \frac{\dot{E}_{20}}{\dot{E}_{19} - \dot{E}_{18}}(\dot{C}_{19} - \dot{C}_{18}) = 0$

- Fuel in doublet: Preposition 3 from TEC

[19] Combustion Gases (Stream 30/31) $\frac{\dot{C}_{30}}{\dot{E}_{30}} = \frac{\dot{C}_{31}}{\dot{E}_{31}} \rightarrow \dot{C}_{30} - \frac{\dot{E}_{30}}{\dot{E}_{31}}\dot{C}_{31} = 0$

[20] Combustion Gases (Stream 31/32) $\frac{\dot{C}_{31}}{\dot{E}_{31}} = \frac{\dot{C}_{32}}{\dot{E}_{32}} \rightarrow \dot{C}_{31} - \frac{\dot{E}_{31}}{\dot{E}_{32}}\dot{C}_{32} = 0$

E2.2 Lab-scale twin-auger pyrolysis plant: Thirteen auxiliary equations (8 components – 21 flows)

- External resources: Preposition 1 from TEC

[1] Natural Rubber (Stream 1) $\dot{C}_1 = \dot{E}_1$

[2] Synthetic Rubber (Stream 2) $\dot{C}_2 = \dot{E}_2$

[3] Carbon Black (Stream 3) $\dot{C}_3 = \dot{E}_3$

[4] Ash (Stream 4) $\dot{C}_4 = \dot{E}_4$

[5] Power (Motor Feeder) (Stream 6) $\dot{C}_6 = \dot{E}_6$

[6] Power (Motor Reactor) (Stream 7) $\dot{C}_7 = \dot{E}_7$

[7] N_2 (Stream 9) $\dot{C}_9 = \dot{E}_9$

[8] Power Electric Heater (Stream 10) $\dot{C}_{10} = \dot{E}_{10}$

[9] Water Condenser (Stream 17) $\dot{C}_{17} = \dot{E}_{17}$

[10] Air Burner (Stream 19) $\dot{C}_{19} = \dot{E}_{19}$

- Multiple products from one component Preposition 4 from TEC

[11] Volatile Matter / rCB (Stream 12/14) $\frac{\dot{C}_{12}}{\dot{E}_{12}} = \frac{\dot{C}_{14}}{\dot{E}_{14}} \rightarrow \dot{C}_{12} - \frac{\dot{E}_{12}}{\dot{E}_{14}}\dot{C}_{14} = 0$

[12] TPO / TPG (Stream 15/16) $\frac{\dot{C}_{15}}{\dot{E}_{15}} = \frac{\dot{C}_{16}}{\dot{E}_{16}} \rightarrow \dot{C}_{15} - \frac{\dot{E}_{15}}{\dot{E}_{16}}\dot{C}_{16} = 0$

[13] TPG/Cold Fluid (Stream 16/18-17) $\frac{\dot{C}_{16}}{\dot{E}_{16}} = \frac{\dot{C}_{18} - \dot{C}_{17}}{\dot{E}_{18} - \dot{E}_{17}} \rightarrow \dot{C}_{18} - \dot{C}_{17} - \frac{\dot{E}_{18} - \dot{E}_{17}}{\dot{E}_{16}}\dot{C}_{16} = 0$

After defining the auxiliary equations, the Cost Matrix: $\mathbb{A}(\mathrm{m} \times \mathrm{m})$ and the Exergy Amortization Cost Vector: $\mathbb{Y}(\mathrm{m} \times 1)$ were built. Then, the exergy cost balance can be written as shown in Equation VI.23:

$$\mathbb{A}(\mathrm{m} \times \mathrm{m}) \times \dot{\mathrm{C}}\,(\mathrm{m} \times 1) = \mathbb{Y}(\mathrm{m} \times 1) \quad \textbf{(E.23)}$$

The Exergy Cost Balance can be solved through Equation E.24 – 27, where α and ω are the auxiliary matrix and the auxiliary vector, respectively, obtained from the auxiliary equations:

$$\mathbb{A}(\mathrm{m} \times \mathrm{m}) = \begin{bmatrix} \mathrm{A} \\ \alpha \end{bmatrix} \quad \textbf{(E.24)}$$

$$\mathbb{Y}(\mathrm{m} \times 1) = \begin{bmatrix} 0 \\ \omega \end{bmatrix} \quad \textbf{(E.25)}$$

$$\mathbb{A}\,.\,\dot{\mathrm{C}} = \mathbb{Y} \quad \textbf{(E.26)}$$

$$\dot{\mathrm{C}} = \mathbb{A}^{-1}\mathbb{Y} \quad \textbf{(E.27)}$$

The total cost of fuels and products for each component in the plant can be calculated by combining the fuel and product matrices along with the cost vector:

$$\dot{\mathrm{C}}_{\mathrm{F}} = \mathrm{A}_{\mathrm{F}}.\dot{\mathrm{C}} \qquad \dot{\mathrm{C}}_{\mathrm{P}} = \mathrm{A}_{\mathrm{P}}.\dot{\mathrm{C}} \quad \textbf{(E.28)}$$

The cost balance including the non-thermodynamic costs in the system was conducted in line with Equation E.29:

$$\mathbf{A}\,.\,\dot{\mathrm{C}} + \dot{\mathbf{Z}} = 0 \quad \textbf{(E.29)}$$

where $\mathrm{A}\,(\mathrm{n} \times \mathrm{m})$, $\dot{\mathrm{C}}\,(\mathrm{m} \times 1)$, and $\mathrm{Z}(\mathrm{n} \times \mathrm{m})$, are the incidence matrix, the vector of exergoeconomic cost, and the vector of non-thermodynamic costs.

E3. Exergoeconomic analysis

The rate of non-thermodynamic costs for any component in the system was expressed according to Equation E.30 [9]:

$$\dot{Z}_k = \frac{\varphi_k\,.\,f\,.\,PEC_k}{N} \quad \textbf{(E.30)}$$

where φ_k, f, PEC_k, and N are the maintenance factor, the annuity factor, purchase equipment cost, and the annual plant operation time (h/year), respectively. The annuity factor (f) is obtained following Equation VI.31 and Equation VI.32 [9].

$$f = \left[\frac{q^{(a+b)} - 1}{(q-1)q^{(a+b)}} - \frac{q^b - 1}{(q-1)q^b}\right]^{-1} \quad \textbf{(E.31)}$$

$$q = \left(1 + \frac{in}{100}\right)\left(1 + \frac{ri}{100}\right) \quad \textbf{(E.32)}$$

Here, a, b, in, and ri are related to the lifespan of the component (years), duration of the plant construction (years), effective annual interest rate for debt (%/year), and annual inflation rate (%/year), respectively. In order to conduct the cost balance including the non-thermodynamic costs, the vector of unit exergoeconomic costs of external flows ($\mathrm{c_e}$) must be defined. This vector contains the non-thermodynamic costs (monetary unit/kWh) of the external resources. Based on this information, the const balance can be written as shown in Equation E.33 where $\dot{\mathbb{Z}}$ $(\mathrm{m} \times 1)$ is the vector of thermoeconomic amortization.

$$\mathbb{A}\,.\,\dot{\mathbf{C}} + \mathbb{Z} = \mathbf{0} \;\rightarrow\; \dot{\mathbf{C}} = \mathbb{A}^{-\mathbf{1}}.-\mathbb{Z} \qquad \textbf{(E.33)}$$

$$\dot{\mathbb{Z}} = \begin{bmatrix} \dot{\mathbf{Z}} \\ -\mathrm{c_e}.\,\omega \end{bmatrix}$$

Table E1. Purchase equipment cost of the equipments in the pyrolysis plant (updated 2020)

Equipment	PEC (USD)	Zi	Source
Reactor	1512000.00	58.365	[10]
Feeding System	200000.00	7.720	Quotation: local manufacturer (2019)
Electric Motor/Transmission system	1500.00	0.058	[11]
rCB Receiver	0.00	0.000	--
Condenser	27000.00	1.042	[12]
Scrubber	274000.00	10.577	[13]
Solution Tank	55000.00	2.123	[12]
Pump (Scrubber)	3077.42	0.119	[12]
Separation Unit	0.00	0.000	--
Compressor TPG	4525.06	0.175	[12]
Fan (Burner)	600.00	0.023	[12]
Preheater	6000.00	0.232	[12]
Burner	30000.00	1.158	[12]
Stack	0.00	0.000	--
Recycling Tank	55000.00	2.123	[12]
Alternative Hopper//Transmission system	80000.00	3.088	Quotation: local manufacturer (2019)

E4. Decomposition of exergy according to external resources

The methodology developed by Agudelo *et al.* [14] establishes the exergy of streams is supposed to be made up of as many types of exergy as many different types of exergy as external resources of different nature the system has. This concept is expressed mathematically as shown in Equation E. 34. Parameters $A_P^{(-1)}$, $\langle P|$, and $\langle FP\rangle$ are calculated in line with the symbolic exergoeconomic principles. The complete procedure to determine them can be found elsewhere.

$${}^{k}\dot{E} = A_P^{(-1)}\left({}^{k}P - A_P\,{}^{k}\dot{E}_e\right) + {}^{k}\dot{E}_e \qquad \textbf{(4.2)}$$

$${}^{k}P = \langle P|\,{}^{k}F_e'$$

$$^{k}F_e' = (A_F - \langle FP \rangle A_P)^{k}\dot{E}_e$$

Industrial Plant

Incidence Matrix: $A_{Reference\ Process}$ (15 x 35) / $A_{Alternative\ Process}$ (16 x 38)

A =

0	0	0	0	1	0	0	1	1	-1	0	-1	0	0	0	0	0	0	0	0	0	0	0	0	0	0	0	0	1	-1	0	0	0	0	0	0	1
1	1	1	1	-1	1	0	0	0	0	0	0	0	0	0	0	0	0	0	0	0	0	0	0	0	0	0	0	0	0	0	0	0	0	0	0	0	0	0
0	0	0	0	0	0	1	-1	0	0	0	0	0	0	0	0	0	0	0	0	0	0	0	0	0	0	0	0	0	0	0	0	0	0	0	0	0	0	0
0	0	0	0	0	0	0	0	0	1	-1	0	0	0	0	0	0	0	0	0	0	0	0	0	0	0	0	0	0	0	0	0	0	0	0	0	0	0	0
0	0	0	0	0	0	0	0	0	0	0	1	-1	-1	1	-1	0	0	0	0	0	0	0	0	0	0	0	0	0	0	0	0	0	0	0	0	0	0	0
0	0	0	0	0	0	0	0	0	0	0	0	0	1	0	0	0	1	-1	-1	0	0	0	0	0	0	0	0	0	0	0	0	0	0	0	0	0	0	0
0	0	0	0	0	0	0	0	0	0	0	0	0	0	0	0	-1	0	0	0	0	0	0	0	0	0	0	0	0	0	0	0	0	0	1	0	0	0	0
0	0	0	0	0	0	0	0	0	0	0	0	0	0	0	0	1	-1	0	0	1	0	0	0	0	0	0	0	0	0	0	0	0	0	0	0	0	0	0
0	0	0	0	0	0	0	0	0	0	0	0	0	0	0	0	0	0	0	1	0	-1	-1	0	0	0	0	0	0	0	0	0	0	0	0	0	0	0	0
0	0	0	0	0	0	0	0	0	0	0	0	0	0	0	0	0	0	0	0	0	1	0	1	-1	0	0	0	0	0	0	0	0	0	0	0	0	0	0
0	0	0	0	0	0	0	0	0	0	0	0	0	0	0	0	0	0	0	0	0	0	0	0	0	1	1	-1	0	0	0	0	0	0	0	0	0	0	0
0	0	0	0	0	0	0	0	0	0	0	0	0	0	0	0	0	0	0	0	0	0	0	0	0	0	0	1	-1	0	1	-1	0	0	0	0	0	0	0
0	0	0	0	0	0	0	0	0	0	0	0	0	0	0	0	0	0	0	0	0	0	0	0	0	1	0	0	0	0	0	1	-1	0	0	0	0	0	0
0	0	0	0	0	0	0	0	0	0	0	0	0	0	0	0	0	0	0	0	0	0	0	0	0	0	0	0	0	0	0	0	1	-1	0	0	0	0	0
0	0	0	0	0	0	0	0	0	0	0	0	0	0	0	0	0	0	0	0	1	0	0	0	0	0	0	0	0	0	0	0	0	0	0	-1	0	0	0
0	0	0	0	0	0	0	0	0	0	0	0	0	0	0	0	0	0	0	0	0	0	0	0	0	0	0	0	0	0	0	0	0	0	0	0	1	1	-1

Industrial Plant

Fuel Matrix: $A_{\text{Reference Process}}$ (15 x 35) / $A_{\text{Alternative Process}}$ (16 x 38)

$$A_F = \left|\begin{array}{ccccccccccccccccccccccccccccccccccc|ccc}
0 & 0 & 0 & 0 & 1 & 0 & 0 & 1 & 1 & 0 & 0 & 0 & 0 & 0 & 0 & 0 & 0 & 0 & 0 & 0 & 0 & 0 & 0 & 0 & 0 & 0 & 0 & 0 & 0 & 1 & -1 & 0 & 0 & 0 & 0 & 0 & 0 & 0 \\
1 & 1 & 1 & 1 & 0 & 1 & 0 & 0 & 0 & 0 & 0 & 0 & 0 & 0 & 0 & 0 & 0 & 0 & 0 & 0 & 0 & 0 & 0 & 0 & 0 & 0 & 0 & 0 & 0 & 0 & 0 & 0 & 0 & 0 & 0 & 0 & 0 & 0 \\
0 & 0 & 0 & 0 & 0 & 0 & 1 & 0 & 0 & 0 & 0 & 0 & 0 & 0 & 0 & 0 & 0 & 0 & 0 & 0 & 0 & 0 & 0 & 0 & 0 & 0 & 0 & 0 & 0 & 0 & 0 & 0 & 0 & 0 & 0 & 0 & 0 & 0 \\
0 & 0 & 0 & 0 & 0 & 0 & 0 & 0 & 0 & 1 & 0 & 0 & 0 & 0 & 0 & 0 & 0 & 0 & 0 & 0 & 0 & 0 & 0 & 0 & 0 & 0 & 0 & 0 & 0 & 0 & 0 & 0 & 0 & 0 & 0 & 0 & 0 & 0 \\
0 & 0 & 0 & 0 & 0 & 0 & 0 & 0 & 0 & 0 & 0 & 1 & 0 & 0 & 0 & 0 & 0 & 0 & 0 & 0 & 0 & 0 & 0 & 0 & 0 & 0 & 0 & 0 & 0 & 0 & 0 & 0 & 0 & 0 & 0 & 0 & 0 & 0 \\
0 & 0 & 0 & 0 & 0 & 0 & 0 & 0 & 0 & 0 & 0 & 0 & 0 & 1 & 0 & 0 & 0 & 0 & 0 & 0 & 0 & 0 & 0 & 0 & 0 & 0 & 0 & 0 & 0 & 0 & 0 & 0 & 0 & 0 & 0 & 0 & 0 & 0 \\
0 & 0 & 0 & 0 & 0 & 0 & 0 & 0 & 0 & 0 & 0 & 0 & 0 & 0 & 0 & 0 & 0 & 0 & 0 & 0 & 0 & 0 & 0 & 0 & 0 & 0 & 0 & 0 & 0 & 0 & 0 & 0 & 0 & 1 & 0 & 0 & 0 & 0 \\
0 & 0 & 0 & 0 & 0 & 0 & 0 & 0 & 0 & 0 & 0 & 0 & 0 & 0 & 0 & 0 & 0 & 0 & 0 & 0 & 1 & 0 & 0 & 0 & 0 & 0 & 0 & 0 & 0 & 0 & 0 & 0 & 0 & 0 & 0 & 0 & 0 & 0 \\
0 & 0 & 0 & 0 & 0 & 0 & 0 & 0 & 0 & 0 & 0 & 0 & 0 & 0 & 0 & 0 & 0 & 0 & 0 & 1 & 0 & 0 & 0 & 0 & 0 & 0 & 0 & 0 & 0 & 0 & 0 & 0 & 0 & 0 & 0 & 0 & 0 & 0 \\
0 & 0 & 0 & 0 & 0 & 0 & 0 & 0 & 0 & 0 & 0 & 0 & 0 & 0 & 0 & 0 & 0 & 0 & 0 & 0 & 0 & 0 & 0 & 1 & 0 & 0 & 0 & 0 & 0 & 0 & 0 & 0 & 0 & 0 & 0 & 0 & 0 & 0 \\
0 & 0 & 0 & 0 & 0 & 0 & 0 & 0 & 0 & 0 & 0 & 0 & 0 & 0 & 0 & 0 & 0 & 0 & 0 & 0 & 0 & 0 & 0 & 0 & 0 & 0 & 1 & 0 & 0 & 0 & 0 & 0 & 0 & 0 & 0 & 0 & 0 & 0 \\
0 & 0 & 0 & 0 & 0 & 0 & 0 & 0 & 0 & 0 & 0 & 0 & 0 & 0 & 0 & 0 & 0 & 0 & 0 & 0 & 0 & 0 & 0 & 0 & 0 & 0 & 0 & 0 & 0 & 0 & 1 & -1 & 0 & 0 & 0 & 0 & 0 & 0 \\
0 & 0 & 0 & 0 & 0 & 0 & 0 & 0 & 0 & 0 & 0 & 0 & 0 & 0 & 0 & 0 & 0 & 0 & 0 & 0 & 0 & 0 & 1 & 0 & 0 & 0 & 0 & 0 & 1 & 0 & 0 & 0 & 0 & 0 & 0 & 0 & 0 & 0 \\
0 & 0 & 0 & 0 & 0 & 0 & 0 & 0 & 0 & 0 & 0 & 0 & 0 & 0 & 0 & 0 & 0 & 0 & 0 & 0 & 0 & 0 & 0 & 0 & 0 & 0 & 0 & 0 & 0 & 0 & 0 & 1 & 0 & 0 & 0 & 0 & 0 & 0 \\
0 & 0 & 0 & 0 & 0 & 0 & 0 & 0 & 0 & 0 & 0 & 0 & 0 & 0 & 0 & 0 & 0 & 0 & 1 & 0 & 0 & 0 & 0 & 0 & 0 & 0 & 0 & 0 & 0 & 0 & 0 & 0 & 0 & 0 & 0 & 0 & 0 & 0 \\
0 & 0 & 0 & 0 & 0 & 0 & 0 & 0 & 0 & 0 & 0 & 0 & 0 & 0 & 0 & 0 & 0 & 0 & 0 & 0 & 0 & 0 & 0 & 0 & 0 & 0 & 0 & 0 & 0 & 0 & 0 & 0 & 0 & 0 & 0 & 1 & 1 & 0
\end{array}\right|$$

Industrial Plant

Product Matrix: $A_{Reference\ Process}$ (15 x 35) – $A_{Alternative\ Process}$ (16 x 38)

$A_P =$

0	0	0	0	0	0	0	0	0	1	0	1	0	0	0	0	0	0	0	0	0	0	0	0	0	0	0	0	0	0	0	0	0	0	0	0	0	0
0	0	0	0	1	0	0	0	0	0	0	0	0	0	0	0	0	0	0	0	0	0	0	0	0	0	0	0	0	0	0	0	0	0	0	0	0	0
0	0	0	0	0	0	0	1	0	0	0	0	0	0	0	0	0	0	0	0	0	0	0	0	0	0	0	0	0	0	0	0	0	0	0	0	0	0
0	0	0	0	0	0	0	0	0	0	1	0	0	0	0	0	0	0	0	0	0	0	0	0	0	0	0	0	0	0	0	0	0	0	0	0	0	0
0	0	0	0	0	0	0	0	0	0	0	0	1	1	-1	1	0	0	0	0	0	0	0	0	0	0	0	0	0	0	0	0	0	0	0	0	0	0
0	0	0	0	0	0	0	0	0	0	0	0	0	0	0	0	0	-1	1	1	0	0	0	0	0	0	0	0	0	0	0	0	0	0	0	0	0	0
0	0	0	0	0	0	0	0	0	0	0	0	0	0	0	0	1	0	0	0	0	0	0	0	0	0	0	0	0	0	0	0	0	0	0	0	0	0
0	0	0	0	0	0	0	0	0	0	0	0	0	0	0	0	-1	1	0	0	0	0	0	0	0	0	0	0	0	0	0	0	0	0	0	0	0	0
0	0	0	0	0	0	0	0	0	0	0	0	0	0	0	0	0	0	0	0	1	1	0	0	0	0	0	0	0	0	0	0	0	0	0	0	0	0
0	0	0	0	0	0	0	0	0	0	0	0	0	0	0	0	0	0	0	0	-1	0	0	1	0	0	0	0	0	0	0	0	0	0	0	0	0	0
0	0	0	0	0	0	0	0	0	0	0	0	0	0	0	0	0	0	0	0	0	0	0	0	-1	0	1	0	0	0	0	0	0	0	0	0	0	0
0	0	0	0	0	0	0	0	0	0	0	0	0	0	0	0	0	0	0	0	0	0	0	0	0	-1	1	0	0	0	0	0	0	0	0	0	0	0
0	0	0	0	0	0	0	0	0	0	0	0	0	0	0	0	0	0	0	0	0	0	0	0	0	0	0	1	0	0	0	0	0	0	0	0	0	0
0	0	0	0	0	0	0	0	0	0	0	0	0	0	0	0	0	0	0	0	0	0	0	0	0	0	0	0	1	0	0	0	0	0	0	0	0	0
0	0	0	0	0	0	0	0	0	0	0	0	0	0	0	0	0	0	0	0	0	0	0	0	0	0	0	0	0	1	0	0	0	0	0	0	0	0
0	0	0	0	0	0	0	0	0	0	0	0	0	0	0	0	0	0	0	0	0	0	0	0	0	0	0	0	0	0	1	0	0	0	0	0	0	0
0	0	0	0	0	0	0	0	0	0	0	0	0	0	0	0	0	0	0	0	0	0	0	0	0	0	0	0	0	0	0	1	0	0	0	0	0	0
0	0	0	0	0	0	0	0	0	0	0	0	0	0	0	0	0	0	0	0	0	0	0	0	0	0	0	0	0	0	0	0	1	0	0	0	0	0
0	0	0	0	0	0	0	0	0	0	0	0	0	0	0	0	0	0	0	0	0	0	0	0	0	0	0	0	0	0	0	0	0	1	0	0	0	0
0	0	0	0	0	0	0	0	0	0	0	0	0	0	0	0	0	0	0	0	0	0	0	0	0	0	0	0	0	0	0	0	0	0	1	0	0	0
0	0	0	0	0	0	0	0	0	0	0	0	0	0	0	0	0	0	0	0	0	0	0	0	0	0	0	0	0	0	0	0	0	0	0	1	0	0
0	0	0	0	0	0	0	0	0	0	0	0	0	0	0	0	0	0	0	0	0	0	0	0	0	0	0	0	0	0	0	0	0	0	0	0	1	0
0	0	0	0	0	0	0	0	0	0	0	0	0	0	0	0	0	0	0	0	0	0	0	0	0	0	0	0	0	0	0	0	0	0	0	0	0	1

Industrial Plant

$$
\alpha = \left|\begin{array}{cccccccccccccccccccccccccccccccccccccc}
1 & 0 & 0 & 0 & 0 & 0 & 0 & 0 & 0 & 0 & 0 & 0 & 0 & 0 & 0 & 0 & 0 & 0 & 0 & 0 & 0 & 0 & 0 & 0 & 0 & 0 & 0 & 0 & 0 & 0 & 0 & 0 & 0 & 0 & 0 & 0 & 0 & 0 \\
0 & 1 & 0 & 0 & 0 & 0 & 0 & 0 & 0 & 0 & 0 & 0 & 0 & 0 & 0 & 0 & 0 & 0 & 0 & 0 & 0 & 0 & 0 & 0 & 0 & 0 & 0 & 0 & 0 & 0 & 0 & 0 & 0 & 0 & 0 & 0 & 0 & 0 \\
0 & 0 & 1 & 0 & 0 & 0 & 0 & 0 & 0 & 0 & 0 & 0 & 0 & 0 & 0 & 0 & 0 & 0 & 0 & 0 & 0 & 0 & 0 & 0 & 0 & 0 & 0 & 0 & 0 & 0 & 0 & 0 & 0 & 0 & 0 & 0 & 0 & 0 \\
0 & 0 & 0 & 1 & 0 & 0 & 0 & 0 & 0 & 0 & 0 & 0 & 0 & 0 & 0 & 0 & 0 & 0 & 0 & 0 & 0 & 0 & 0 & 0 & 0 & 0 & 0 & 0 & 0 & 0 & 0 & 0 & 0 & 0 & 0 & 0 & 0 & 0 \\
0 & 0 & 0 & 0 & 0 & 1 & 0 & 0 & 0 & 0 & 0 & 0 & 0 & 0 & 0 & 0 & 0 & 0 & 0 & 0 & 0 & 0 & 0 & 0 & 0 & 0 & 0 & 0 & 0 & 0 & 0 & 0 & 0 & 0 & 0 & 0 & 0 & 0 \\
0 & 0 & 0 & 0 & 0 & 0 & 1 & 0 & 0 & 0 & 0 & 0 & 0 & 0 & 0 & 0 & 0 & 0 & 0 & 0 & 0 & 0 & 0 & 0 & 0 & 0 & 0 & 0 & 0 & 0 & 0 & 0 & 0 & 0 & 0 & 0 & 0 & 0 \\
0 & 0 & 0 & 0 & 0 & 0 & 0 & 0 & 1 & 0 & 0 & 0 & 0 & 0 & 0 & 0 & 0 & 0 & 0 & 0 & 0 & 0 & 0 & 0 & 0 & 0 & 0 & 0 & 0 & 0 & 0 & 0 & 0 & 0 & 0 & 0 & 0 & 0 \\
0 & 0 & 0 & 0 & 0 & 0 & 0 & 0 & 0 & 0 & 0 & 0 & 0 & 0 & 1 & 0 & 0 & 0 & 0 & 0 & 0 & 0 & 0 & 0 & 0 & 0 & 0 & 0 & 0 & 0 & 0 & 0 & 0 & 0 & 0 & 0 & 0 & 0 \\
0 & 0 & 0 & 0 & 0 & 0 & 0 & 0 & 0 & 0 & 0 & 0 & 0 & 0 & 0 & 0 & 0 & 0 & 0 & 0 & 1 & 0 & 0 & 0 & 0 & 0 & 0 & 0 & 0 & 0 & 0 & 0 & 0 & 0 & 0 & 0 & 0 & 0 \\
0 & 0 & 0 & 0 & 0 & 0 & 0 & 0 & 0 & 0 & 0 & 0 & 0 & 0 & 0 & 0 & 0 & 0 & 0 & 0 & 0 & 0 & 0 & 1 & 0 & 0 & 0 & 0 & 0 & 0 & 0 & 0 & 0 & 0 & 0 & 0 & 0 & 0 \\
0 & 0 & 0 & 0 & 0 & 0 & 0 & 0 & 0 & 0 & 0 & 0 & 0 & 0 & 0 & 0 & 0 & 0 & 0 & 0 & 0 & 0 & 0 & 0 & 0 & 1 & 0 & 0 & 0 & 0 & 0 & 0 & 0 & 0 & 0 & 0 & 0 & 0 \\
0 & 0 & 0 & 0 & 0 & 0 & 0 & 0 & 0 & 0 & 0 & 0 & 0 & 0 & 0 & 0 & 0 & 0 & 0 & 0 & 0 & 0 & 0 & 0 & 0 & 0 & 1 & 0 & 0 & 0 & 0 & 0 & 0 & 0 & 0 & 0 & 0 & 0 \\
0 & 0 & 0 & 0 & 0 & 0 & 0 & 0 & 0 & 0 & 0 & 0 & 0 & 0 & 0 & 0 & 0 & 0 & 0 & 0 & 0 & 0 & 0 & 0 & 0 & 0 & 0 & 0 & 0 & 0 & 0 & 0 & 0 & 1 & 0 & 0 & 0 & 0 \\
0 & 0 & 0 & 0 & 0 & 0 & 0 & 0 & 0 & 0 & 0 & 0 & 0 & 0 & 0 & 0 & 0 & 0 & 0 & 0 & 0 & 0 & 0 & 0 & 0 & 0 & 0 & 0 & 0 & 0 & 0 & 0 & 0 & 0 & 0 & 1 & 0 & 0 \\
0 & 0 & 0 & 0 & 0 & 0 & 0 & 0 & 0 & 0 & 0 & 0 & 0 & 0 & 0 & 0 & 0 & 0 & 0 & 0 & 0 & 0 & 0 & 0 & 0 & 0 & 0 & 0 & 0 & 0 & 0 & 0 & 0 & 0 & 0 & 0 & 1 & 0 \\
0 & 0 & 0 & 0 & 0 & 0 & 0 & 0 & X_1 & 0 & 1 & 0 & 0 & 0 & 0 & 0 & 0 & 0 & 0 & 0 & 0 & 0 & 0 & 0 & 0 & 0 & 0 & 0 & 0 & 0 & 0 & 0 & 0 & 0 & 0 & 0 & 0 & 0 \\
0 & 0 & 0 & 0 & 0 & 0 & 0 & 0 & 0 & 0 & 0 & 0 & 1 & -X_2 & 0 & 0 & 0 & 0 & 0 & 0 & 0 & 0 & 0 & 0 & 0 & 0 & 0 & 0 & 0 & 0 & 0 & 0 & 0 & 0 & 0 & 0 & 0 & 0 \\
0 & 0 & 0 & 0 & 0 & 0 & 0 & 0 & 0 & 0 & 0 & 0 & 0 & -X_3 & -1 & 1 & 0 & 0 & 0 & 0 & 0 & 0 & 0 & 0 & 0 & 0 & 0 & 0 & 0 & 0 & 0 & 0 & 0 & 0 & 0 & 0 & 0 & 0 \\
0 & 0 & 0 & 0 & 0 & 0 & 0 & 0 & 0 & 0 & 0 & 0 & 0 & 0 & 0 & 0 & 0 & 0 & 0 & 0 & 0 & 1 & -X_4 & 0 & 0 & 0 & 0 & 0 & 0 & 0 & 0 & 0 & 0 & 0 & 0 & 0 & 0 & 0 \\
0 & 0 & 0 & 0 & 0 & 0 & 0 & 0 & 0 & 0 & 0 & 0 & 0 & 0 & 0 & 0 & 0 & X_5 & -X_5 & 1 & 0 & 0 & 0 & 0 & 0 & 0 & 0 & 0 & 0 & 0 & 0 & 0 & 0 & 0 & 0 & 0 & 0 & 0 \\
0 & 0 & 0 & 0 & 0 & 0 & 0 & 0 & 0 & 0 & 0 & 0 & 0 & 0 & 0 & 0 & 0 & 0 & 0 & 0 & 0 & 0 & 0 & 0 & 0 & 0 & 0 & 0 & 0 & 1 & -X_6 & 0 & 0 & 0 & 0 & 0 & 0 & 0 \\
0 & 0 & 0 & 0 & 0 & 0 & 0 & 0 & 0 & 0 & 0 & 0 & 0 & 0 & 0 & 0 & 0 & 0 & 0 & 0 & 0 & 0 & 0 & 0 & 0 & 0 & 0 & 0 & 0 & 0 & 1 & -X_7 & 0 & 0 & 0 & 0 & 0 & 0
\end{array}\right|
$$

$$x1 = \frac{\dot{E}_{10}}{\dot{E}_{12}} \qquad x2 = \frac{\dot{E}_{13}}{\dot{E}_{14}} \qquad x3 = \frac{\dot{E}_{14}}{\dot{E}_{16} - \dot{E}_{15}} \qquad x4 = \frac{\dot{E}_{22}}{\dot{E}_{23}} \qquad x5 = \frac{\dot{E}_{20}}{\dot{E}_{19} - \dot{E}_{18}} \qquad x6 = \frac{\dot{E}_{30}}{\dot{E}_{31}} \qquad x6 = \frac{\dot{E}_{31}}{\dot{E}_{32}}$$

Lab-scale pyrolysis Plant

$$A\ (8x21) = \begin{vmatrix} 0 & 0 & 0 & 0 & 1 & 0 & 0 & 1 & 1 & 0 & 1 & -1 & 0 & -1 & 0 & 0 & 0 & 0 & 0 & 0 & 0 \\ 1 & 1 & 1 & 1 & -1 & 1 & 0 & 0 & 0 & 0 & 0 & 0 & 0 & 0 & 0 & 0 & 0 & 0 & 0 & 0 & 0 \\ 0 & 0 & 0 & 0 & 0 & 0 & 1 & -1 & 0 & 0 & 0 & 0 & 0 & 0 & 0 & 0 & 0 & 0 & 0 & 0 & 0 \\ 0 & 0 & 0 & 0 & 0 & 0 & 0 & 0 & 0 & 1 & -1 & 0 & 0 & 0 & 0 & 0 & 0 & 0 & 0 & 0 & 0 \\ 0 & 0 & 0 & 0 & 0 & 0 & 0 & 0 & 0 & 0 & 0 & 1 & -1 & 0 & 0 & 0 & 0 & 0 & 0 & 0 & 0 \\ 0 & 0 & 0 & 0 & 0 & 0 & 0 & 0 & 0 & 0 & 0 & 0 & 0 & 1 & -1 & -1 & 1 & -1 & 0 & 0 & 0 \\ 0 & 0 & 0 & 0 & 0 & 0 & 0 & 0 & 0 & 0 & 0 & 0 & 0 & 0 & 0 & 1 & 0 & 0 & 1 & -1 & 0 \\ 0 & 0 & 0 & 0 & 0 & 0 & 0 & 0 & 0 & 0 & 0 & 0 & 0 & 0 & 0 & 0 & 0 & 0 & 0 & 1 & -1 \end{vmatrix}$$

$$A_F\ (8x21) = \begin{vmatrix} 0 & 0 & 0 & 0 & 1 & 0 & 0 & 1 & 1 & 0 & 1 & 0 & 0 & 0 & 0 & 0 & 0 & 0 & 0 & 0 & 0 \\ 1 & 1 & 1 & 1 & 0 & 1 & 0 & 0 & 0 & 0 & 0 & 0 & 0 & 0 & 0 & 0 & 0 & 0 & 0 & 0 & 0 \\ 0 & 0 & 0 & 0 & 0 & 0 & 1 & 0 & 0 & 0 & 0 & 0 & 0 & 0 & 0 & 0 & 0 & 0 & 0 & 0 & 0 \\ 0 & 0 & 0 & 0 & 0 & 0 & 0 & 0 & 0 & 1 & 0 & 0 & 0 & 0 & 0 & 0 & 0 & 0 & 0 & 0 & 0 \\ 0 & 0 & 0 & 0 & 0 & 0 & 0 & 0 & 0 & 0 & 0 & 1 & 0 & 0 & 0 & 0 & 0 & 0 & 0 & 0 & 0 \\ 0 & 0 & 0 & 0 & 0 & 0 & 0 & 0 & 0 & 0 & 0 & 0 & 0 & 1 & 0 & 0 & 0 & 0 & 0 & 0 & 0 \\ 0 & 0 & 0 & 0 & 0 & 0 & 0 & 0 & 0 & 0 & 0 & 0 & 0 & 0 & 0 & 1 & 0 & 0 & 1 & 0 & 0 \\ 0 & 0 & 0 & 0 & 0 & 0 & 0 & 0 & 0 & 0 & 0 & 0 & 0 & 0 & 0 & 0 & 0 & 0 & 0 & 1 & 0 \end{vmatrix}$$

$$A_P\ (8x21) = \begin{vmatrix} 0 & 0 & 0 & 0 & 0 & 0 & 0 & 0 & 0 & 0 & 0 & 1 & 0 & 1 & 0 & 0 & 0 & 0 & 0 & 0 & 0 \\ 0 & 0 & 0 & 0 & 1 & 0 & 0 & 0 & 0 & 0 & 0 & 0 & 0 & 0 & 0 & 0 & 0 & 0 & 0 & 0 & 0 \\ 0 & 0 & 0 & 0 & 0 & 0 & 0 & 1 & 0 & 0 & 0 & 0 & 0 & 0 & 0 & 0 & 0 & 0 & 0 & 0 & 0 \\ 0 & 0 & 0 & 0 & 0 & 0 & 0 & 0 & 0 & 0 & 1 & 0 & 0 & 0 & 0 & 0 & 0 & 0 & 0 & 0 & 0 \\ 0 & 0 & 0 & 0 & 0 & 0 & 0 & 0 & 0 & 0 & 0 & 0 & 1 & 0 & 0 & 0 & 0 & 0 & 0 & 0 & 0 \\ 0 & 0 & 0 & 0 & 0 & 0 & 0 & 0 & 0 & 0 & 0 & 0 & 0 & 0 & 1 & 1 & -1 & 1 & 0 & 0 & 0 \\ 0 & 0 & 0 & 0 & 0 & 0 & 0 & 0 & 0 & 0 & 0 & 0 & 0 & 0 & 0 & 0 & 0 & 0 & 0 & 1 & 0 \\ 0 & 0 & 0 & 0 & 0 & 0 & 0 & 0 & 0 & 0 & 0 & 0 & 0 & 0 & 0 & 0 & 0 & 0 & 0 & 0 & 1 \end{vmatrix}$$

$$\alpha\ (13x21) = \begin{vmatrix} 1 & 0 & 0 & 0 & 0 & 0 & 0 & 0 & 0 & 0 & 0 & 0 & 0 & 0 & 0 & 0 & 0 & 0 & 0 & 0 & 0 \\ 0 & 1 & 0 & 0 & 0 & 0 & 0 & 0 & 0 & 0 & 0 & 0 & 0 & 0 & 0 & 0 & 0 & 0 & 0 & 0 & 0 \\ 0 & 0 & 1 & 0 & 0 & 0 & 0 & 0 & 0 & 0 & 0 & 0 & 0 & 0 & 0 & 0 & 0 & 0 & 0 & 0 & 0 \\ 0 & 0 & 0 & 1 & 0 & 0 & 0 & 0 & 0 & 0 & 0 & 0 & 0 & 0 & 0 & 0 & 0 & 0 & 0 & 0 & 0 \\ 0 & 0 & 0 & 0 & 0 & 1 & 0 & 0 & 0 & 0 & 0 & 0 & 0 & 0 & 0 & 0 & 0 & 0 & 0 & 0 & 0 \\ 0 & 0 & 0 & 0 & 0 & 0 & 1 & 0 & 0 & 0 & 0 & 0 & 0 & 0 & 0 & 0 & 0 & 0 & 0 & 0 & 0 \\ 0 & 0 & 0 & 0 & 0 & 0 & 0 & 0 & 1 & 0 & 0 & 0 & 0 & 0 & 0 & 0 & 0 & 0 & 0 & 0 & 0 \\ 0 & 0 & 0 & 0 & 0 & 0 & 0 & 0 & 0 & 1 & 0 & 0 & 0 & 0 & 0 & 0 & 0 & 0 & 0 & 0 & 0 \\ 0 & 0 & 0 & 0 & 0 & 0 & 0 & 0 & 0 & 0 & 0 & 0 & 0 & 0 & 0 & 0 & 1 & 0 & 0 & 0 & 0 \\ 0 & 0 & 0 & 0 & 0 & 0 & 0 & 0 & 0 & 0 & 0 & 0 & 0 & 0 & 0 & 0 & 0 & 0 & 1 & 0 & 0 \\ 0 & 0 & 0 & 0 & 0 & 0 & 0 & 0 & 0 & 0 & 0 & 1 & 0 & -X_1 & 0 & 0 & 0 & 0 & 0 & 0 & 0 \\ 0 & 0 & 0 & 0 & 0 & 0 & 0 & 0 & 0 & 0 & 0 & 0 & 0 & 0 & 1 & -X_2 & 0 & 0 & 0 & 0 & 0 \\ 0 & 0 & 0 & 0 & 0 & 0 & 0 & 0 & 0 & 0 & 0 & 0 & 0 & 0 & 0 & 1 & X_3 & -X_3 & 0 & 0 & 0 \end{vmatrix}$$

$$x1 = \frac{\dot{E}_{12}}{\dot{E}_{14}} \qquad x2 = \frac{\dot{E}_{15}}{\dot{E}_{16}} \qquad x1 = \frac{\dot{E}_{18} - \dot{E}_{17}}{\dot{E}_{16}}$$

Vectors containing the exergy characteristics of external resources

Industrial Plant

$$\omega_{\text{Refence Process}} = \begin{vmatrix} E_1 \\ E_2 \\ E_3 \\ E_4 \\ E_6 \\ E_7 \\ E_9 \\ E_{15} \\ E_{21} \\ E_{24} \\ E_{26} \\ E_{27} \\ E_{34} \\ 0 \\ 0 \\ 0 \\ 0 \\ 0 \\ 0 \end{vmatrix} \qquad \omega_{\text{Alternative Process}} = \begin{vmatrix} E_1 \\ E_2 \\ E_3 \\ E_4 \\ E_6 \\ E_7 \\ E_9 \\ E_{15} \\ E_{21} \\ E_{24} \\ E_{26} \\ E_{27} \\ E_{34} \\ E_{36} \\ E_{37} \\ 0 \\ 0 \\ 0 \\ 0 \\ 0 \\ 0 \end{vmatrix}$$

Lab-scale plant

$$\omega = \begin{vmatrix} E_1 \\ E_2 \\ E_3 \\ E_4 \\ E_6 \\ E_7 \\ E_9 \\ E_{10} \\ E_{17} \\ E_{19} \\ 0 \\ 0 \\ 0 \end{vmatrix}$$

E4. Results

Table E2. Thermodynamic properties of the streams in the model industrial pyrolysis plant

Stream	Temperature (ºC)		Pressure (kPa)		$\dot{m}$ (kg/h)		$\dot{H}$ (kW)		$\dot{E}$ (kW)	
	Ref.	Alt.	Ref.	Alt.	Ref.	Alt.	Ref.	Alt.	Ref.	Alt.
1	25	25	101.3	101.3	299.52	299.52	3502	3502	3742.337	3742.337
2	25	25	101.3	101.3	332.496	332.496	4169	4169	4449.337	4449.337
3	25	25	101.3	101.3	299.012	299.016	2647	2647	2762.337	2762.337
4	25	25	101.3	101.3	69.01	69.01	0.00	0.00	0.00	0.00
5	25	25	101.3	101.3	1000.08	1000.08	10317	10317	10954	10954
6	--	--	--	--	--	--	0.01	0.01	0.01	0.01
7	--	--	--	--	--	--	0.013	0.013	0.013	0.013
8	--	--	--	--	--	--	0.012	0.012	0.012	0.012
9	25	25	120	120	20.30	20.30	1.74	1.74	0.085	0.085
10	700	700	101.3	101.3	367.92	518.04	2947	2964	3040	3053
11	700	700	101.3	101.3	367.92	518.04	2947	2964	3040	3053
12	700	700	120	120	632.16	632.16	7984	7986	7879	7870
13	70	70	101.3	101.3	470.88	470.88	5355	5355	5627	5627
14	70	70	101.3	101.3	181.30	181.30	2389	2407	2129	2129
15	25	25	101.3	101.3	10342.80	9630	0.00	0.00	0.00	0.00
16	60	60	101.3	101.3	10342.80	9630	240.40	223.90	22.92	21.34
17	25	25	101.3	101.3	16.00	16.00	0.00	0.00	0.00	0.00
18	25	25	130	130	16.00	16.00	0.47	0.47	0.000128	0.000128
19	25	25	101.3	101.3	34.64	18.26	0.00	0.00	0.00015	0.00013
20	25	25	101.3	101.3	162.648	179.03	2389	2414	2127	2126
21	--	--	--	--	--	--	0.00032	0.00032	0.00032	0.00032
22	25	25	101.3	101.3	121.268	131.76	1699	1695	1513	1493
23	25	25	101.3	101.3	41.112	47.30	689.80	719.10	614	633
24	--	--	--	--	--	--	1.12	1.12	1.12	1.12
25	25	25	120	120	101.268	131.76	1700	1696	1514	1493
26	25	25	101.3	101.3	3288.24	3783.60	0.00	0.00	0.00	0.00
27	--	--	--	--	--	--	0.02	0.02	0.02	0.02
28	28.05	28.05	120	120	3288.24	3783.60	2.759	3.174	0.014	0.017
29	348.35	348.35	120	120	3288.24	3783.60	314.6	362	100.6	115.80
30	988.85	925.85	101.3	101.3	3329.28	3830.40	1002	1078	554.50	581.60
31	400.05	400.05	101.3	101.3	3329.28	3830.40	389.8	448.5	137.40	158.10
32	99.95	99.95	101.3	101.3	3329.28	3830.40	77.96	89.71	8.420	9.688
33	99.95	99.95	101.3	101.3	3329.28	3830.40	77.96	89.71	8.420	9.688
34	--	--	--	--	16.00	16.00	0.00	0.00	0.00	0.00
35	--	--	0.00	0.00	34.64	18.26	0	0.00	0.00015	0.00013
36	--	25	101.3	101.3	--	150.012	--	0.00	--	0.00
37	--	--	0.00	0.00	--	0.00	--	0.01	--	0.01
38	--	25	101.3	101.3	--	150.01	--	0.00	--	0.00

Table E3. Thermodynamic properties of the streams in the pyrolysis process

Stream	*Temperature (ºC)*	*Pressure (kPa)*	$\dot{m}$ *(g/s)*	$\dot{H}$ *(W)*	$\dot{E}$ *(W)*
1	25	101.3	0.097	4062	4341
2	25	101.3	0.11	4836	5161
3	25	101.3	0.097	3070	3204
4	25	101.3	0.02	0	0
5	25	101.3	0.32	11970	12706
6	25	101.3	--	1	1
7	--	--	--	1.23	1.23
8	--	--	--	1.17	1.17
9	25	120	0.0063	1.93	0.094
10	--	--	--	747.10	747.10
11	--	--	--	709.70	467.40
12	475	120	0.12	3493	3607
13	475	101.3	0.12	3493	3607
14	475	101.3	0.21	9165	9073
15	70	101.3	0.15	6210	6525
16	70	101.3	0.06	2771	2470
17	25	101.3	2.20	0.00	0.00
18	45	101.3	2.20	184.30	5.92
19	25	101.3	2.22	0.00	0.00
20	1106.85	101.3	2.28	2771	1597
21	1106.85	101.3	2.28	2771	1597

Table E4. Exergy balances for by component: Industrial-scale pyrolysis plant

Component	*Fuel (kW)*		*Product (kW)*		*Irreversibilities (kW)*		*% $E_{Destroyed}$*	
	Reference	*Alternative*	*Reference*	*Alternative*	*Reference*	*Alternative*	*Reference*	*Alternative*
Reactor	11371.20	11377.60	10919	10923	452.20	454.60	60.40	60.51
Feeding System	10954.02	10954.02	10954	10954	0.02	0.02	0.0028	0.0028
Electric Motor	0.01228	0.01228	0.01167	0.01167	0.00061	0.00061	0.000082	0.000081
rCB Receiver	3040.00	3053.00	3040.00	3053.00	0.00	0.00	0.00	0.00
Condenser	7879.00	7870.00	7778.92	7777.34	100.08	92.66	13.47	12.33
Scrubber	2129	2129	2127	2126	1.99	3.00	0.27	0.40
Solution Tank	0.00	0.00	0.00	0.00	0.00	0.00	0.00	0.00
Pump (Scrubber)	0.00032	0.00032	0.00013	0.00013	0.00019	0.00019	0.000025	0.000025
Separation Unit	2127	2126	2127	2126	0.00	0.00	0.00	0.00
Compressor TPG	1.12	1.12	1.00	1.00	0.12	0.12	0.012	0.015
Fan (Burner)	0.02	0.02	0.014	0.017	0.0062	0.0033	0.00084	0.00044
Preheater	128.98	148.41	100.59	115.78	28.40	32.63	3.82	4.34
Burner	714.60	748.80	554.50	581.60	160.10	167.20	21.55	22.26
Stack	8.42	9.69	8.42	9.69	0.00	0.00	0.00	0.00
Recycling Tank	0.00015	0.00013	0.00015	0.00013	0.00	0.00	0.00	0.00
Alternative Hopper	--	0.00013	--	0.00	--	0.00013	--	0.000017

Table E5. Exergy balances for by component: Lab-scale pyrolysis plant

Component	Fuel (W)	Product (W)	Irreversibilities (W)	% $E_{Destroyed}$
Reactor	13174.66	12680.00	494.66	28.75
Feeding System	12707	12706.00	1.00	0.06
Electric Motor	1.228	1.167	0.061	0.00
Electric Heater	747.10	467.40	279.70	16.26
rCB Receiver	3607.00	3607.00	0.00	0.00
Condenser	9073.00	9000.92	72.08	4.19
TPG Burner	2470.00	1597.00	873.00	50.74
Stack	1597.00	1597.00	0.00	0.00

Table E6. Exergy decomposition

Stream	*Natural Rubber*	*Synthetic Rubber*	*Carbon Black*	*Total*	*Exergy Distribution*	
	E_1 (kW)	*E_2 (kW)*	*E_3 (kW)*	*E_T (kW)*	*Renewable (%)*	*Fossil (%)*
1	3742.33700	0.00	0.00	3742.34	100	0
2	0.00	4449.34	0.00	4449.34	0.00	100
3	0.00	0.00	2762.34	2762.34	0.00	100
4	0.00	0.00	0.00	0.00	--	--
5	3742.33	4449.33	2762.33	10953.99	34.16	65.84
6	0.00	0.00	0.00	0.00	--	--
7	0.00	0.00	0.00	0.00	--	--
8	0.00	0.00	0.00	0.00	--	--
9	0.00	0.00	0.00	0.00	--	--
10	0.00	0.00	3039.97	3039.97	0.00	100
11	0.00	0.00	3039.97	3039.97	0.00	100
12	3685.20	4193.72	0.00	7878.92	46.77	53.23
13	2631.88	2995.06	0.00	5626.94	46.77	53.23
14	995.78	1133.19	0.00	2128.98	46.77	53.23
15	0.00	0.00	0.00	0.00	--	--
16	10.72	12.20	0.00	22.92	46.77	53.23
17	0.00	0.00	0.00	0.00	--	--
18	0.00	0.00	0.00	0.00	--	--
19	0.00001	0.00001	0.00	0.00002	46.77	53.23
20	994.85	1132.13	0.00	2126.98	46.77	53.23
21	0.00	0.00	0.00	0.00	--	--
22	707.67	805.32	0.00	1512.98	46.77	53.23
23	287.18	326.81	0.00	613.99	46.77	53.23
24	0.00	0.00	0.00	0.00	--	--
25	707.67	805.32	0.00	1512.98	46.77	53.23
26	0.00	0.00	0.00	0.00	--	--
27	0.00	0.00	0.00	0.00	--	--
28	0.00	0.00	0.00	0.00	--	--
29	47.05	53.54	0.00	100.58	46.77	53.23
30	259.35	295.13	0.00	554.48	46.77	53.23

Stream	Natural Rubber	Synthetic Rubber	Carbon Black	Total	Exergy Distribution	
	E_1 (kW)	E_2 (kW)	E_3 (kW)	E_T (kW)	Renewable (%)	Fossil (%)
31	64.26	73.13	0.00	137.40	46.77	53.23
32	3.94	4.48	0.00	8.42	46.77	53.23
33	3.94	4.48	0.00	8.42	46.77	53.23
34	0.00	0.00	0.00	0.00	--	--
35	0.00001	0.00001	0.00	0.00002	46.77	53.23

References

[1] X. Wang, W. Lv, L. Guo, M. Zhai, P. Dong, G. Qi, Energy and exergy analysis of rice husk high-temperature pyrolysis, Int. J. Hydrogen Energy. 41 (2016) 21121–21130.

[2] Y. Zhang, G. Ji, D. Ma, C. Chen, Y. Wang, W. Wang, A. Li, Exergy and energy analysis of pyrolysis of plastic wastes in rotary kiln with heat carrier, Process Saf. Environ. Prot. 142 (2020) 203–211.

[3] S.E. Jorgensen, Exergy, in: Syst. Ecol., 2008: pp. 1498–1509.

[4] M. Atienza-Martínez, J. Abrego, J.F. Mastral, J. Ceamanos, G. Gea, Energy and exergy analyses of sewage sludge thermochemical treatment, Energy. 144 (2018) 723–735.

[5] Y. Tang, J. Dong, Y. Chi, Z. Zhou, M. Ni, Energy and exergy analyses of fluidized-bed municipal solid waste air gasification, Energy Fuels. 30 (2016) 7629−7637.

[6] S.C. Kaushik, O.K. Singh, Estimation of chemical exergy of solid, liquid and gaseous fuels used in thermal power plants, J. Therm. Anal. Calorim. 115 (2014) 903–908.

[7] M.A. Lozano, A. Valero, Theory of exergy cost, Energy. 18 (1993) 939–960.

[8] A. Valero, S. Usón, C. Torres, W. Stanek, Theory of exergy cost and thermo-ecological, in: Thermodyn. Sustain. Manag. Nat. Resour., Springer, 2017: pp. 167–202.

[9] J.L. Silveira, C.E. Tuna, Thermoeconomic analysis method for optimization of combined heat and power systems. Part I, Prog. Energy Combust. Sci. 29 (2003) 479–485.

[10] Niuetech, Tire pyrolysis plant, (2020). https://www.pyrolysistooil.com/ (accessed November 12, 2020).

[11] Weg, Electric motors, (2020). https://www.weg.net/institutional/RO/en/ (accessed November 12, 2020).

[12] Honeywell, UnitSim Design R461.1 Cost and Size Analyzer, (2018).

[13] YARA, Exhaust gas cleaning technology, (2020). https://yaramarine.com/exhaust-gas-cleaning-technology/?gclid=CjwKCAiA17P9BRB2EiwAMvwNyCutfAc0qTjTMC_xXqqzs5zV-TO0hFordWCQ57jGu7Qtd_G4WM-sTBoCE3IQAvD_BwE (accessed November 12, 2020).

[14] A. Agudelo, A. Valero, S. Usón, The fossil trace of CO2 emissions in multi-fuel energy systems, Energy. 58 (2013) 236–246.